Examining Soil Based Construction Materials through X-Ray Computed Tomography

JONATHAN CHASE SMITH

Examining Soil Based Construction Materials through X-Ray Computed Tomography

Jonathan Chase Smith

Thesis submitted for the
degree of Doctor of Philosophy

Mechanics Group
School of Engineering
and Computing Sciences
Durham University
United Kingdom

May 2015

Examining Soil Based Construction Materials through X-Ray Computed Tomography

Jonathan Chase Smith

Abstract

X-ray computed tomography (XRCT) enables the non-destructive analysis of samples internal structures down to a sub-micron resolution and has been used to examine the macrostructure of unstabilized soil based construction materials (SBCMs) alongside experiments on the materials unconfined compressive strength. SBCMs are manufactured mixtures of clay, sand and gravel which should be considered as highly unsaturated compacted soil where suction is the key source of strength. The use of XRCT in geotechnical literature is comprehensively reviewed before three laboratory investigations are described. Firstly crack propagation in SBCMs following unconfined compression is investigated and key lessons about XRCT scanning highlighted. Secondly the impact of altering sample size to match optimum XRCT scanning conditions is explored through experiments on void size distribution and unconfined compressive strength. Finally the effects of adding expansive clay to SBCM mixes on macrostructure are investigated and insights on how the unconfined compressive strength develops as SBCM dries are given. Conclusions from this thesis have applicability to both the SBCM industry, as the insights into the fundamental behaviour of SBCM can be used to inform building practice, and geotechnical researchers where the extensive use and development of XRCT can be applied to investigate the internal structure of a wide range of geotechnical materials.

Declaration

The work in this thesis is based on research carried out in the Mechanics Group, School of Engineering and Computing Sciences, Durham University. No part of this report has been submitted elsewhere for any other degree or qualification and it is all my own work unless referenced to the contrary in the text.

Parts of this work have been published in the following:

Journals

J.C. Smith and C.E. Augarde. Optimum water content tests for Earthen Construction materials *Proceedings of the ICE: Construction Materials* 167(2): 114-123 (2014).

Technical Reports

J.C. Smith and C.E. Augarde. A new classification for soil mixtures with application to earthen construction *ECS Technical Reports* available online at http://www.dur.ac.uk/resources/ecs/research/technical reports/2013 04.pdf (2013).

Conferences

J.C. Smith and C.E. Augarde. The role of clay and sand in the mechanics of Soil-Based Construction Materials In *Rammed Earth Construction*, Proceedings of ICREC2015, Perth, Australia, 2015.

J.C. Smith and C.E. Augarde. XRCT Scanning of Unsaturated Soils: Microstructure at different scales? In *Geomechanics from Micro to Macro*, Proceedings of IS-Cambridge - From Micro to Macro, Cambridge, UK, 2014.

J.C. Smith, C.E. Augarde and C. Beckett. The use of XRCT to investigate highly unsaturated soil mixtures In *Unsaturated Soils: Research & Applications*,Proceedings of UNSAT2014, Sydney, Australia, 2014.

J.C. Smith. Determining the Optimum Water Content of Rammed Earth In *Proceedings of the Young Geotechnical Engineers Symposium 2012*, Young Geotechnical Engineers Symposium, Leeds, UK, 2012.

Acknowledgements

I would first like to thank Professor Charles Augarde for his constant support, patience and advice throughout my PhD. Charles, without your guidance and wisdom during our supervision meetings, our conversations on journeys to conferences and whilst we ate some amazing curry, this research would never have been possible and I want to offer my sincerest thanks.

I also want to thank all those around the department (Adam, JD, Jack, Chris, Tim, Andrew, Steve, Kev and Tom to name but a few) who have helped me throughout my PhD. The assistance given in the lab and the many conversations in the coffee bar and pub regarding research and the world at large have been invaluable. Thank you all for making the last four years in the engineering department a great place to be.

On a more formal and practical note, this research would not have been possible without generous funding from the UK Engineering and Physical Sciences Research Council (EPSRC) via the doctoral grant EP/J500215/1. I would also like to acknowledge the assistance provided by the Durham XRCT Facility, which was funded in part by the EPSRC (grants EP/K036084/1 & EP/K024698/1).

I can not write this without a big thank you my whole family and closest friends. Your support, love and prayers throughout my life have been amazing and I know could never have got to where I am today without you all. Thank you so much for believing in me and your willingness to hear me talk about mud and x-rays during this PhD has been astonishing, I promise I'll try not to talk about it so much any more!

Finally, and most importantly, I want to thank my wonderful fiancée Kathleen. When I started my PhD I always thought I would to do some research and hopefully get an academic qualification but I never dreamt at the end of the four years I would also have found my best friend and we would be starting a new chapter of our lives together here in Durham. Kathleen, thank you for always being there for me and loving me all the way.

Jonathan Smith
Durham, April 2015

Contents

List of Figures

List of Tables

Acronyms

SBCM	unstabilized soil based construction material
XRCT	laboratory x-ray computed tomography
MIP	mercury intrusion porosimetry
LR5K	Lloyd LR5K Plus testing machine
SS1174	SkyScan1174 compact micro-CT scanner
XRM410	XRadia/Zeiss XRM 410
df	dryness fraction
w_{opt}	optimum water content
ρ_{dmax}	maximum dry density

Chapter 1

Introduction

1.1 Soil based construction materials

Building in earth is one of the simplest and oldest building techniques using sub-soil to create earth structures which develop strength and durability as the water evaporates and the structure reaches equilibrium with the environmental conditions. A wide range of techniques exist which use different soil types, construction techniques and building traditions and can be categorised using two different descriptors. Firstly the soil used in construction is either: *stabilized*, in which other materials such as cement or lime are added to the soil mixture to improve the mechanical properties of the finished structure; or *unstabilized*, in which the particle size distribution or mineralogy of the soil may be altered through the sieving and mixing of different soils but no chemical stabilizer is added to the material. Secondly the form of construction is either *monolithic in-situ construction*, in which the soil is formed directly into a structure on site and left to dry, or *unit based construction*, in which independent units of soil are constructed, dried, transported and constructed into a wall using mortar following similar techniques to masonry construction. The different combinations of stabilized and unstabilized soil materials using monolithic and unit-based construction can be captured using the term *soil based construction materials* which includes the whole range of building techniques in which soil is the predominant construction material used.

Throughout this thesis only *unstabilized soil based construction materials* will be discussed and in these materials the particle-air-water interactions commonly studied in unsaturated soil mechanics provide the soil its strength. The manufacture of samples used in the experiments described in this thesis follows rammed earth construction (one of the most common soil based construction material construction techniques) guidelines however, by approaching the study of soil based construction materials from an unsaturated soil mechanics perspective, the findings are applicable to any unstabilized soil based construction material including unstabilized rammed earth, adobe, or compressed earth blocks. Throughout the remainder of this thesis, for brevity and consistency, when referring to a unstabilized soil based construction material the prefix 'unstabilized' will be dropped and the acronym SBCM used.

1.1.1 Construction techniques

All SBCM construction techniques, whether monolithic or unit-based, have the same key stages. Detailed descriptions of the four main SBCM construction techniques (rammed earth, cob, adobe and compressed earth brick) can be found in Jaquin and Augarde (2012) and the following is a summary of the information presented in that work. The five broad stages of SBCM techniques are as follows:

- Obtaining the raw unsaturated subsoil by the digging of the soil from the ground. The soil used in SBCMs is ideally taken from above the water table, ensuring the soil is not too wet for construction, and below the layer of topsoil, which contains large amounts of organic matter.
- Altering the soil to achieve the desired soil mix for manufacture. The particle size distribution and mineralogy of the soil mix is typically adjusted, through the sieving and mixing of a number of different raw soils, to ensure the soil used is suitable for the desired construction method.
- Wetting or drying the soil to ensure the soil is at the correct water content for construction. Typically the soil needs mixing with additional water and this was traditionally done through manually walking on the soil although is now more frequently done through mechanical means, i.e. rotary mixers.
- The moulding of the soil mixture, at the desired water content, into the appropriate shape for construction. This is either blocks for unit-based construction or continuous walls for monolithic structures.
- The equilibration of the SBCM to the environmental conditions and the development of strength. This is predominately a drying process immediately following manufacture which involves the evaporation of water.

In monolithic SBCM construction two basic methods exist depending on whether formwork is used to shape the walls or not. *Rammed earth* construction involves the compaction of the soil using hand or mechanical rammers in layers and once the formwork is filled with compacted soil it is removed to allow the rammed earth to dry, and then moved to a new location on-site and a different section of the wall is constructed. *Cob* construction involves the direct placement of soil, without any mould or formwork, and the treading or hand tamping of the wet soil to compact and shape the wall. Cob walls are between 0.5m and 1m thick and can taper as the wall rises whilst rammed earth walls are typically 300-400mm thick and a constant thickness for their entire height. Soil used in rammed earth contains a range of particle sizes from 10mm diameter gravel down to clay particles whilst cob soils contain fewer gravel sized particles, are compacted at higher water contents and straw can be added to provide resistance to cracking and improve post-failure response.

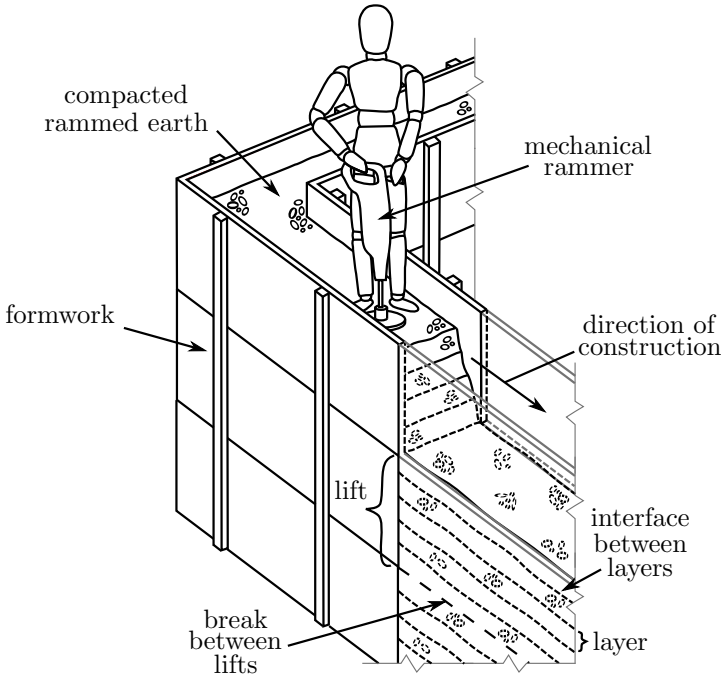

Figure 1.1: A simplified sketch of rammed earth construction.

In unit-based construction the significant difference between the building techniques is found in the compaction effort applied to the SBCM block (or 'unit') during construction. *Adobe* blocks are formed through the filling of a mould with wet soil following which the blocks are allowed to dry slightly before the mould is removed and adobe block left to dry completely. Typically the soils used in adobe construction contain more clay than rammed earth and cob, and can contain straw to resist shrinking. Crucially, however, in adobe construction no compaction force is applied to the blocks during manufacture whilst in *compressed earth blocks* the blocks are manufactured using a press which imparts a large compressive force on the block during moulding. The increased compactive effort used means a lower water content is required during manufacture and the finished manufactured block has a higher dry density than an adobe block. For all in-situ construction techniques, similar bond patterns are used as in masonry construction, and the mortar to secure the blocks is manufactured from a similar soil mixture to that used in the manufacture of the blocks.

1.1.2 Rammed earth construction

A very thorough description of the history and development of the rammed earth building technique can be found in Jaquin et al. (2008) and a summary of this work, with the addition of new evidence and an updated map of key regions in the development of rammed earth, can be found in Beckett (2011). Figure 1.1 is a sketch of the rammed earth construction technique and shows the use of formwork, the presence of *layers* and *lifts* within the wall and the use of a mechanical rammer to compact the

soil. The formwork used in modern rammed earth construction is very similar to that used in concrete construction and provides the shape of the rammed earth structure. Once a formwork block has been filled with compacted rammed earth the boards are removed, to allow the rammed earth to dry, and construction of the the wall at another location is performed. This sequential compaction of sections of rammed earth wall results in distinct repeated *lifts* visible in a wall arising from the use of formwork of a fixed size. In some rammed earth construction techniques, where formwork is supported on timbers placed on the rammed earth wall of the lift below, holes can be visible denoting the vertical height of each lift. Within each lift of rammed earth distinct layers are also visible because the wall is typically compacted in 100mm thick layers to ensure a constant density of the soil throughout its entire height. The rammer used in modern rammed earth construction will often be a pneumatic or electric hammer, fitted with a flat rectangular foot plate, which produces a more consistent and higher density compacted wall than traditional hand tampers.

Many different guidelines exist which provide advice on rammed earth construction covering a wide range of information including: soil suitability, in terms of particle size, plasticity and colour; architectural design features, including the use of render or large roof overhangs to prevent weathering; and construction techniques and traditionally used on-site tests (Houben and Guillaud, 1989; Maniatidis and Walker, 2003). Rigorous national building standards exist in New Zealand for the design and construction of earth buildings which provide clear performance driven criteria for SBCM structures, including a minimum compressive strength of 1.3MPa, a maximum floor live load not exceeding 1.5kN/m^2 and more general requirements regarding reinforcement and bracing design, surface finish and quality control (Standards New Zealand, 1998). National handbooks for the design of rammed earth structures also exist in Australia (Standards-Australia, 2002), Germany (Dachverband et al., 1999) and New Mexico (New-Mexico-Standards, 1991) which set out the principles of accepted good practice for rammed earth construction although without national building code status. The lack of rigorous national building codes for rammed earth and SBCMs in general, in all countries excluding New Zealand, is due in part to a lack of understanding and awareness of SBCMs by practising engineers and architects and the minimal academic research performed into classifying and understanding the behaviour of SBCMs.

In a geotechnical context there are two key elements of SBCM guidance which have particular relevance to sample manufacture: the selection of soil for construction and the determination of water content for compaction. The following two sections provide a brief discussion on these two aspects of SBCM construction before a final section which provides an overview of the academic research performed into SBCMs.

1.1.3 Soil suitability

Table 1.1 shows the range of different minimum and maximum percentage values by mass given for the proportions of clay, silt, sand and gravel content within rammed earth in different construction handbooks, as collected by Maniatidis and Walker (2003). It is clear from Table 1.1 that despite individual guidelines providing small ranges for acceptable particle size percentages there is no clear consensus on particle size limits for SBCMs, although the clay content should not exceed 35% and the sand and gravel content, excluding the limits in Alley (1955), should be greater than 45%. The description of the particle size of SBCMs using only the clay, silt and combined sand and gravel fractions also provides little indication of variability within a soil mix and the proportions of sand and gravel as separate particle fractions. A soil mixture classification for SBCMs is proposed in Smith and Augarde (2013a) which provides more information regarding the soil fractions within a SBCM mix and has four key steps:

- *Particle classification* according to EN ISO 14688-1:2002 section 4.2 (British-Standards, 2002). The four soil fractions within SBCMs are defined as clay (2μm< Cl), silt (2μm≤ Si <63μm), sand (63μm≤ Sa <2mm) and gravel (2.0mm≤ Gr <10mm), since SBCM mixes are typically sieved to less than 10mm.
- *Mix specification* which states the intended proportions by mass of the soil fractions with the SBCM mix of interest as Cl:Si:Sa:Gr. Where no specific silt content is required the silt and clay fractions are combined, indicated using an asterisk, as follows (Cl+Si)*:Sa:Gr.
- *Measurement of the manufactured SBCM mix* using wet sieving and sedimentation tests. The manufacture of SBCM mixes using natural materials will introduce variability into the soil mix proportions and therefore detailed particle size distributions are obtained and the percentage of particles within the four soil fractions are calculated: a, b, c and d for the measured clay, silt, sand and gravel fractions respectively.

Table 1.1: The minimum and maximum limits on particle size distribution for rammed earth construction, as collected by Maniatidis and Walker (2003).

Publication	**Clay (%)**		**Silt (%)**		**Sand & Gravel (%)**	
	min.	**max.**	**min.**	**max.**	**min.**	**max.**
Alley (1955)	25	30	50	80	10	20
Houben and Guillaud (1989)	0	20	10	30	45	75
McHenry (1984)	30	35	0	0	65	75
Norton (1997)	10	25	15	30	45	75
Standards New Zealand (1998)	5	15	15	30	50	70

- *Determining the maximum weighted percentage error (MWPE) term* to provide an indication of how closely the manufactured soil mixture meets the designed mix specification. The error term is recorded in square brackets following the designed fraction proportions and is calculated using $MWPE = max|Cl - a|, |Si - b|, |Sa - c|, |Gr - d|$.

Throughout this thesis particle size distributions obtained for each of the SBCM mixes used are presented. Mixes are additionally described according to the soil mixture classification outlined in Smith and Augarde (2013a) with the generic form

$$(Cl + Si)* : Sa : Gr[MWPE]. \tag{1.1}$$

Other factors which affect the suitability of soil for SBCM mixes, including particle shape, salt content and plasticity, have also been detailed in construction guidelines however the limits are typically non-quantitative or when values are provided, as with the particle size distribution, the quantitative limits in different guides often contradict one another (Delgado and Guerrero, 2007). Therefore as concluded in Ciancio et al. (2013), following a review of soil suitability criteria, existing guidance on soil suitability can be used as an initial indication of the whether a soil can be used in SBCM projects however performance testing of prototype rammed earth materials is the more appropriate approach for assessing soil suitability. Throughout this thesis the aim of the experiments performed is to better understand the fundamental behaviour of SBCMs, rather than to design a soil mixture suitable for construction, and therefore many of the samples used do not achieve the performance requirements for construction but allow insights to be drawn into how the different sized particles influence the material's structure, the compressive strength and the effect of altering the clay mineralogy within a SBCM mix.

1.1.4 Optimum water content

Ensuring the soil used in SBCM construction is at the correct, or 'optimum', water content prior to compaction is a crucial stage of the construction process (Jaquin and Augarde, 2012). Optimum water content and maximum dry density are described briefly in relation to unsaturated soil mechanics in Chapter 2 and in SBCM construction it is understood that for a soil to achieve its maximum dry density and hence compressive strength following manufacture it is important to ensure the soil mixture is compacted at, or close to, its optimum water content for the given compactive effort (Houben and Guillaud, 1989; Walker et al., 2005).

The traditional method for determining whether a soil is suitable for compaction on an SBCM construction site was the simple *drop test*, and a range of different procedures have been defined using this name, including in Houben and Guillaud (1989) and in Walker et al. (2005). The generic drop test procedure is very simple and involves the dropping of a fist sized ball of SBCM mixture and then using the number of pieces into which it breaks to determine whether the SBCM mixture is at optimum water

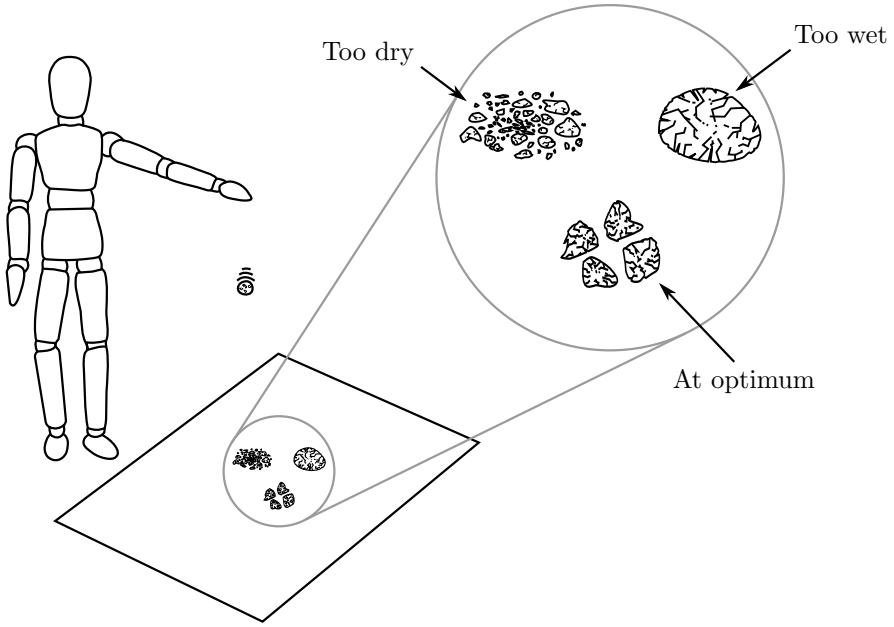

Figure 1.2: A simplified sketch of the drop test, modified from Keable (1996).

content or not (Figure 1.2). However the drop test was shown to be unsuitable for use on site by a series of experiments described in Smith and Augarde (2013b) due to the results showing that it lacked both accuracy and reliability. The authors, following a series of tests on existing geotechnical methods for determining optimum water content, propose the use of the vibrating hammer test (described in British Standard BS1377 (British-Standards, 2002)) to determine the optimum water content and maximum dry density of any SBCM mixture within a laboratory before construction commences (Smith and Augarde, 2013b).

1.1.5 Academic research

Interest in SBCMs from an academic research perspective has grown over the past decade with a small number of academic journal articles published related to SBCMs, investigating the material from a hygrothermal, environmental, structural and geotechnical perspective. Unfortunately many report results and conclusions relate to specific case studies or to particular soil types and this limits the applicability of the findings with respect to other SBCM research, and prevents meaningful discussion and comparison of results. For example, the research presented in Silva et al. (2013) describes experimental investigations into four different granular soils local to northern Portugal and concludes, following an assessment of soil suitability and compression testing, that all four soils are unsuitable for unstabilized rammed earth construction. No further discussion regarding the behaviour of the SBCM mix is provided and no reasons for the unsuitability of the specific soils tested is given, other than that they failed to meet the performance criteria specified in existing SBCM construction guidelines. A second example of typical SBCM academic

research can be seen in Nowamooz and Chazallon (2011) in which a series of experimental tests, including particle size distribution, soil water retention curve, triaxial compression, and finite element modelling, are performed on Missillac sand. Despite rigorous testing only very minimal discussion of the results is presented which severely limits the results' applicability to improving the use of SBCMs in construction or to deepening a fundamental understanding of the material's behaviour. A case study of the thermal and environmental performance of a single rammed earth building is discussed in Taylor et al. (2008) and compared to two other more conventional buildings. The very small scope of the study however (one rammed earth building which did not adequately achieve thermal comfort in a Mediterranean climate, with long-hot summers and cool/cold-wet winters), means drawing any firm conclusions regarding the thermal performance of SBCM buildings in general is nearly impossible.

A very small number of rigorous scientific publications do however exist in which the experimental results can be applied to SBCMs in a wider context, either through improving experimental methods, considering the structural or mechanical response of SBCMs or exploring the fundamental behaviour of SBCMs from an unsaturated soils perspective. An investigation discussing the relationship between particle size distribution and the compressive strength of ten different SBCM mixes is presented in Hall and Djerbib (2004) in which the particle size distributions of the SBCMs is carefully controlled through the blending of graded quarry material. The use of quarry material reduced variability in mineralogical composition and grain shape which can arise from the use of natural soils and was, to this author's knowledge, the first attempt to test SBCMs using heavily controlled materials. In Hall and Djerbib (2004) the authors hypothesis, following the analysis of the results, is that the binder/aggregate ratio may be an important factor in determining or controlling compressive strength although they acknowledge this has not been clearly proven by their results and suggest that more work is required. In addition, a novel technique for the production of cube samples is also developed in Hall and Djerbib (2004) which replicates on-site wall compaction, produces samples of highly consistent density and satisfies the New Zealand earth building standards, clearly promoting rigorous scientific testing methods for SBCM investigations. A study described in Maniatidis and Walker (2008) investigates the validity of using masonry design rules for SBCM structures and presents a series of tests at a range of scales (including full-size columns and small 100mm diameter 200mm high cylinders) focussing on the load eccentricity and slenderness ratio of the samples. Despite variation between theoretical and experimental results for high load eccentricities, the authors conclude that existing codes and guidance predicting the structural performance of rammed earth provide a good estimate of measured experimental performance for small load eccentricities up to 10%. Significant variation in the performance of SBCMs between samples at the different scales of testing is also highlighted in Maniatidis and Walker (2008) and the subsequent discussion in the paper emphasises that the effects of scaling samples needs to be carefully considered during any experimental laboratory

testing. Both these investigations into SBCMs (Hall and Djerbib (2004) and Maniatidis and Walker (2008)) show that it is possible to examine the compressive behaviour of SBCMs using rigorous scientific methods in which results and findings can be applied to a context wider than a specific SBCM building or potential source of soil. Additionally by discussing in detail the experimental methods improvements to testing of SBCMs were presented, namely the use of blended soil mixes and an appreciation of the effect of scale on the compressive testing of samples, which enabled fellow researchers to build upon the work presented in each paper, for example work published by Beckett and Augarde (2011) and Ciancio et al. (2014).

Changes in the internal macrostructure of SBCMs under compressive loading discussed in Beckett et al. (2013) is one of the first publications which discusses SBCMs at a particle level. Laboratory x-ray computed tomography (XRCT) is used to identify the development of cracks within small SBCM samples and investigate the heterogeneity of SBCM void structure through a compacted layer. The results presented provide an initial insight into the interaction of the sand and clay particles within SBCMs and the XRCT methods described are used as a starting point for the XRCT experimentation described later in this thesis. The analysis of resistance of walls to lateral wind loading is described in Ciancio and Augarde (2013) which investigates the suitability of two different structural design methods for SBCM wall design, elastic analysis and ultimate strength analysis. The comparison of laboratory testing and results from the two analyses initially shows that elastic analysis can overestimate a wall's capacity to lateral load, if failure of the wall does not occur at the central point vertically in the wall, and that the ultimate strength analysis significantly under estimates the maximum wind pressure a wall can sustain. However by considering the fracture energy required to propagate a crack through a SBCM wall, the results in Ciancio and Augarde (2013) show that the capacity of the wall can be reasonably predicted using an extended ultimate strength analysis. These two papers (Beckett et al. (2013) and Ciancio and Augarde (2013)) show that significant insights into the behaviour of SBCMs can be gained by considering the material at a particle level, in these cases focussing on the propagation of cracks at the macrostructural level and the impact of the fracture energy in propagating these cracks on the bearing capacity of an entire SBCM wall. It is therefore suggested that further investigations into SBCMs at this scale should prove insightful when considering material behaviour.

The investigation of SBCMs from an unsaturated soils geotechnical perspective is an emerging approach to understand the behaviour of the material and published work includes Jaquin et al. (2009), Beckett (2011) and Bui et al. (2014a) and the background knowledge required to understand SBCMs using unsaturated soil mechanics is outlined in Chapter 2. The small programme of geotechnical tests described in Jaquin et al. (2009), which measured matric suction of SBCM cylindrical samples during constant water content compression tests, showed that suction is a source of strength in SBCMs and that

the compressive strength increases as water content decreases. The experimental test procedure described in Bui et al. (2014a) further builds upon these findings showing that similar suction values are obtained across a range of SBCMs. The analytical and experimental investigations described in Beckett (2011), including experiments into the effect of relative humidity and temperature on the compressive strength of SBCMs, the changing water content and presence of dissolved ions on the tensile strength of SBCMs and the relationship between the void size distribution of SBCMs and its water retention properties, are a good example of how unsaturated soils knowledge can be applied to analyse SBCMs as a geotechnical material.

Finally publications such as Gallipoli et al. (2014), Augarde (2015) and Augarde et al. (2015) have begun to introduce SBCMs to a wider academic audience within the geotechnical community, providing overviews of the rigorous unsaturated soils research into SBCMs that has been performed to date. It is hoped that by engaging with the knowledge of unsaturated soils research community the understanding of the fundamental particle-void-water interactions occurring within SBCMs will provide insight into the design of modern SBCM structures. It is this approach of studying SBCMs from an unsaturated soils geotechnical perspective which is used throughout this thesis to examine the material in detail.

1.2 Thesis aims

The discussion in Section 1.1.5 highlights the minimal number of rigorous scientific publications presenting geotechnical experimental results on SBCMs and therefore the scope for performing new and innovative research into SBCMs is very large. In this thesis therefore the primary aim of the research is to use XRCT to study SBCMs and better understand its mechanical behaviour and void structure. The main focus of the investigations described in the following chapters are to provide knowledge to the SBCM industry regarding:

- the void structure of SBCMs prior to and following loading;
- the change in their internal structure following compressive loading and how cracks propagate through a sample during loading;
- the role of the constituent materials within the mix and how the mix design affects mechanical behaviour; and
- the effect of using expansive clay within a SBCM mix on the materials unconfined compressive strength and the evolution of its macrostructure during drying.

Additionally the experience gained from the considerable use of XRCT to study highly unsaturated soil materials provides insights for the geotechnical research community including:

- the current state of the use of XRCT in geotechnical research;

- the suitability of current XRCT technology for geotechnical research; and
- how current image-processing techniques provide quantitative data which is understood by geotechnical researchers.

1.3 Thesis overview

Following the basic overview of SBCMs presented in this chapter an introduction to unsaturated soil mechanics is provided in Chapter 2 which aims to describe the key elements of unsaturated soil behaviour, including suction, particle mineralogy, compaction and water retention behaviour, required to examine SBCMs in detail. Chapter 3 then provides an overview of the current use of XRCT within the geotechnical research community and assesses the capabilities of two current XRCT machines to investigate the internal structure of SBCMs.

The following three chapters then utilise XRCT scanning and compressive strength testing to investigate different aspects of the behaviour of SBCMs, referring to unsaturated soil mechanics and the abilities of XRCT previously described. The macrostructural response of SBCM samples to compressive loading is discussed in Chapter 4, with particular focus on the propagation of cracks through SBCM samples and the impact of removing the gravel fraction from the SBCM mix prior to sample manufacture.

The internal void structure of SBCM samples is investigated in Chapter 5 where the scanning and analysis of three different sample sizes, containing different fractions of the SBCM mix, enables the examination of the void structure of SBCMs. The role of the different voids with respect to the development of suction and the compressive strength achieved is also discussed.

An investigation into the impact of including a small amount of expansive clay in a SBCM mix is described in Chapter 6. Typically in SBCM construction the use of expansive clay is avoided however no quantitative results describing the effects on SBCMs could be found in published literature. Experiments performed at different stages of drying reveal the mechanical response of the material during compression and the evolution of void structure which is discussed before conclusions are drawn regarding the use of small amounts of clay in SBCM structures.

Finally in Chapter 7 conclusions are drawn from the research discussed in Chapters 3 to 6 and implications for SBCM mix design presented.

Chapter 2

An introduction to unsaturated soil mechanics

2.1 Introduction

The study of unstabilized soil based construction materials (SBCMs) throughout this thesis considers the material as a highly unsaturated manufactured soil and this chapter therefore aims to provide the reader with an overview of the unsaturated soil fundamentals necessary to understand the analysis of SBCMs. Soil is the unbonded granular material formed from the physical and chemical weathering of the earth's crust. In a geotechnical context 'soils' refer to the underlying geological deposits and do not include topsoil (i.e. the top layer of soil in which plants grow) due to its high organic content, variable mineralogy, the influence of the water table and high compressibility (Powrie, 2004). In SBCMs the topsoil is also discounted, due to its high organic content and unpredictable character, and a broad range of particle sizes are used with only basic tests performed to determine the mineralogy of the soil mixture (Houben and Guillaud, 1989).

A soil is usually formed of three different phases, as shown in Figure 2.1a: *solid particles*, of all sizes and mineralogy; a *liquid phase*, containing water; and a *gaseous phase*, containing air. It is the presence of all three phases within the the soil, rather than simply solid particles and water or solid particles and air, that differentiates unsaturated soil mechanics from classical soil mechanics.

The quantitative descriptions of the relationship between the three phases is discussed in Section 2.2 before an overview of suction, which is the predominant source of strength within unbonded unsaturated soils, is provided in Section 2.3. The mineralogy and structure of the solid particles is then described in Section 2.4 and how the voids which surround the solid phase are classified and measured is discussed in Section 2.5. The impact of compaction on the structure of a soil and the link between water content and suction are briefly outlined in Sections 2.6 and 2.7 respectively. Finally in Section 2.8 the implications of the discussed unsaturated soil theory is applied to examining SBCMs.

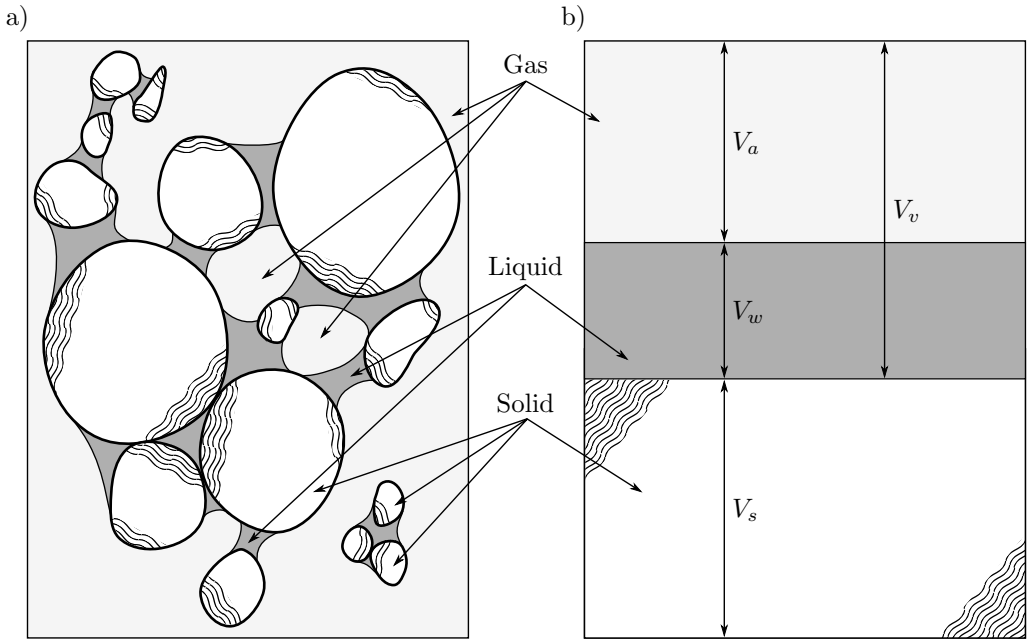

Figure 2.1: A simplified sketch of (a) a volume of soil and (b) its associated phase diagram.

2.2 Phase relationships

The relationship between the three phases which exist within an unsaturated soil can be described using a number of fundamental definitions which describe the relative volume or mass of one phase within the soil to the remaining phases (Powrie, 2004). Figure 2.1b shows a simplified phase diagram of the solid, water (liquid) and air (gas) phases which have been combined into bulk forms and have been attributed the volumes V_s, V_w and V_a respectively. The water and air phases can also be combined and described as the volume of voids, V_v. The mechanical properties of a soil are affected by the interactions between the three phases and the state of the soil, and hence the interactions between the three phases, therefore enables the mechanical behaviour of the whole soil to be better understood (Mitchell and Soga, 2005).

Three key dimensionless phase relationships describe the solid skeleton and surrounding voids within a unit volume of soil. Firstly the *void ratio* (e) compares the volume of solid particles and the volume of voids and is calculated as

$$e = \frac{V_v}{V_s}. \tag{2.1}$$

Secondly the actual volume that a unit volume of solid particles will fill is defined as the *specific volume* (v), a ratio that can also be linked to the void ratio as follows

$$v = \frac{V_s + V_v}{V_s} = 1 + e. \tag{2.2}$$

Thirdly the volume of voids within a unit volume of soil is described as the *porosity* (n) calculated as

$$n = \frac{V_v}{V_s + V_v} = \frac{e}{1+e} = \frac{v-1}{v}. \tag{2.3}$$

The behaviour of a soil is not only affected by the solid and air phases however and describing the liquid phase is crucial. A soil is commonly described using the ratio between the mass of water (m_w) and mass of solids (m_s) using the *gravimetric water content* (w) as this can be easily measured within a laboratory and is defined as

$$w = \frac{m_w}{m_s}. \tag{2.4}$$

The gravimetric water content however relates the liquid phase to the solid phase and therefore provides no indication of how 'full' the voids are with water. The *degree of saturation* (S_r) can therefore be used to link the volume of water within the sample to the volume of voids and is defined as

$$S_r = \frac{V_w}{V_v}. \tag{2.5}$$

The degree of saturation must be a value between zero and one, in which a fully dry soil has a degree of saturation equal to zero and a fully saturated soil has a degree of saturation equal to one.

2.3 Suction

Suction is the potential energy of water found within the voids of an unsaturated soil compared with free, pure water under the same conditions (Lu and Likos, 2004; Beckett, 2011). The difference in potentials results in an increase in bonding between solid particles and suction is therefore required as an independent stress variable to characterise unsaturated soil (Alonso et al., 1990; Gallipoli et al., 2003; Tarantino, 2007). The water within the voids has a lower potential than free water and results in negative values of pressure being measured however, for convenience in unsaturated soils practice, suctions are traditionally quantified as positive. Despite the use of units of pressure the difference in chemical potential arises from a number of different sources, each discussed below, and as proposed by Gens (2010) suction is most appropriately thought of as a variable that expresses the degree of attachment between the solid and liquid phase.

2.3.1 Matric suction

Matric suction, ψ_m, arises from the combination of the curvature of water menisci between particles and the adsorption of a film of water molecules onto particle surfaces and is defined as

$$\psi_m = C(\kappa) + A(t) \tag{2.6}$$

where C is the capillary component described in its simplest form as a function of the liquid-gas curvature, κ, and A is the adsorptive component which is a function of the film thickness, t (Philip, 1977; Tuller et al., 1999; Lu and Likos, 2004; Gens, 2010).

The adsorptive component, $A(t)$, of matric suction is a complex combination of solid-water interactions by which soil particles acquire a layer of water molecules on their surface, which include electrostatic and van der Waals forces, hydrogen bonding and surface-dipole attraction. Surface tension and interface curvature develops in menisci, or liquid bridges, between solid particles and results in a difference in water and air pressure. This difference in pressure generates inter-particle forces which has a stabilising effect on the soil skeleton and it is this which is described by the capillary component, $C(\kappa)$, of matric suction (Gens, 2010; Beckett, 2011).

The complex structure of soil, and the interactions of the three distinct phases, mean that separately determining the adsorptive and capillary components is very difficult however this use of a single matric suction term does not mean that their effects on a soil's mechanical behaviour are equivalent (Baker and Frydman, 2009). When a soil has a relatively high degree of saturation, and the water exists as a funicular (continuous) regime, the capillary component will dominate however at relatively low degrees of saturation, when the water exists as a pendular (discontinuous) regime, the adsorptive component of matric suction will dominate (Sheng, 2011; Lu and Likos, 2004).

2.3.2 Osmotic suction

For two solutions separated by a semi-impermeable membrane, if one solution has a higher concentration of solute than the other a net diffusion of solute will occur causing a hydrostatic pressure. Semi-impermeable membranes do not exist in real soils however the presence of very small voids between clay particles, and the surface charges of the clay particles, lead to effects similar to semi-impermeable membranes within a soil (Beckett, 2011). Dissolved solutes are introduced to the pore water from external processes, such as leaching, or from the solutes adsorbed onto the soil mineral surfaces, particularly clay. The presence of these solutes reduces the chemical potential of the pore water, which would result in a difference in pressure between the pore water and free water, and it is this which is referred to as *osmotic suction*, ψ_o (Lu and Likos, 2004; Beckett, 2011).

2.3.3 Total suction

The brief discussion above shows that the suction developed within unsaturated soils is a combination of both the matric suction, including the capillary and adsorptive components, and the osmotic suction, arising from dissolved solutes within the pore water. The algebraic sum of both matric and osmotic suction is commonly referred to as *total suction* (ψ_t) (Tuller et al., 1999; Lu and Likos, 2004; Baker and Frydman, 2009; Gens, 2010; Beckett, 2011) and can be written as follows:

$$\psi_t = \psi_m + \psi_o = C(\kappa) + A(t) + \psi_o \tag{2.7}$$

2.4 The solid phase

Solid particles within a soil result from the erosion of rocks by many natural processes including weathering, chemical changes and biological activity (Powrie, 2004). Physical erosion and transportation processes will affect the size and shape of the resultant soil particles and classifying the soil material using these easily observable parameters is commonplace in geotechnical engineering. EN ISO 14688-1:2002 establishes the basic principles for classifying all natural and man-made soils and defines three broad fractions for which soil particle size can be described: *fine soil* (<0.063mm), *coarse soil* (>0.063mm and <63mm) and *very coarse soil* (>63mm). Very coarse soil can be ignored for SBCM mixes, as they are typically sieved to less than 20mm, whilst the two smaller fractions can be further divided into into *clay* (<0.002mm), *silt* (>0.002mm and <0.063mm), *sand* (>0.063mm and <2mm) and *gravel* (>2mm and <63mm) (British-Standards, 2002).

Describing the size and shape of the solid particles within a soil however is insufficient to fully characterize the soil particles since the mineralogy of the parent rock, and any chemical changes which may have occurred over time, will also affect their behaviour. For instance, the physical erosion of rocks will produce particles from large boulders through to fine rock flour which all retain the chemical properties of the parent rock regardless of their particle size (Beckett, 2011) whilst two identically sized particles of limestone and marble will have very different mechanical properties. Mineralogical differences in particles will also alter the behaviour of the soil and the key difference in mineralogy for geotechnical soils is between *clay materials*, associated with a net negative electrical charge, high plasticity when mixed with water and high weathering resistance, and *granular* (or non-clay mineral) *materials* associated with bulky inert particles (Mitchell and Soga, 2005). The chemical composition of the common minerals found within both granular and clay soils is discussed below as is the implications the mineral structure has on the clay and non-clay particles' behaviour.

2.4.1 Granular materials

Granular soils, typically with a high percentage of gravel, sand and silt particles, are products of the weathering of pre-existing rocks and soils and therefore contain mineral constituents that are either very abundant in the source material or highly resistant to weathering, impact and abrasion. The typical composition of igneous rock (from which many soils are formed) contains approximately 60% feldspars, 17% pyroxenes and amphiboles, 12% quartz, 4% micas and 7% other minerals. Pyroxenes, amphiboles and micas are rapidly broken down chemically during weathering and transportation and feldspar minerals have an open structure, caused by the presence of potassium, sodium or calcium, which is easily broken down through cleaving and splitting along the weakly bonded planes. Quartz (SiO_2) however is chemically and mechanically very stable. The lack of weakly bonded ions in its structure, and quartz already being an oxide, makes it resistant to chemical action whilst its silica tetrahedral spiral structure means it has no cleavage planes along which the material can easily split. The high stability of quartz compared to feldspars, pyroxenes and amphiboles therefore means that the most abundant non-clay mineral in soils is generally quartz, with small amounts of feldspar and mica also present (Powrie, 2004; Mitchell and Soga, 2005).

Quartz is a relatively hard material, with a rated hardness equal to seven (on Mohs' 10-point scale of mineral hardness described by Powrie (2004) where talc, the softest material, equals one and diamond, the hardest, equals ten). The surface texture of quartz particles depends on their origin and the associated mechanical and chemical actions. For example quartz originating from a desert environment will often have a rough surface texture whilst particles from a beach, or salt sea-water, environment will have relatively smooth, pitted surface. The predominance of quartz within granular materials means that they can be treated as relatively inert with interactions that are predominantly physical in nature and are described by particle size, surface texture, shape and size distribution (Mitchell and Soga, 2005).

2.4.2 Clay soils

The term 'clay' in a geotechnical context can refer to a size of particle (<2μm) but can also be used to describe the mineralogy of a soil as having high plasticity when mixed with water, a net negative electrical charge, high resistance to weathering and an alumino-silicate mineralogy (Powrie, 2004; Beckett, 2011). Clays are predominantly formed from the chemical weathering of feldspars and the reactions result in ion exchange with the surrounding environment and/or mineral layer structural transformation. Three general mechanisms of clay formation exist, as defined by Eberl et al. (1984):

- *inheritance*, whereby a clay originated from reactions occurring at a previous stage in the rock cycle and its stability ensures it remains in its present environment;

- *neoformation*, in which the clay precipitates from solution or is the result of reactions of amorphous (non-crystalline) materials; and
- *transformation*, where a clay maintains some of its inherited structure whilst undergoing chemical reactions involving ion exchange or structural modifications.

These three mechanisms are clear simplifications of what is a very complex and varied process and possible isomorphous substitutions are nearly endless producing crystal structures which can range from nearly perfect crystals to very poor crystals. However, for engineering purposes a detailed understanding of the subtleties of each specific mineral is not required and a knowledge and understanding of the structural and compositional characteristics of the main mineral groups is sufficient (Mitchell and Soga, 2005).

Clay minerals can be understood to be made up of repeated layers, which comprise of two or three alternating silicon tetrahedral and aluminum or magnesium octahedral sheets. The bonding between the sheets within each layer is strong but the bonding between layers is likely to be weak and some clay minerals in soils contain loosely bonded metal ions which can be easily exchanged for other cations within the pore water (Powrie, 2004). To clarify the nomenclature used here, and throughout the remainder of the discussion, the following terms are used in accordance with the Clay Minerals Society (as defined by Bailey (1971)): a *plane* of atoms; a *sheet* of base structural units; and a *layer* of unit cells composed of two, three, or four sheets.

The composition and structure of the elemental sheets is described below and followed by a description of the three most common clay minerals; *kaolinite clay*, *illite clay* and *montmorillonite clay*. Schematic representations of the structures are used as simplified diagrams of the clay minerals but are highly idealised as they show no irregular substitutions or mixed-layer structures and do not indicate the correct width-to-length ratios for the assembled particles. A more detailed description of the formation and mineralogy of clays can be found in Powrie (2004) and Mitchell and Soga (2005) and the descriptions presented here are a brief summary of those works relevant to the thesis.

Silica sheets

The base structural unit within a silica sheet is a silicon tetrahedron formed of four oxygen atoms bonded to a single silicon atom, a diagrammatic representation of which can be seen in Figure 2.2a. These silica tetrahedra are interconnected to form a sheet structure in which three of the four oxygens are shared with adjacent tetrahedra to form a hexagonal net, as shown in Figure 2.2b. The bases of all tetrahedra are in the same plane, with the tips pointing in the same direction, and the sheet can be represented in clay mineral structural schematics showing the tips pointing either up or down, as shown in Figure 2.2c. Electrical neutrality for an individual silica sheet is achieved through the replacement of the four oxygen molecules with hydroxyls (-OH) or by union with a positively charged sheet of a different

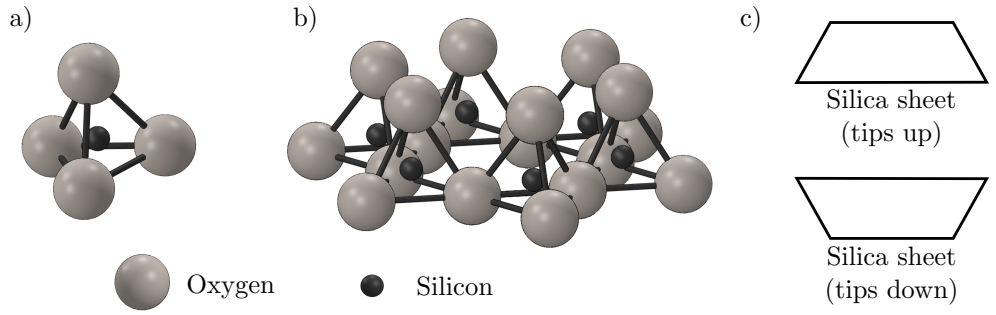

Figure 2.2: A diagrammatic representation of the silicon a) tetrahedron b) tetrahedra sheet and c) schematic.

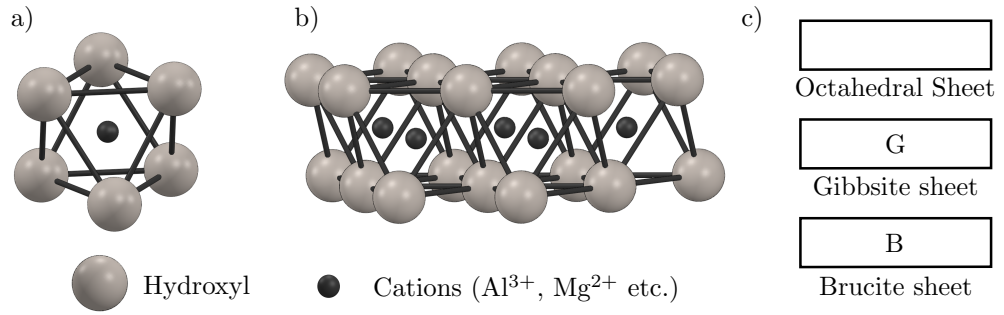

Figure 2.3: A diagrammatic representation of the octahedral a) base unit b) sheet and c) schematic.

composition. The hexagonal net structure, containing six silicon tetrahedra, can be repeated indefinitely and has the composition

$$(Si_4O_{10})^{4-}\,. \tag{2.8}$$

Octahedral sheets

The base structural unit within octrahedral sheets is composed of cations in octahedral coordination with oxygens or hydroxyls, as shown in Figure 2.3a. The cations can be a range of molecules including iron (Fe^{2+}, Fe^{3+}), manganese (Mn^{2+}), nickel (Ni^{2+}) and chromium (Cr^{3+}) however the most common octahedral sheets are formed from aluminum or magnesium cations (Al^{3+} and Mg^{2+}). If the cation is divalent, as with magnesium, all possible cation sites are occupied and the structure is *trioctahedral* whereas when the cation is trivalent, i.e. aluminum, only two-thirds of the possible cation sites are occupied and the structure is *dioctahedral*. The octahedral units combine in octahedral sheets sharing hydroxyls or oxygens with adjacent octahedrals, as shown in Figure 2.3b, to form brucite minerals and gibbsite minerals, for magnesium and aluminium respectively, and have the following compositions

$$Mg_3\,(OH)_6 \text{ and } Al_2\,(OH)_6\,. \tag{2.9}$$

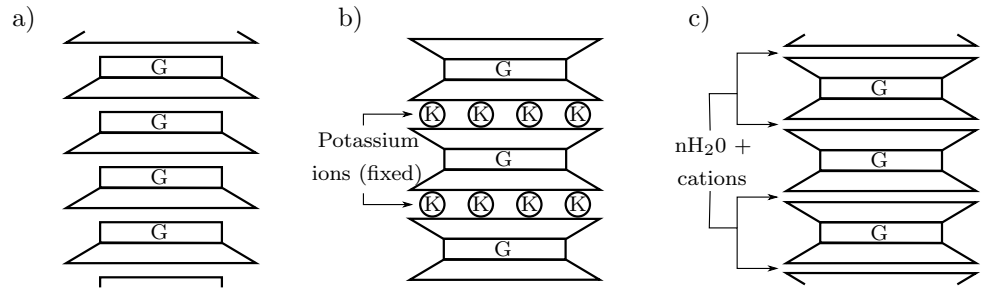

Figure 2.4: A schematic representation of a) kaolinite b) illite and c) montmorillonite clay minerals.

These octahedral sheets will, in the case of clay mineral structures, be either a *brucite sheet* or a *gibbsite sheet* and the schematic representation of a generic octahedral sheet, and both the brucite and gibbsite sheets, is shown in Figure 2.3c.

Kaolinite clay

A single layer of kaolinite clay has a two sheet structure comprising of a sheet of silica and a sheet of gibbsite. The bonding between the layers is both by van der Waals forces and stronger hydrogen bonds. This bonding is sufficiently strong that there is no inter-layer swelling in the presence of water and forms particles which, for clay, are relatively large. The lack of inter-layer separation means cations must adsorb on the exterior surface and edges of the particle to balance any negative charge. Figure 2.4a shows a schematic representation of kaolinite clay minerals and the structural formula can be written

$$(OH)_8\, Si_4 Al_4 O_{10}. \tag{2.10}$$

The formation of kaolinite clay is favoured when silica is scarce and alumina is abundant, often in low electrolyte content and low pH environments. Therefore kaolinite forms in areas where precipitation is relatively high and good drainage exists to ensure leaching of cations and iron. Well crystallized kaolinite particles form hexagonal plates, between 0.05µm and 2µm thick with lateral dimensions between 0.1µm and 4µm, whilst poorly crystallized kaolinite will form platey particles which are smaller and less clearly hexagonal.

Illite clay

A layer of illite clay has a three sheet structure, formed of a gibbsite sheet between two silica sheets, and the layers are separated by potassium ions (K^+). The layers in illite particles may contain magnesium and iron, as well as aluminum, in the gibbsite sheet. Figure 2.4b shows a schematic representation of an

pure illite clay mineral and the structural formula is

$$(OH)_4 K_2 (Si_6 Al_2) Al_4 O_{20}. \tag{2.11}$$

The weathering of feldspar in cool climates often leads to the development of illite and the formation of illite clay requires an abundance of silica and the presence of potassium (in the form of igneous or metamorphic parent rock) is essential. Interstratifications with mica and chlorite are common and, despite being the most commonly found clay due to its high stability, the existence of high purity deposits is unknown. Illite clay particles therefore usually occur mixed with other clay and non-clay minerals and are generally flaky and small, down to 3nm thick and between 0.1µm and 3µm in length.

Montmorillonite clay

Montmorillonite clay layers, as with illite clay, has a three sheet structure formed of a single gibbsite sheet between two silica sheets. In montmorillonite clay there is substitution of silicon by aluminum in the silica sheets and of aluminum by magnesium in the gibbsite sheet. The isomorphous substitution results in a structure that is almost exactly dioctahedral, with every sixth aluminum replaced by a magnesium ion, and the layers have additional negative charges. These negative charges are balanced by exchangeable cations, such as sodium and calcium, located on the surface of the particle or between individual layers. This cation bonding between layers, coupled with van der Waals forces, provides only weak inter-layer bonding which can be easily separated by cleavage and the adsorption of water between layers results in significant swelling of montmorillonite clay particles. A schematic of the montmorillonite clay structure is shown in Figure 2.4c and the structural formula is written

$$(OH)_4 Si_8 (Al_{3.34} Mg_{0.66}) O_{20}. \tag{2.12}$$

Montmorillonite clay forms where silica is abundant, both silica and alumina are flocculated and conditions ensure high pH, high electrolyte content and the prescience of more magnesium and calcium ions (Mg^{2+} and Ca^{2+}) than sodium and potassium ions (Na^{+} and K^{+}). Igneous rocks, volcanic ash and their derivatives are usual parent rocks and semi-arid or arid climatic conditions, where evaporation exceeds precipitation and there is poor leaching and drainage, favour the formation of montmorillonite clays. The clay particles are typically between 1µm and 2µm in length and particle thicknesses occur in multiples of 1nm (the thickness of a single layer) from 1nm to approximately one-hundredth of a particles length.

Inter-sheet and inter-layer bonding

The inter-sheet bonds between tetrahedral and octahedral sheets are primary valence bonds which, relative to the weight of a single atom, are very strong. Three types of primary valence bonds exist,

covalent bonds, *ionic bonds* and *metallic bonds*, although a combination of only ionic and covalent bonding is typical in the non-metallic minerals found in soil. Covalent bonds share one or more of the bonding electrons within the outer energy level of electrons and, since only certain electrons participate in the bonding, covalent bonds are directional and result in fixed bond angles. Ionic bonds form between cations (positively charged) and anions (negatively charged) and result in strong electrical attractions between the oppositely charged ions. Since each cation will attract all neighbouring anions, the ionic bond is nondirectional and geometric considerations, and the presence of any covalent bonds, determines the actual arrangement of bonded atoms.

The bonds between layers, containing the primary valence bonded sheets, will be a combination of different secondary bonds which are relatively weak when compared to ionic and covalent bonds. The bonds may be sufficiently weak that the chemical and physical behaviour of the clay is influenced by the response of these inter-layer bonds to the environmental conditions. As outlined in Marshall (1964) different types of inter-layer bonding can be found in within soil particles and include:

- *van der Waals forces*, or fluctuating dipole attraction, which bond neutrally charged parallel layers. In isolation these bonds are weak and result in non-clay minerals, such as pyrophyllite and talc, which cleave easily between layers.

- *Hydrogen bonding*, or permanent dipole attraction, which form between opposing layers of oxygens and/or hydroxyls and are approximately an order of magnitude stronger than van der Waals forces. This additional strength of the hydrogen bond is also coupled with the fact it remains stable in the presence of water to form larger stable particles such as kaolinite clay.

- *Isomorphous substitution*, i.e. the exchange of ions within sheet structures, can result in the ready adsorption of polar molecules between silicate layers. The inter-layer bond strength is low and the additional adsorption of water between layers, through the hydration of the adsorbed cations, can result in layer separation or expansion. This swelling between layers is particularly prevalent in montmorillonite clays and results in expansive soils prone to shrinking upon drying.

The isomorphous substitution occurring within clay minerals results in clay particles having a net negative charge. To preserve electron neutrality cations are attracted to the particles and, in the case of montmorillonite clays and illite clays, are held between layers. In all clays cations are adsorbed on the edges and surfaces of clay particles resulting in positively charged edges. These adsorbed cations may be replaced by cations of a different type and are therefore referred to as exchangeable cations. The quantity of exchangeable cations can be measured, and expressed as milliequivelents (meq)[3] per 100g of dry clay, and is called the *cation exchange capacity*.

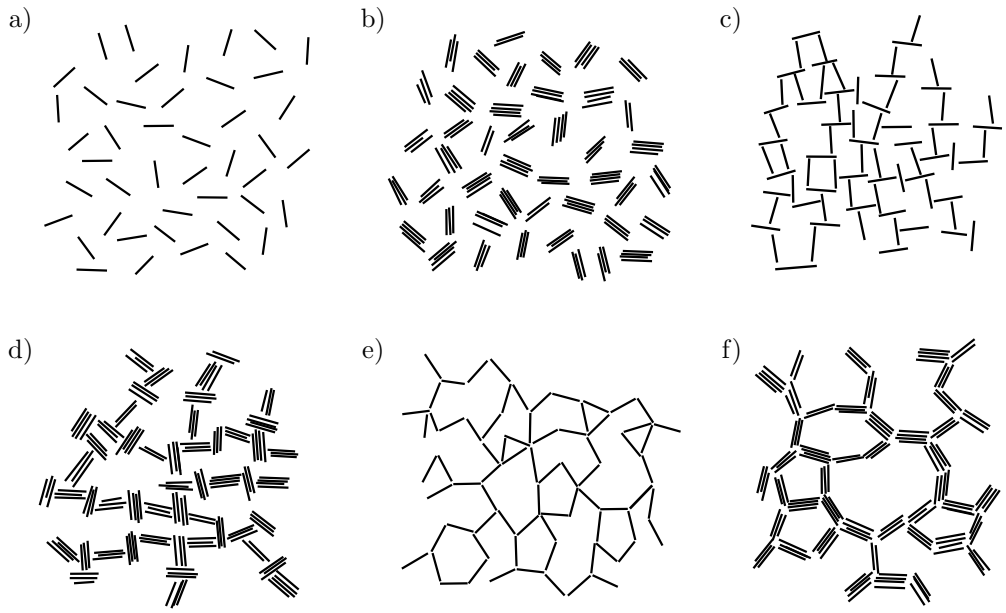

Figure 2.5: A sketch of clay particle associations, modified from Van Olphen (1977).

2.4.3 Particle assemblages and soil fabric

Dry particles have a known particle size distribution and measurable shape, often with predictable mechanical interaction through physical contacts and frictional forces. However when water is added to a soil the smaller particles group together and form particle assemblages due to suction (Beckett, 2011). The fabric of the soil is the arrangement of the individual particles, the particle assemblages and the surrounding void space. Many different terms have been used to describe the soil fabric including clusters (Olsen, 1962; Yong and Sheeran, 1973), peds (Brewer, 1964; Baker and Frydman, 2009) and aggregations (Collins and McGown, 1974; Van Olphen, 1977). The term structure has also been used in geotechnical literature interchangeably with fabric however in this thesis '*structure*' is used to refer to the combined effects of soil mineralogy, inter-particle forces (including suction), and the soil fabric. Additionally, for clarity and consistency throughout this thesis, the term '*aggregations*' will be used to describe a group of particles combined together to form a single entity.

In pure sands and gravels the soil fabric is usually formed of arrangements of single grains however when clay particles are included the particle associations become more complex and aggregations form. Figure 2.5 shows a sketch of different clay particle interactions, as defined in Van Olphen (1977). The interactions can be separated into three main groups:

- *dispersed* and *deflocculated*, shown in Figure 2.5a, in which there is no association between clay particles;

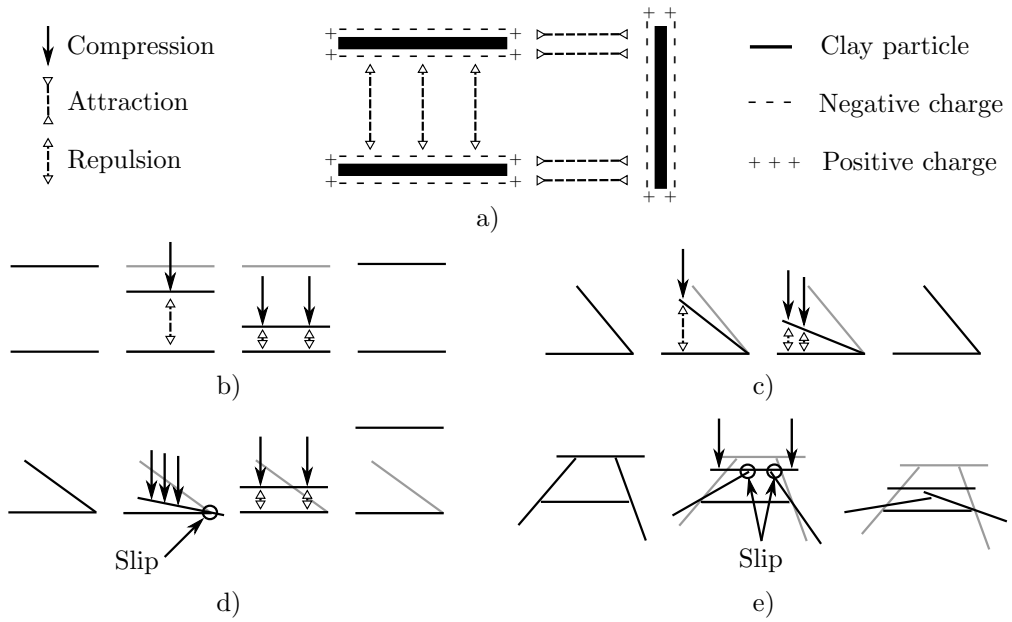

Figure 2.6: A sketch of clay particle association deformations showing a) charged particle interaction b) reversible face-to-face deformation c) reversible edge-to-face deformation d) irreversible edge-to-face deformation and e) particle collapse.

- *aggregated*, shown in Figure 2.5b, in which *face-to-face* associations occur between several particles; and
- *flocculated* in which *edge-to-face* or *edge-to-edge* associations occur between particles, shown in Figure 2.5c and 2.5e, and aggregations, shown in Figure 2.5d and 2.5f.

Thicker and larger aggregations result from face-to-face associated particles whilst edge-to-face and edge-to-edge associations form voluminous compressible clay particles (Van Olphen, 1977).

A kaolinite clay particle has negatively charged faces and positively charged edges and the generated electric fields result in face-to-face interactions being repulsive in nature and edge-to-face interactions being attractive, as shown in Figure 2.6a. Both face-to-face and edge-to-face associations can result in reversible volume change of a particle during and following compression, as shown in Figure 2.6b and Figure 2.6c respectively. During compression of the two particles their negatively charged faces are moved closer together and an electrostatic repulsion force exists between the faces, which increases as the particles are forced closer together under increased load. When the compression load is reduced the electrostatic repulsion force results in the particle faces moving away from one another and, following complete removal of the load, back to their original position, i.e. a *reversible deformation* is said to have occurred to the particles under loading. However under sufficient compressive force edge-to-face associations can result in slippage between particles causing irreversible changes to particle associations and in certain cases volumetric particle collapse. Figure 2.6d shows that when sufficient load is applied to an edge-to-face association to cause the electrostatic attractive force, between the positively charged

edge and negatively charged face of the two particles, to be overcome the particles will slip across one another. This slippage can result in a change from an edge-to-face association to a face-to-face association and, upon a reduction in load, the particles will move apart causing an *irreversible deformation* between the two particles. For particle assemblages of more than two particles the interactions are more complex and Figure 2.6e shows a group of four particles which originally contain a void in their centre. When subjected to a compressive loading the slipping of the edge-to-face associations, of the particles connected to the top horizontal particle, results in a change in the particle associations which, following reduction in the compressive loading, prevents the return to the original structure. This new structure contains a significantly smaller void within the group of four particles and *volumetric particle collapse* is said to have occurred (Pedrotti and Tarantino, 2014). Particle associations in soils in which clay and non-clay particles exist relate in some way to the combinations of interactions shown in Figure 2.5, depend on water content and the density of the soil mix, and almost always are composed of multi-particle aggregations.

2.5 Voids

Voids are a crucial part of the structure of a soil which is often ignored within the study of SBCMs and affects many aspects of the soil behaviour including the development of suction and its wetting and drying behaviour. The terms 'voids' and 'pores' (which is also used in unsaturated soil literature) are synonymous and *voids* are used throughout this thesis to maintain a clear distinction between particle size distributions (psd) and void size distributions (vsd). Traditionally voids have been separated into four different classes, illustrated in Figure 2.7, as defined by Collins and McGown (1974):

- *intra-elemental voids* which exist between individual particles to form elementary particle arrangements of clays, shown in Figure 2.7a;
- *intra-assemblage voids* which exist within particle assemblages between elementary particle arrangements and between individual grains of silt and sand, shown in Figure 2.7b;
- *inter-assemblage voids* which exist between particle assemblages, shown in Figure 2.7c; and
- *trans-assemblage voids* which exist between groups of particle assemblages and large grains (i.e. gravel) so that their boundaries can not be defined using the aggregation type, shown in Figure 2.7d.

In general, the void size will increase from intra-elemental to trans-assemblage voids. This however is not guaranteed when a broad range of particle sizes are used as voids will be formed by the grouping of particles of different sizes. Therefore, in more recent unsaturated soils literature, the void sizes are defined as either intra-aggregate or inter-aggregate and a critical void size is used to differentiate between the two classes. This defining of two distinct void sizes has led to unsaturated soils being described as having a *double structure*.

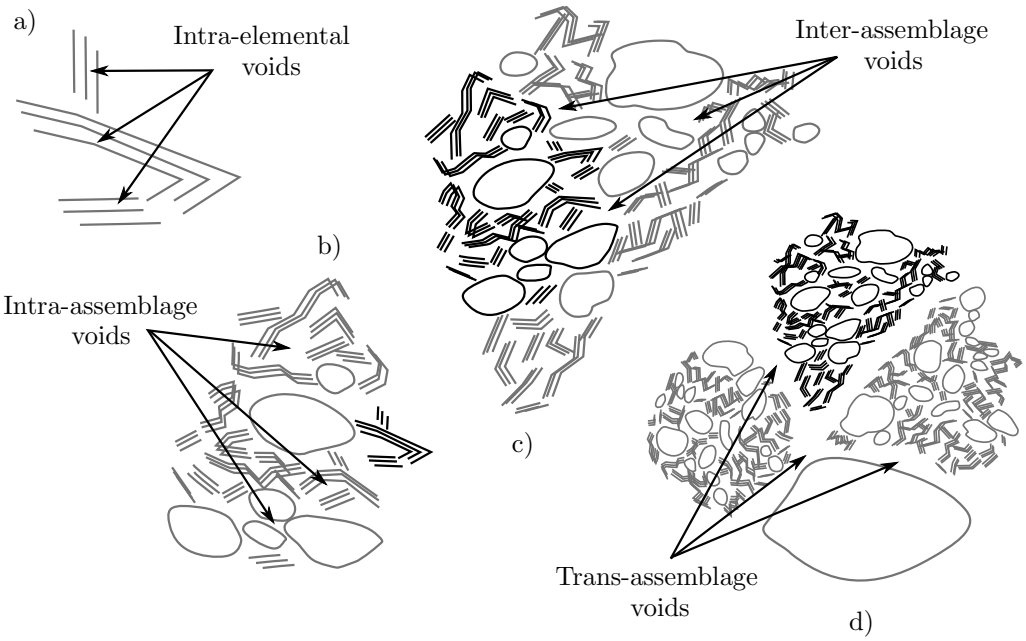

Figure 2.7: A sketch of the four void classes defined by Collins and McGown (1974) a) intra-elemental b) intra-assemblage c) inter-assemblage d) trans-assemblage.

2.5.1 Double structure models

The double structure model for describing soil has been focussed on clay materials and describes two clearly distinct sets of void sizes: the voids that form between individual clay particles within the aggregations and the voids that form between aggregations (Sánchez et al., 2005; Baker and Frydman, 2009). Throughout this thesis the structure of the SBCMs will be differentiated using the terms *microstructure*, which focusses on the individual clay particles and the voids which form between them, and the soil *macrostructure*, which describes the aggregations of clay, the sand and gravel fractions and the voids which form between these larger particles. The mathematical modelling of expansive clay has been a particular focus and, whilst this is not a topic for detailed study within this thesis, certain key principles of importance still can be established with respect to the mechanical and structural response of clays during mechanical and hydraulic loading.

A conceptual model for expansive soils was presented in Gens and Alonso (1992) in which swelling of the clay particles occurs at a microstructural level and any major soil fabric changes occur at the macrostructural level. Additionally four key assumptions about the double structure of expansive clays are proposed in Gens and Alonso (1992):

- the voids within the microstructure are mainly saturated, meaning saturated soil effective stress concepts apply;
- any microstructural behaviour is volumetric and elastic;

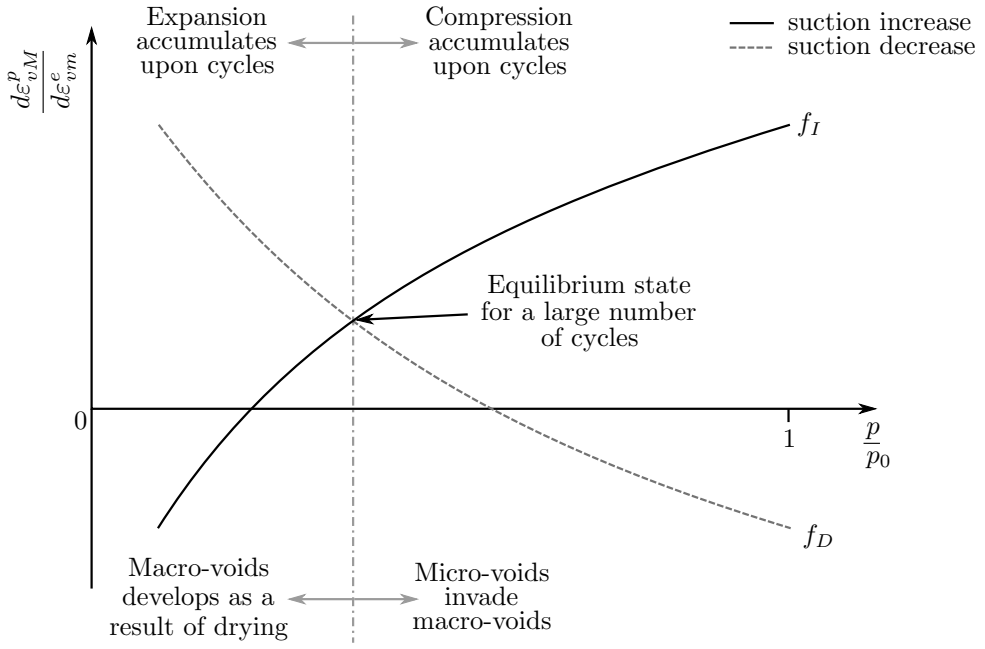

Figure 2.8: A summary of the interaction mechanism for micro- (intra-aggregation) voids and macro- (inter-aggregation) voids, modified from Alonso et al. (1999).

- hydraulic, mechanical and chemical equilibrium is maintained between the microstructure and macrostructure; and
- a build up of macrostructural plastic strains can occur as a result of coupled elastic microstructural strains.

The coupling between the macrostructural plastic strain ($d\varepsilon^p_{vM}$) and the volumetric elastic microstructural strain ($d\varepsilon^e_{vm}$) is expressed in Alonso et al. (1994) as

$$\begin{aligned} d\varepsilon^p_{vM} &= f_D d\varepsilon^e_{vm} \text{ (when suction is decreasing)} \\ d\varepsilon^p_{vM} &= f_I d\varepsilon^e_{vm} \text{ (when suction is increasing)} \end{aligned} \tag{2.13}$$

where f_D and f_I are coupling functions which depend on the current stress state and its relation to the macrostructural yield surface (p/p_0), in which p is the net mean stress applied to the soil and p_0 is the preconsolidation pressure. The implications of the coupling functions, and their detailed mathematical formulation, can be found in Alonso et al. (1999) and is summarised in Figure 2.8. During wetting and drying cycles of soils with a closed (dense) macrostructure the inter-aggregation voids will grow upon drying, as the aggregations shrink with the loss of water from intra-aggregate voids, and encounter less invasion of the inter-aggregation voids by aggregations during wetting as the aggregations have less room to swell within the dense macrostructure as water tries to enter the intra-aggregate voids. The limited swelling of aggregates in a closed structured soil during wetting, whilst the aggregations are still able to

shrink more readily during drying, results in an accumulated expansion of the inter-aggregation voids. In contrast during wetting and drying cycles of soil with an open (less dense) macrostructure aggregations are able to swell significantly during wetting (as water enters the intra-aggregation voids) with no limitation from other aggregations in very close proximity (due to the less dense structure) which causes an invasion of the inter-aggregation voids by the expanding aggregations (or intra-aggregate voids) and result in an accumulated compression of the soil (Alonso et al., 1999; Mašín, 2013).

The hydromechanical loading of soils containing expansive clays therefore has a large effect on the microstructure, since aggregations will swell and shrink during wetting and drying, but the overall soil volumetric behaviour depends on the soil's overall stability and whether the swelling of the intra-aggregate voids results in changes to the overall changes to the macrostructure. However, when a soil is subjected to mechanical loading, i.e. compressive loading under constant suction or constant water content, inter-aggregation voids within the soil will close up with increasing load whilst the intra-aggregation voids will remain unaltered, or increase slightly in quantity due to the contraction of inter-aggregation voids (Sivakumar et al., 2006; Thom et al., 2007; Alonso et al., 2011; Mašín, 2013). Therefore the two levels affect the soil behaviour in different, albeit interlinked ways, with the microstructure primarily responding to the wetting and drying of an unsaturated clayey soil whilst changes to the macrostructure are predominantly driven by mechanical loading (Alonso et al., 1999; Mašín, 2013).

2.5.2 Measuring voids

In order to investigate the voids within a soil, and hence elements of the material's microstructure and macrostructure, a range of techniques exist to determine the *void size distribution*, which shows the volumes of voids within a sample of a given size. As only the size of the voids is shown it is not possible to classify the voids according to the four void types illustrated in Figure 2.7, which depends on the solid phases which surround the voids, and therefore the more general terms *intra-aggregate voids* and *inter-aggregate voids*, determine by the critical void size, are used when discussing the void size distribution (Beckett, 2011).

Traditionally in geotechnical research mercury intrusion porosimetry (MIP) has been used to determine the void size distribution for soils. MIP involves the application of an absolute pressure (p) to mercury (a non-wetting fluid) in order for it to enter empty voids within a sample. As the pressure increases the mercury enters voids with smaller and smaller entrances and the size of these entrances (r) can be determined using the Washburn equation

$$r = -\frac{2\gamma_{_{Hg}} cos\left(\theta_{slv}\right)}{p} \tag{2.14}$$

where $\gamma_{_{Hg}}$ is the liquid-vapour surface tension of mercury, 0.484N/m, and θ_{slv} is the solid-liquid contact

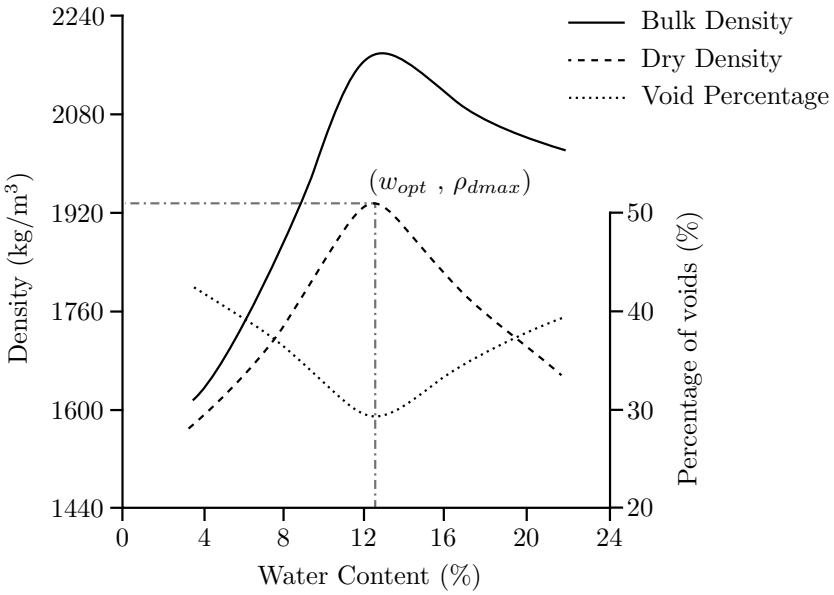

Figure 2.9: A representative compaction curve of a sandy-clay soil, modified from Proctor (1933).

angle for mercury, between 139^o and 147^o for different types of clay (Diamond et al., 1970).

MIP is a regularly used, and widely trusted, technique for determining the void size distribution of a soil between 10nm and 0.4mm however it does have a number of drawbacks including the need to use very small samples (less than 1g), the fact that trapped pores inaccessible from the outside of the sample are not measured and the requirement that samples must be devoid of water prior to testing, which is achieved through oven or freeze drying of samples. Additionally, a typical void size distribution plots the volume of intruded mercury against the void entrance diameter which is not a true measure of void size (Diamond et al., 1970; Romero and Simms, 2008; Beckett, 2011).

Laboratory x-ray computed tomography (XRCT) is an emerging technique within geotechnical research that is capable of determining void size distributions within much larger soil samples and providing three-dimensional quantitative data regarding the macrostructure of any scanned samples. XRCT is limited however to observing voids down to $1\mu m^3$ in volume and development of automated methods to produce void size distributions is still required before the technology is readily accepted. Chapter 3 of this thesis provides a detailed overview of the XRCT technique and its current uses in geotechnical research applications.

2.6 Compaction

Compaction of soil was first investigated in detail by Proctor (1933) to explore the design of earthfill dams and is also a key step in the process of SBCM manufacture. Figure 2.9, modified from Proctor (1933), shows a representative compaction plot of density and void volume against water content for a

sandy-clay soil. It is clear from Figure 2.9 that the bulk density, dry density and volume of voids within a soil is affected by the water content of the soil at compaction. The increase and subsequent decrease in density with increasing water content is as a result of the formation and distribution of aggregations within the soil due to suction. At low water contents large aggregations form which are not easily deformed, due to the high suctions present, and large voids exist around these aggregations. At high water contents water within the voids prevents the compaction of the solid structure. The most efficient packing of aggregations is achieved at the point at which the air phase becomes discontinuous and the maximum density of the compacted material is obtained. The *optimum water content* (w_{opt}) of a soil, for a given compactive effort, is therefore determined as the water content for which the *maximum dry density* (ρ_{dmax}) is obtained (Tarantino and Tombolato, 2005; Mitchell and Soga, 2005).

Soil compacted at water contents less than optimum water content generally are *bi-modal* in structure, i.e. two clear peaks are evident within their void size distribution, whilst soil compacted above optimum water content are generally *mono-modal* in structure and the division between the microstructure and macrostructure is less evident. Suctions for water contents below optimum water content during compaction are generally constant suggesting that only the arrangement of the aggregations is being altered whilst the intra-aggregation voids are unaffected. For soils compacted above optimum water content however the suctions are not constant and both the physical arrangement of the aggregations and the internal voids are changed during the compaction (Tarantino, 2009; Baker and Frydman, 2009). The bi-modal or mono-modal structure of a soil is not fixed however as wetting, drying and further mechanical loading can alter the soil fabric and it is therefore necessary to characterize the soil fabric, and obtain a sample's void size distribution, following all mechanical and hydraulic processes to which it will be subjected.

2.7 Suction regimes and the soil-water retention curve

When an unsaturated soil has a relatively high water content, and therefore a correspondingly low value of suction, the capillary component of suction dominates. In contrast for a soil with relatively low water content and higher suction values, where pore water is primarily found as thin films on particle surfaces, the adsorptive component of suction will dominate the water retention behaviour (Romero et al., 1999; Lu and Likos, 2004; Romero and Simms, 2008). The transition between the high suction regime dominated by adsorption and the low suction regime dominated by capillary suction is highly dependent on soil material properties (including void size distribution, particle size distribution, density, clay content etc.) and therefore a *soil water retention curve* is used to describe the relationship between soil suction and soil water content for a soil given its current structure and past hydraulic and stress history (Lu and Likos, 2004; Nuth and Laloui, 2008; Baker and Frydman, 2009; Gens, 2010; Beckett, 2011).

A key feature of soil water retention curves is that the relationship between water content and suction

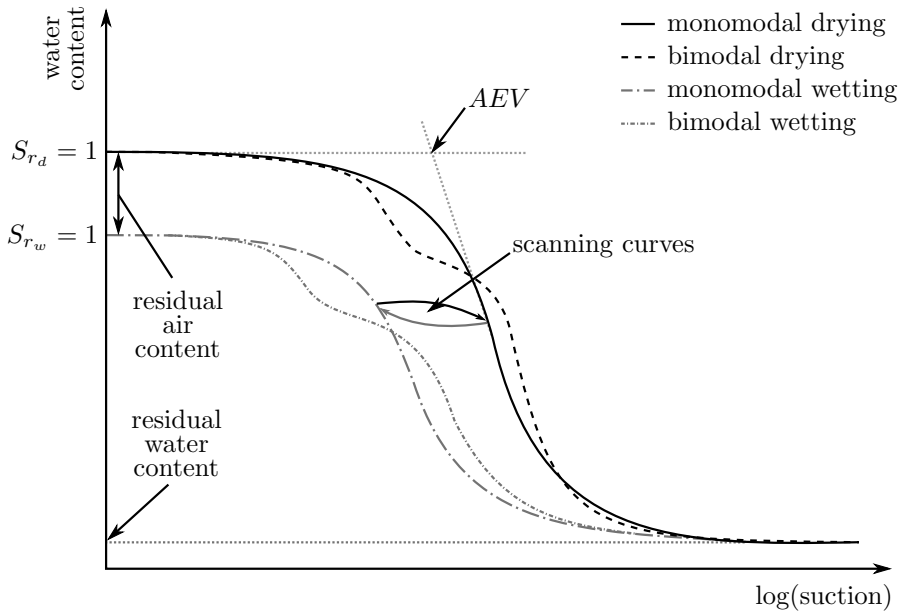

Figure 2.10: An example sketch of a monomodal and bimodal soil water retention curve during drying and wetting, modified from Beckett (2011).

is hysteretic as the water retention behaviour of a soil drying from its saturated state will be different from the behaviour of the same soil as it is wetted from an initially dry state. The main drying and wetting curves mark the hysteretic domain of the soil water - suction relationship however if a saturated soil is dried to an intermediate degree of saturation before being wetted again the water retention curve will move towards the main wetting curve and can be referred to as a scanning curve. The behaviour within the scanning region is often thought as reversible whilst water retention along the main wetting and drying curves is irreversible (Karube and Kawai, 2001; Tarantino, 2009). Figure 2.10 shows an idealised soil water retention curve, modified from Beckett (2011), in which the hysteresis is clearly visible and the following key features can be observed (Fredlund et al., 2011; Lu and Likos, 2004; Beckett, 2011):

- the *air entry value* (AEV), at which value of suction the largest voids begin to empty;
- the *residual water content*, i.e. the water that remains in the soil at very high suctions, and associated with water in adsorbed films and the smallest intra-aggregate voids; and
- the *residual air content*, which is the difference in saturated water contents before and after wetting ($S_{r_d} = 1$ and $S_{r_w} = 1$ respectively) and associated with air trapped within voids surrounded by water.

In the case of bimodal soil structures, in which a clear microstructure and macrostructure can be observed within the soil, the soil water retention curve steepens and flattens in two separate locations associated with the air entry values of the two distinct void sizes (Karube and Kawai, 2001; Tarantino, 2009) and this is also shown in Figure 2.10.

2.8 Implications for examining unstabilized soil based construction materials

The phase relationships of unsaturated soils are of key importance to the study of SBCM structures, which are essentially a three phase compacted unsaturated soil structure containing solid particles, liquid water and air within voids. In has been shown in Jaquin et al. (2009), among others, that suction developed within SBCMs is a primary source of strength and an understanding of total suction, and its constituent capillary, adsorptive and osmotic components, is crucial for understanding the mechanical response of SBCM structures. The origins of the solid particles found within SBCMs and understanding the mineralogy of clay particles is of particular importance when examining of expansive clay within SBCMs. In addition, an understanding of the formation of particle assemblages within the macrostructure of SBCMs and the characterising of the material voids is vital to examine the change in macrostructure during compressive loading and to understand the void size distribution of SBCMs. Finally, knowledge of the compaction of soil from a geotechnical perspective and the water retention behaviour of unsaturated materials is required to study SBCMs, in which compaction of the soil mixture and the subsequent drying of the compacted material are two key elements of the construction procedure.

As has been discussed here and in Chapter 1, it seems sensible that examining SBCMs from an unsaturated soils geotechnical perspective will provide insights into the design of modern SBCM structures. In this thesis particular focus is given to how the mineralogy and particle sizes in a SBCM mix design can affect the mechanical response to compressive loading and the void size distribution of SBCMs.

Chapter 3

The role of x-ray computed technology in geotechnical research

3.1 Introduction

This chapter introduces the laboratory x-ray computed tomography (XRCT) technique and its current use and future suitability in geotechnical research. Following a detailed literature review a number of shortcomings in the current use of XRCT are identified. An investigation into the suitability of two different XRCT machines and three analysis procedures, performed using two different software packages, shows that these shortcomings can be overcome and that XRCT has real potential to provide valuable information regarding the macrostructure of soil samples. Finally a number of additional conclusions are drawn to aid other geotechnical researchers as they use XRCT as part of an experimental programme.

It is acknowledged that the second half of this chapter is unusual in style as it refers to three investigations described in considerable detail later in this thesis. However by discussing the XRCT technique in detail, and highlighting the limitations and common misconceptions about the analysis techniques, separate to the detailed discussion of results related to the internal structure of unstabilized soil based construction material (SBCM) samples it is intended that the reader will have a better understanding of the XRCT technique, with respect to its advantages and disadvantages, before the results and conclusions are discussed in relation to SBCMs.

3.2 Introduction to x-ray computed tomography

X-ray computed tomography is a non-destructive 3D imaging process capable of imaging and analysing internal structures within solid samples to a resolution of less than one micron. The technique was first used for medical purposes (Hendee, 1979) followed quickly by the evaluation of its usefulness in material sciences (Reimers and Goebbels, 1983). X-ray computed tomography can be split into three different strands: medical, synchrotron, and laboratory. In medical x-ray computed tomography the focus is on

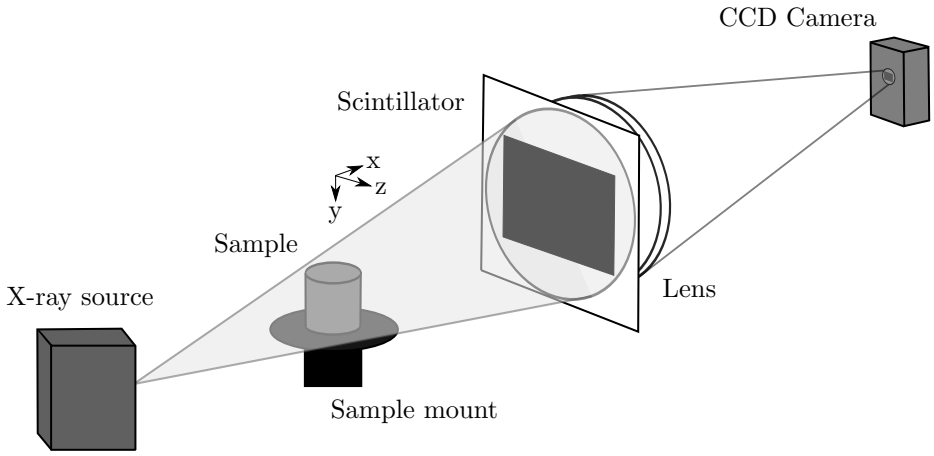

Figure 3.1: A simple sketch of a typical XRCT machine setup.

very fast scans of human patients at spatial resolutions of several hundred microns. A good overview of the medical technique's principles and developments can be found in Goldman (2007). An overview of advances in synchrotron x-ray computed tomography scanning is given in Baruchel et al. (2006). The synchrotron technique provides very high quality, sub-micron resolution images although access to these facilities is very limited and the operational costs are very high. Laboratory scanners span a wide range of spatial resolutions from several hundred microns through to the sub-micron resolutions achieved by synchrotron XRCT, but require much longer scan times and operate at much lower x-ray energies (Cnudde and Boone, 2013). Throughout this thesis the acronym XRCT will be used to refer to laboratory x-ray computed tomography scanners for which high quality overviews of its development and technology are available in Ketcham and Carlson (2001), Kruth et al. (2011), Cnudde and Boone (2013) and Helliwell et al. (2013). A combined summary of these overviews is provided in Section 3.2.1.

3.2.1 The technology

A simple sketch of an XRCT machine setup is shown in Figure 3.1. At its most basic level an XRCT machine contains three elements:

- the x-ray source, typically a conventional x-ray tube;
- a sample stage, which rotates the sample to enable a series of X-ray images to be obtained at incremental angular positions;
- and a detector, either a x-ray detector or a scintillator screen followed by a CCD camera focussed via a lens.

The x-ray tube consists of a focused electron beam directed at a target which, when hit, decelerates the electrons and generates x-rays. This x-ray beam is then shaped into a cone as it passes through a

circular aperture upon exiting the tube. The effectiveness of an x-ray source is controlled by:

- the focal spot size, which defines the possible source-detector paths that can intersect at any given point within the sample. A smaller spot size leads to less blurring and the ability to detect smaller features.
- the x-ray intensity, which affects directly the signal-to-noise ratio. Higher x-ray intensities improve the counting statistics and hence the image quality although they often require larger spot sizes which can increase blurring of images.
- the x-ray energy spectrum produced, which affects the level of detail achieved for differing density regions within a sample. Higher energy x-rays penetrate more effectively through a material, enabling the scanning of more dense samples, however are less sensitive to material density and composition variations, which reduces the identification of density fluctuations within the less dense regions of a sample.

As the x-rays pass through the sample the signal is attenuated through scattering and absorption and the detector produces a 2D grey-scale image of the sample showing the attenuation of the x-rays having passed through the entire sample. The linear attenuation coefficient, μ, for each pixel is defined using Beer's law, where I is the intensity remaining after the x-ray has passed through the sample of thickness h and I_0 is the incident x-ray intensity (Wellington and Vinegar, 1987)

$$\frac{I}{I_0} = exp(-\mu h). \tag{3.1}$$

By rotating the sample in small known increments, through use of the sample stage, a series of grey-scale attenuation images, or 2D projections, are captured and used to perform a mathematical reconstruction of the sample. The mathematical reconstruction, via the means of a back filtered projection, converts the series of 2D x-ray absorption images, captured in the y-z plane, into a series of 2D greyscale slices in the x-z plane which provide an indication of the density at any point within the sample. The series of 2D x-z plane slices are then stacked one above each other and a 3D data set is created in which the sample is described by a series of voxels. Voxels are the 3D equivalent of pixels within a 2D image and therefore are cubes with a fixed edge length mapping the entire sample volume each containing a grey-scale value related to the x-ray attenuation of the sample at the voxel's location. The reconstructed 3D model of the scanned sample can be used for visual inspection and quantitative analysis. A simplified sketch of the reconstruction process is shown in Figure 3.2.

3.2.2 Artefacts

The reconstructed 3D data obtained following XRCT scanning will contain imperfections and anomalies not representative of the sample. These unwanted effects are referred to as *image artefacts* and can

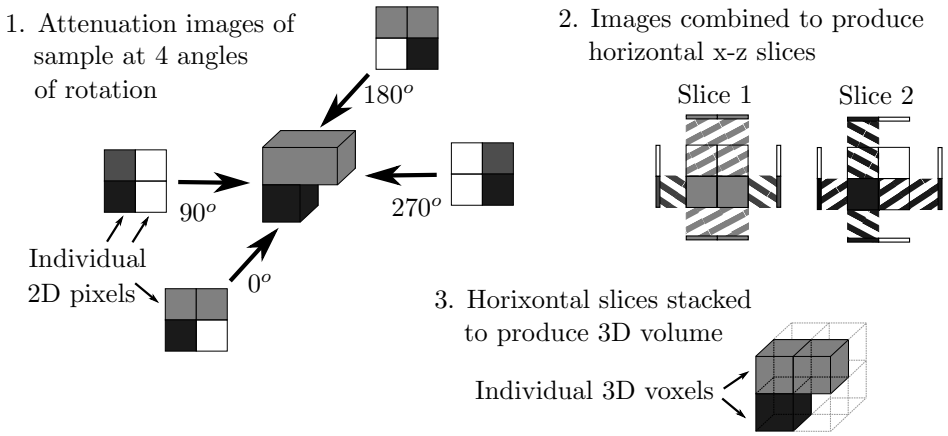

Figure 3.2: A simple sketch of the reconstruction process.

be problematic as they can obscure details of interest within the sample (Helliwell et al., 2013). The main image artefacts are described below and the mechanisms used to reduce their impact are outlined.

Beam hardening

Beam hardening occurs because low energy x-rays are more readily attenuated than high energy x-rays and will therefore be extinguished having passed a short distance into the sample. This in turn results in an evolution of the x-ray energy spectrum towards a higher mean energy and the outside edges of a material can appear to be more dense than identical material closer to the centre of the sample. The effect of beam hardening can be reduced in two ways: the introduction of a filter to remove the low energy x-rays before they reach the sample ensuring only the high energy x-rays pass through the sample (Kruth et al., 2011; Helliwell et al., 2013) and the use of software correction algorithms during reconstruction to manually correct for any observed beam hardening occurring within a material of known uniform density.

Ring artefacts

Ring artefacts are caused through inhomogeneities within the detector or the source and result in sharp contrast rings concentric to the centre of rotation. Ring artefacts can, as with beam hardening, be removed through software correction during reconstruction but can also be minimised by randomly moving the sample a known amount between each rotation increment.

Star artefacts

Star artefacts appear as star shaped distortions around metal objects and are caused by inaccurate measurement of the x-ray attenuation at localised high density regions within a surrounding lower density material. The use of homogeneous metal filters can reduce secondary radiation from high density regions within a sample and suppress the magnitude of star artefacts although it is difficult to remove completely.

Speckle

Constant density regions within a sample can appear to contain single voxel locations with a very high density or very low density. This speckling, also referred to as 'hot and cold spots' or 'salt and pepper speckle', occurs due to imperfections in the x-ray detector causing an incorrect measurement of x-ray attenuation for a single voxel within the sample data. Speckle can be minimised by randomly moving the sample a known amount between each rotation increment and further reduced using filters during post-processing of the data.

Partial volume effect

The partial volume effect appears as the blurring of edges between two different materials within a sample. Because the reconstructed 3D XRCT data is formed of voxels in a fixed grid formation any transition between two materials is unlikely to occur aligned with the edges of voxels. The volume region which a given voxel is representing can therefore contain two different materials with different attenuation properties and will have a grey-scale intensity which is an average of their properties. This results in a blurred transition between the materials and whilst filters to sharpen edges in an image can be applied during post-processing of the data, the blurring of material boundaries can never be completely avoided.

Incorrect rotation centre identification

Before the reconstruction of a scan is performed it is necessary to precisely locate the centre of rotation about which the sample has moved and the reconstruction should be performed (Kruth et al., 2011). The incorrect placing of the rotation centre leads to blurred images and, in the worst cases, features appear duplicated or are completely obscured. This artefact is minimised through the reconstruction software requiring an operator to inspect a series of images of a single slice through the sample, each with a slightly different rotation centre, and to identify the clearest image before reconstruction of the full scanned volume is performed.

3.3 Use of x-ray computed tomography in geotechnical research

The non-destructive nature of XRCT, its ability to scan large samples at resolutions of 100μm or better, and the opportunity to combine results with other techniques, such as scanning-electron microscopy, has made it an ideal technique for the investigation of soil and rock samples (Taina et al., 2008). Technological advances in XRCT over the past decade have seen the increasing use of the technique in fields of soil science and engineering geology where resolutions of 50-100μm capture features of interest. Excellent detailed literature reviews on the use of XRCT in these fields appear in Helliwell et al. (2013) and Jacobs and Cnudde (2009) respectively. However no similar overview of the use of XRCT in geotechnical research has been published to the author's knowledge and therefore this section provides a review of published

work in geotechnical research which has utilised XRCT, highlighting key trends and making some general observations about the use of XRCT in this area.

Three key journals, Géotechnique, Géotechnique Letters and Granular Matter, and the proceedings from two recent international conferences, UNSAT2014 and IS-Cambridge, were surveyed for any published work which used x-ray computed tomography. For the three journals they were searched from their first publication date, 1948, 2011 and 1998 respectively, until the end September 2014 and the international conferences were held in 2014. A total of 40 papers were found which used x-ray computed tomography and two papers, Smith et al. (2014) and Smith and Augarde (2014), are conference proceedings of the research presented in Chapter 4 and Chapter 5 of this thesis. These two papers are therefore are not included within this review. The remaining 38 papers were analysed and from each paper, where the information was provided, the following were recorded:

- material analysed, including the sample's particle size distribution;
- sample size, for testing and scanning;
- voxel size, or resolution;
- XRCT scan descriptions;
- results presented.

Each of these is now discussed in turn.

3.3.1 Material analysed

Thirty papers were found which provide relevant information regarding the material scanned. The information was either given as maximum and minimum particle sizes found within the sample or the material d_{50} value. Figure 3.3 shows the range of particle sizes across all the papers and it is clear that the majority of samples contain particle sizes between 0.1mm and 2mm, i.e. sands. Many geotechnical soils of interest however are not formed of a single particle size and very few exist on-site in which no particles below 0.1mm can be found. Taylor et al. (2014) highlight some of the difficulties which arise when scanning gap-graded or broadly graded samples during sample preparation, image processing and image analysis. Whilst Taylor et al. (2014) suggest a few methods to overcome these difficulties including iterative segmentation, where fine and coarse solid particles are identified separately, and the development of statistical tools, to reduce the error induced by deleting particles at the edge of scanned volumes, it is clear that the difficulties of scanning more broadly graded materials still need to be overcome. It is suggested therefore that the currently available XRCT technology is frequently restricting the scanning of materials to only a single material with a small range of particle sizes and for XRCT to become a more widely used technique in geotechnical research development is required into the scanning and analysing of samples containing a wider range of particles, particularly samples containing particles less than 0.1mm.

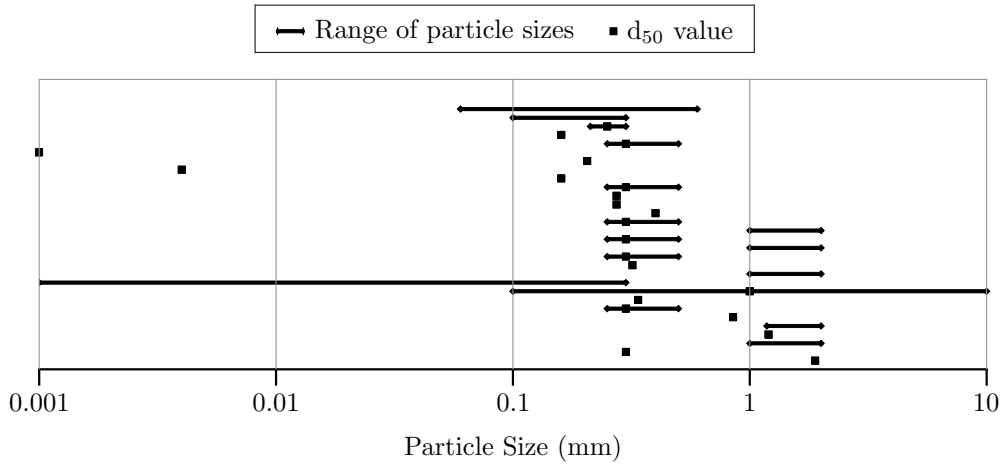

Figure 3.3: A plot of the particle size of the XRCT samples from all 30 papers.

3.3.2 Sample size

Thirty one papers provide information regarding the size and shape of the sample scanned within the XRCT machine. Three papers, Orense et al. (2013), Yan et al. (2014) and Zhao et al. (2014), consider only a single particle and Oda et al. (2004) discuss the results from the scanning of a parallelopiped sample 180mm high, 160mm wide and 80mm thick. The remaining 27 papers describe results obtained from the scanning of cylindrical samples of varying heights and diameters. Five of these investigations took smaller cores from larger samples on which other laboratory experiments had already been performed, including Fonseca et al. (2013) who performed triaxial compression tests on 38mm diameter, 76mm high cylinders before extracting resin impregnated 'mini-cores' 3-6mm in diameter from regions within the shear band and the bulk of the sample. Figure 3.4 plots the diameter of the samples scanned in each of the 27 papers using cylinders. It can be seen from Figure 3.4 that a large proportion of investigations scanned small cylindrical samples (<12mm) whilst a significant minority, 5 investigations, have performed scans on much larger oedometer samples 70mm in diameter. Whilst no discussion of the choice of sample size can be found in any papers, including Fonseca et al. (2013) where small cores were taken, it is presumed that the XRCT machines performing the scans required small sample sizes to obtain the required resolution or to fit within the scanning chamber.

The predominant use of cylindrical samples with a diameter smaller than 15mm raises an interesting question of whether these small samples are appropriate for the purposes of geotechnical research. Whilst the XRCT scanners used may be limiting the sample size, either in the size of scanning chamber or to achieve a required resolution, testing such small samples will have an effect on other properties of the material, including mechanical behaviour (Ciancio and Gibbings, 2012), and this should be acknowledged by the authors when publishing their work. The utilisation of small cores extracted from a larger sample

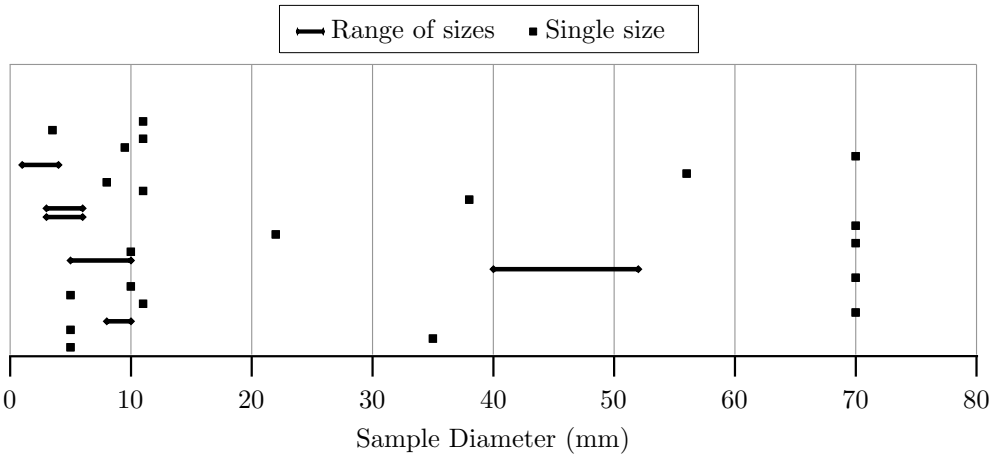

Figure 3.4: A plot of the XRCT sample diameters from all 27 papers using cylindrical samples.

may appear to be a sensible method of testing larger samples however this removes a major advantage of the XRCT analysis technique, its non-destructive nature. Subjecting a sample to resin impregnation and then extracting a core is clearly an irreversible process and prevents any further testing on the scanned sample. Therefore it seems sensible to avoid coring samples wherever possible and instead where possible adapt the XRCT procedures to ensure a single sample can be scanned before, during and after testing to ensure direct comparisons can be made.

Finally it should be noted that the 38mm diameter triaxial cylinder, the standard sample used in many geotechnical testing procedures, has according to the findings of this survey only been used in a single piece of published work, the investigation described by Gens et al. (2011). This therefore suggests that the majority of investigations have been adapting their experimentation to meet the perceived requirements of the XRCT analysis rather than utilising or adapting the XRCT technique to investigate more common samples used in geotechnical research. The investigation described in Chapter 5 of this thesis is in direct response to this observed trend towards smaller, non-standard, geotechnical sample sizes and Section 3.4 in this chapter discusses the feasibility of scanning larger samples.

3.3.3 Voxel size and data collected

Eight papers provided no information relating to the size of the voxels within the 3D reconstructed data or the final resolution of the XRCT scans they performed. Twenty eight of the remaining 30 papers gave specific voxel sizes for the scans performed and the results are shown in Figure 3.5. The final two investigations described in Bruchon et al. (2013) and Yan et al. (2014) provide only the maximum spatial resolution of the scanner, 5μm and 4μm respectively, but do not state the resolution at which the samples were actually scanned. From Figure 3.5 it is clear that there is a range of voxel sizes from 1μm to 51μm with the majority of the scans being performed at voxel sizes below 20μm.

Fonseca et al. (2013) presents a table of voxel size to d_{50} grain size, from their paper and four prior investigations, in order to state that their scans were a significant improvement on previous studies. That the authors provide justification for their chosen voxel size, and imply that it is sufficient for their work, is a positive step towards honest critiquing of XRCT data, however this voxel size to d_{50} grain size ratio is only an appropriate measure for identifying solid particles of known particle size distribution. Additionally the authors do not actually discuss how any reduction in the voxel size to d_{50} grain size ratio results in improvements over their previous work and simply state that the ratio is lower than in previous investigations.

Despite its prevalent use, the voxel size of a scan does not provide a complete picture of the data set collected. The final resolution of the image has a bigger impact on the quality of the quantitative and qualitative conclusions drawn from any XRCT scans performed (further discussion can be found in Section 3.4.2). Surprisingly then, only two papers make any reference to the final resolution of the XRCT data and both indicate the resolution is approximately twice the voxel size, 25µm voxels & <50µm resolution (Bruchon et al., 2013) and 1.0µm voxels & 1.8µm resolution (Zacher et al., 2014).

When presenting results from XRCT scans, as with any experimental technique, it is important that the reader can judge the the quality and appropriateness of the scans and providing only the voxel size is not sufficient. The appropriate resolution for a scan depends on the feature being identified and the material analysed meaning that high resolution images are not always necessary. Additionally XRCT scans are also performed to identify different descriptors of features, such as the connectivity of voids in unsaturated soils or the size and orientation of granular particles, and all of this affects the required resolution. Orientation of a feature may be obtained from low resolution images in which the predominant shape can be identified whereas connectivity of small voids with connections less than 5µm will clearly require identification of features less than 5µm. Therefore it is suggested that resolution, i.e. the smallest identifiable feature of interest within the scan, should be the variable used to describe XRCT data rather than the current use of voxel size. Firstly this is because resolution includes other variables which have an impact on XRCT data, such as analysis procedures, the presence of noise and the partial volume effect, and secondly resolution is a better measure to present in geotechnical literature since it is less easily misunderstood by geotechnical engineers.

3.3.4 Scanning procedures

Figure 3.6 shows the x-ray computed tomography machine types used across all 38 investigations. Both the bench-top and free-standing machines are laboratory XRCT facilities as opposed to synchrotron or medical facilities, but have been recorded separately due to the large difference in cost and the sample size which can be scanned within the two types of machine. It is clear that the majority of the scanning was performed using free-standing XRCT machines although the fact that nine papers provided no

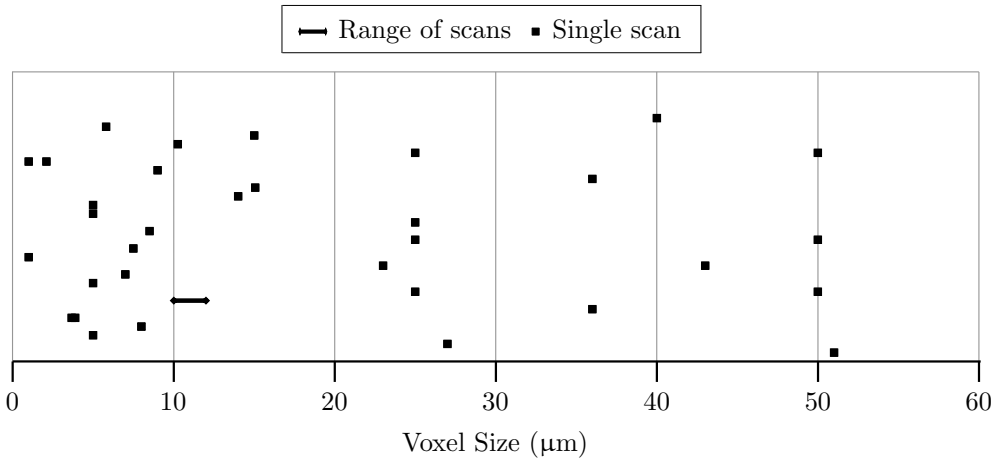

Figure 3.5: A plot of the voxel sizes from all the scans performed in 28 papers.

information about the machine used is more of a concern, since the type of machine will have a major impact on the resolution and type of data collected.

When discussing the experimental programmes very few papers give any information regarding the number of XRCT scans performed or the number of repeats run for a given sample type. Only six papers provided sufficient information to establish how many scans or repeats had been performed. Of these only the investigation by Pender et al. (2014) ran the test in triplicate, i.e. scanned three samples for any given stage to enable results comparison, and two investigations, by Fonseca et al. (2013) and Zhao et al. (2014), ran scans in duplicate with the remainder appearing to only perform scans on single samples. Since laboratory experimentation introduces an element of uncertainty and variability into any results obtained, good experimental practice dictates that, wherever possible, repeats should be performed to ensure measurements taken truly reflect the reality. In addition the XRCT scanning and analysis procedures involve extra factors which can affect results, often including a large amount of operator input, which can therefore increase the variability in results obtained (Taylor et al., 2014). Logic would dictate that more repeats, not less, are performed to reduce this variability however the review of the literature suggests this not currently the case within the geotechnical research community using XRCT. Collecting XRCT data, and particularly analysing the reconstructed data into useful information, is a time consuming process and time on XRCT machines is often limited or expensive, and it is likely that these are the main reasons for the lack of repeats, rather than poor experimental practice or design.

Figure 3.7 shows the information given regarding the image post-processing of the XRCT scan data. Immediately obvious is that over 30% of papers where XRCT results are discussed provide no information regarding the image processing. As discussed in Section 3.4.2, image processing has a major impact on the results obtained and is a key part of the XRCT scanning process. Even if the results are shown exactly as produced by the XRCT machine the lack of filtering, smoothing or processing should be stated so that

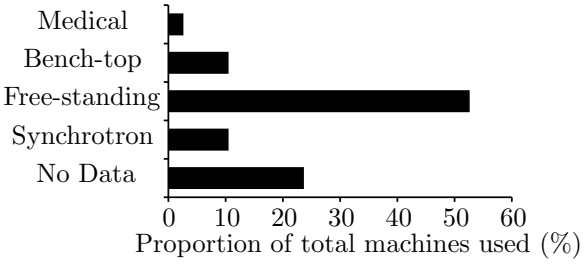

Figure 3.6: A histogram showing the different types of x-ray computed tomography equipment used.

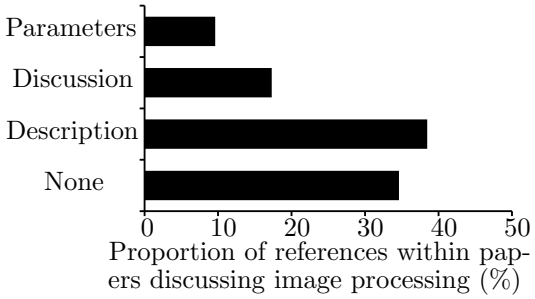

Figure 3.7: A histogram showing the information presented relating to image processing.

this is clear to the reader. A larger proportion did provide a description, for example 'a 3D watershed algorithm is applied and the particles are separated' (Strege et al., 2014), however a description such as this is insufficient information considering the number of variables that can be adjusted during these image processing steps. In order for a reader to fully understand the results or attempt to replicate any experimental results presented the exact parameters used need presenting as part of the image processing discussion and it is clear from Figure 3.7 that this only occurred in 10% of cases seen in this survey. With XRCT techniques only recently being used more regularly in geotechnical research it is even more important for these parameters, and the associated discussions, to be presented alongside the results since without it no real assessment of the analysis techniques can be performed or accepted procedures implemented across the geotechnical community.

In any experimental work it is important to provide information on the tests performed, in order that the results may be properly understood and repeated or verified. The lack of information provided about the data collection processes, the number of scans performed and the means by which the data is processed suggests that the XRCT scanning stage within geotechnical research is currently not seen as a stage in the experimental procedure but as a black box analysis technique which produces perfect information and the results should be accepted as shown. The discussion in Section 3.4 indicates this is not the case and it is important for the development of XRCT within geotechnical research that authors provide clear information regarding the scanning and data processing procedures.

Table 3.1: The change in presentation of results over time.

Presentation	**Year**						
Method	2008	2009	2010	2011	2012	2013	2014
None	0	0	1	0	0	0	2
Quantitative	1	0	1	0	1	6	10
Qualitative	1	0	3	2	0	9	16

3.3.5 Results presented

The results presented across the papers varies considerably because of the broad range of questions being answered by each individual research paper. It is possible however to differentiate the mode by which the data collected from XRCT scanning is presented into three distinct sections: *qualitative*, where the paper presents reconstructed images of the scanned specimen and makes comments about its behaviour referring to these images; *quantitative*, where graphs and corresponding values are presented having processed and analysed the reconstructed data to produce quantitative measures; and *none*, where no data relating to the XRCT appeared to have been shown. Table 3.1 shows that the vast majority of XRCT results presented in geotechnical research are accompanied by a minimum of one image (31 of 38) whilst only half of the publications (19 of 38) provide any quantitative results.

The predominant presentation of qualitative results should not be seen necessarily as negative. One of the major advantages of XRCT scanning is the three-dimensional visualisation of the scanned sample and therefore presenting images to inform discussion and analysis of results can be a useful tool. However, another major advantage of the XRCT data set is the large amount of digital information available from the scans and there are a range of computational analysis programs, including Avizo Fire® (FEI, 2014) and ImageJ® (Schneider et al., 2012), which can provide quantitative data following post-processing. It is the lack of quantitative results presented in the papers surveyed, or any real sign of quantitative results becoming more common as the use of the technique grows in geotechnical research, which is an area for concern as without quantitative results it will be hard to convince readers of published work of the validity of findings or the real usefulness of XRCT for scientific investigation.

3.3.6 Observations and trends

This review of the use of XRCT within geotechnical literature has identified a number key shortcomings in the discussed publications. These shortcomings are not meant as a criticism of previous work but identify the areas in which the use of XRCT in geotechnical research could be improved. A summary of the survey is given below.

- There is a tendency to scan narrowly graded geotechnical materials, usually sands containing no particles smaller than 0.1mm, and more development of the XRCT technique is required to enable scanning of samples with a larger range of particles sizes;
- The scanning of samples smaller than 15mm predominates, small cores are often extracted removing the non-destructive nature of XRCT and 'standard' geotechnical samples are rarely used in XRCT scanning. It therefore appears that the geotechnical community are currently adapting and compromising their experimental investigations to fit the XRCT technique, rather than developing methods of XRCT which meet the needs of a given experiment;

- The presentation of voxel size information to describe the scan currently predominates and the final resolution of the processed images is rarely discussed. For the wider geotechnical community to properly understand any results obtained through XRCT it is the final image resolution, rather than voxel size, which must be presented in any publication of results;
- Minimal information is provided within published work about the scanning procedures used or the image post-processing performed and XRCT is being presented as a 'black-box analysis technique' to provide perfect information about any given sample rather than as a key stage within the experimental procedure. This attitude may be limiting the development of new methods specific to solving the needs of geotechnical researchers or giving a false impression of the accuracy of any data obtained.
- There is a disappointing lack of quantitative results presented in the literature and no apparent increase in the presentation of quantitative results as XRCT has been more widely used. The visualisation capabilities of XRCT are powerful however if few quantitative results are ever presented the full potential of the XRCT is not being realised and it will be hard to convince the wider geotechnical community of the usefulness of XRCT as an analysis tool.

3.4 Investigation into the capabilities of laboratory x-ray computed tomography for use in geotechnical laboratory experiments

Three separate investigations into SBCMs are described in this thesis and all these utilise XRCT scanning to investigate the internal structure of the material. The first investigates the propagation of cracks within SBCM samples during unconfined compressive loading, the second investigates the void structure of SBCM samples of different sizes and the third the effect of the presence of expansive clay on the macrostructure of the clay-sand matrix within SBCMs. The detail of the experimental programmes implemented and any conclusions related to SBCMs are presented in Chapter 4, Chapter 5 and Chapter 6 of this thesis respectively. However in these three investigations two XRCT machines and three analysis procedures are used to inform the discussions regarding the internal structure of SBCMs and great deal of information relating to the capabilities of XRCT has been collected which cannot only be applied to SBCM research but to the much wider field of geotechnical research. This section of Chapter 3 therefore discusses the capabilities of the XRCT machines and subsequent analysis procedures from a XRCT scanning and imaging perspective, addresses some of the shortcomings in the current use of XRCT in geotechnical literature outlined in Section 3.3.6 and draws some instructive conclusions which can hopefully aid other geotechnical researchers as they use XRCT.

Figure 3.8: An image of the SS1174 from http://www.skyscan.be/products/1174.htm

Figure 3.9: An image of the XRM410 from http://www.dur.ac.uk/xrdur/facilities/xrct

3.4.1 The machine capabilities

In assessing the capability of the two XRCT machines certain goals were imposed on the scanning following the review of current use of XRCT in Section 3.3 and the requirements of the investigations into crack propagation, void structure and expansive clay. Firstly the output following scanning and post-processing had to capture a wide range of void volumes since all samples were manufactured from broadly graded SBCM mixes of varying clay, sand and gravel proportions. Secondly, in order to minimise the change in mechanical behaviour and reduce the need to sieve larger particles from the mixtures before manufacture, the samples needed to be as large as practicable. Thirdly samples could not be impregnated with resin or cores extracted as had been done in previous geotechnical XRCT studies by other authors, for example Fonseca et al. (2013), as further tests were performed on the sample after scanning. Fourthly all the scans and data analysis needed to be practicable and realistic, i.e. scans should not take longer than 24 hours to perform in the machine and analysis had to be performed on desktop computers. Finally the scans and analysis needed to be repeatable and any data comparable, whether that was between one sample and the next or a single sample at two stages in an experimental procedure.

The specifications of the two machines are briefly outlined before four key factors are discussed to assessed the suitability of the XRCT machines for use in geotechnical experimentation.

Machine specifications

The SkyScan1174 compact micro-CT scanner (hereafter referred to as SS1174), shown in Figure 3.8, is a table-top XRCT scanner capable of scanning small samples at a pixel size between 6µm and 30µm. The SS1174 has the option of fitting additional stages within the scanning chamber to provide additional functionality, such as micro-positioning, material testing and cooling (SkyScan-Brucker, 2012). The XRadia/Zeiss XRM 410 (hereafter referred to as XRM410), shown in Figure 3.9, is a much larger laboratory based machine designed to provide high-resolution scans to 1.0µm on a large range of sample

sizes for analytical scanning within research and industry. The XRM410 has a large working area within the machine enabling in-situ experimentation through the use of purchased, or custom built, stages (XRadia-Inc., 2011). Additional machine specifications are provided in Table 3.2 for both scanners.

Additional capabilities

The SS1174 was used for the investigation into crack propagation in which a series of tests were performed which utilised the SkyScan material testing stage in order to scan samples during compressive loading. In-situ load testing of samples was not required for any of the work performed using the XRM410 and so similar stages for the XRM410 were not investigated. The material testing stage was capable of applying tension or compression to a sample whilst in the SS1174 and was used in this instance to compressively load 12mm diameter samples of the SBCM up to failure, pausing at 25N load increments to perform an XRCT scan. The ability to subject samples to compressive loading during scanning is a very useful tool and has the potential to provide information about a geotechnical sample's behaviour during loading, for instance tracking the evolution of a shear band, changes in void size distribution or crack propagation.

Unfortunately, however, the material testing stage had a number of limitations which had a serious impact on the results obtainable during this programme of experimentation. Firstly the load stage had to be controlled using a separate program to the one which controlled the scanning procedures. This meant that any sample loading and XRCT scans had to be performed whilst an operator was present as they were required to start and stop the material testing stage and commence each scan by the SS1174. Whilst an operator is clearly required to initially set up any scans being performed, XRCT scans can take any time between 5 minutes and 48 hours, often finishing outside of 'normal working hours' and therefore needing an operator to run loading tests or start scans means the efficiency of the machine scanning could be severely affected.

Secondly there was no reliable mechanism for pausing the material testing stage at predefined loads or for controlling the loads during scanning. The control program suggested that the material testing stage

Table 3.2: The manufacturers stated specifications for both XRCT machines.

Machine	**Specification**				
Name	X-ray source	X-ray detector	Pixel Size	Object Size	Dimensions
SkyScan1174 compact micro-CT scanner	20-50kV, 40W max.	1.3Mp CCD coupled to 1:6 zoom lens & scintillator	6-30 µm	5-30mm diameter, 50mm length	width:810mm depth:325mm height:420mm
XRadia/Zeiss XRM 410	40-150kV, 10W max.	4.0Mp CCD coupled to 0.4x, 4x, 10x or 20x lens' & scintillator	1 - 40 µm	maximum 300mm diameter, 15kg mass	width:3m depth:1.5m height:2m

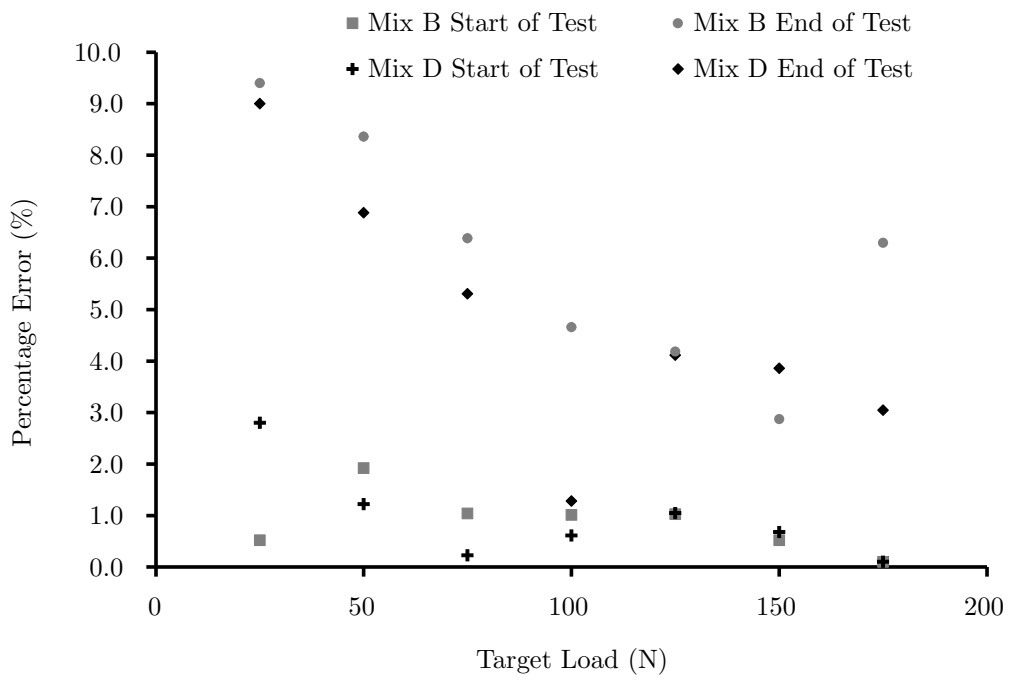

Figure 3.10: The percentage error in compressive loads applied by the material testing stage.

could be load controlled and an option to fix the load applied by the material testing stage was available. However initial tests performed found that the load applied by the material testing stage could drop during a scan by up to 25N over a 30 minute period, despite the control program being set to maintain a fixed compressive load, and therefore it was necessary to perform very fast scans when any load was being applied. The reasons for this drop in load was not explored in detail however it appeared that the material testing stage was displacement controlled, i.e. did not move during scanning, and the option to set the load during scanning only fixed the displacement at the position at which the desired load was first applied by the material testing stage.

Figure 3.10 plots the percentage error between the target and achieved applied compressive loads at the beginning and end of the scans using the material testing stage for two samples tested in the crack propagation investigation. It can be seen in Figure 3.10 that even when the scans were limited to 10 minutes the load applied to sample would change during the duration of the scan and it was not uncommon for the load applied to have an error greater than 5% of the target load. In fact, across all the scans performed using the material testing stage, 57.6% of all scans finished with the load applied having decreased by more than 5%.

Finally, the XRM410 has an additional function during scanning designed to prevent any ring artefacts appearing during a scan. This 'dynamic ring reduction' function moves the sample a very small amount between each rotation of the sample, ensuring any error which may be introduced by a single pixel does not result in a ring artefact and instead is removed through the averaging of all the other images. The

SS1174 does not have this feature and instead provides a parameter to remove any ring artefacts during reconstruction. This 'ring artefact reduction' algorithm relies on operator judgement and computational post-processing, rather than simply removing the artefact from the original scan data, and therefore the SS1174 mechanism for removing ring artefacts, whilst capable, is a less desirable solution than that provided by the XRM410.

Sample size

The SS1174 is capable of scanning a range of sample sizes up to 30mm in diameter and two different sample sizes were used for the investigation into crack propagation, a 27.6mm diameter sample and a 12mm diameter sample. The 27.6mm diameter sample was clearly close to the upper size limit imposed by the machine and was used to ensure the sample fitted within the physical limits of the machine and the entire sample was visible to the detector during scanning. The 12mm diameter sample was scanned within the material testing stage and was chosen to ensure compressive failure of the SBCM samples would occur, using an estimated ultimate compressive strength of 1.3MPa (Standards New Zealand, 1998) and maximum capacity of the material testing stage was 200N. For both scans the maximum power settings, 50kV and 800μA, was required to enable sufficient x-rays to reach the detector and for any data to be recorded. Therefore the use of soil samples close to the 30mm diameter was pushing the SS1174 to the limit of its scanning ability.

The XRM410 has the capacity to fit samples of up to 300mm diameter into the scan chamber. This does not mean however that the full sample could always be scanned since the detector size and voxel size dictated the scan field of view and in samples larger than 50mm it is only possible to scan a region of the sample placed within the chamber of the XRM410. Three different sample sizes were used during the investigations into void structure and expansive clay, 12mm, 38mm and 100mm diameter samples with a diameter:height ratio 1:2. The 12mm sample was chosen as it was the largest possible sample size for which a 1μm resolution could be reasonably obtained and the 38mm and 100mm samples are the standard sample sizes used in triaxial testing. Prior to the manufacture of the samples it was necessary to sieve the 30*:60:10 mix (2mm for ϕ12, 5mm for ϕ38 and 10mm for ϕ100) to prevent the larger particles interfering with the compaction and loading behaviour. In contrast to the observed trend within current geotechnical investigations using XRCT, discussed in Section 3.3.1, no sieving was performed to remove the smallest particles to produce a narrowly graded particle distribution for the scanned sample.

For all three sample sizes a 'small field of view' and a 'large field of view' was performed. The large field of view scan was set up to view the largest amount of the sample possible whilst the small field of view sample scan was set up to obtain the maximum resolution possible, hence reducing the field of view. Table 3.3 shows the field of view obtained and from this it is clear that it was not possible to see the entire 100mm diameter samples. In addition, the small field of view 100mm diameter scans were not of

sufficient quality to use as the XRM410 was not powerful enough to successfully scan such a large sample at such a high resolution. Low x-ray counts at the detector resulted in an inability to clearly identify the solid and air phases during post-processing. The large field of view 100mm diameter sample scans were still able to provide quantitative void size distribution information for the investigations into void structure however it is suggested that 100mm samples are too large for XRCT scanning if high resolution data is required given the technological capabilities of the XRM410.

Scanning times

The SS1174 scan times were predominantly dictated by limitations enforced from other experimental procedures and limited access to the SS1174 meant in order to complete the full testing program it was necessary to process two samples within a single working day. The 27.6mm samples were scanned in the SS1174 before and after compression testing using a separate Lloyd LR5K Plus testing machine (LR5K) and since four scans were required per day each scan could not take longer than 2 hours. The exposure time for each image was already set at the maximum 7500µs, due to the size and material of the sample. This meant that a rotation step of 1° was chosen and, with two images captured per increment, each scan took approximately 100 minutes. These scan settings were adequate to provide the necessary data for post-processing however reducing the rotation step would have undoubtedly increased the quality of images obtained and, if the scan times were not so limited by machine time, taking longer to scan samples would have been beneficial, particularly since the SS1174 was operating at the limits of its capabilities.

The 12mm sample's scan parameters were also affected by the capabilities of the material testing stage which dictated the length of scans between loading stages. As previously discussed, the load applied by the material testing stage dropped dramatically during scanning, up to 25N in 30 minutes, and therefore all the fast scans had to be limited to a maximum of 10 minutes. Despite this limit the exposure time still had to be set at the maximum 7500µs and so only the number of scans taken per step could be reduced and the rotation interval increased to shorten the scan duration. This meant that the fast scans had to be performed without repeat images at each step and a rotation interval of 5° was chosen giving a scan time of 580 seconds. The remaining three scans performed for each sample, a blank reference, a pre-loading

Table 3.3: The XRM410 scan parameters for all three sample sizes. LFOV indicates a large field of view scan whilst SFOV indicates a small field of view scan.

Sample Size	**Diameter (mm)**	**Height (mm)**	**Scan Type**	**Voxel Size (µm)**	**Field of view (mm)**	**Scan Time (hr)**
ϕ12	12	24	LFOV	12.3	25.2 x 25.2	2
ϕ12	12	24	SFOV	1.0	2.0 x 2.0	19
ϕ38	38.1	76.2	LFOV	20.3	42.4 x 42.4	7
ϕ38	38.1	76.2	SFOV	2.1	4.2 x 4.2	19
ϕ100	100	200	LFOV	37.8	79.9 x 79.9	6.5
ϕ100	100	200	SFOV	7.8	19.1 x 19.1	25.5

and a post-loading scan, were then dictated by the fact that the entire scan procedure was limited to 4 hours. These three scans therefore were performed with a rotation step of 2° and took approximately 25 minutes.

While the scanning times for the SS1174 did enable two samples to be processed within a single day this restriction on scanning time did cause problems when post-processing. The scan settings chosen provided suitable data under visual inspection however the post-processing techniques could not adequately identify the transitions between solid and air phases for the scans on the 12mm samples. This was largely due to insufficient information defining the reconstructed data which had arisen through the lack of images taken during scanning, when the rotation step was increased above 1°. This highlighted a key problem that only using visual inspection to check scan quality can lead to considerable problems during analysis and that determining scan times by factors other than that required for high XRCT scan quality can lead to data from which no useful quantitative results can be obtained.

The XRM410 scan times are given in Table 3.3 and, in contrast to the method for determining scan settings for the SS1174, all samples were scanned following procedures which would ensure maximum scan quality. No limits were placed on the scan time and, due to the increased scanning capabilities of the XRM410, two small field of view scans and a single large field of view scan could be performed. It is very clear from Table 3.3 that the detailed scans took considerably longer than the full sample scans. Whether a 25.5 hour scan, as in the case of the detailed scan of the 100mm sample, is an appropriate length of time to scan depends on other factors from the experimental programme, such as whether a sample will continue to dry perhaps changing its structure, and it is rare that XRCT scans will be performed in isolation from any other experimental time constraints or limitations on access to an XRCT scanner. It is clear however that XRCT scans at the highest available resolutions when using the XRM410 can take considerable time and this must be factored into any experimental planning and machine time booking if detailed scans of larger XRCT samples are required.

Voxel size obtained

The voxel size obtained for all the scans using the SS1174 was fixed at 30.8µm, due to the physical constraints of the machine and the sample sizes used. The XRM410 scans were performed at a range of voxel sizes, from 1µm to 37.8µm, as shown in Table 3.3. From this it is quite clear that the XRM410 had the ability to achieve a smaller voxel size than the SS1174 when scanning the entire sample; 20.2µm and 12.3µm for the 38mm and 12mm diameter samples respectively. In addition even smaller voxel sizes, 1.0µm and 2.1µm, could be obtained with the XRM410 through the use of a detailed scan of a small region of interest. This smaller voxel size, when coupled with correct analysis techniques, is clearly a great advantage as it enables the identification of smaller sized features and the description of larger features with more confidence.

The voxel size of the final reconstruction however is not only dependant on the zoom applied by the XRCT scanner but also on the number of slices in the reconstruction, affecting the resolution in the vertical plane, and the angle of rotation of the sample, affecting the resolution in the horizontal plane. When using the XRM410 the reconstruction software automatically maintained the same voxel size in the vertical plane whereas for the SS1174 it was necessary to set the number of horizontal slices created during reconstruction. Using 840 slices through the depth of the sample ensured that the scan resolution of 30.8µm was maintained during reconstruction of all scans performed using the SS1174.

The XRM410 scans were all performed using 1601 images (0.225° per rotation) and the 5°, 2° & 1° angles of rotation of the samples when scanning using the SS1174 also ensured the 30.8µm resolution was maintained in the plane of rotation, with points moving a maximum of 22.8µm on the very edge of each sample with each rotation of the sample relative to the x-ray detector. It might be suggested that the 2° and 1° angles of rotation were unnecessary for the SS1174 scans, since the 5° rotation was acceptable to achieve 30.8µm however, as discussed in relation to scanning times, this increase in rotation step led to data from which no void size distribution could be produced. By reducing the rotation angle, and in turn increasing the number of images, the quality of the sample reconstruction was improved as the construction algorithms utilised by both XRCT softwares had far more information to describe each voxel within the sample and therefore could calculate the information regarding it with far greater confidence. It is therefore important to note that reducing the number of slices, or increasing the angle of rotation, can be very attractive when trying to reduce the time required to scan but this must be done with great care. The impact on the scan quality and the true resolution of the resulting reconstruction must be calculated and, as discussed in detail in Section 3.4.2, it cannot be assumed that since the XRCT scanner was set to a specific voxel size that this resolution will still hold once the 3D reconstruction of the sample is complete.

3.4.2 Data analysis capabilities

There are a great diversity of image analysis protocols used by the XRCT research community (Helliwell et al., 2013) and as highlighted in Section 3.3 the discussion of these image analysis methods is not commonly found within geotechnical research literature. Additionally the various different procedures have been shown to produce a variety of quantitative results, Marcelino et al. (2007) demonstrate the different results obtained from using manual, semi-automatic and automatic 2D-image analysis to determine soil porosity on a set of three images, and Baveye et al. (2010) performed a so-called 'round-robin' study on thresholding, with manual thresholding performed by 13 different experts from around the world and the implementation of a range of automatic procedures, which produced a variation in porosity estimates from 13 to 73% for the same reconstructed XRCT image. It has however been acknowledged that providing the analysis procedures are kept constant across a series of scans direct comparisons can be

drawn from the quantitative results obtained between scans, and meaningful conclusions made (Cnudde and Boone, 2013; Marcelino et al., 2007). The need for standardisation has been called for by many authors (Thompson et al., 1992; Marcelino et al., 2007; Helliwell et al., 2013) to enable comparison of results from different experiments performed in different laboratories but as observed by Baveye et al. (2010) this does not seem to have yet been heeded.

This section provides an overview of the three different analysis procedures used in the investigations into crack propagation, void structure and expansive clay focussing on the techniques used to analyse the data. Progression towards full automation, in an attempt to increase repeatability and minimise operator interaction and error, can been seen in the evolution of the three procedures discussed. Additionally, in order to facilitate discussion and analysis of the material behaviour and enable meaningful comparison between scans, the production of quantitative results was essential for all the analysis performed.

Two different data analysis softwares were used to process the reconstructed XRCT data. ImageJ, an open-source, plug-in and macro based, scientific image-analysis program (Schneider et al., 2012), was used to analyse the data produced by the SS1174 whilst Avizo Fire, a commercial 3D analysis program capable of providing high quality 3D visualisation, data processing and analysis techniques (FEI, 2014), was used to analyse the data produced by the XRM410. In both cases the analysis was performed on desktop computers, the ImageJ analysis on a Stone desktop (Intel Core i5-2400 CPU @ 3.2GHz, 4GB of RAM, ATI Radeon HD 5400 GPU with 1.7Gb of available graphics memory) whilst the Avizo Fire analysis was performed on a much more powerful Dell desktop (Intel Xeon E5-2603 CPU @ 1.8GHz, 128Gb of RAM, NVIDIA Quadro 6000 GPU with 71Gb of available graphics memory).

The SS1174 XRCT raw data, obtained in the investigation into crack propagation, was analysed using custom written ImageJ macros outlined in Figure 3.11. To enable the batch processing of the large number of data sets MATLAB® (MATLAB, 2011) and FIJI® (Schindelin et al., 2012) were used to run the ImageJ macros. The XRM410 XRCT data for the investigations into void structure and expansive clay were analysed using custom written procedures within Avizo Fire. In order to automate the process the procedures were all scripted using .tcl code and Avizo Fire was run through the Windows command line with no graphical user interface. The first analysis procedure for the investigation into void structure, outlined in Figure 3.12, was updated for the second Avizo Fire analysis procedure for the investigation into expansive clay, outlined in Figure 3.13, which utilised additional features within a later version of Avizo Fire.

All three analysis techniques used different tools within the given software package and were written to produce results which described different aspects of the samples, the size and location of cracks and aggregations within the SBCM sample or the void size distribution of the scanned SBCM sample. Despite these differing work flows, comparable elements exist however within all three analysis procedures and it

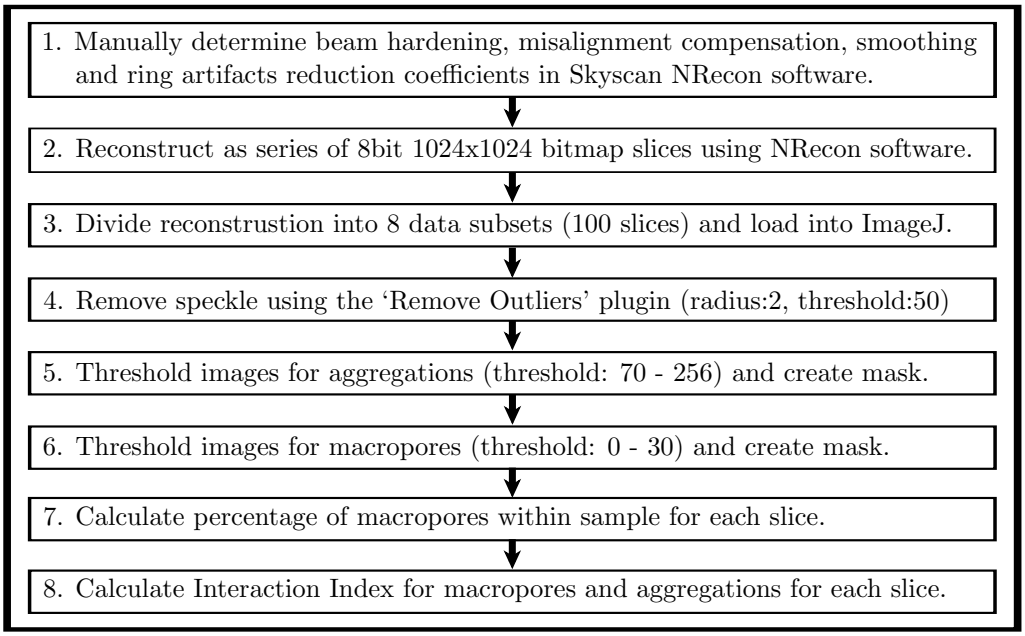

Figure 3.11: Flowchart of the ImageJ analysis used for XRCT data processing in the investigation into crack propagation.

is these which are discussed from an image processing perspective. The five key stages are:

- reconstruction, to convert the 2D image data into 3D volume data;
- reduction of file size, through file conversion and extraction of subvolumes;
- enhancing image quality, through filtering and the removal of noise;
- identifying phases within the volume, through thresholding and segmentation;
- production of quantitative results.

Reconstruction

The reconstruction of the original XRCT scan data into three dimensional volume data was the step which involved most operator input for all three analysis procedures. This was largely because this step had to be performed by an operator using proprietary reconstruction software, provided specifically for each XRCT machine, and each sample had to be reconstructed individually with no option to automate or batch process the reconstruction procedures. The SS1174 scan data was reconstructed using the Skyscan NRecon software provided with the scanner and the XRM410 scans were reconstructed using the XRadia XMReconstructor software provided with the XRM410.

Included in both the NRecon and XMReconstructor software were parameters to correctly locate the central point about which the reconstruction should be performed and the correction which should be applied for the beam hardening effect. The 'misalignment compensation' parameter in the NRecon software was automatically obtained and, whilst it was possible for the operator to override this value

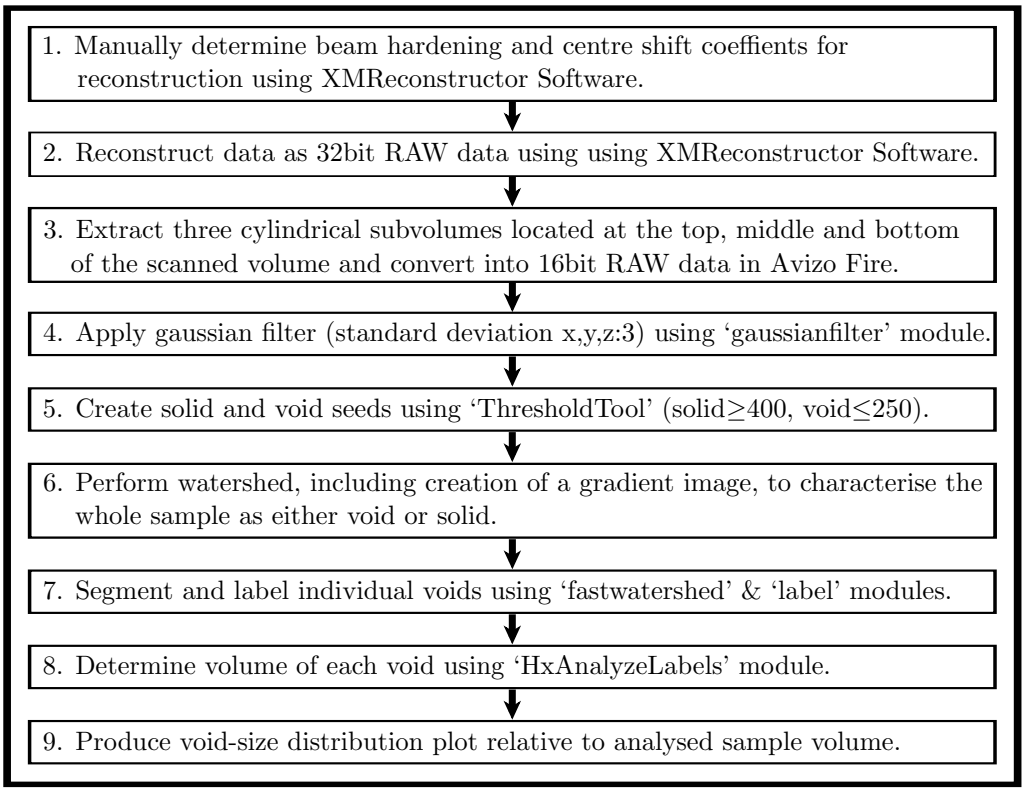

Figure 3.12: Flowchart of the Avizo Fire analysis used for XRCT data processing in the investigation into void structure.

and perform a manual inspection of the parameter, the automatic value was always used to improve the repeatability of the reconstruction and reduce the chance for human influences on the analysis. The 'centre shift' parameter in the XMReconstructor software could also be automatically determined but always required an operator to check the result and ensure the correct value had been determined. Because of this the software determined value was used as an initial guide for all XRM410 scan reconstructions and then adjusted upon by the operator when required. The 'beam hardening parameter' required, for both reconstruction softwares, the operator to determine the value following the inspection of a single slice reconstructed for a range of different parameter values. This decision was aided by the ability to inspect the histogram of grey-scale values within the data set and the operator was able to choose the parameter which provided the most consistent grey-scale value for the clay matrix located within the sample. Having chosen a beam-hardening correction value this was maintained for all scans run under the same machine settings, ensuring the choice of the beam-hardening correction parameter did not affect any comparisons drawn between samples.

The XMReconstructor and the NRecon software had options to remove ring artefacts from any scans performed. For the XMReconstructor software this option was not required due to the use of the 'dynamic ring reduction' feature used during scanning which meant no ring artefacts were observed in any of the

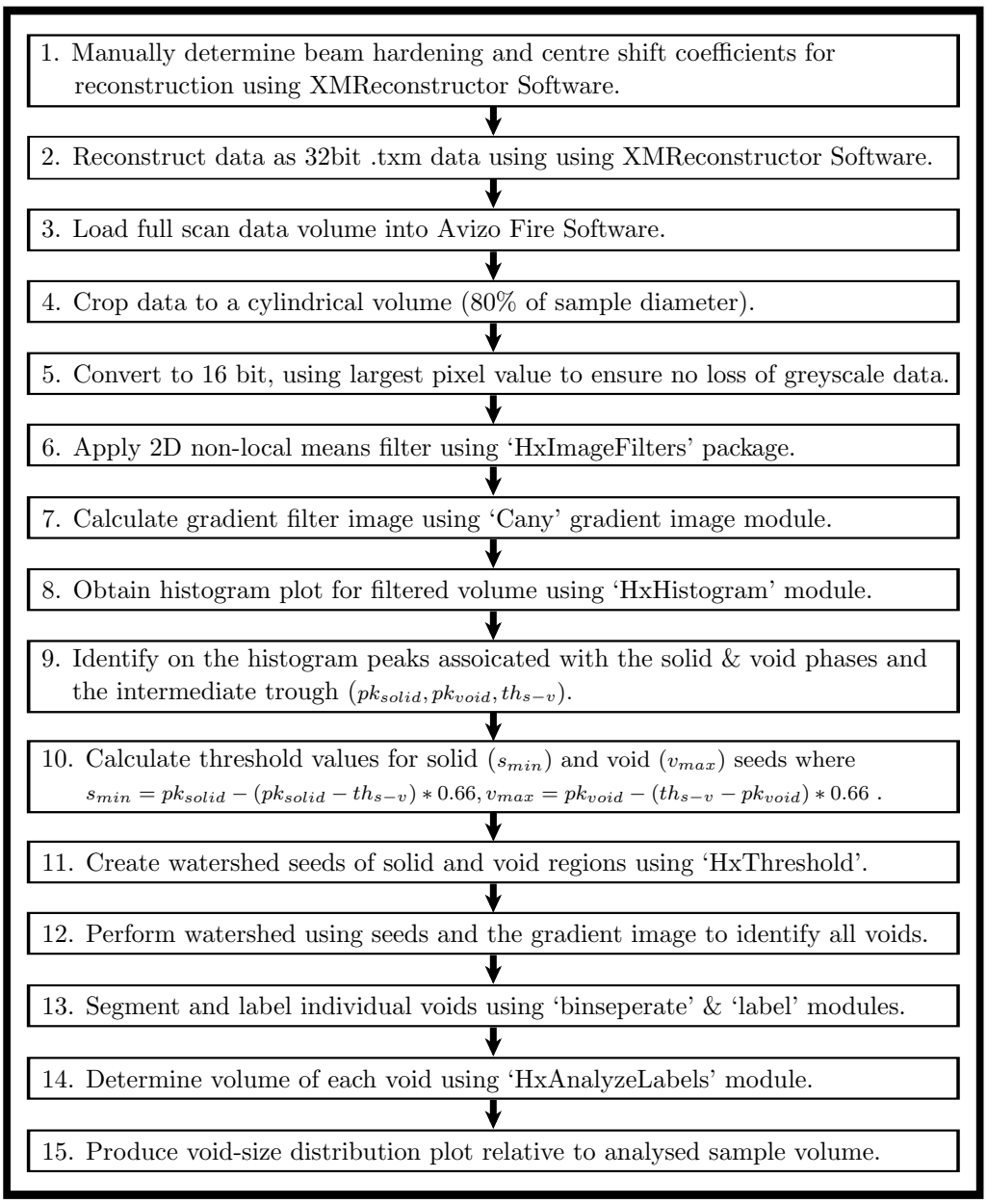

Figure 3.13: Flowchart of the Avizo Fire analysis used for XRCT data processing in the investigation into expansive clay.

XRM410 scans. The 'ring artefact reduction' parameter within the NRecon software was required for the SS1174 scans and the value of this parameter was determined for each sample by the operator performing the reconstruction. No automated procedure was possible for determining the value of the ring reduction parameter and therefore the choice of this parameter introduced an element of human influence on the final result of the analysis and reduced, in a small way, the repeatability of the analysis since the operator may not choose the identical ring reduction value if repeating the reconstruction.

The NRecon software also included a 'smoothing' parameter designed to reduced noise within the sample and acted as a filter for the image processing. The determination of this parameter is discussed in detail below, regarding the improvement of image quality, and can be considered more as part of the methods used to improve image quality, rather than alter the reconstruction. The value was however kept constant for all scans ensuring that no additional variation between scans was introduced and the repeatability of the reconstruction was not detrimentally affected.

Finally, the data format in which the reconstruction data was presented could be chosen in both software packages and the size of these files had a big impact on the eventual results obtained at the end of the analysis. The series of bitmap images (or 'stack of slices') produced by the NRecon software were chosen to enable analysis within ImageJ, while the Avizo Fire analysis was performed using single RAW or .txm files. Since XRCT images represent the density of each voxel within the reconstruction through the use of a greyscale value, the range of material densities within the sample and the size of the file determines the relationship between the grey scale and density within each scan. The reconstructions performed using the XMReconstructor software had the option to reconstruct the data in 8bit and 16bit formats, where scaling would be performed, however the 32bit data formats had 2^{32} incremented greyscale values which provided sufficient increments for no scaling to occur and therefore scans performed on a single sample using identical settings could be directly compared without problems arising from the reconstruction process. The NRecon software produced 8bit bitmap images in which each voxel could take one of 255 incremented greyscale values and chose the density-grey scale correlation for every scan to provide maximum clarity related to the most dense point within the sample. This resulted in every scan reconstructed using the NRecon software, whether it was two different samples or two scans on the same sample, having a slightly different density-grey scale correlation which affected any further analysis steps, including the thresholding as discussed in Section 3.4.2. Whilst nothing could be done retrospectively for the investigation into crack propagation, it is suggested that in future investigations the addition of a high density reference material could be added on the edge of a sample within scans to fix the upper value of the auto-scaling applied and limit the impact when comparing scans.

Reduction of file size

For all three analysis procedures it was necessary to reduce the file size of the data before quantitative analysis could be performed. This was due to the large file sizes involved (1Gb for the SS1174 scans and 32Gb for the XRM410 scans) and the limited memory available on the desktop computers used to perform the analysis. The ImageJ data, saved as individual images, was simply separated into sub-volumes each containing 100 slices and analysed in sections. The analysis within ImageJ was performed on each slice in isolation and therefore this extraction of a series of sub-volumes had no influence on the results obtained and the only factor limiting the size of the sub-volumes was the memory requirements of the desktop computer.

The Avizo Fire analysis procedures used a single file containing information on the entire volume and did not analyse the sample through use of isolated slices but through voxels with reference to voxels surrounding it in all three dimensions. Both the analysis procedures used in the investigations into void structure and expansive clay converted the sample from 32bit data to 16bit data within the Avizo Fire software. However, unlike the automatic conversion performed in the NRecon software, it was possible to obtain more detailed information about the histograms of all the scans and the same conversion factor was applied across all scans by scaling all the data using the largest grey-scale value occurring across all the scans being analysed. Figure 3.14b shows an example horizontal data slice following conversion to 16bit data and, when compared to Figure 3.14a, no noticeable loss in image detail can be observed. In addition to the conversion of the data it was still necessary to further reduce the file sizes to perform the computationally expensive procedures within Avizo Fire and for the analysis used in the investigation into expansive clay extraction of a single sub-volume 80% of the 38mm sample diameter was sufficient to enable the analysis to be successfully performed. In the analysis used in the investigation into void structure it was necessary to extract three smaller sub-volumes, 1.5Gb in size, to improve the stability of the analysis and also to enable the comparison of different regions within a single scan.

The analysis of a sub-set of a total volume is common in almost all image analysis techniques, for the reduction of file size or for the removal of edge-effects, however can lead to the skewing of any quantitative results obtained. However, as discussed by Taylor et al. (2014), the magnitude of any error introduced into a particle size distribution by analysing a sub-volume is small for well-graded materials and, with the equivalent of a 'well-graded'void size distribution obtained in the investigations into void structure and expansive clay, the error from the impact of analysing sub-samples is not a major concern. In addition it would not have been possible to perform any analysis on the entire volume scanned, due to extremely large data sets, and therefore sub-sampling was an unavoidable occurrence to ensure quantitative results were produced.

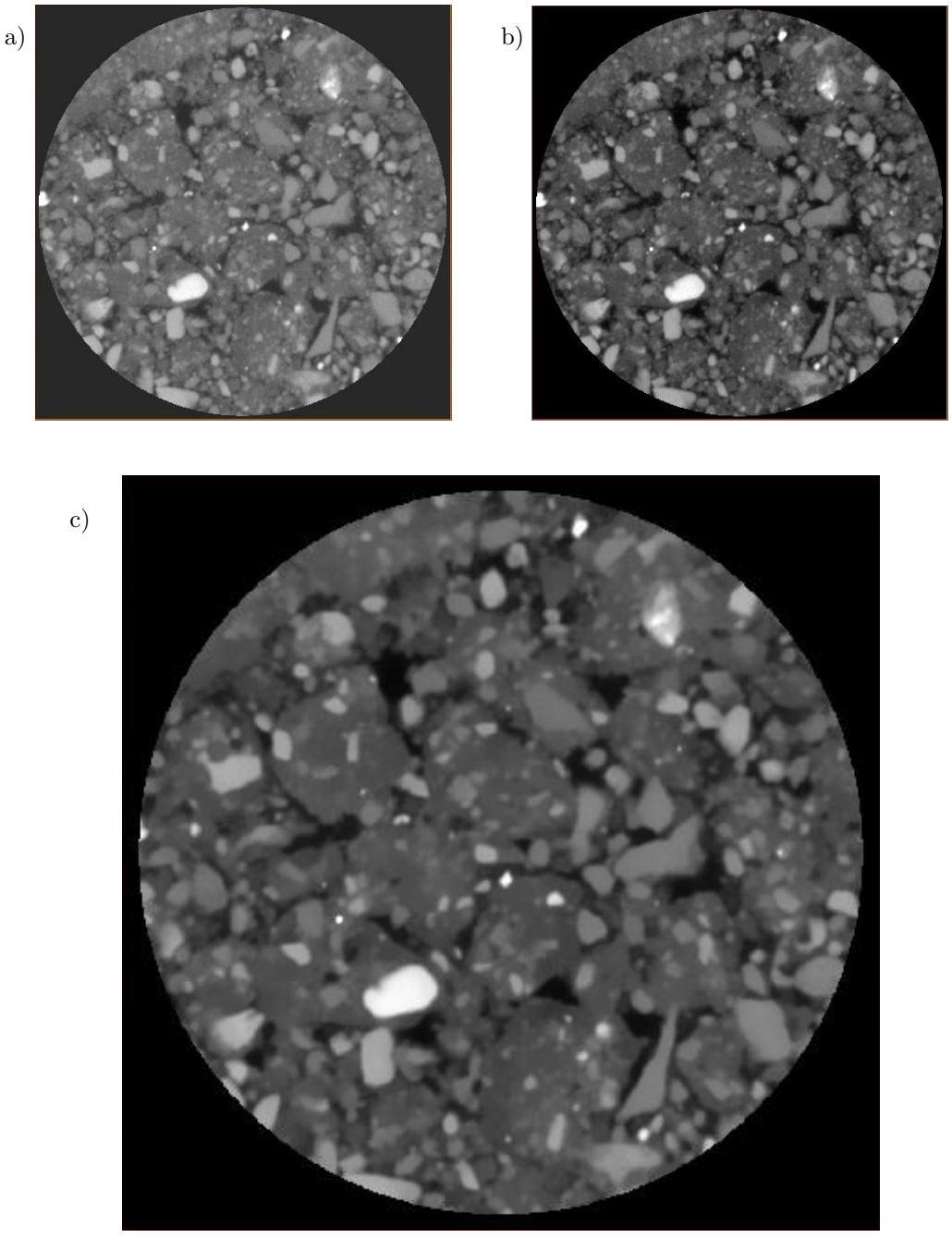

Figure 3.14: Horizontal data slice (from $F1_{0.0}$) showing the initial image processing of XRCT data including a) the cropped 32bit input data b) the converted 16bit data and c) the non-local means filtered data.

Improvement of image quality

In order to improve the quality of all the scans performed on both the SS1174 and the XRM410 it was necessary to apply certain filters to reduce any noise arising during scanning. The processing performed on the SS1174 data involved a 3D smoothing of the data during reconstruction in the NRecon software followed by a despeckling using an ImageJ plugin. The smoothing function, or filtering, was performed during reconstruction as it was found that applying a smoothing filter during analysis in ImageJ was very unstable and often caused crashing of post-processing procedures due to the large memory requirements for applying 3D image filters within ImageJ. The asymmetrical box function smoothing algorithm, described by SkyScan-Brucker (2011), was used as default within the NRecon software, with a smoothing level of 2. This smoothing reduced noise although the data still required an additional despeckle filter, a selective median filter which replaced outlying pixels with the median of pixels in the surrounding region (Ferreira and Rasband, 2012), to be applied on a slice-by-slice basis within ImageJ to remove clear hot and cold spots from the reconstruction. The Avizo Fire analysis used in the investigation into void structure used a 3D gaussian filter which performed a lowpass filtering smoothing the data using a gaussian distribution (FEI, 2013). The analysis performed in the investigation into expansive clay used a non-local means filter, which had been improved considerably in version 8.0 of the Avizo Fire software, and after which the denoised value of a voxel had a value equal to the mean of the values of all points in its vicinity which looked like the neighbourhood of the pixel (Buades et al., 2005). In essence the non-local means filter smoothed each voxel by considering only the voxels which were similar to it, i.e. of the same phase, and therefore maintained the contrast and sharpness at edges, or phase transitions, but removed noise within each phase. This filter produced considerably sharper images than the gaussian filter used in the investigation into void structure although was computationally more expensive and took approximately five times longer than the gaussian filter. Figure 3.14c shows an example horizontal data slice following the application of the non-local means filter and, when compared to Figure 3.14b the solid phase is visibly smoothed and the edges of the void regions are noticeably sharper.

The filters used to reduce noise within the data were all chosen through operator judgement and visual inspection of small regions within samples before the full analysis was performed. Relying on an operator's visual inspection of data could have led to potential shortcomings in the later analysis, since other filters may have performed better, however no rigorous procedures could be found outlined in published literature for the handling of similar data and time was not available to perform complete parametric studies on the effect of different filters on results. In addition the focus of the experimental programmes were to use the XRCT data to provide information for understanding material behaviour, rather than solely to produce scanning and image-analysis procedures, and therefore to enable comparison between samples it was sufficient to simply ensure that the filtering of the image data was kept consistent

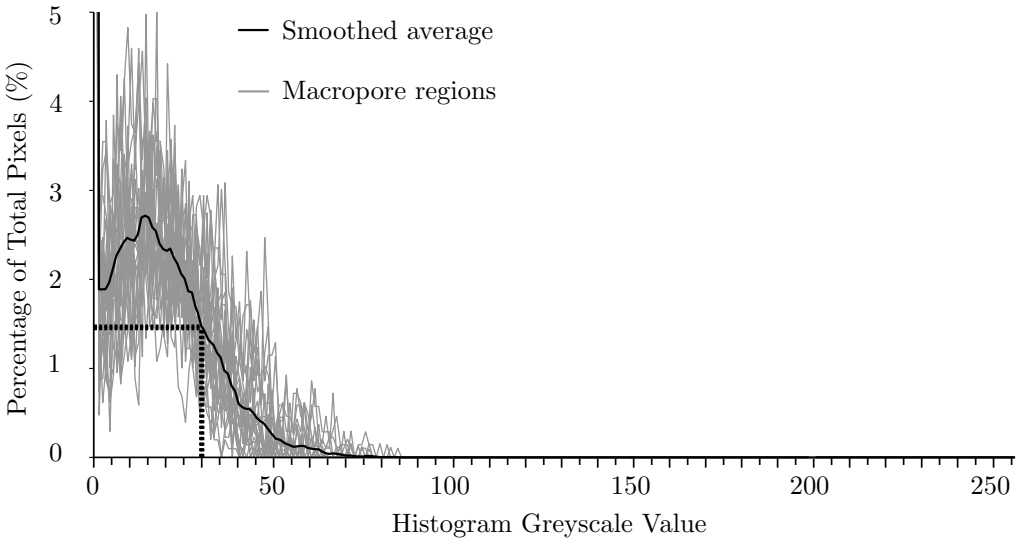

Figure 3.15: Macropore histogram values and threshold determination.

for all scans within an experimental programme.

Phase identification

In all three analysis procedures phase identification was performed through the thresholding of the grey-scale image and assigning each pixel to the appropriate phase. Within the investigation into crack propagation ImageJ analysis was required to identify three phases, macropores (the air phase), solid matrix (the solid phase not defined as aggregations) and aggregations (gravel particles or high density assemblages), whilst the Avizo Fire analyses performed for the investigations into void structure and expansive clay needed to produce a void size distribution for each sample and therefore required the identification of two phases, solid and air.

The threshold values used in the ImageJ analysis, and stated in Figure 3.11, were determined prior to the full analysis through the sampling of small regions within a sub-set of reconstructed data slices. The use of the same threshold value was required for all scans to ensure results could be compared across scans and operator judgement of the threshold values for each scan was avoided to reduce the impact of human interaction on the results. Fifteen image slices taken from five different scanned samples, were used to produce a small sub-set of reconstructed data in which regions that were clearly macropores or aggregations were manually identified. Greyscale histograms were obtained for the 24 regions identified as macropores and the 21 regions identified as aggregations and these are shown in Figure 3.15 and Figure 3.16 respectively. From these histograms average greyscale histograms were calculated for the macropores and the aggregations and the peak coordinates of each region were identified. Following a series of trial threshold values it was found that the threshold greyscale value which most closely identified the macropore and aggregation regions coincided with point at which the percentage of total pixels equalled

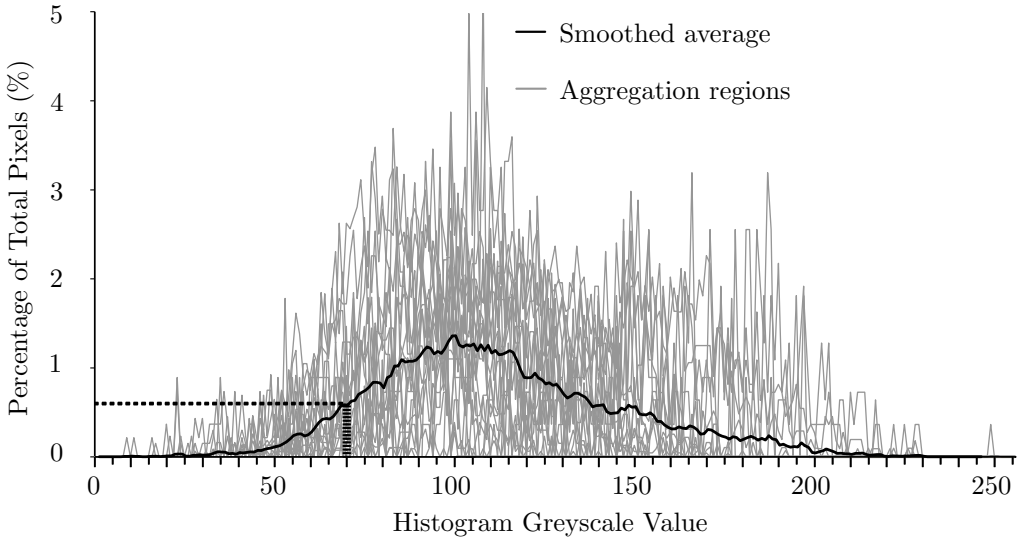

Figure 3.16: Aggregations histogram values and threshold determination.

half the peak value and these threshold values (<30 for macropores and >70 for aggregations) were used to define the macropore and aggregation regions in all the reconstructed data. Unfortunately however the use of a single threshold still produced some uncertainties in the final conclusions drawn because of the auto-scaling during reconstruction performed by the NRecon software, described in the discussion on reconstruction above, and this method of threshold determination would have been much more powerful if the initial auto-scaling could have been avoided.

For the Avizo Fire analyses two watershed algorithms were performed, first to separate the volume into phases and then to segment the air phases into individual voids. The watershed algorithm simulates the flooding of the data set from a series of seed points using a gradient image (FEI, 2013) and therefore requires the initial threshold to only identify regions which are definitely part of a phase, rather than needing to exactly locate the edges of each phase as in the ImageJ processing. For the Avizo Fire analysis for the void structure investigation these initial seed points were identified following manual inspection of a sub-set of sample histograms to determine the initial threshold values. The analysis performed in the investigation into expansive clay improved upon this step by automatically identifying the phase peaks within each sample and calculating threshold values accordingly. This final technique, whereby the peaks are automatically identified, is a totally automated process and therefore removes all need for operator input in the thresholding stage of any analysis and is a considerable improvement on the simple thresholding applied in the ImageJ analysis. As discussed by Iassonov et al. (2009) the development of new reliable, consistent algorithms for grey-scale image segmentation which contain no operator bias, i.e are fully automated, is needed in the analysis of all XRCT data. Unfortunately however the automated method used in the investigation into expansive clay did not successfully identify both the void and

solid peaks within the grey-scale histogram for all samples and resulted in two separate groups of data depending on the location of automatically found void peak. Clearly the automated method outlined in Figure 3.13 is not the solution to all the image segmentation shortcomings however it does provide an initial foundation onto which further techniques can be developed by the geotechnical community for the thresholding of the air voids to enable XRCT to become a commonly used technique for accurately determining and comparing void size distributions.

Production of quantitative results

In the production of quantitative results the Avizo Fire analyses held a major advantage over the ImageJ analysis as Avizo Fire was capable of quickly and easily providing detailed geometric information on individual voids within the scans, including volume and orientation, rather than being limited to calculating percentages of each phase within the scan as available in ImageJ. The detailed geometrical information obtained for the individual voids within the Avizo Fire analysis was obtained through the 'HXAnalyzeLabels' module and the use of the more advanced segmentation procedures previously discussed. It is possible to obtain geometric information on individual features using the ImageJ software however this requires the segmentation of phases and further image processing only achievable from a fully 3-dimensional analysis, rather than the slice by slice approach used in the crack propagation investigation, and would have required more computational power than available for the analysis. Despite this lack of detailed geometric information the ImageJ analysis still provided sufficient quantitative results, in the form of percentage of each phase per slice and a measure of the interactions between phases, to enable clear findings and detailed discussion to be drawn from the scans obtained as is evidenced by the discussion of results in Chapter 4.

The individual geometric information produced in the Avizo Fire analyses performed in the investigation into void structure show very clearly the difference between voxel size, the level of detailed at which data is being collected, and resolution, which is the smallest identifiable feature following scanning and image processing. Table 3.4 shows that the true resolution of the data does not equal the voxel size of the scan for any of the six scan settings performed and, in the case of the detailed 100mm scan no features could be measured despite a voxel size value indicating information could be obtained at 7.9μm. Additionally, as discussed further in Chapter 5, the apparent increase in detail obtained from using a 12mm sample, where voxel sizes approximately half the size of 38mm samples were achieved, did not result in a significant increase in information obtained about structure as only 0.09% of the total sample volume was accounted for by voids only observed using a 12mm sample. This loss of detail in the final measured smallest dimension was due to a range of factors, including the post-processing steps applied to the scan data and the physical structure of the samples being scanned, and therefore highlights the need for this final resolution to be considered when planning experimental procedures.

3.4.3 Key observations

The description of the three investigations performed using XRCT in this Chapter, and the detailed discussion of the results which will follow in the remainder of this thesis, stands in stark contrast to a number of the current trends in the use of XRCT within geotechnical research outlined in Section 3.3. Firstly the simple length and depth of discussion required in Section 3.4.1 and Section 3.4.2 to discuss the scanning, image processing and analysis procedures clearly show that XRCT is a complex technique and the procedures used need describing and discussion in publications, rather the current presentation of XRCT as a 'black box' technique. Secondly the range of sample sizes and the broadly graded particle mixes used across the investigations show that it is not necessary to always scan narrowly-graded materials or to only scan small samples smaller than 15mm. In fact Table 3.4 and the discussion in Section 3.4.2 show that using the smaller sample size of 12mm did not result in any considerable benefit in detection of smaller features following analysis and the standard triaxial sample size, 38mm diameter, was the best sample size to use for XRCT scanning of geotechnical samples.

A number of other instructive conclusions can also be extracted from the observations made which should hopefully aid other geotechnical researchers as they use XRCT as part of an experimental programme.

- The material testing stage used in the investigation into crack propagation had a number of limitations, including the drift in load applied during scanning and a lack of mechanism to export load-deflection data, which severely affects its appropriateness for material testing in geotechnical research applications.
- The scanning of any sized soil sample within the SS1174 was performed at the limit of its capabilities and it is suggested that the SS1174 is not an ideal machine for scanning soil samples and other scanners, with more powerful sources, should be used wherever possible. It is clear that the 100mm diameter cylindrical samples were too large for the XRM410 if high resolution scans are required.
- The balance required between optimising scan parameters and other time constraints is complex and there will often be many reasons why shorter scans are beneficial however optimising scan parameters should never be comprised too far as this can lead to unusable data.

Table 3.4: The smallest void dimension, both theoretical (using voxel size) and measured (using smallest feature size) obtained following the XRM410 scans and analysis performed in the investigation into void structure.

Smallest Dimension (μm)	ϕ12F	ϕ12D	ϕ38F	ϕ38D	ϕ100F	ϕ100D
Theoretical	12.3	1.0	20.3	2.2	37.1	7.9
Measured	35.7	2.7	43.5	4.6	63.0	None

- Both the ImageJ and Avizo Fire analyses used in the investigations produced quantitative data in a repeatable manner which minimised human judgement in the analysis procedure. However all of the five key steps outlined have an impact upon the results obtained and, with minimal discussion of analysis techniques in other publications, it is hard to develop or establish techniques that will be accepted across the geotechnical community.

3.5 Summary and conclusions

This chapter has provided an overview of the technology and processes involved in the scanning of samples using the laboratory XRCT technique before performing a detailed literature review of the use of XRCT in geotechnical research. This comprehensive review in Section 3.3 has identified a number shortcomings in the current use of XRCT within geotechnical literature including a tendency to scan materials containing no particles smaller than 0.1mm, i.e. sand, and use small cores extracted from larger samples. Additionally the minimal presentation of information regarding scanning and image post-processing procedures could be limiting the development of improved scanning or analysis techniques and a lack of quantitative results suggests that the full potential of XRCT scanning is not currently being realised by the geotechnical community. The investigation into the suitability of two different XRCT machines and three analysis procedures performed using two different software packages described in Section 3.4 however demonstrates that many of these shortcomings can be overcome.

Finally throughout this chapter a number of additional lessons have been highlighted which should aid other geotechnical researchers as they use XRCT as part of an experimental program. Firstly, specific to the XRCT scanners discussed in this chapter, the scanning of any sized soil sample within the SS1174 is performed at the limit of its capabilities and 100mm diameter soil samples are too large for the XRM410, due to their high density, despite the ability to fit 300mm samples within the scanning chamber. Secondly, when designing any experimental programme using XRCT scanning, it has been shown that the determining of scan parameters with respect to experimental time constraints, rather than optimum scan settings, can lead to unusable data and should be avoided wherever possible. Finally, from a data processing and analysis perspective, all stages within image processing will have an impact upon the results obtained and, with minimal discussion of analysis techniques in other geotechnical publications, it is hard to develop or establish techniques that will be accepted across the geotechnical community. By discussing the XRCT technique in detail here in this chapter, before the XRCT results relating to the internal structure of SBCM samples are presented in Chapters 4, 5 and 6, it is hoped that the reader will have a better understanding of the XRCT technique, its advantages and disadvantages and the analysis techniques used later in this thesis.

Chapter 4

Studying compressive loading behaviour using laboratory x-ray computed tomography

4.1 Introduction

The compressive strength of unstabilized soil based construction materials (SBCMs) has been studied by a number of different authors and the range of different compressive strength results for SBCMs presented in the scientific literature is large, between 0.62MPa and 4.00MPa (Miccoli et al., 2014). This range in compressive strength results, which has arisen through differences in laboratory testing procedures and variations in the material being investigated, has meant comparisons between the results has been limited and any clear consensus on the material behaviour is lacking. As discussed in Chapter 2 the internal structure of unsaturated soils, and hence SBCMs, can have a considerable affect on their mechanical response. The aim of this investigation therefore is to examine the change in internal structure of SBCMs after compressive loading through the use of laboratory x-ray computed tomography (XRCT). Four different SBCM mixes are investigated each containing different proportions of clay, sand and gravel. Unconfined compression tests are performed on two different sized samples, containing different maximum particle sizes, with XRCT scans performed before, during and after the compression tests. The results and conclusions are divided into three areas: the mechanical behaviour, lessons that can be learnt about XRCT scanning, and the changes in material structure.

4.2 Compressive behaviour of soil based construction materials

Early investigations into the compressive strength of SBCMs tend to present compressive cube strength results and Lilley and Robinson (1995) appear to be the first authors to do this. They discuss the strength of rammed earth walls containing openings and determine the mean compressive cube strength of three

different laterite soils, containing 11%, 15% and 21% clay, as 1.9MPa, 2.3MPa and 2.0MPa respectively. However the authors' main focus is the influence of the shape of wall openings on ultimate strength and therefore no real discussion of the difference in compressive strength of the three soil mixtures is presented. Hall and Djerbib (2004) investigated ten different rammed earth mixes to propose a consistent and reliable technique for producing rammed earth samples to control the dry density of the manufactured material. The unconfined compressive strength results presented range between 0.78MPa and 1.48MPa and the authors find no link between the variation in compressive strength and the dry density of the given soil mixture. The authors tentatively hypothesise that the ratio between the mass of clay and mass of gravel, which they describe as the binder/aggregate ratio, may be a more important factor in controlling compressive strength although acknowledge this is not proven in their work.

Maniatidis and Walker (2008) studied rammed earth in compression to investigate the validity of using masonry design rules for SBCM design, and performed tests on both small 'laboratory' samples and 'full scale columns'. In unconfined compressive strength tests on an unstabilized rammed earth mix, classified as 25*:45:30, the authors obtained an average unconfined compressive strength of 2.46MPa when using 200mm high x 100mm diameter cylinders, in which particles larger than 20mm had been removed prior to manufacture, but only 1.9MPa for 600mm high x 300mm diameter cylinders and 0.62-0.97MPa for 600mm high x 300mm square cubes. No detailed discussion of this result is presented but the authors conclude that the significant variation in material performance between the sample sizes is due to variation in the material grading and the variation in compactive effort.

Bui et al. (2014b) also presents compressive strength results for SBCM samples at two different scales, 320mm high x 160mm diameter cylinders and 1000x1000x300mm walls, and reports mean compressive strengths of 1.9MPa and 1.22MPa respectively. These compressive strength values are used to propose a relationship between tensile and compressive strength, where tensile strength should be taken as 10% of the compressive strength, but no discussion of the material behaviour during compression is presented.

The mechanical behaviour of three different SBCMs, rammed earth, cob and earth block masonry, is discussed by Miccoli et al. (2014) where mean compressive strengths are reported as 3.73MPa, 1.59MPa and 3.28MPa respectively. Unfortunately the authors state that the values of compressive strength cannot be directly compared because the raw soil mixture was not kept consistent across the three manufacturing techniques. One important finding reported by Miccoli et al. (2014) however is the brittle behaviour observed for the rammed earth and earth block masonry in contrast to the cob, which shows considerably increased ductility. The authors make the obvious proposal that it is the constituent materials (i.e. the addition of straw in cob) that effects the compressive stress-strain behaviour of SBCMs but do not then investigate or discuss this proposal further.

One of the earliest works that links compressive strength of SBCMs to the suction developed as the material dries is Jaquin et al. (2009). The authors promote the characterisation of these materials in geotechnical frameworks to ensure the understanding of their behaviour is rooted in a stronger scientific basis. The results presented in Jaquin et al. (2009) show that the strength of rammed earth increases as the water content decreases due to the increase in suction and that this is the source of strength in unstabilized rammed earth. The experiments were performed on only a single soil mixture, 15*:60:25, and the effect of changing the proportions of the constituent materials on the development of suction is not discussed. Bui et al. (2014a) builds upon Jaquin et al. (2009) by investigating three different unstabilized rammed earth mixes at a range of water contents, measuring suction values using a modified filter paper test. The authors show that a single linear relationship exists, irrespective of the soil composition, between increasing compressive strength and the log(suction) used but that the water content and suction relationship varies with the soil mix. Bui et al. (2014a) therefore suggest that the suction developed within the SBCM depends on the mix composition, particularly in relation to the variation in suction with respect to water content, and support Jaquin et al. (2009) that it is suction which is an important factor in the compressive strength of SBCMs.

Finally Beckett et al. (2013) studied through the use of XRCT scans the macrostructural changes in SBCMs under compressive loading to recommend procedures for sample manufacture and investigate the changes to the material structure of SBCM which occur on loading. Due to the limitation on sample size and the need to sieve the mix to 2mm, the authors were only able to investigate the 'intra-aggregate soil matrix' material within SBCMs using a single mix containing 70% sand and 30% clay. The samples achieved an average unconfined compressive strength of 1.63MPa. Consecutive scanning of single samples at different loads was not possible due to XRCT machine availability and therefore direct comparisons between the macrostructure before and after compressive loading could not be obtained. Despite this Beckett et al. (2013) show that cracking occurs under compressive load causing an increase in the size and interconnectivity of the macropores within SBCMs and the work provides a valuable initial insights into the material behaviour of SBCMs under compressive loading.

As can be seen from this overview of the published literature, the range of materials and different experimental methods used in both testing and sample manufacture mean many questions remain about the behaviour of SBCMs under compressive loading. In particular, further insight is required into changes in the internal structure of SBCMs during loading and the effect of different soil mix compositions on the ultimate compressive strength and suction developed as the material dries. This study aims to investigate the changes in material structure following compressive loading and what impact different soil mix compositions has on the compressive strength.

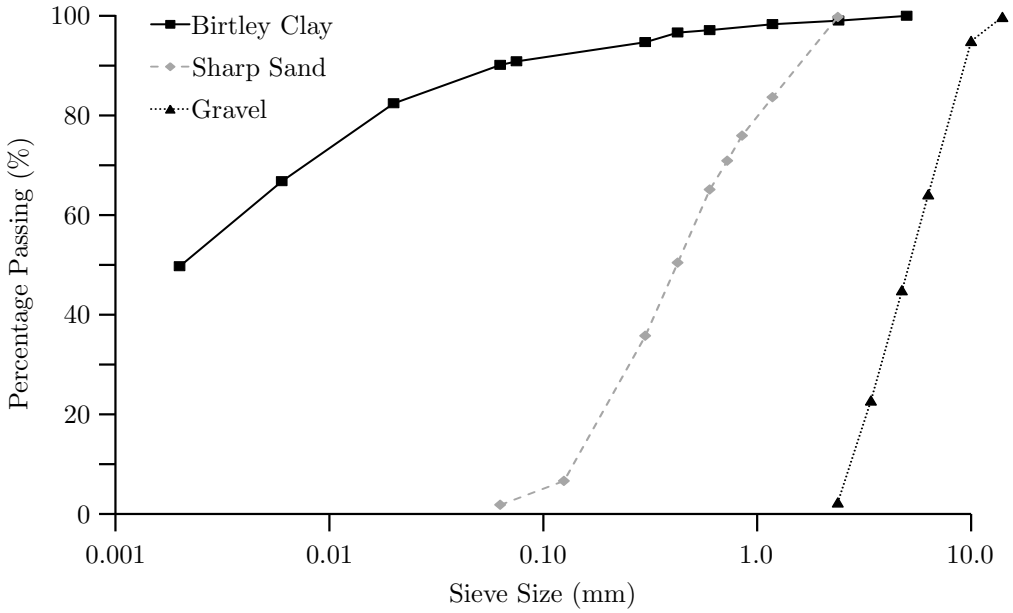

Figure 4.1: Particle grading curves for the Birtley clay, sieved sharp sand and gravel fractions.

4.3 Methodology

4.3.1 Materials

Four different SBCM mixes, 20*:70:10, 30*:60:10, 30*:50:20 and 40*:50:10, were used throughout this investigation each containing different proportions of silty-clay, sand and gravel. These four mixes were selected as all lay within the limits of recommended particle size distribution by Houben and Guillaud (1989) and were manufactured in the laboratory by combining appropriate amounts by mass of Birtley clay, sharp sand and pea gravel. Birtley clay (LL 58.8%, PL 25.7%, PI 33.1%) is a locally available natural clay material which contains 50% clay sized particles by mass and of which the primary mineral type is kaolinite (Teasdale and Hughes, 1999; Beckett, 2011). The Birtley clay was oven dried at 105°C before being pulverised and passed through a 2mm sieve, which ensured the particle aggregates were small enough to mix uniformly within the soil mix. Both the sharp sand and the pea gravel were also oven dried at 105°C and passed through 2mm and 10mm sieves respectively to ensure the particle size distribution could be more accurately controlled. To improve the particle grading the sieved pea gravel (<10mm) and the retained sharp sand (>2mm) were combined in a 1:1 ratio by mass, identical to that performed by Beckett (2011), and used as the gravel fraction within the SBCM. The particle grading curves for the Birtley clay, the sieved sharp sand and the gravel fractions are shown in Figure 4.1.

Figure 4.2 shows the particle grading curves for all the four SBCM mixtures after manufacture. From the grading the maximum weighted percentage error term for each mix was calculated and this enabled

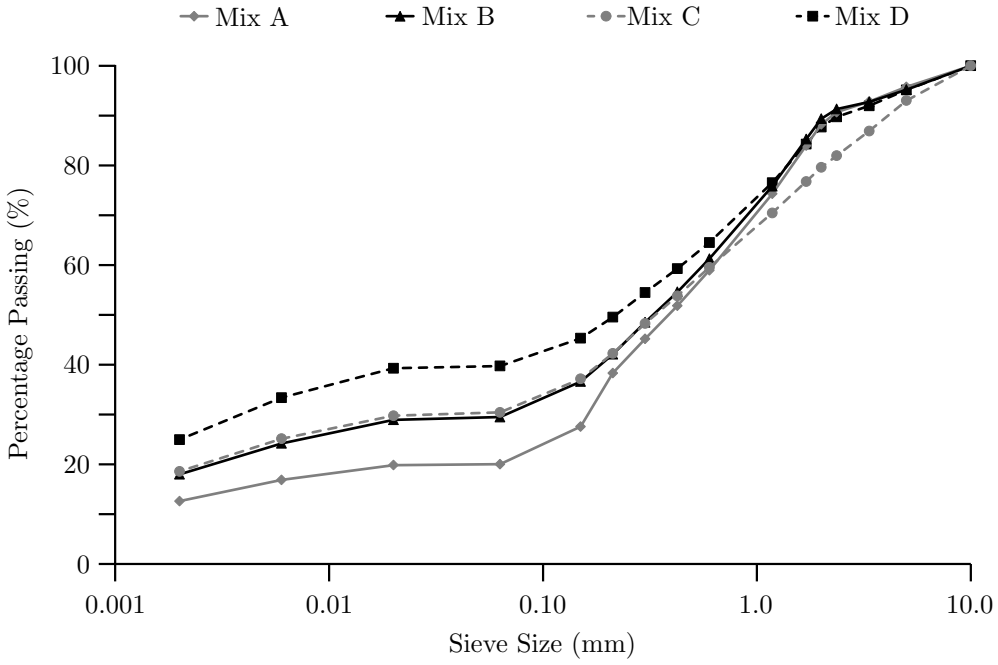

Figure 4.2: Particle grading curves for all four SBCM mixes.

each mix to be fully described using the soil mixture classification proposed by Smith and Augarde (2013a). The four mixes were therefore classified as 20*:70:10[1.8], 30*:60:10[0.6], 30*:50:20[0.8] and 40*:50:10[2.3]. For clarity, throughout the remainder of this chapter the four mixes will be referred to as Mix A, Mix B, Mix C and Mix D respectively.

The optimum water contents (w_{opt}) for all four mixes along with the maximum dry density (ρ_{dmax}) values were determined using the on-site equivalence test used by Smith and Augarde (2013b) to replicate the compaction of SBCMs performed on a construction site. The on-site equivalence test procedure is outlined in Table 4.1. The optimum water content and maximum dry density ranges from Smith and Augarde (2013b), obtained from three on-site equivalence tests per mix, are given in Table 4.2 for all four SBCM mixes and the target water content and dry density values used in during manufacture of the samples used here were taken as the centre of these ranges.

4.3.2 Sample manufacture

Two different cylindrical sample sizes were used to perform the experimentation and both sizes contained two equal layers of compacted SBCM. The larger samples were 27.6mm in diameter, to ensure the entire sample could be scanned when placed within the SkyScan1174 compact micro-CT scanner (SS1174), and 55.2mm high, to maintain the 2:1 ratio of height to diameter found in standard triaxial samples. The smaller samples were 12mm in diameter and 24mm in height, again maintaining the 2:1 height:diameter ratio. The 12mm diameter was chosen to ensure compressive failure of the samples would occur, using an

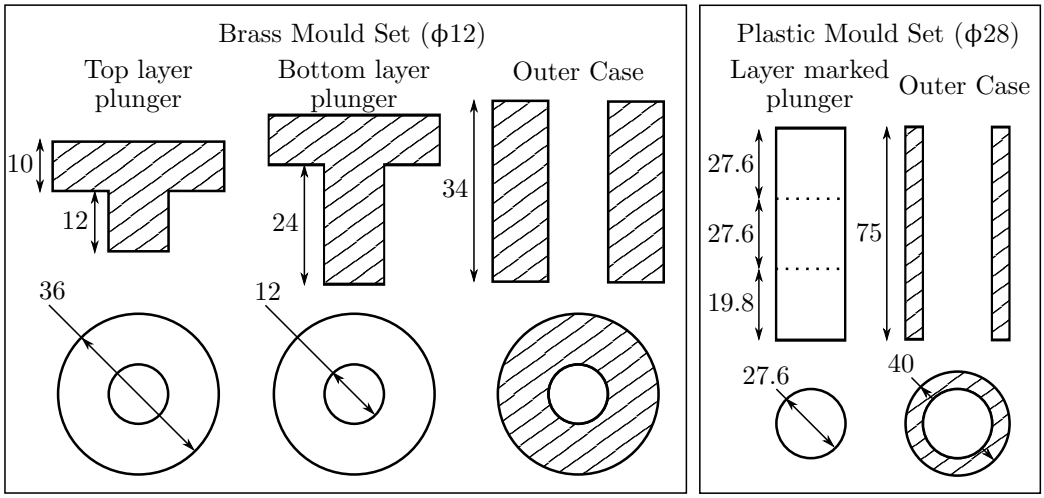

Figure 4.3: Manufacturing sketch for sample moulds (not drawn to scale).

estimated failure stress of 1.3MPa (Standards New Zealand, 1998), when compressed within the material testing stage which had a maximum capacity of 200N. For clarity the larger samples are hereafter referred to as ϕ28 samples and the smaller samples as ϕ12 samples.

Two equal layers of compacted SBCM were used to manufacture the samples following work by Beckett et al. (2013), which showed that for 20mm deep single layer specimens the macrostructural density continuously reduces close to the bottom of a layer producing a highly heterogenous material, whilst a largely homogenous material could be manufactured when using double layer specimens. The similarity in sample size and method of manufacture used for the ϕ12 samples in this investigation and the 20mm high x 10mm diameter samples used in Beckett et al. (2013) meant it could be assumed a homogeneous

Table 4.1: On-site equivalence test procedure used to determine optimum water content and maximum dry density values for all four SBCM mixes

	Description
1.	Water is added to the SBCM mix (approx 13kg dry) to achieve the first target water content.
2.	The SBCM is placed in a mould (305mm by 150mm by 200mm deep) to a depth of 150mm.
3.	The sample is compacted for 60 seconds using the pneumatic hammer. This is sufficient time for a ringing noise to be heard, which is used on-site to indicate full compaction (Walker et al., 2005).
4.	The depth to the SBCM surface is measured in 6 positions and averaged to obtain the volume of the compacted SBCM block.
5.	The block is removed from the mould and weighed on the double scale arrangement rated to 20kg ± 2g.
6.	Three samples of the SBCM block are taken to determine the true water content.
7.	The block is then broken down, returned to the SBCM mix and water added to reach the next target water content.
8.	Steps 2 to 7 are repeated for all six target water contents (5.0, 6.5, 8.0, 9.5, 11.0, 12.5%).
9.	The bulk and dry density obtained for each of the six water contents are calculated.
10.	Dry density is plotted against water content and a quadratic line of best fit plotted.
11.	The optimum water content (w_{opt}) and maximum dry density (ρ_{dmax}) values are then obtained from the peak of this curve.

material was manufactured. Two equal layers were also used for the ϕ28 samples to maintain continuity between the two sample sizes. The homogeneity of these samples was assessed following the XRCT scanning.

Prior to the manufacture of the samples the SBCM mixtures were sieved to 5mm for the ϕ28 samples and 2mm for the ϕ12 samples to prevent the larger particles interfering with the compaction and loading behaviour of the small diameter samples. The sieved SBCM mixtures were wetted to the optimum water content by the addition of the appropriate amount of water, mixed to ensure the water was distributed evenly throughout the SBCM mixture, sealed within a plastic container and left to equilibrate for 24 hours. It is acknowledged that the removal of the larger particles from the SBCM mixtures will have altered the materials' optimum water content and maximum dry density values however to maintain consistency across both samples sizes the optimum water content and maximum dry density values determined for the SBCMs containing the full range of particle sizes was used.

To compact the SBCM sample custom moulds were required and the manufacturing drawings are shown in Figure 4.3. Wet mixture was added to the mould, the mass of which was carefully controlled to ensure the target bulk density was achieved for each layer, and then statically compacted to achieve the the required layer depth. Following compaction the sample was pushed from the mould by hand, ensuring no disturbance was caused on the sides of the sample, and left to dry in a temperature monitored room at 22°C ±2°C until a stable mass was obtained, at which point no further water was lost to the atmospheric conditions. Five samples of each size and SBCM mixture was manufactured, 40 samples in total, and three samples from each batch were then selected for testing using those closest to the batch mean stable mass to ensure the smallest variation in dry density across the samples. Following testing it was found that all samples were within 0.6% of the target dry density.

To differentiate between samples during the remainder of this chapter the samples will be referred to using the following system: first the size of the sample is stated, using ϕ12 or ϕ38; second the mix is stated, either A, B, C or D; and third a number states which of the three samples within a triplicate is being discussed. For example, ϕ12C2 is the 12mm diameter sample, loaded and scanned within the SS1174, manufactured from mix C, classified using the system from Smith and Augarde (2013a) as

Table 4.2: The range of maximum dry density and optimum water content values from three on-site equivalence tests and the target dry density and water content values used in manufacture for all four SBCM mixes.

SBCM	w_{opt} **range (%)**		ρ_{dmax} **range** (gcm^{-3})		**Target**	**Target** ρ_d
Mix	**min.**	**max.**	**min.**	**max.**	w_{opt} **(%)**	(gcm^{-3})
A	8.76	9.54	2.14	2.15	9.15	2.15
B	9.60	9.92	2.08	2.11	9.76	2.10
C	9.46	9.78	2.06	2.04	9.62	2.05
D	10.40	10.65	2.00	2.01	10.53	2.01

30*:50:20[0.8], and is the second of three samples within the triplicate.

4.3.3 Experimentation

All samples were scanned using the SS1174 XRCT scanner and performed at a 30.8μm voxel size using the maximum power settings of 50kV, 800μA, a 0.75mm Aluminium filter and an exposure of 7500μs. The SS1174, discussed in considerable detail in Chapter 3, is capable of variable magnification 6-30μm 3D spatial resolution. Unconfined compression constant water content tests were performed on all the samples at a constant displacement rate and failure was observed though the evidence of a load peak and deemed to correspond to the maximum load applied. Constant strain rates, 0.01mm/min for the ϕ12 samples and 0.1mm/min for the ϕ28 samples, were chosen in accordance with British-Standards (1990) ensuring the strain rate did not exceed 2% per minute and failure occurred within 15 minutes.

The ϕ12 samples in turn were placed inside the Skyscan material testing stage installed within the SS1174, capable of compressive loading 20mm diameter samples to 200N. A pre-loading scan was performed taking approximately 25 minutes using the rotation step of 2°. At 25N intervals up to failure, and immediately after failure, the SkyScan material testing stage was paused to enable fast scans to be performed on the SS1174, taking 10 minutes using a rotation step of 5°. The load was then released and a post-loading scan performed using the pre-scan settings. The fast scans were required due to the poor load control from the material testing stage during scans, as discussed in Chapter 3, and to ensure a constant load was maintained during scanning. In turn, the pre-loading and post-loading time was chosen to ensure two samples could be scanned and tested within a single working day.

The three selected ϕ28 samples from each batch were first scanned using the SS1174 XRCT scanner, with the Skyscan material testing stage removed. Each scan took approximately 100 minutes and a rotation step of 1° and an averaging of 2 frames was used. This enabled multiple scans to be run within a working day whilst ensuring the scan quality was high enough for reconstruction to take place. The scan obtained was taken as the pre-loading scan. The samples were then compressed using a Lloyd LR5K Plus testing machine, with a load cell rated at 5kN±0.5%, until failure was observed and the load immediately released. During compression the load applied and displacement of the loading plate was recorded. The sample, with great care, was then placed inside the SS1174 and re-scanned. This was taken as the post-loading scan.

4.3.4 XRCT post-processing

The methods used to post process XRCT scan data are discussed in detail in Chapter 3 and the analysis procedure used here is outlined in Figure 4.4 (a replicate of Figure 3.11). The post-processing calculated the macropore percentage and interaction index for each horizontal slice taken through the reconstructed data, the key steps being:

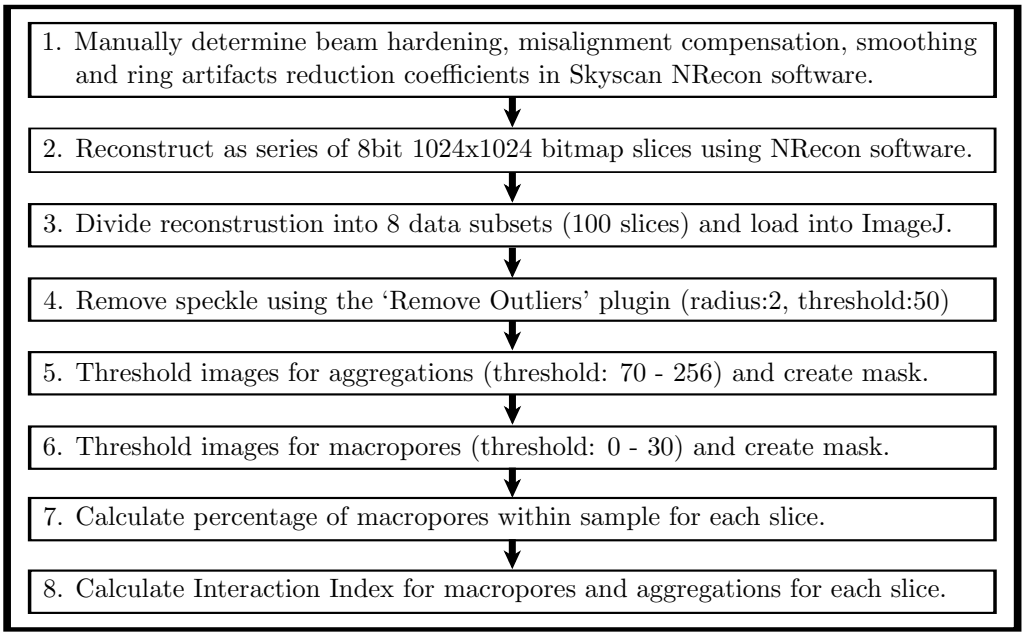

Figure 4.4: Flowchart of the ImageJ analysis used for XRCT data processing. Please note this is a replication of Figure 3.11 and included here for the readers convenience.

- reconstruction of the data, using the Skyscan NRecon software software provided with the scanner;
- reduction of file size, through the separation of the scanned data into subvolumes;
- enhancement of image quality, through smoothing and de-speckling filters;
- identification of macropores and aggregations within the sample, using calculated threshold values;
- and the production of quantitative results for macropore percentage and interaction index.

Figure 4.5 shows a single reconstructed XRCT data slice from the post loading ϕ28D1 sample. Clear aggregations of clay and sand or gravel within the sample were separated during the image post-processing by thresholding the image to identify the brightest regions within the sample. Discussed in detail in Section 3.4.2 a threshold of 70 was selected following the analysis of a sub-set of regions clearly identified as aggregations. The brighter regions within the reconstructed XRCT scan data correspond to the densest material within the SBCM and will clearly contain the gravel fraction, predominantly formed of quartz, but also may contain assemblages of sand and clay or silt in which the quartz sand proportion dominates. These higher density regions within the SBCM, identified as all voxels with a greyscale intensity value above 70, are therefore either gravel particles or high density assemblages and are referred to as the *aggregation phase* throughout the results and discussion presented here.

The XRCT scan voxel size of 30.8µm meant no intra-elemental or intra-assemblage voids occurring between individual particles could be identified and therefore any air identified within the pre-loading samples can be assumed to be part of an inter-assemblage voids, either between aggregations or the within the solid matrix. Following the unconfined compression tests cracks are expected to be introduced during

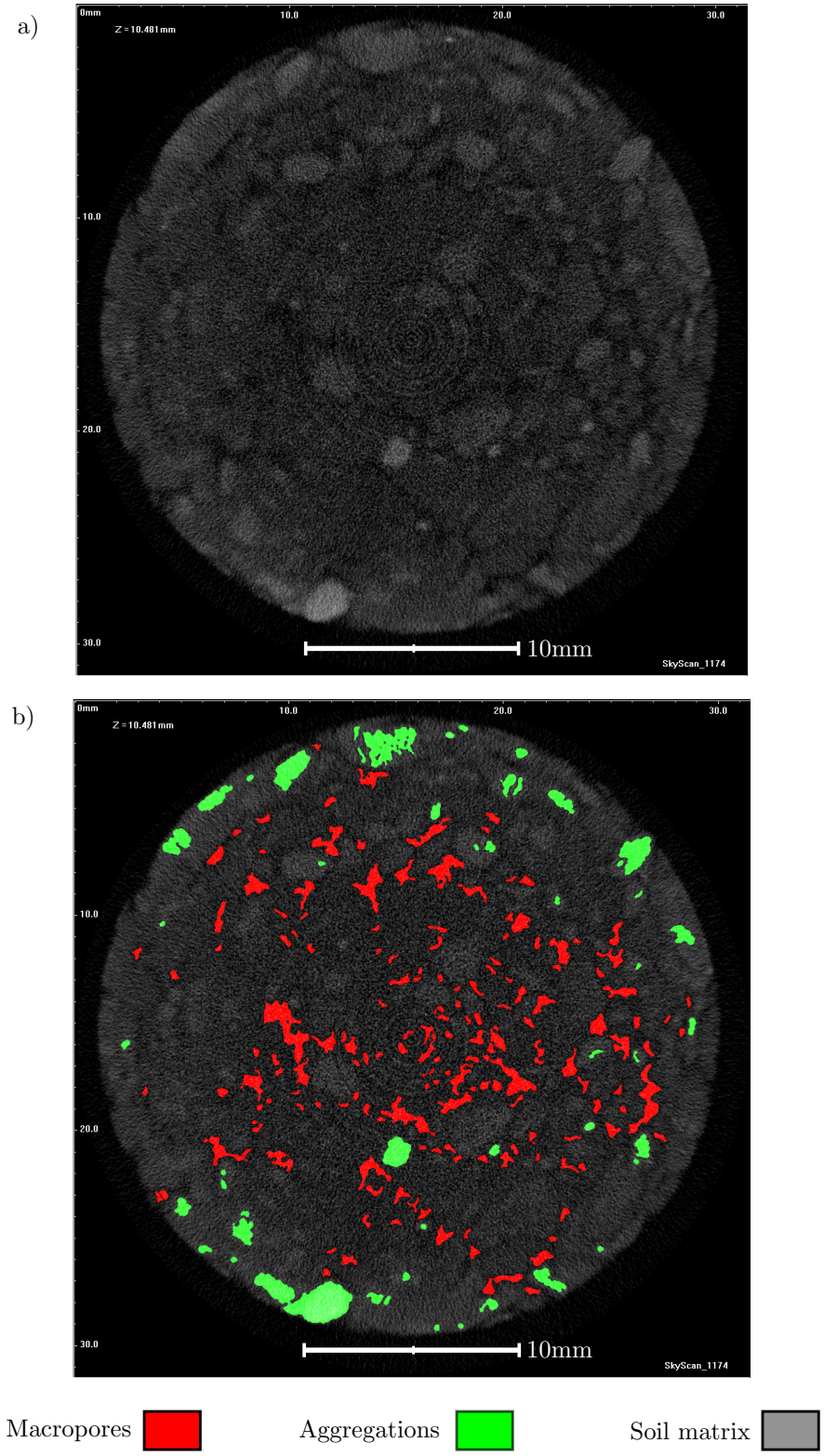

Figure 4.5: Reconstruction slice 340 from ϕ28D1 showing a) the original reconstructed XRCT data and b) the masked macropore and aggregation regions identified following image analysis.

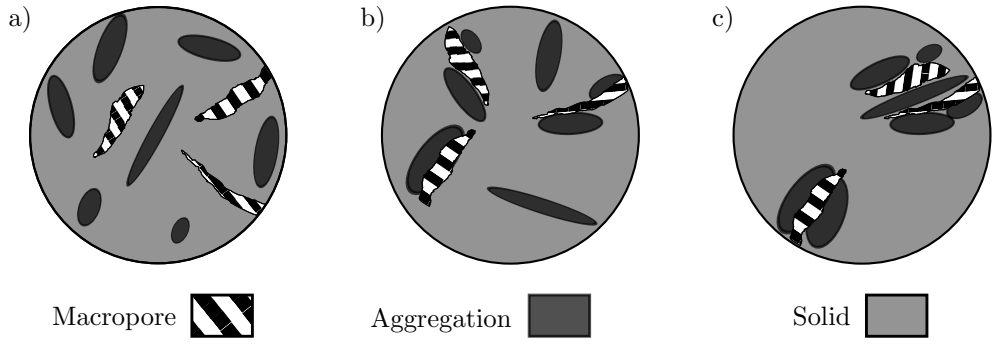

Figure 4.6: Sketch of examples of interaction index values, approximately a) 0% b) 50% and c) 100%.

brittle failure and would also form part of the air phase. Therefore during the results and discussion the air phase, identified as all voxels within the sample with a greyscale intensity below 30 during the post-processing of the XRCT scans, is referred to as the *macropore percentage* and can be taken as a quantitative measure of the cracks and inter-aggregate pores within the SBCM.

An additional measure to describe the internal structure of the samples, the *interaction index* between the macropores and aggregations, was also obtained using a purpose-specific coded ImageJ macro, in order to investigate any changes in the macropores locations relative to the aggregation regions following the unconfined compression tests. An 'interaction' was said to occur when a macropore pixel was in close proximity to pixel masked as a aggregation. It was necessary to use the proximity of macropores to the aggregation regions, rather than simply counting those pixels masked as macropores which were directly next to an aggregation pixel, due to a lack of instant transition between the two phases caused by the partial volume effect, the smoothing applied to the images and the predetermined threshold values. To determine what was meant by 'close proximity' a visual inspection of a series of cracks observed to be 'cutting through' an aggregation was performed and ten pixels was measured as the maximum distance between the two phases. The interaction index was then calculated as the percentage of the total number of possible interactions, i.e. the number of pixels on the edges of all macropores within a slice. Considering the interaction index in a physical form, as sketched in Figure 4.6, a value of 100% indicates all edges of macropores were close to aggregations, whilst a value of 0% indicates all macropores were away from the aggregations.

4.4 Results and analysis

4.4.1 Mechanical behaviour of ϕ28 and ϕ12 samples

Table 4.3 shows the compressive strength values obtained for all ϕ28 and ϕ12 samples, which was taken as the maximum compressive stress achieved by each sample during the unconfined compression, constant water content tests. Six compressive strength values were found to be clear outliers as when

included the corresponding sample set's range of compressive strength had a standard deviation larger than 0.08, for example the ϕ12A samples had a standard deviation of 0.32 which was reduced to 0.01 when one result was disregarded. These outlying results where therefore taken as anomalous and the samples were disregarded for the remainder of the analysis.

Figures 4.7 to 4.10 show the stress - strain results obtained for the remaining 18 samples. For all the ϕ12 and ϕ28 samples two distinct regions within the loading curve can be identified up to and including to failure and a third region is visible within the ϕ28 samples after failure of the sample has occurred. The first region visible in all the sample loading curves is the period of *bedding in* which occurs at the beginning of the tests, when vertical compressive strain is imparted on the sample without any significant increase in the compressive load applied being measured. The duration of this bedding in region varies across samples but in all cases the transition to the next region within the loading curve is marked by an increase in the gradient of the curve and the measurement of significant compressive load, typically more than 0.15MPa. The longest bedding in period, in terms of increase in vertical strain, is exhibited by the sample ϕ12B1 (shown in Figure 4.8) for which a change in the gradient of the stress-strain curve is not observed until 0.05με has been applied whilst the smallest bedding in periods are exhibited by samples ϕ12B2 and ϕ12C1 in which the increase in measured compressive load occurs almost immediately. No clear trend can be seen that links the duration of the bedding in period and the sample size or SBCM mix used. This can be explained by considering the predominant reason for the existence of the bedding in period, the imperfections in the sample's top and bottom surfaces during manufacture. Any protruding grains of sand from the surface of the sample will have prevented the sample caps sitting flush on the surface of the sample and therefore a small compressive load will have been measured as the sample caps are first pressed against the protruding grains but before they make contact with the majority of the sample loading surface. This period of bedding in will not have affected the compressive strength of the sample, since the ultimate compressive stress measured at failure will not have been significantly changed by the slight material imperfections at the surface of the samples, however it does prevent an easy determination of the failure strain as it is difficult to determine the exact point at which the entire cross section of the sample started being loaded.

The second region visible within the loading curves is the *linear elastic region* in which a significant

Table 4.3: The compressive strength values for all samples. Entries in bracketed italics were deemed anomalous.

SBCM	**Compressive Strength (MPa)**					
Mix	**ϕ28-1**	**ϕ28-2**	**ϕ28-3**	**ϕ12-1**	**ϕ12-2**	**ϕ12-3**
A	*(0.62)*	0.80	0.75	*(0.65)*	1.19	1.21
B	1.11	1.17	*(0.75)*	1.60	1.52	1.54
C	0.73	0.71	*(0.95)*	1.75	1.64	*(1.20)*
D	1.27	1.28	1.25	1.26	1.29	*(1.46)*

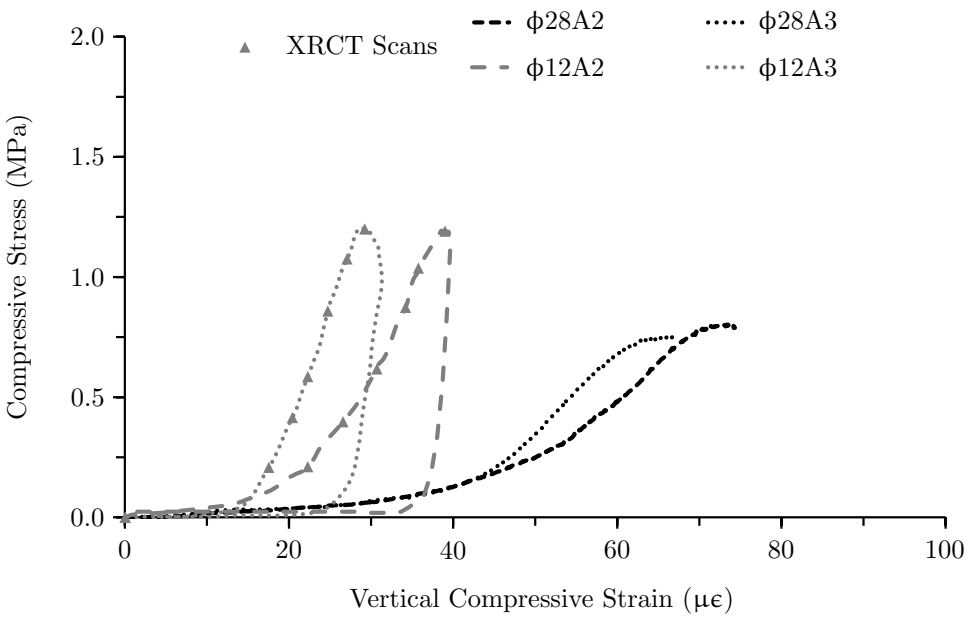

Figure 4.7: Stress-strain results for all six samples manufactured using mix A.

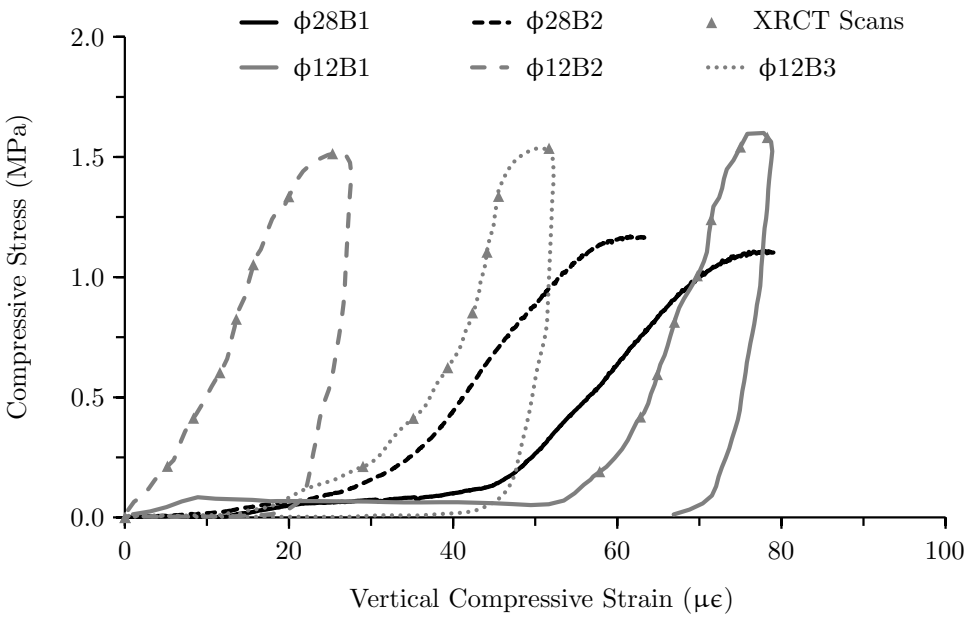

Figure 4.8: Stress-strain results for all six samples manufactured using mix B.

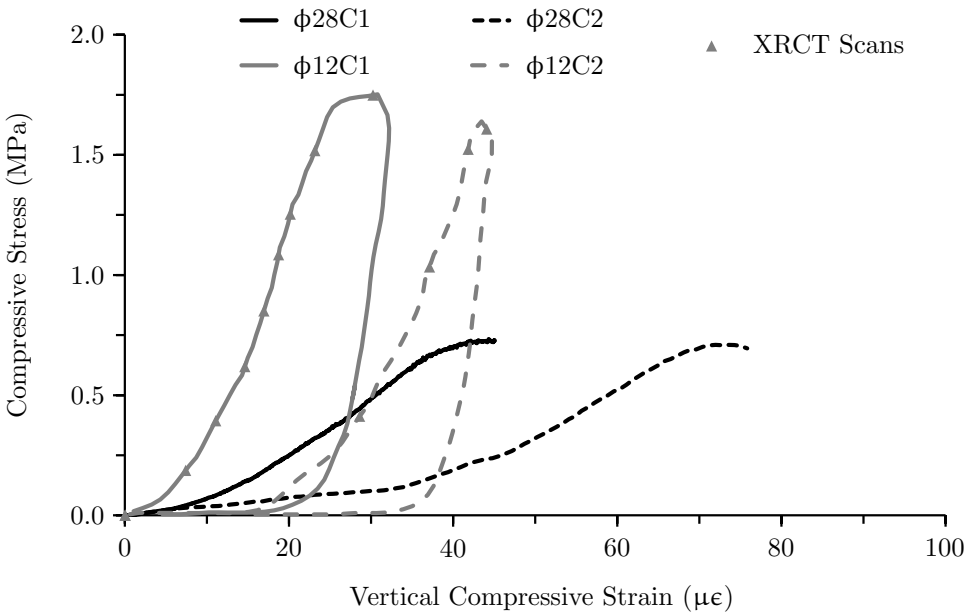

Figure 4.9: Stress-strain results for all six samples manufactured using mix C.

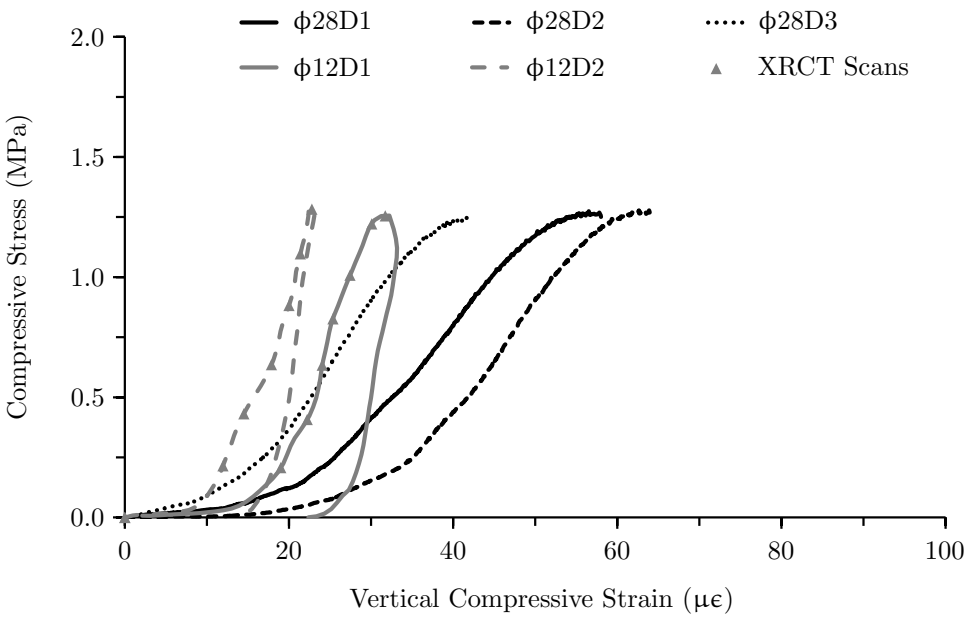

Figure 4.10: Stress-strain results for all six samples manufactured using mix D.

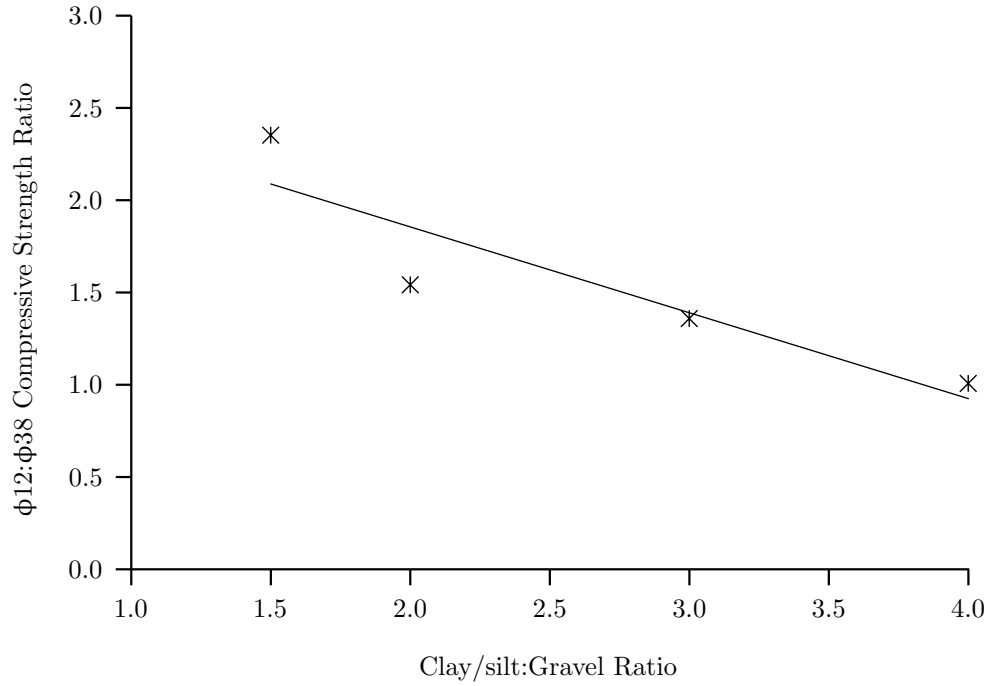

Figure 4.11: The ratio of clay/silt:gravel plotted against the ratio of compressive strength for ϕ12:ϕ28.

increase in applied load is measured as the sample is compressed. During this phase of the compression tests it is possible to determine the Young's modulus of the sample, E, which is a measure of the stiffness of the SBCM and is defined as the ratio of applied stress to strain in the region in which the sample behaves elastically. To determine the Young's modulus of each sample the gradient of the curve is calculated following the bedding in phase and before the stress-strain curve flattens out prior to failure.

A third region of the stress-strain curve is visible within the ϕ12 samples and can be described as the *unloading region*. This region, which occurs after the failure of the sample, is recording the the return of the loading platens to their original zero strain position, and the subsequent reduction in the compressive load measured by the Skyscan material testing stage as the platens are removed from the sample. This region is not visible in the ϕ38 samples as the Lloyd LR5K Plus testing machine stopping recording the load-displacement data post failure and returned to the zero-displacement position without logging the load or displacement.

It is clear from Figures 4.7 to 4.10 that the two different sized samples produced different vertical axis stress-strain plots and resulted in different compressive strength values for the same SBCM mixes. A variation in compressive strength with respect to shape and size of cement-stabilized rammed earth samples was also identified by Ciancio and Gibbings (2012) and the authors show that this is due to the variation in slenderness ratio for the cylindrical samples, which varied between 0.75 and 2.0 for their tests. In this investigation however the slenderness ratio is the same for both sample sizes and it is therefore necessary to consider other factors which differed between the ϕ28 and ϕ12 samples.

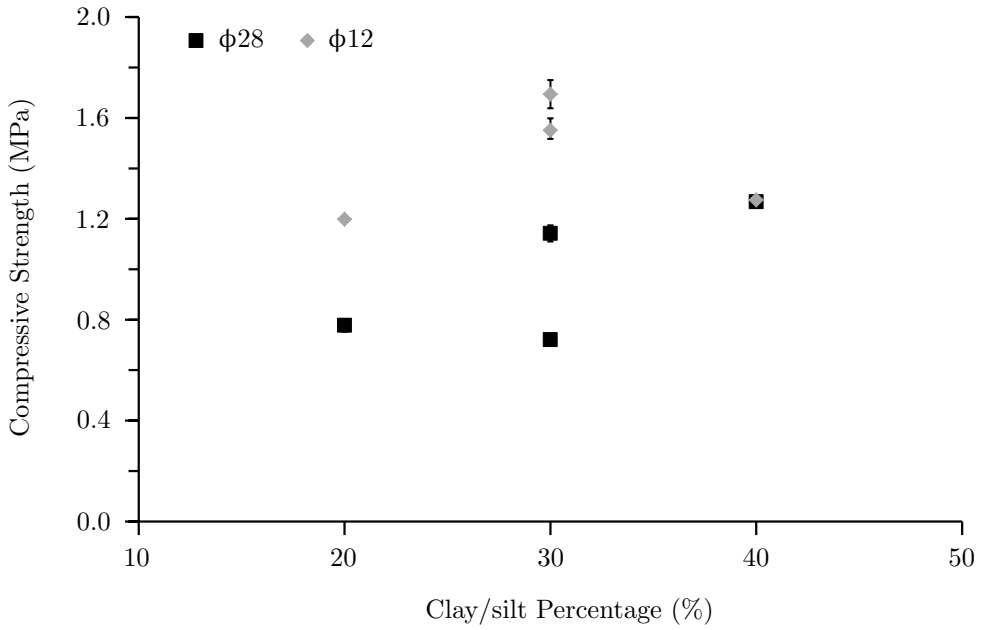

Figure 4.12: The percentage of clay/silt within each SBCM mix plotted against the average compressive strength.

Figure 4.11 shows an increasing discrepancy between the compressive strength of the two sizes of sample tested as the ratio between the gravel and silt/clay fractions decrease and it is suggested that the sieving of different particle sizes, $>$ 2mm and $>$ 5mm, out of the soil mixture prior to manufacture is likely to be altering the sample's compressive strength. For the mixes where clay/silt fraction dominates the gravel fraction, i.e. mix D, the removing of the largest particles has minimal affect on the final failure load whilst the mixes where the two fractions are more similarly proportioned, i.e. mix C, the removing of the gravel particles dramatically increases the compressive strength. Maniatidis and Walker (2008) also report a 30% increase in average unconfined compressive strength following the removal of all particles larger than 20mm, which accounted for approximately 5% of the soil grading from their unstabilized rammed earth mix classified as 25*:45:30.

Figure 4.12 compares the unconfined compressive strength of the four different SBCM mixes. When considering the ϕ12 samples a peak strength response at 30% clay percentage can clearly be seen with a reduction in compressive strength when the clay content is closer to the upper and lower limits of 20% and 40% recommended by Houben and Guillaud (1989). No clear peak can be observed using the ϕ28 results and it is possible to suggest that the compressive strength increases with an increase in clay content. However it is unlikely that the strength will continue to increase indefinitely with increasing clay content and a peak strength would be observed if a mix design had been used where the clay percentage was above the 40% upper limit proposed by Houben and Guillaud (1989).

The existence of a specific percentage of clay content for a given mix, or binder-aggregate ratio as hypothesised by Hall and Djerbib (2004), which results in the largest unconfined compressive strength is to be expected when the role of the different materials within the material structure are considered. Jaquin et al. (2009) and Bui et al. (2014a) have clearly demonstrated that suction is a main source of strength within SBCMs and this suggests that the clay present is the key binder within SBCMs. Too little clay will therefore result in insufficient binder between the larger aggregates whilst too much clay results in a material which is much more similar to a unsaturated silty clay.

The Young's modulus values obtained for all the analysed samples are shown in Table 4.4 along with the average Young's modulus calculated for each set of samples. No link between the proportion of any of the particle fractions within the SBCM mixes and the obtained Young's modulus for either sample size could be observed. It is however very clear that the Young's modulus of the ϕ28 samples is significantly lower than the ϕ12 samples, in fact in the case of the mix C samples the Young's modulus for the ϕ28 samples is a less than a quarter of the ϕ12 samples. No clear trend could be found between the reduction in Young's modulus from the ϕ12 to the ϕ28 samples and the gravel-silt/clay ratio however it is suggested that the removal of the gravel particles within the ϕ12 samples is still the predominant reason for the change in Young's modulus of the different sample sizes.

Due to the small sample sizes used throughout this investigation the exact role of the gravel within SBCMs is difficult to determine and the difference in unconfined compressive strength and Young's modulus for the ϕ12 and ϕ28 samples is difficult to discuss in detail using the results obtained. It is therefore suggested that further laboratory testing should be performed using larger sample sizes which specifically investigates the role of the gravel within the SBCM structure.

4.4.2 Insights from the ϕ12 samples into XRCT scanning

Following visual inspection the quality of the scans performed on the ϕ12 samples appeared sufficient, since the cracks could be manually identified. However the thresholds applied and analysis techniques used were unable to identify the required features with sufficient autonomy for the analysis to be batch processed and run on a total of $>10^5$ slices. Therefore all the ϕ12 reconstructions were not of sufficient quality to analyse and no numerical data could be obtained. Despite this lack of useful XRCT scan

Table 4.4: The Young's modulus values obtained for all analysed samples.

SBCM Mix	**Young's Modulus (MPa)**							
	ϕ28 Sample				**ϕ12 Sample**			
	1	**2**	**3**	**Average**	**1**	**2**	**3**	**Average**
A	-	26.8	31.5	29.2	-	61.3	91.0	76.1
B	38.0	41.54	-	39.8	78.8	75.8	67.9	74.1
C	23.3	16.6	-	20.0	84.4	84.0	-	84.2
D	39.1	44.2	51.5	44.9	103.5	93.5	-	98.5

results from the ϕ12 samples a number of clear observations and lessons of note can be drawn.

Firstly, using visual inspection to assess the quality of a scan can lead to problems when writing analysis techniques to identify objects or areas of interest. The human brain is very adept at filtering out unnecessary information, such as 'hot' or 'cold' pixels, and dealing with incomplete information such as discontinuous shape outlines. This means that when visually inspecting a sample scan it is likely that the quality will appear higher to the inspecting individual than is actually the case when being processed by the computer analysis software. It is therefore suggested that preliminary scans are not only checked visually but are analysed using the computational post-processing software to ensure the required quality of results are obtainable.

Secondly, speeding up the scanning process to increase the samples scanned during a day is ultimately unproductive if the resulting scans are not of sufficient quality. The pre and post loading zero-load ϕ12 scans were not constrained by any time factors other than a desire to scan more samples in a given time and decreasing the scan time resulted in all the scans simply producing some indicative 3D models rather than scans capable of producing quantitative data for analysis. Had the first lesson discussed been implemented, where preliminary scans were analysed rather than only visually inspected, the same scan settings used in the ϕ28 scans, taking approximately an hour, could have been implemented and the resulting scans would have been suitable for the post-processing analysis. It is therefore suggested that the driving factor behind the scan settings should not be time, which can be tempting when there is limited time available on a given XRCT scanner, but the ensuring of sufficient scan quality to enable valid quantifiable results and conclusions to be drawn after post processing.

Finally, caution must be taken when reducing scan times or reconstruction times through the increase of rotation angle or the reduction in number of slices, as discussed in Section 3.4.1. The resolution of the final reconstruction is not only dependant on the zoom applied by the XRCT scanner but also on the number of slices in the reconstruction, affecting the resolution in the vertical plane, and the angle of rotation of the sample, affecting the true resolution in the horizontal plane. For both the ϕ28 and ϕ12 scans the use of 1000 slices ensured the scan resolution of 30.8μm was maintained during reconstruction, since the total vertical height of the scan was less than 30mm. The 5°, 2° & 1° angles of rotation of the samples also ensured the 30.8μm resolution was maintained in the plane of rotation, with points moving with each rotation of the sample relative to the x-ray detector a maximum of 22.8μm on the very edge of each sample. It could therefore be suggested that the 2° & 1° angles of rotation were unnecessary, since the 5° rotation was acceptable, however by reducing the rotation angle, and in turn increasing the number of x-ray images taken, the quality of the sample reconstruction was improved enabling the post-analysis techniques to be applied. It is therefore important to note that reducing the number of slices, or increasing the angle of rotation, can be very attractive when trying to reduce the time required

to process a given sample but this must be done with great care. The impact on the scan quality and the true resolution of the resulting reconstruction must be calculated and it cannot be assumed that since the XRCT scanner was set to a specific resolution that this will still hold once the 3D reconstruction of the sample is complete.

4.4.3 Development of material structure in the ϕ28 samples

Five of the fifteen ϕ28 samples, scanned within the SS1174 XRCT scanner and processed using ImageJ, were successfully analysed and provided some clear quantifiable results with respect to the change in internal structure of the samples following compressive loading. Six of the samples were discounted following anomalous compressive strength results and for a further two samples, ϕ28A2 and ϕ28C1, the image analysis could not be performed on the scanned images preventing any quantifiable data being obtained. Despite the small number of samples it is possible to gain insights into both the quantity of macropores pre- and post- loading, the initiation of the new cracks during loading and the location of the propagating cracks relative to the aggregations following the unconfined compression tests.

Firstly, for all five samples no increase in macropore percentage with respect to depth within the layer can be observed. This suggests that the two layer method of manufacture for the ϕ28 samples was sufficient to avoid a reduction in macrostructural density at the base of a compacted layer as reported by Beckett et al. (2013). The percentage of macropores within horizontal slices taken through the reconstructed samples is shown in Figure 4.13 where the slice number relates to the depth below the top surface of the sample with each slice spaced at 29.8μm.

Secondly, all five samples show an increase in the percentage of macropores within the sample following compressive failure. This is to be expected as the application of compressive load on dry soils results in brittle failure through the formation, growth and joining of cracks (Atkinson, 1987) and this brittle failure of specimens at low water contents is due to frictional failure and the breaking of liquid bridges at the interparticle contacts (Rondeau et al., 2003; Dehandschutter et al., 2005; Beckett et al., 2013). It is therefore likely that the increase in macropore percentage observed in all five samples is due to the development of cracks through the material during the compression testing and this suggests that the XRCT images following post processing are at a sufficient resolution to identify and track the evolution of the cracks through the SBCM samples.

Thirdly, the similar shape of the pre-loading and post-loading macropore percentage lines for each given sample suggests that the initial macropores within the sample, either existing cracks or as a result of compaction during manufacture, have grown rather than new cracks forming. If new cracks were being initiated within the sample it would be expected that new peaks would be observed on the post-loading macropore percentage at depths different to those on the pre-loading scan. The increase in size of peaks already visible on the pre-loading data however suggests crack propagation as the associated peak is seen

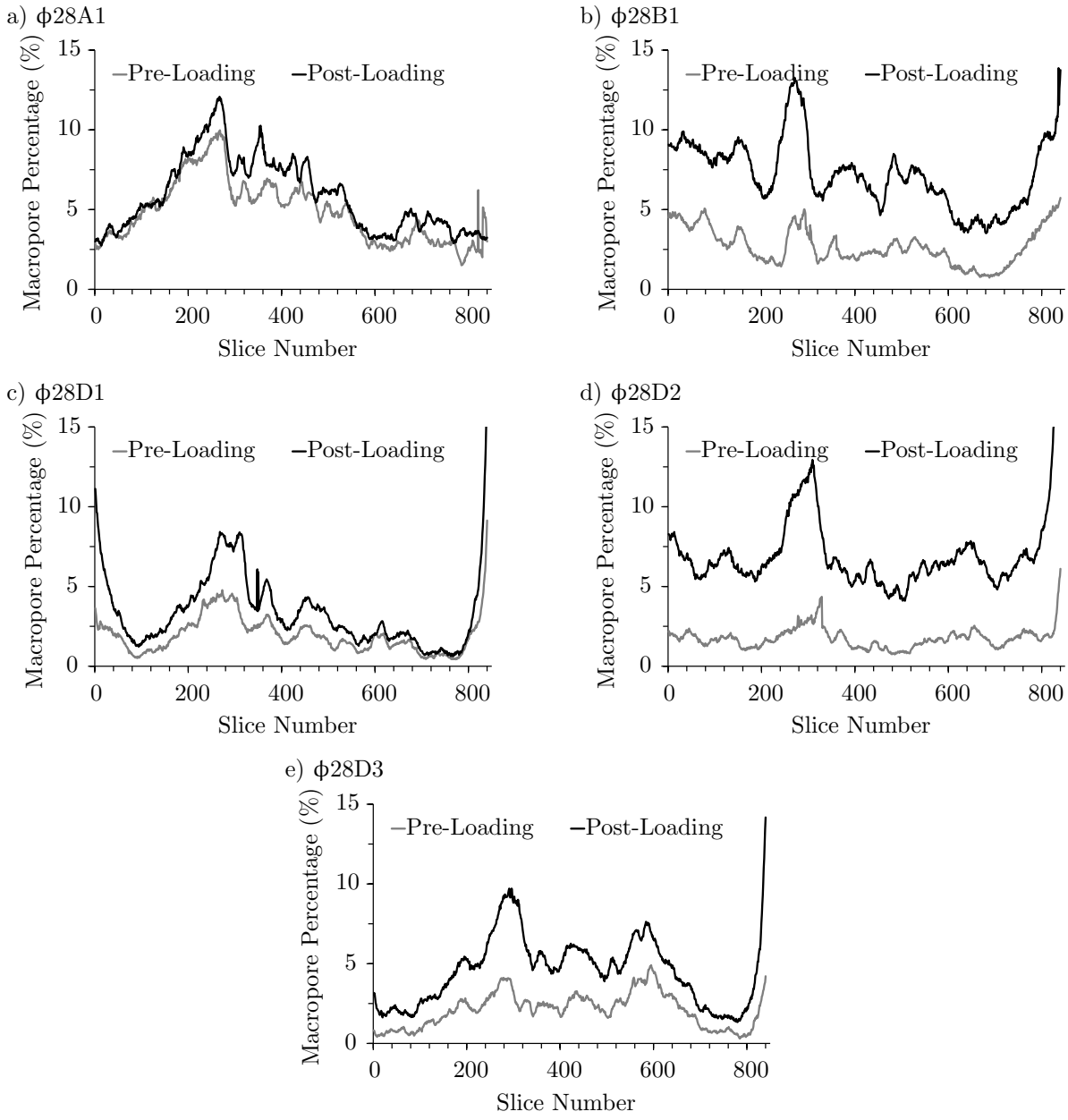

Figure 4.13: Percentage of macropores per slice for all five successfully analysed samples.

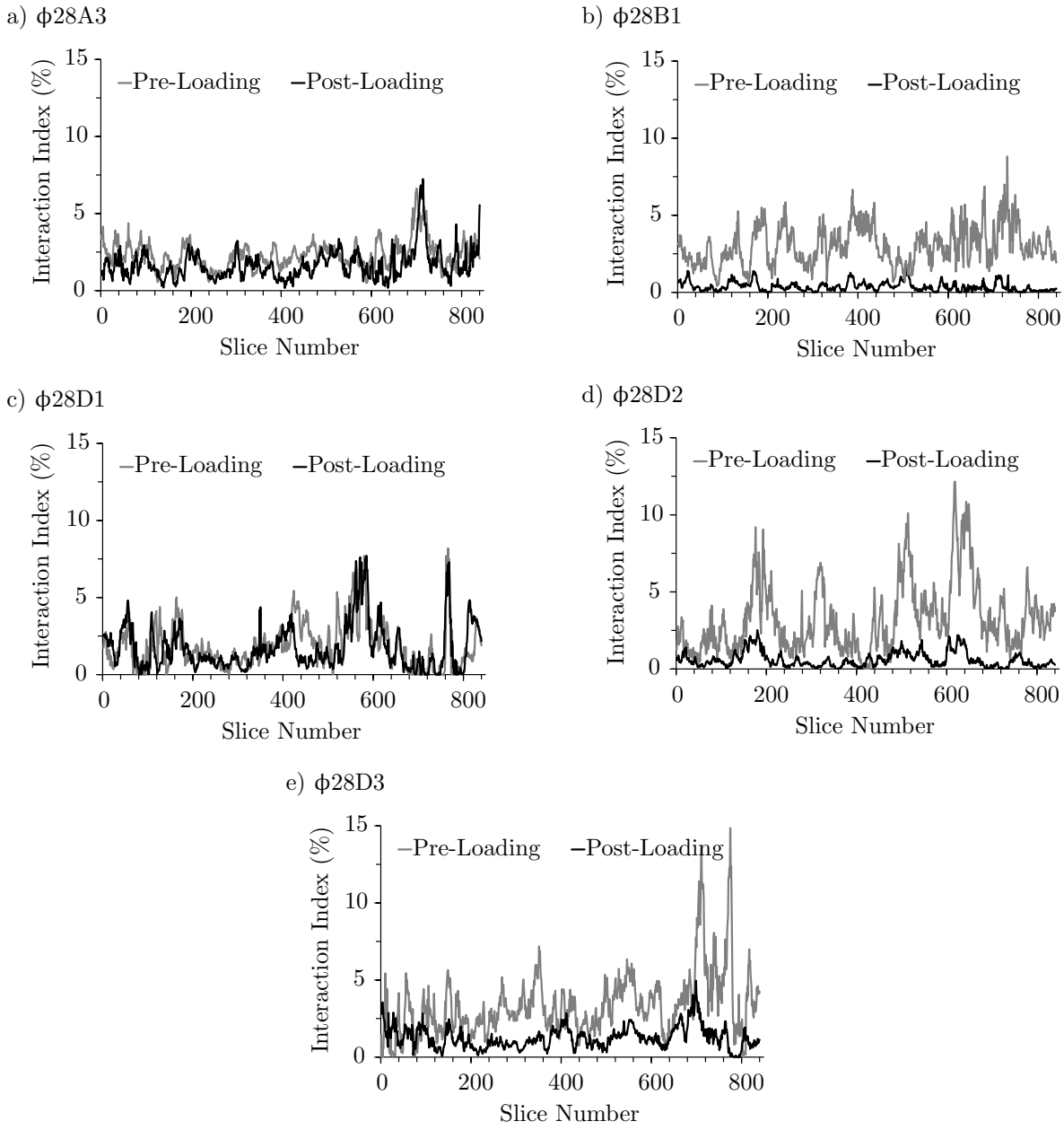

Figure 4.14: Interaction index per slice for all five successfully analysed samples.

to increase in size within a limited region about which it existed pre-loading. Additionally, it is logical to assume that the larger macropores within the sample prior to loading will propagate most during loading and this is supported by the greater macropore percentage increase in slices that had a larger macropore percentage prior to loading when compared to the regions within the sample which had a lower pre-loading macropore percentage.

Finally the changes in interaction index for each of the five samples successfully analysed, shown in Figure 4.14, can be used to examine crack propagation. The change in interaction index for the ϕ28B2, ϕ28D2 and ϕ28D3 samples show a clear reduction between the pre-loading and post-loading results whilst the ϕ28D1 and ϕ28A3 samples show a small decrease. A lower value of interaction index, as illustrated in Figure 4.6, means that less of the macropore edges are within very close proximity to aggregations and therefore the results suggest that during the tests the cracks have propagated into regions of the sample further away from the aggregations.

The propagation of the cracks can be further explored by considering the magnitude of the changes in interaction index and macropore percentage for each given sample. The ϕ28D1 and ϕ28A3 samples show only a small decrease in interaction index and are also the two samples in which the smallest increase in macropore percentage is observed. In contrast, the remaining three samples, all of which have a larger decrease in interaction index also show a greater increase in the percentage of macropores following loading. This can be explained by considering the geometrical impact of an increase in macropore percentage since, assuming no new cracks form, a larger increase in macropores will be a result of larger cracks and crack growth can be related to the distance which the crack propagates. Therefore when the macropore percentage only increases by a small amount it is unlikely that the cracks will have propagated any great distance whereas for the samples in which a larger increase in macropore percentage is observed it is likely that cracks will have propagated further through sample and away from the aggregations.

4.5 Summary and conclusions

The results discussed in Section 4.4.1 show that the removal of large particles prior to compaction significantly increases the Young's Modulus of the samples, by up to 400%. Additionally the removal of the largest particles may also have an impact on the unconfined compressive strength of SBCM samples, in some cases more than doubling the strength and this discrepancy however is dramatically reduced when the clay/silt fraction dominates the gravel fraction. An optimum clay percentage of 30% was observed for the ϕ12 samples to obtain maximum unconfined compressive strength although this was not observed for the ϕ28 samples and no clear conclusions could be drawn regarding which SBCM mix achieved the highest Young's Modulus values. It is suggested that to better understand the role of gravel within SBCMs larger samples should be investigated which do not require sieving prior to compaction.

The XRCT scan data obtained from the ϕ12 samples unfortunately did not yield any insights into the material structure but did result in three clear lessons. Firstly visual inspection of scan data is insufficient to assess the suitability of scans for quantitative analysis and wherever possible preliminary scans should be analysed using the post-processing computational procedures. Secondly, despite the considerable limits on XRCT machine time, allowing external time constraints to dictate XRCT scan times should be avoided wherever possible as it can have considerable impact on the final obtained scan quality. Thirdly the resolution of the XRCT scan is affected by both the number of horizontal slices produced by the reconstruction software and the angle of rotation of the sample between each 2D x-ray image and any initial resolution obtained through the machine zoom cannot be assumed to still hold once 3D reconstruction of the data is complete.

Finally the XRCT scanning and quantitative data analysis of the ϕ28 samples have provided an insight into the changes to the macrostructure following unconfined compressive loading. A clear increase in macropore percentage can be observed following compressive failure and the lack of new peaks within the macropore percentage suggests that the failure occurs through the propagation of existing cracks through inter-aggregate pores, rather than the initiation of cracks at new locations within the sample. Additionally the reduction in interaction index following compression shows that the cracks have propagated away from the aggregations within the SBCM and through the clay matrix which surrounds these aggregations.

Chapter 5

Structural changes due to loading

5.1 Introduction

The investigation of the compressive loading behaviour of unstabilized soil based construction materials (SBCMs) in Chapter 4 showed that reducing sample size, and having to remove the largest fractions from the SBCM prior to manufacture, considerably altered the unconfined compressive strength and Young's modulus of the material. Additionally the review of the use of laboratory x-ray computed tomography (XRCT) in geotechnical research in Chapter 3 showed there is a large variation in the size of samples scanned by XRCT with a growing trend towards small non-standard samples with diameters smaller than 12mm. This chapter investigates the differences in compressive strength using three cylindrical sample sizes, the macrostructure of the SBCM through the use of XRCT and aims to establish the role of the different constituents within the SBCM mix. Additionally the use of three different sample sizes enables further observations to be drawn about the current trend towards smaller samples within geotechnical research.

Each sample was scanned using the XRadia/Zeiss XRM 410 XRCT scanner, hereafter referred to as XRM410, before and after unconfined compression constant water content testing. The compressive strength results obtained are discussed in Section 5.4. A full XRCT scan of a sample involved three individual scans: the first a large field of view scan, at a lower resolution, ensuring the whole sample could be scanned and the second and third scans were small field of view scans performed at the highest resolution possible for the given sample size. The void size distribution was then determined by analysing the XRCT reconstructions in Avizo Fire. The results across the three sample sizes and two image resolutions are discussed in Section 5.5. Links between the material structure and the compressive strength of SBCMs are discussed in Section 5.6 and conclusions are also drawn in Section 5.7 on whether an optimum sample size exists for XRCT investigations of SBCMs.

5.2 Internal structure of soil based construction materials

As discussed in Chapter 2 the internal structure of unsaturated soils is an important topic of investigation and there exists a good level of understanding about the structure of soils containing only clay or sand particles. The development of XRCT technology, as described in Chapter 3, has provided researchers the opportunity to study the internal structure of geotechnical samples in greater detail and has allowed better descriptions of the macrostructural voids present within unsaturated soils. This use of XRCT however has been poorly embraced by researchers within the SBCM community and a detailed understanding of SBCMs material structure is still lacking in the current literature. Consequently a fundamental knowledge about the role of each constituent within the SBCM mixture is still missing and a model for describing the void structure of such a broadly graded soil mixture, as exists for the double void structure of clay soils, is yet to be well established.

Beckett et al. (2013) used XRCT to observe the changes to the macrostructure of rammed earth following compressive loading and how compaction during manufacture affects the macrostructure within individual layers of rammed earth. Due to limitations on sample size, only the inter-aggregate soil matrix, formed of clay and sand particles, was investigated. The results from Beckett et al. (2013) show that the interconnectivity and size of voids significantly increases following loading and that the effect of cracking is greater within poorly compacted material. Beckett et al. (2013) also show that single layer specimens have a highly heterogeneous macrostructure whilst double layer specimens are largely homogeneous, and the macrostructure of a compacted layer is not affected by the compaction of additional material above it. The work performed by Beckett et al. (2013) provides a valuable insight into the macrostructure of SBCMs however the analysis was only performed in 2D, preventing void volumes being determined, and the lack of gravel particles within the mix is likely to have significantly altered the void structure.

Hall et al. (2013) also used XRCT to characterise the void geometry of cement-stabilized soils for earthen construction. However the addition of cement to the soil mixture will have fundamentally altered the material properties, since the cement will act as a chemical binder between the particles, and therefore it is difficult to apply results to the study of unstabilized SBCMs.

5.3 Methodology

5.3.1 Sample size

Three cylindrical sample sizes, 12mm diameter x 24mm high, 38mm diameter x 76mm high and 100mm diameter x 200mm high, were used in this investigation and are referred to hereafter as ϕ12, ϕ38 and ϕ100 respectively. The ϕ12 sample was chosen as it was the largest sample size for which a high resolution scan with a voxel size of less than 1µm could be easily obtained using the XRM410 whilst the

ϕ38 sample was close to the maximum sample size which could be easily placed within the XRM410 and have its entire width scanned in a single XRCT image. The ϕ100 sample was used as it was close to the maximum diameter soil sample which could be scanned within the XRM410 before insufficient x-rays passed through the sample and no data could be obtained. From a material testing perspective the ϕ38 and ϕ100 samples are both standard geotechnical triaxial testing sizes ensuring samples could be easily manufactured, and unconfined compression tests performed without the need for new testing equipment or techniques.

The investigation in Chapter 3 into the sample sizes commonly used in geotechnical research has shown that the use of samples smaller than 15mm diameter predominates, very few samples are scanned between the sizes of 20mm and 60mm diameter and the largest sample size scanned is 70mm. Because the ϕ12 sample are of a similar size to the small samples predominately used, the ϕ38 samples are within the size range rarely used and the ϕ100 samples are larger than the 70mm diameter samples these three sample sizes enable an investigation into whether an optimum sample size exists for the scanning of SBCM samples and, more generally, if the current trend of using small samples is valid within geotechnical research into soil mixtures.

5.3.2 Materials

A single SBCM mix, 30*:60:10, was used throughout the investigation and chosen as it lay in the centre of the limits suggested by Houben and Guillaud (1989) and the SBCM mixes used in Chapter 4. The 30*:60:10 SBCM mix was manufactured in a manner similar to Chapter 4 by combining appropriate amounts of speswhite clay, sharp sand and pea gravel. Speswhite clay (LL 64%, PL 34%, PI 31%) is a pure kaolin clay supplied by IMERYS Performance Minerals (Imerys, 2008) and used as it closely matches the mineralogy of the Birtley clay, which is primarily kaolinite, as used in Chapter 4. The speswhite clay however has a key advantage during manufacture of the samples over the Birtley clay as it requires no pulverisation or processing prior to manufacturing the samples. Both the sharp sand and the pea gravel were oven dried at 105°C and then passed through 2mm and 10mm sieves respectively, using the same preparation technique as implemented in Chapter 4. To improve the particle grading the sieved pea gravel (<10mm) and the retained sharp sand (>2mm) were combined in a 1:1 ratio by mass and used as the gravel fraction within the SBCM.

Figure 5.1 shows the particle grading curve for the SBCM mix after manufacture. The maximum weighted percentage error term for the mix was calculated and the mix is fully described as 30*:60:10[0.9]. The BS1377 Vibrating Hammer Test (British-Standards, 2002) was used to determine the optimum water content and target dry density for the SBCM mixture (Smith and Augarde, 2013b). The vibrating hammer test results for the SBCM mix are shown in Figure 5.2 from which optimum water content (w_{opt}) and maximum dry density (ρ_{dmax}) values of 8.93% and 2060kg/m^3 were obtained.

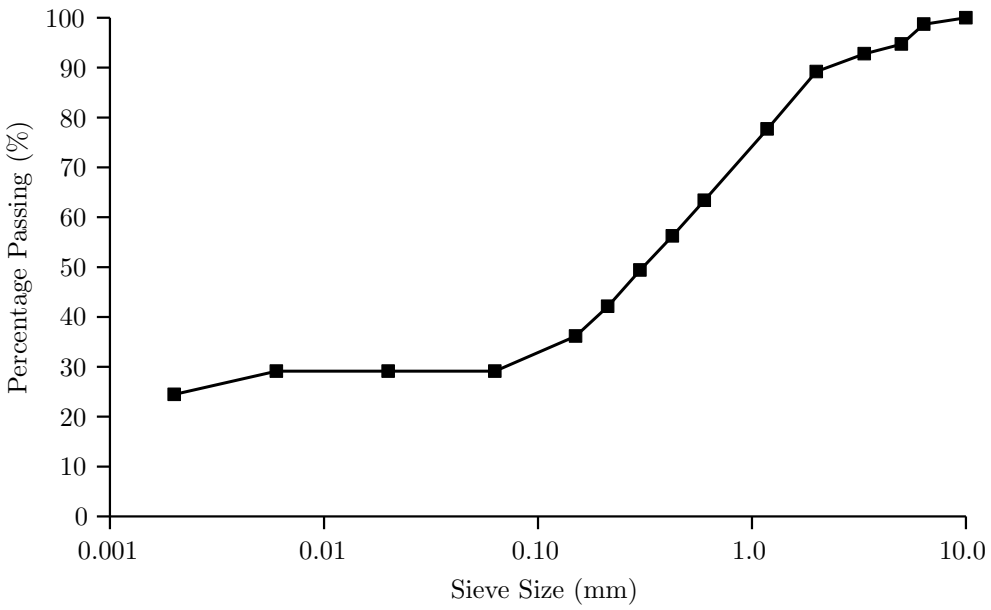

Figure 5.1: Particle grading curve for the 30*:60:10[0.9] SBCM mix.

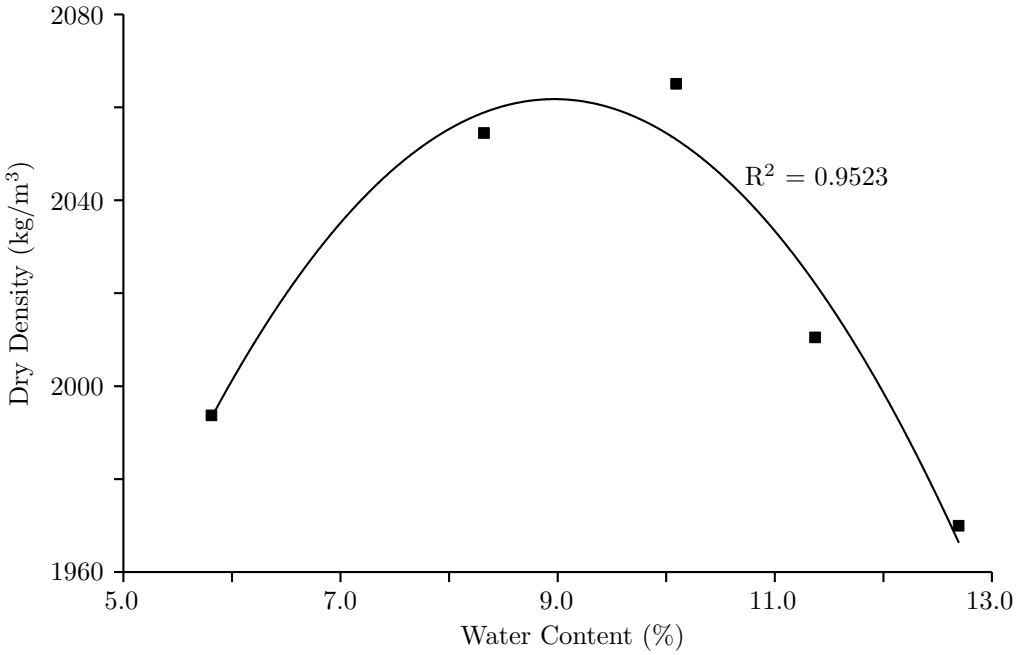

Figure 5.2: The BS1377 Vibrating Hammer Test result for the 30*:60:10[0.9] SBCM mix.

5.3.3 Sample manufacture

Five samples were manufactured for each of the ϕ12, ϕ38 and ϕ100 sample sizes. Prior to sample manufacture the 30*:60:10[0.9] soil mixture was sieved to 2mm for the ϕ12 samples and 5mm for the ϕ38 samples, to prevent the larger particles interfering with the compaction and loading behaviour. The soil for the ϕ100 samples was not sieved in order to closest match an on-site soil mix and had a maximum particle size of 10mm. The appropriate amount of water was added to each mixture to reach w_{opt} and the mixture left to equilibrate overnight. Since SBCM structures are often constructed by compacting layers of soil within formwork all three samples were constructed from layers of compacted material. The exact dimensions of the samples and the number of compacted layers can be found in Table 5.1.

The correct mass of wet soil mixture for an individual layer was added to the sample mould to ensure each sample layer would be at the target optimum dry density of 2060kg/m^3, and statically compacted to achieve the required layer depth. Once the appropriate number of layers had been compacted the sample was pushed from the mould by hand, ensuring no disturbance was caused on the sides of the sample, and left to dry in a temperature monitored room at 22°C ±2°C until a stable mass was obtained (between 0.8% and 1.2% water content), at which point no further water was lost to the atmospheric conditions. Three filter paper test samples, each using two cylinders (50mm diameter and 20mm high), were also prepared alongside each of three sample sizes and compacted to the same target density. These were left to dry under the same conditions as the ϕ12, ϕ38 and ϕ100 samples before being placed in a sealed jar to equilibrate for ten days. The filter paper test results provided total suction values for the three different mixtures.

Three samples from each batch of five manufactured samples, those closest to the batch mean dry mass, were selected for scanning and mechanical testing. Following testing it was found that all samples were within 1.8% of the target dry density. To differentiate between different samples within the triplet, each sample was assigned a suffix A, B or C. Once the samples reached their stable dry mass, top and bottom plastic caps were placed on the samples and the sample was sealed within a latex sheath using rubber o-rings, as shown in Figure 5.3. The caps and sheath prevented any further change in water content during scanning, compression testing and re-scanning, provided a flat surface onto with the compressive load could be applied and enabled easy secure mounting of the samples inside the XRM410.

Table 5.1: The dimensions and number of layers for all three sample sizes.

Sample	**Diameter (mm)**	**Height (mm)**	**Number of Layers**
ϕ12	12	24	2
ϕ38	38.1	76.2	2
ϕ100	100	200	3

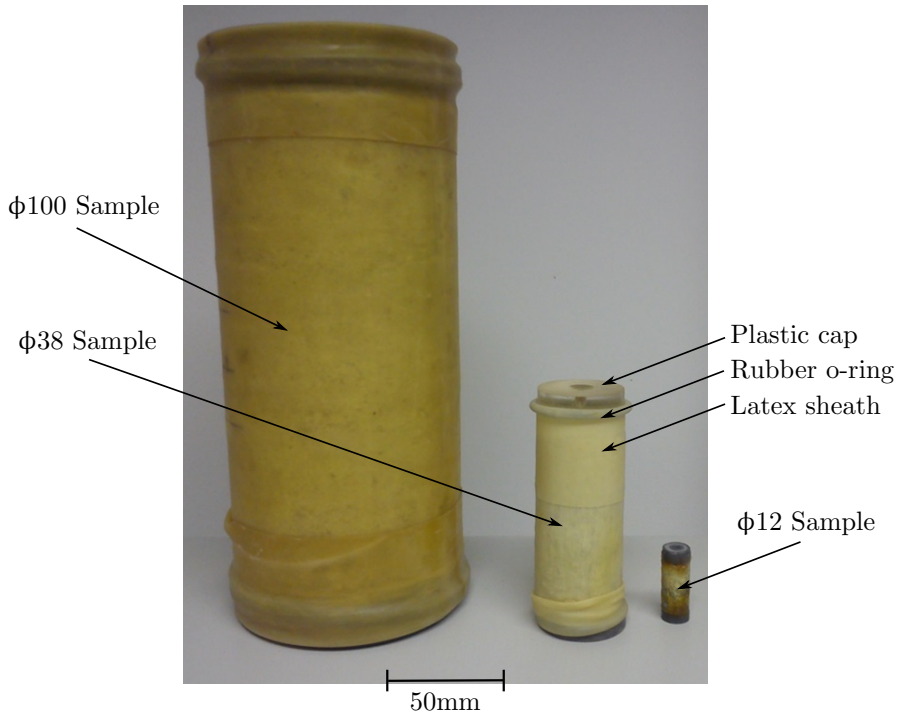

Figure 5.3: Photograph of all three sample sizes following manufacture.

5.3.4 Experimentation

All samples were scanned using the XRM410 before and after unconfined compression constant water tests. Due to the different sizes of the samples, and hence different failure loads, the unconfined compression constant water content tests were performed on two different pieces of equipment. The ϕ12 and ϕ38 samples were tested using a Lloyd LR5K Plus testing machine, with a load cell rated at 5kN±0.5%, whilst the ϕ100 samples were tested using a Wykeham Farrance Tritech 50kN machine, with a load cell rated at 50kN±1.0N. Displacement rates of 0.03mm/minute, 0.1mm/minute and 0.25mm/minute for the ϕ12, ϕ38 and ϕ100 respectively were chosen in accordance British-Standards (1990) ensuring the strain rate did not exceed 2% per minute and failure occurred within 15 minutes. Each sample was tested to failure, observed by evidence of a load peak, after which compression was stopped and the load released.

Both the pre-loading and post-loading XRCT scans involved three specific scans: a large field of view scan, to capture as much of the sample as possible; and two small field of view scans at the maximum resolution achievable for the sample size, located either side of a compaction plane to capture any differences in material structure at the top and bottom of the layers.

The results presented in Chapter 4 led to the conclusion that time should not be a driving factor in the setting of scan parameters and the quality of the image should whenever possible be the key concern. Because of this the scan parameters all strictly followed the manufacturer's guidelines for setting up the

scans and the settings were chosen to maximise the scan quality. The ϕ12 sample's large field of view scan captured the entire sample and the ϕ38 sample's large field of view scan captured the entire sample diameter but was limited by the square x-ray detector within the XRM410 to only half the sample height, centred on the middle of the sample. The large size of the ϕ100 sample and the fixed size of the detector installed in the XRM410 prevented the entire diameter of the sample being seen and the scan settings were chosen to enable the scanning of as much of the sample as possible, approximately 80mm centered on the interface between the bottom and middle compaction layers. The key XRCT scan parameters are given in Table 5.2

5.3.5 XRCT post-processing

The methods used to post-process and quantitatively analyse the XRCT scan data are discussed in detail in Chapter 3 and the analysis procedure is outlined in Figure 5.4 (a replicate of Figure 3.12). The post-processing produced void size distribution plots for the scanned regions showing the cumulative void volume as a percentage of sample volume plotted against the void volume. The key stages in the analysis process were:

- reconstruction of the data, using the XMReconstructor software provided with the scanner;
- reduction of file size, through the extraction of three subvolumes and conversion of the data from 32bit to 16bit RAW data;
- enhancement of image quality, through a guassian filter;
- identification of voids within the sample, using the watershed algorithm;
- and the production of quantitative results, displayed as a void size distribution.

Prior to the image analysis ten different randomly located small regions from each scan type were taken and operator-selected thresholding was used to identify the clear voids and solid matrix within the soil. The threshold values from these regions were averaged and used as the watershed algorithm threshold inputs, which requires only regions definitely part of a phase to be identified using the threshold values (FEI, 2013).

Table 5.2: The XRCT parameters used for the six scan procedures. LFoV indicates the large field of view scans whilst SFoV indicates the small field of view scans.

Sample	**Scan Type**	**Pixel Size (μm)**	**Field of view (mm)**	**Exposure Time (s)**	**Number of Images**	**Scan Time (hr)**
ϕ12	LFoV	12.3	25.2 x 25.2	1.5	3201	2
ϕ12	SFoV	1.0	2.0 x 2.0	40	1601	19
ϕ38	LFoV	20.2	42.4 x 42.4	4	3201	7
ϕ38	SFoV	2.1	4.2 x 4.2	40	1601	19
ϕ100	LFoV	37.8	19.1 x 19.1	12	1601	6.5
ϕ100	SFoV	7.8	79.9 x 79.9	55	1601	25.5

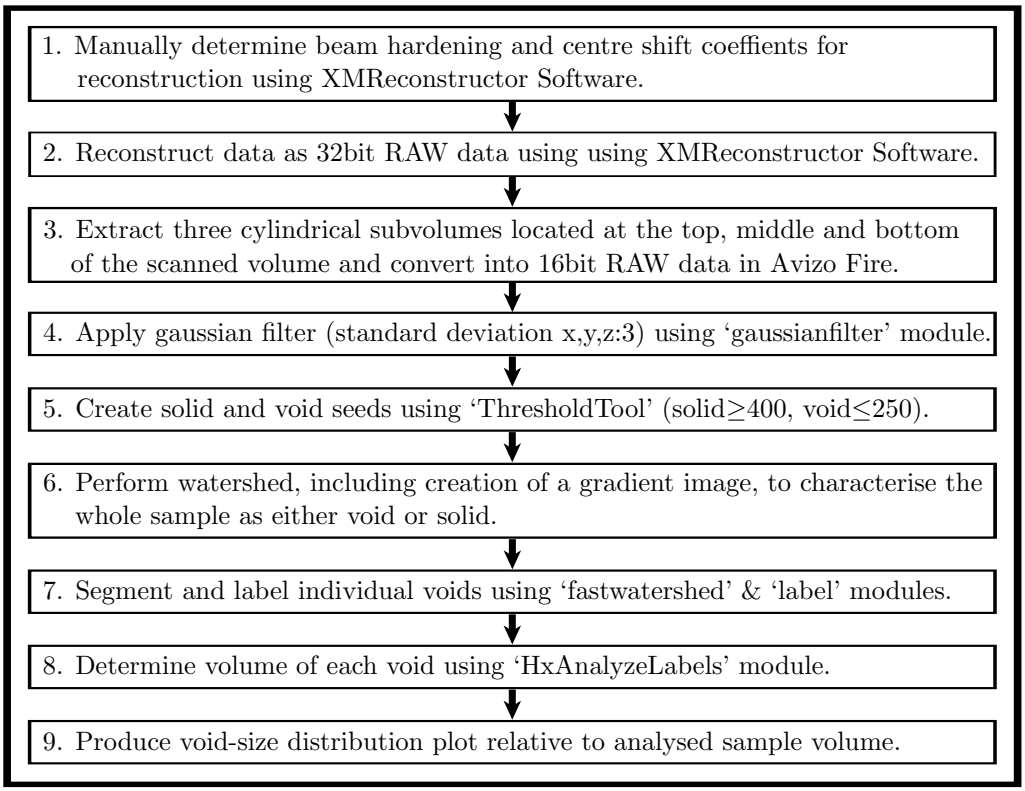

Figure 5.4: Flowchart of the Avizo Fire analysis used for XRCT data processing. (Please note this is a replication of Figure 3.12 and included here for the reader's convenience.)

5.4 Mechanical behaviour results and discussion

Table 5.3 shows the compressive strength values obtained from the unconfined compression tests for all nine samples. The ϕ12C sample was found to be a clear outlier as when included the ϕ12 samples' failure stresses had a standard deviation of 0.29MPa, which was reduced to 0.05MPa when the ϕ12C sample was disregarded. The ϕ38 and ϕ100 sample results had standard deviations of 0.07MPa and 0.05MPa respectively.

In Chapter 4 the unconfined compressive strength of the 30*:60:10[0.6] mixtures was determined as 1.55MPa for ϕ12 samples and 1.14MPa for ϕ28 samples. Comparing the 12mm diameter samples from the two investigations a clear increase in compressive strength from 1.55MPa to 2.20MPa can be seen

Table 5.3: The compressive strength and Young's Modulus values for all samples obtained from the unconfined compression constant water content tests. The entry in bracketed italics was deemed anomalous.

Sample	**Compressive Strength (MPa)**			**Youngs Modulus (MPa)**		
	A	**B**	**C**	**A**	**B**	**C**
ϕ12	2.25	2.15	(*2.80*)	97.7	102.5	(*106.6*)
ϕ38	1.84	1.68	1.82	95.9	102.0	99.5
ϕ100	0.45	0.58	0.49	103.5	130.4	88.0

between the samples tested in Chapter 4 to the samples tested here. The manufacturing process, particle grading and testing procedures were the same in both investigations and therefore the only difference between the two samples was the change from Birtley clay used in Chapter 4 to the speswhite clay used in the manufacture of the samples for this investigation. The difference in size between the ϕ38 samples from this investigation and the ϕ28 samples from Chapter 4 makes comparison more difficult. However a 2:1 height:diameter ratio was maintained, both samples contained two layers of compacted SBCM and they were tested using the same unconfined compression constant water content test procedures. Therefore, as with the ϕ12 samples from both investigations, the key difference in the samples was the clay used, and again it can be seen that the samples manufactured using Birtley clay had a lower average compressive strength of 1.14MPa than the speswhite samples which had an average unconfined compressive strength of 1.78MPa.

The effect of using different clay within SBCMs on their mechanical properties was not a primary investigative aim of this research however this result can still be briefly commented upon. Both the Birtley and speswhite clays are primarily kaolinite in mineralogy and it is therefore suggested that the difference in compressive strength is due to the different quantities of silt fraction within the two SBCM mixes. Whilst both mixtures contained a 30% silty-clay fraction, the speswhite clay used in this investigation contained 100% kaolinite clay and the Birtley clay contained approximately 50% silt and 50% kaolinite clay. The presence of the silt in the Birtley clay will have reduced the percentage of clay material to approximately 15% of the solid constituents and, since suction is predominately generated within the clay fraction at low degrees of saturation, less strength from the clay binder will be developed within the SBCM containing Birtley clay. Additionally had the silt and clay fractions been quantified separately when designing the SBCM mixtures, as allowed for in the soil mixture classification method proposed by Smith and Augarde (2013a), the differences in the two SBCM mixes used here and in Chapter 4 would have been more apparent.

Figure 5.5 shows the compressive stress and vertical compressive strain results obtained from the unconfined compression constant water tests. All eight samples show clear brittle failure, supporting the observation by Miccoli et al. (2014) and agreeing with the results from Chapter 4. The individual values of Young's Modulus, calculated using the average gradient of the stress-strain curve after the initial period of bedding-in, are presented in Table 5.3 for each sample and the average values are 102.3MPa, 99.2MPa and 107.3MPa for the ϕ12, ϕ38 and ϕ100 samples respectively, showing that the results obtained for the three sample sizes are similar. An increase in compressive strength as the sample size decreases however is evident from both Figure 5.5 and Table 5.3.

The aspect ratio of all three cylindrical sample sizes was maintained at 2:1 ensuring that geometrical differences in shape did not affect the results obtained. However one significant difference in the manu-

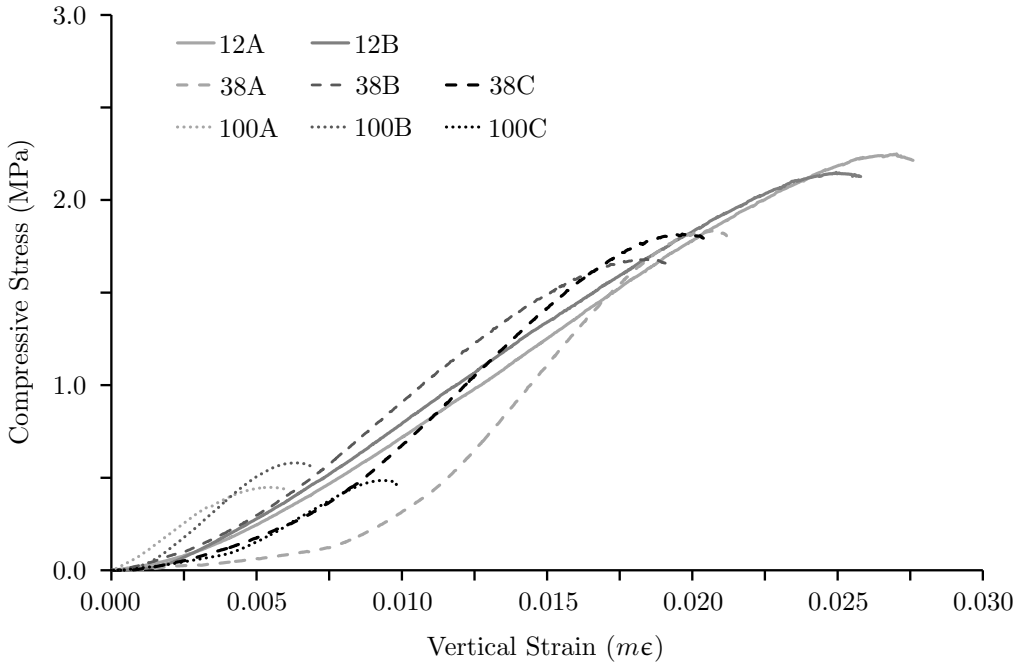

Figure 5.5: Compressive Stress and vertical compressive strain results for all three sample sizes following the unconfined compression constant water content tests.

facture of the ϕ100 samples was the use of three compaction layers rather than the two layers used to manufacture the ϕ12 and ϕ38 samples. This additional compaction layer was included to reduce the depth of each layer and thus the heterogeneity of the individual layers however the three compaction layers will have introduced an additional layer interface and plane of weakness into the sample that may have resulted in the lower compressive strengths obtained. More research is required into the effect of additional layers within samples, whether failure occurs in both layers simultaneously or predominately focussed around a single layer interface and how this alters the compressive strength of SBCMs.

The total suction values obtained from the Filter Paper tests for the ϕ12, ϕ38 and ϕ100 samples were 8.51±0.37MPa, 8.76±0.07MPa and 8.04±0.25MPa respectively. These are of the same magnitude as those measured by Jaquin et al. (2008) for similar SBCMs and the difference can be attributed to the different clay material and mix composition used in this investigation. The filter paper method is an indirect method of suction measurement, rather than the tensiometers used by Jaquin et al. (2008) which provide a direct measurement of matric suction during testing of individual samples. Therefore the suction values presented above are an average of the three tests performed for each sample size.

The only remaining difference between the three samples is the sieving of the largest particles from some of the mixes. As with the two sample sizes discussed in Chapter 4 the compressive strength of the samples has increased following the removal of the gravel fraction. The effect of the removal of gravel fraction on the internal structure of the SBCMs and how this may alter the compressive strength of the

samples is therefore examined in detail in Section 5.5.

The development of suction within unsaturated soils is discussed in detail in Chapter 2 and, at the low water contents found in SBCMs, the water will only be present in the smallest voids between the clay and sand particles. The clay and sand fractions within all three sample sizes are unaltered, in terms of relative proportion (1 part clay to 2 parts sand) and mineralogy (the speswhite clay is 100% kaolinite), which may explain the similarity in total suction values for all three sample sizes. As the water is only present in the smallest voids within the sample when the SBCM has dried the smaller voids within the sample, formed between sand and clay particles, will be the voids which most control the capillary and adsorptive suction terms and therefore the suction values measured will be largely unchanged by the removal of the gravel fraction. The decrease in compressive strength with the addition of gravel particles, despite similar measured total suction values, may therefore suggest that the gravel reduces the strength of the SBCM by introducing initial points of weakness, i.e. cracks and large voids, into the compacted clay-sand mixture which would have achieved higher compressive strengths if the gravel particles were not present, as shown by the ϕ12 samples.

These compressive strength results clearly show the dangers in only testing small samples when investigating SBCMs, particularly if sieving is performed to remove the largest particles prior to manufacture. More work is required into the feasibility of small scale testing for materials which contain a broad range of particle sizes and particular attention needs to be paid to the most appropriate way scale both layer depth, to control homogeneity of density following compaction, and number of layers, to prevent the addition of too many layer interfaces.

5.5 Material structure results and discussion

Void size distributions were successfully obtained for all large field of view XRCT scans performed, and the small field of view scans for the ϕ12 and ϕ38 samples. It was not possible to obtain void size distribution plots from the small field of view scans for the ϕ100 samples as the automated analysis employed was unable to identify individual voids within the sample. This was despite the source operating at the highest power settings, the maximum exposure time being used to obtained images and the pixel size being doubled in order to ensure sufficient x-rays were detected for an image to be captured. It suggests that the ϕ100 samples were too large for the small field of view scans to be performed. The void size distributions for the ϕ12 samples are shown in Figures 5.6 and 5.7 and the void size distributions for the ϕ38 samples are shown in Figures 5.8, 5.9 and 5.10. The ϕ100 large field of view void size distributions for all three samples are shown in Figure 5.11. All the figures show the void size distribution before and after compressive loading and, where necessary, the small field of view results for the bottom of compaction layer and top of compaction layer are differentiated using 'BoL' and 'ToL' respectively and

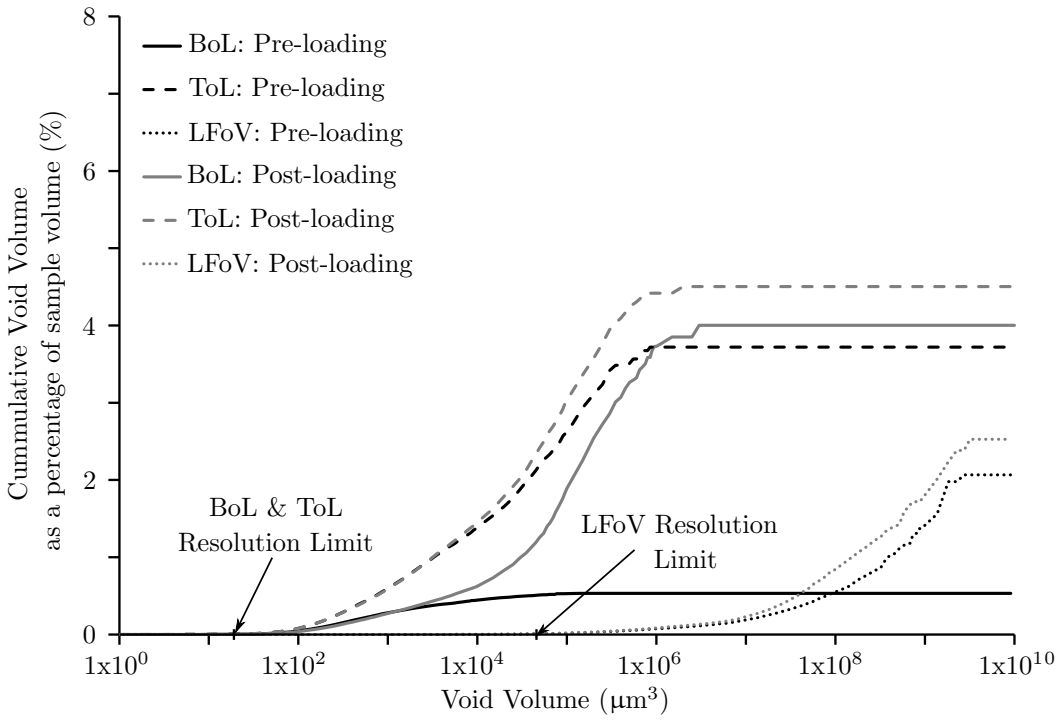

Figure 5.6: Void size distribution plot for the ϕ12A sample.

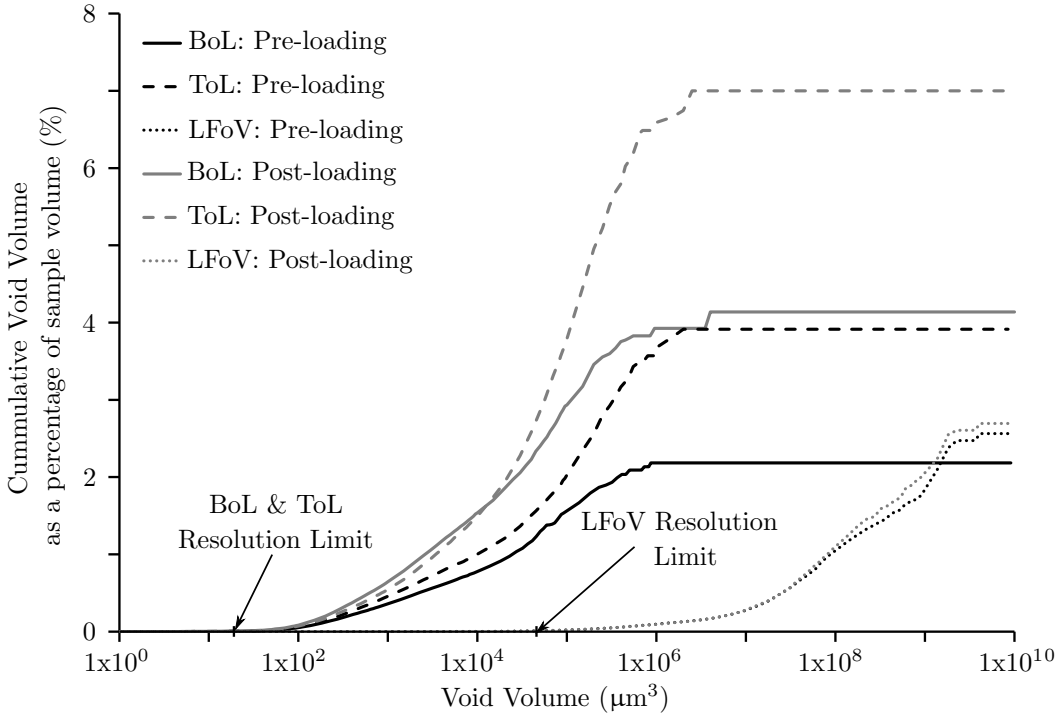

Figure 5.7: Void size distribution plot for the ϕ12B sample.

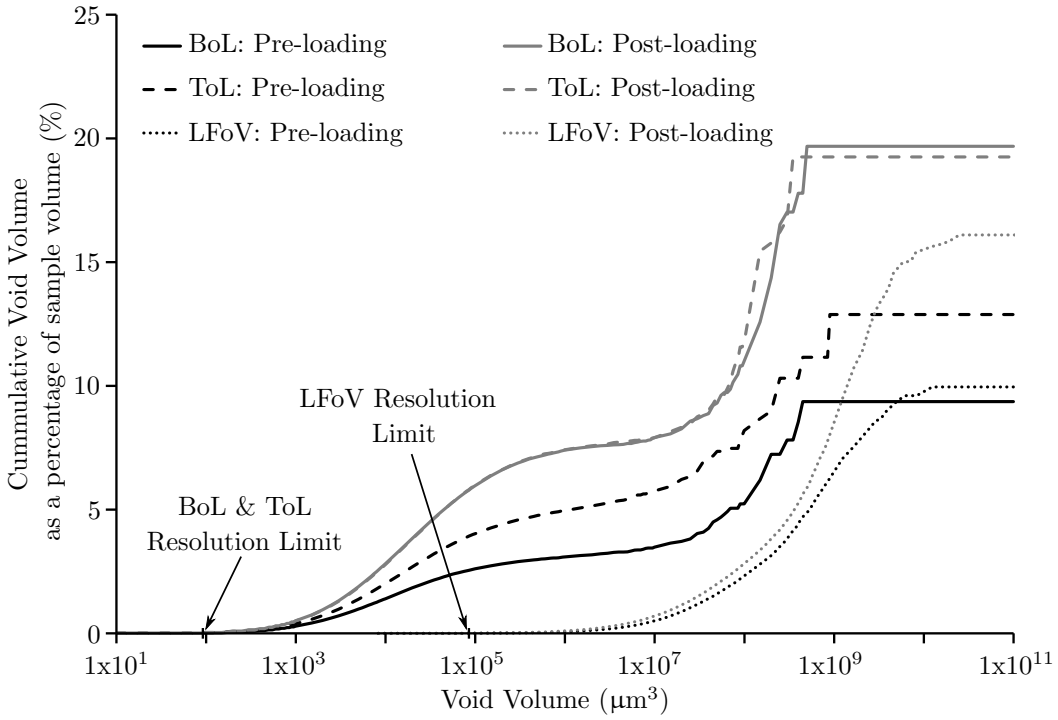

Figure 5.8: Void size distribution plot for the ϕ38A sample.

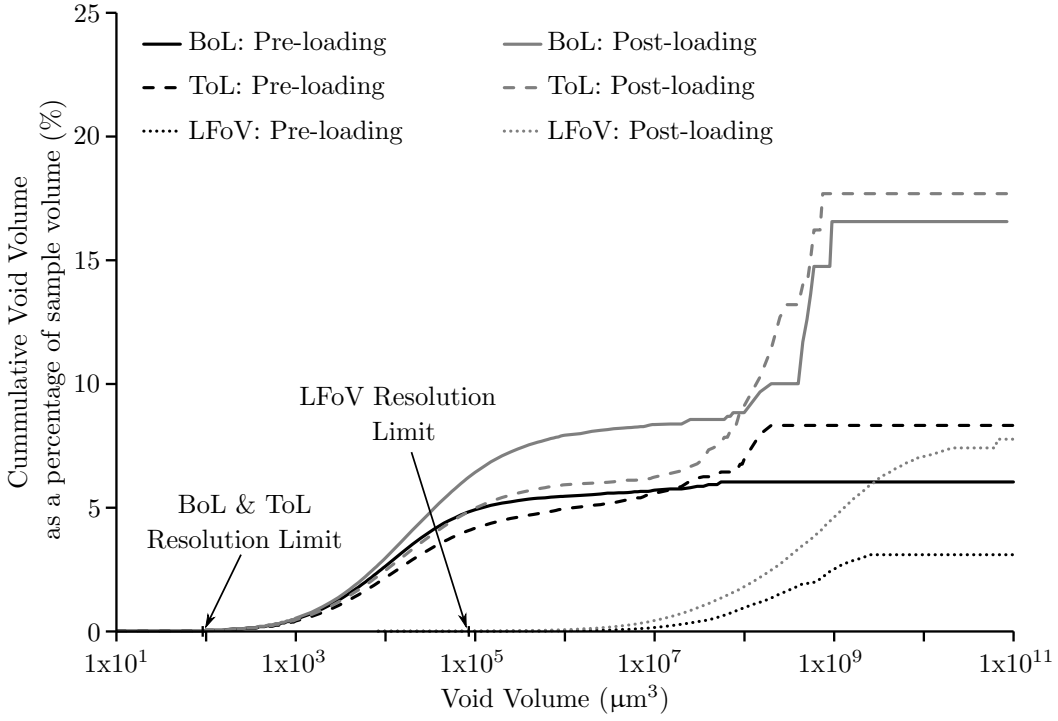

Figure 5.9: Void size distribution plot for the ϕ38B sample.

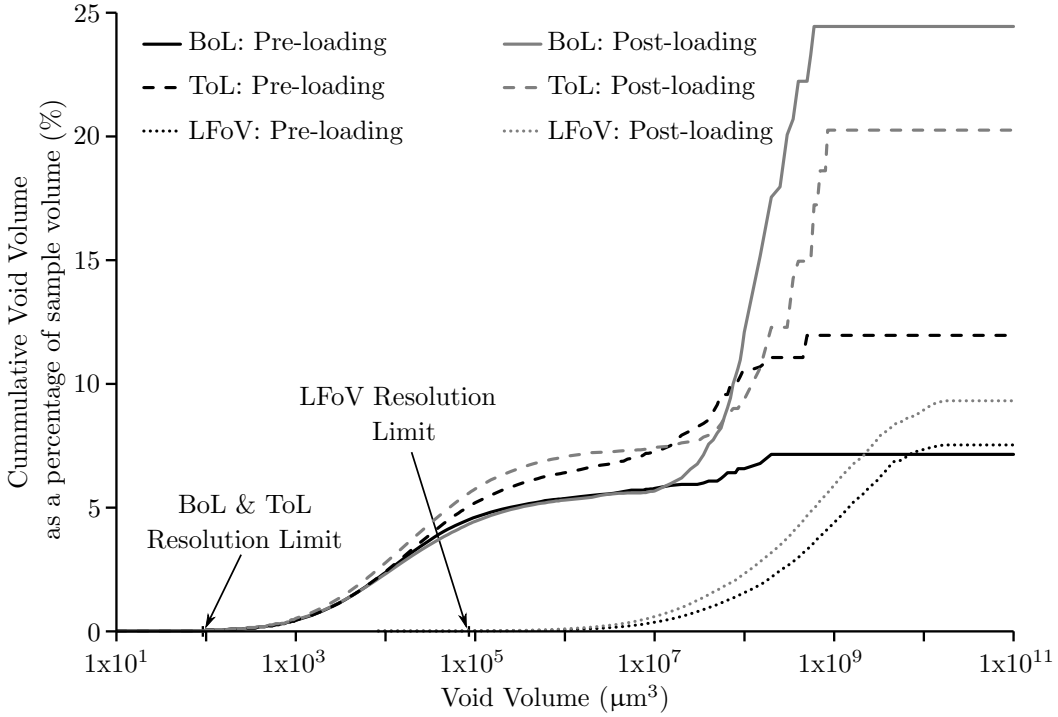

Figure 5.10: Void size distribution plot for the ϕ38C sample.

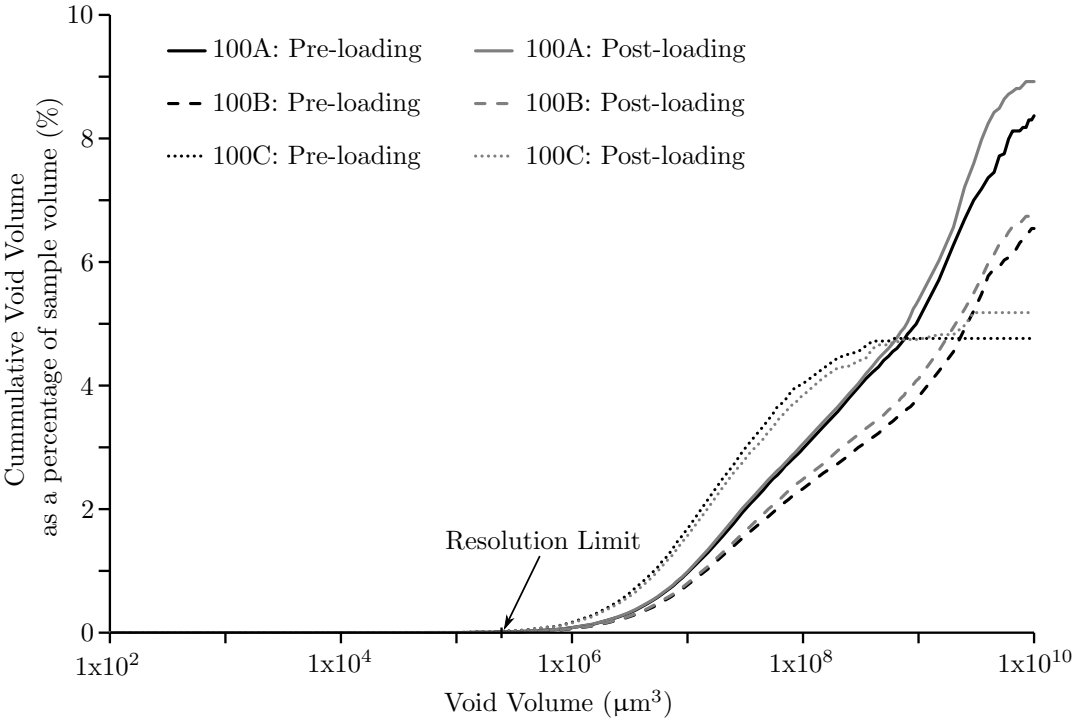

Figure 5.11: Void size distribution plot obtained from the large field of view scans for all three ϕ100 samples.

the large field of view results are described as 'LFoV'.

It is clear that the void size distribution plots used in this thesis differ considerably in form to those commonly presented when void sizes are explored using mercury intrusion porosimetry (MIP). A typical void size distributions from MIP data plots the volume of intruded mercury against the void entrance diameter and it is then it is assumed that a smaller void entrance diameter represents a smaller void volume. In contrast to this, Figures 5.6 to 5.11 plot on the y-axis the cumulative void volume of all voids smaller than and equal to a given void volume, shown on the x-axis, as a percentage of the total sample volume. These plots can therefore be interpreted in a similar way to particle size distribution plots which plot on the y-axis the cumulative mass of all particles which are smaller than a given particle diameter, shown on the x-axis, as a percentage of the total sample mass. The plotting and discussion of void volumes, rather than void entrance diameters, is possible since the post-processing of the XRCT scan data (outlined in Figure 5.4) identified the volume of each void within the sample directly. For MIP data either one or two peaks (for a monomodal void structure and a bimodal pore structure respectively) will be evident which coincide with the most abundant void entrance diameter within the sample and its is assumed that these peaks indicate that a particular void volume within the sample abounds. In the case of the XRCT obtained void size distributions the gradient of the curve at a particular void volume can be used as an indication of the number of voids of that volume within the sample, i.e. a steep region within the curve shows there are a high number of voids of that volume and can be interpreted in a similar way to a peak in MIP data whilst a flat region within the void size distribution curve suggests there are no voids of the given volume within the sample.

All eighteen pre-loading:post-loading pairs of void size distributions show a clear increase in void volume following compressive loading. The increase in void size is more pronounced in the larger void volumes and large field of view scans and this is discussed in Section 5.5.2. The small field of view results are discussed first and they provide valuable insights into the initial void structure of SBCMs and provide a fundamental basis upon which mechanical behaviour is explained.

5.5.1 Observations from the small field of view scan results

For all five samples in which small field of view scans were obtained it is clear that before unconfined compression the regions scanned at the bottom of the compaction layer contained a smaller void fraction than the top of the compaction layer region. This builds upon the work described in Beckett et al. (2013) which shows that the material structure can vary through the depth of a layer although the results presented in Beckett et al. (2013) suggest that only single-layer specimens display a highly heterogeneous material structure and double-layer compacted specimens achieve a largely homogenous material. The results from the investigation described in this chapter however clearly show that double-layer samples

can also exhibit material heterogeneity and, since the ϕ12 and ϕ38 samples used in this investigation followed the same preparation technique as used by Beckett et al. (2013), differences in manufacturing procedure cannot account for the material heterogeneity of the samples investigated here.

It is however possible that difference in XRCT scanning and post-processing techniques used could have resulted in the difference in void structure between the top and bottom of compacted layers being observed in this investigation which were not captured in the work presented in Beckett et al. (2013). The XRCT scans described by Beckett et al. (2013) were performed at a pixel size of 11μm and a minimum pore area of 3x3 pixels which limited the minimum void area identified within the scans to $33\mu m^2$. Only one in every ten slices was analysed in the vertical plane limiting the overall volumetric resolution to approximately $330\mu m^3$. In the XRCT scans performed in this chapter however the highest resolution of the small field of view scans is $20\mu m^3$ and it is therefore suggested that the differences in the image-analysis technique employed, and the improved final resolution, had a considerable part to play in the observation of heterogeneity in the material structure of the samples used in this investigation.

The ϕ12 and ϕ38 sample small field of view scans, performed at the smallest voxel sizes possible for the sample size, provide an insight into the smallest observable voids within the SBCM samples using XRCT scanning. The steep gradient of the curve below $1x10^6\mu m^3$ in the void size distribution curves of the ϕ12 samples, and the flat line visible for voids above this void volume, as shown in Figures 5.6 and 5.7, indicates that the voids within the ϕ12 samples are predominately less than $1x10^6\mu m^3$ in volume. The void size distribution curves for the ϕ38 samples however, shown in Figures 5.8, 5.9 and 5.10, show two clear regions where voids exist (the steep parts of the curve below $1x10^6\mu m^3$ and between $1x10^7\mu m^3$ and $1x10^9\mu m^3$), separated by a plateau between $1x10^6\mu m^3$ and $1x10^7\mu m^3$ and followed by a flat line visible for voids above $1x10^9\mu m^3$. This suggests therefore that the ϕ38 samples contain voids smaller than $1x10^6\mu m^3$ and a second group of voids ranging in volume between $1x10^7\mu m^3$ and $1x10^9\mu m^3$.

Because all the scans were analysed using the same image processing techniques the lack of voids in the small field of view ϕ12 scans is not due to image processing, since voids with volumes larger than $1x10^6\mu m^3$ can be seen in other void size distributions, and can be taken as a true representation of the material structure. The lower limit of the set of voids smaller than $1x10^6\mu m^3$ however cannot be determined, despite the apparent flattening of the void size distribution curves at $2x10^2\mu m^3$, as the resolution of the small field of view scans is limited to $20\mu m^3$. The visible plateau between $1x10^6\mu m^3$ and $1x10^7\mu m^3$, for all twelve small field of view ϕ38 scans, are not all perfectly flat or between identical void volumes which suggests the observed plateau is not a result of the image processing but from the SBCM structure and minimal voids between these volumes exist within the ϕ38 scans.

The ϕ12 samples can be considered as the soil matrix material found in SBCMs (Beckett et al., 2013), as they contained only clay and sand fractions, and the small field of view scans were centred on regions

within a layer. The voids smaller than $1x10^6\mu m^3$, identified in both the $\phi12$ and $\phi38$ samples, are therefore likely to be the intra-aggregate voids found within the assemblages of clay and sand forming the binder matrix within the broader SBCM structure.

The addition of the 2-5mm gravel particles has clearly introduced a second range of void sizes, between $1x10^7\mu m^3$ and $1x10^9\mu m^3$, within the internal structure of the $\phi38$ samples. It is suggested that these voids are inter-aggregate voids which have formed between the larger aggregates now present within the mixture. As discussed in Chapter 2, a double void structure within unsaturated soil mechanics has been well documented however this has predominately focussed on clay-sand mixtures in which the intra-aggregate voids have been identified between clay particles and are therefore far smaller than the resolution of the XRCT scans performed in this investigation. As such the two sets of void volumes identified in this chapter in the $\phi38$ samples, below $1x10^6\mu m^3$ and between $1x10^7\mu m^3$ and $1x10^9\mu m^3$, are all still part of the SBCM macrostructure and a series of intra-elemental voids will also exist, undetectable using current XRCT techniques, between small groups of clay particles and will form the SBCM microstructure.

The lack of small field of view scans for the $\phi100$ samples means it is not possible to observe this double void size macrostructure, or the changes that occur within it, however it is suggested that a similar void size distribution to the $\phi38$ samples would be observed, whereby small voids, less than $1x10^6\mu m^3$, exist within the intra-aggregate matrix and the inter-aggregate voids are then observed between $1x10^7\mu m^3$ and $1x10^9\mu m^3$ forming around the gravel particles.

5.5.2 Observations from the large field of view scan results

The large field of view scans, performed at a considerably larger voxel size, are unable to capture any voids smaller than $8x10^4\mu m^3$ within the sample and do not capture many voids smaller than $1x10^5\mu m^3$. This can both explain why the majority of the small field of view scans show more voids within the sample and why the double void macrostructure is not observed in the $\phi38$ and $\phi100$ large field of view scans. This however does not prevent the large field of view results providing valuable insights.

The increasing void size distribution curve above $1x10^6\mu m^3$, for the $\phi12$ samples large field of view scans, indicates that between 2% and 3% of the total sample volume is voids with volumes greater than $1x10^6\mu m^3$. This is in contrast to the small field of view scans which show no voids larger than $1x10^6\mu m^3$ in volume. Figure 5.12 shows the number of voids plotted with respect to depth through the $\phi12$ large field of view scans and it is clear that the number of voids increases between 40% and 60% sample depth. The $\phi12$ samples were manufactured using two layers of SBCM causing the transition between the two compaction layers to occur at 50% sample depth. It is therefore suggested that larger voids identified within the large field of view scans are located within the sample at the interface between the two layers but not within the clay-sand matrix formed inside an individual layer which is scanned in the small field of view scans. Interestingly there is a much smaller increase in the large voids detected within the $\phi12$

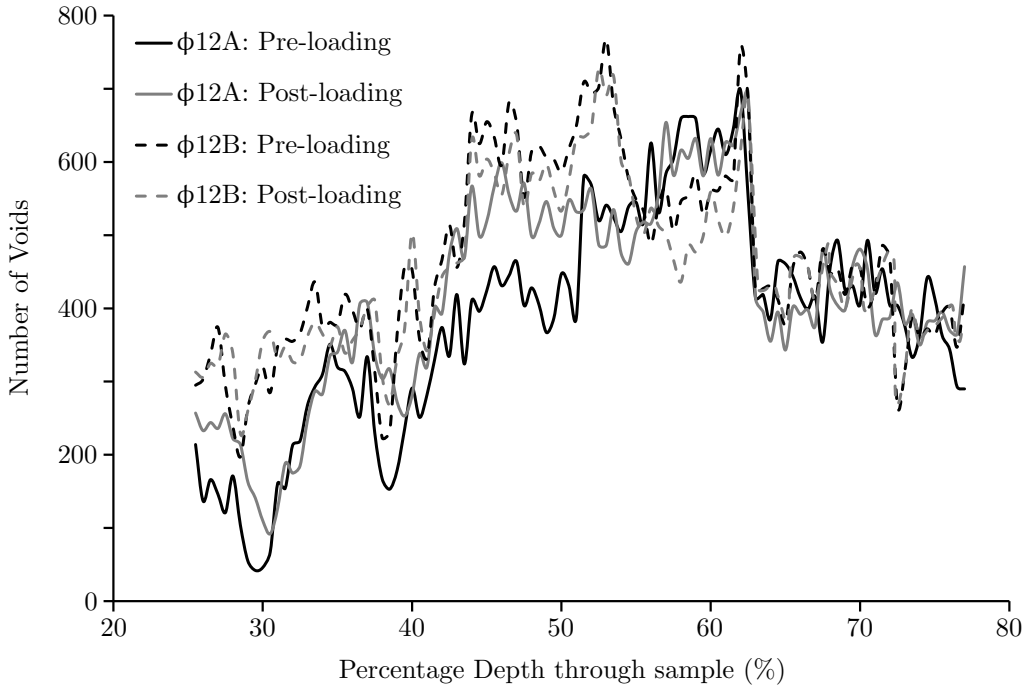

Figure 5.12: A plot of the number of voids against the percentage depth through the sample for all four large field of view ϕ12 scans.

large field of view scans than in the smaller voids within the clay/sand binder matrix and this suggests that, at least for the ϕ12 samples in which only binder material is present, failure occurs within the binder and not at a layer interface.

The ϕ38 and ϕ100 large field of view scans show the largest change in void volume following compressive loading occurs within the largest voids, supporting the findings in Chapter 4, and this suggests that the change in internal structure during loading predominately occurs in the large voids and pre-existing flaws within the SBCM. Figure 5.13 shows the change in void volume for the ϕ38 and ϕ100 large field of view scans following the unconfined compression tests. Two observations can be drawn from these results.

Firstly the ϕ100 samples show a smaller increase in voids following the unconfined compression tests than the ϕ38 samples. It is however possible that the lack of evolution in the ϕ100 samples' macrostructure is due to the scanning of only one region within the ϕ100 samples. A limitation of only scanning one region around the bottom compaction layer interface means that significant macrostructure changes could have occurred around the upper compaction layer interface which would not have been captured during the XRCT scans and, if no major structural changes occurred at the bottom compaction layer interface, only a minimal increase in voids would be observed. In the ϕ38 samples however, since only one compaction layer interface was present within the sample which was at the centre of the region scanned using XRCT, any macrostructural changes which occurred during compression testing of the ϕ38 samples

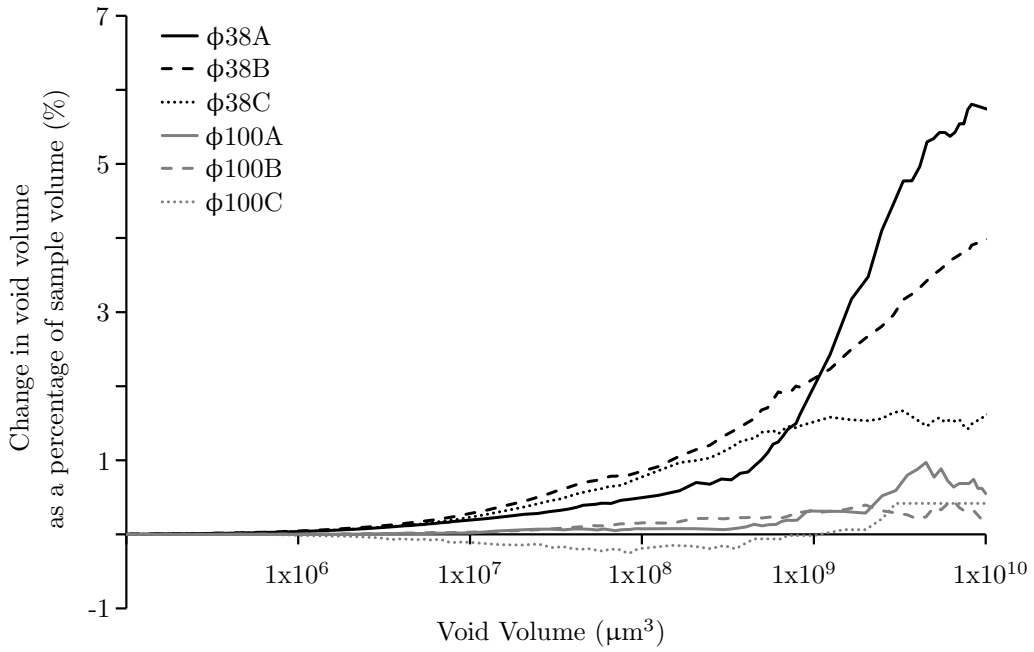

Figure 5.13: The increase in voids following unconfined compression testing for all ϕ38 and ϕ100 large field of view scans.

should have been captured.

Secondly, both the ϕ38 and ϕ100 samples show a variation in the increase in void volume across the set of three samples. The reasons for this are not clear however some variation may have been introduced during the transferring of the samples from the unconfined compression testing apparatus to the XRCT scanner which could have affected the sample structure. The inability to scan the samples during the unconfined compression testing is therefore clearly a shortcoming of this study and being able to apply load to the samples within the XRCT scanner may have helped reduce the variability in the post-failure loading conditions. However, as discussed in Chapter 3, using load cells placed within XRCT scanners can introduce other difficulties including maintaining a constant load during longer scans and the need to use smaller samples to fit within a load cell.

It is therefore difficult to draw firm comparisons between the changes in the largest voids within the ϕ38 and ϕ100 samples, as variability may have been introduced during the transfer of samples to the scanner and not all the macrostructural changes will have been captured within the ϕ100 samples. However all six samples, the three ϕ38 samples and three ϕ100 samples, do show the same trend that the change in void volume increases with void size and this therefore suggests that these large voids are most altered during compressive loading of SBCMs.

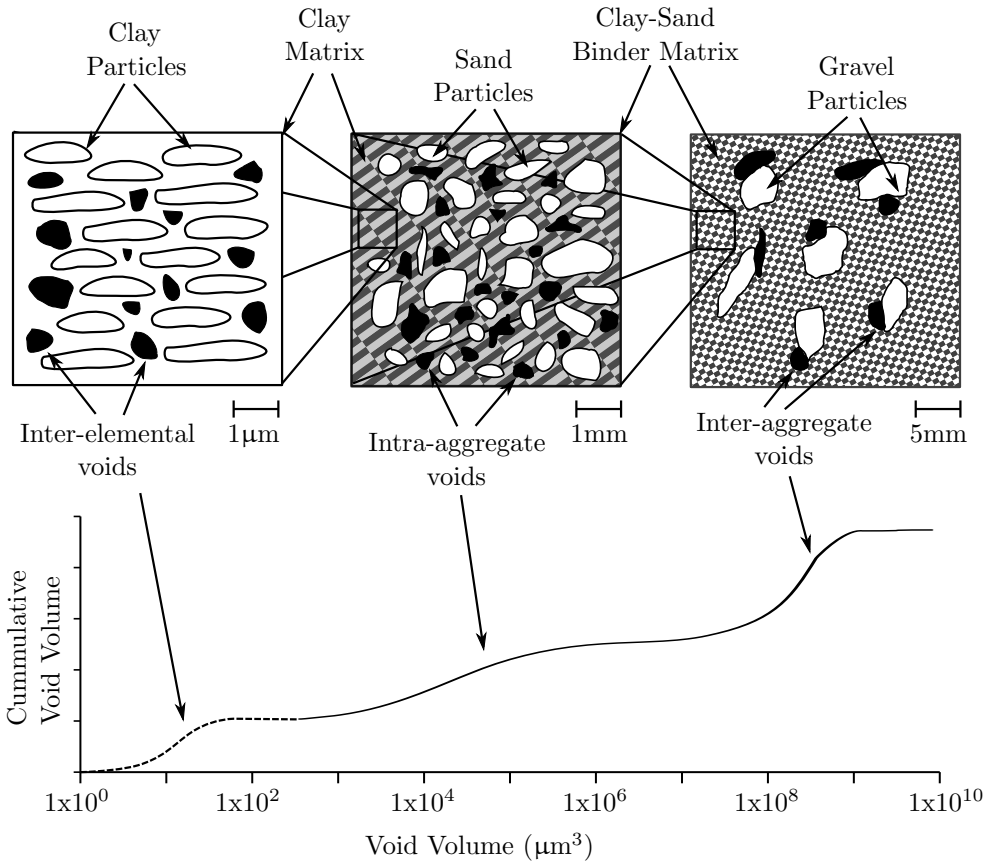

Figure 5.14: A sketch of the proposed SBCM internal structure.

5.6 Links between material structure and compressive strength

The void size distribution results obtained and presented in Section 5.5 show that a double void size macrostructure exists within the SBCM samples because of the inter-aggregate voids linked to the presence of large gravel particles and intra-aggregate voids which exist within the clay-sand binder matrix. Current unsaturated soil theory also suggests that a range of smaller voids exists between clay particles, which are too small to be detected using laboratory XRCT techniques, and these inter-elemental voids form a third range of voids within the internal structure of SBCMs.

Based on these findings Figure 5.14 illustrates a proposed internal structure of SBCM samples, using both the results from the small field of view $\phi 38$ samples to describe the intra-aggregate and inter-aggregate voids and the assumed existence of inter-elemental voids between the clay particles which remained undetected in this investigation. This double void size macrostructure coupled with the third range of smaller inter-elemental voids is key to explaining the compressive strength results described in Section 5.4 and can also help form a basic understanding of the fundamental roles of each constituent material within the SBCM mix.

The similar total suction values obtained for all three sample sizes, discussed in Section 5.4, and the

similarity in the void size distributions in the voids smaller than $1x10^6\mu m^3$ for the ϕ12 and ϕ38 samples, discussed in Section 5.5.1, suggest that it is within the clay-sand matrix that suction is developed within the SBCM. Since suction is a key source of strength it is clear that changing the clay type used, as between Chapter 4 and this investigation, affects the suction developed and hence affects the compressive strength. Studying the intra-aggregate voids below $1x10^6\mu m^3$ in different clays will undoubtedly provide an interesting insight into the role of clay within SBCMs. However the results from this investigation also show that, despite similar total suctions being developed within the samples and similar void sizes existing below $1x10^6\mu m^3$, the clay is not the only factor influencing compressive strength.

The reduction in compressive strength as larger particles are introduced to the SBCM mixture, discussed in Section 5.4, and the largest change in void sizes being observed in the inter-aggregate voids greater the $1x10^7\mu m^3$, as discussed in Section 5.5.2, suggest that the gravel fraction within the SBCM has a large influence on the compressive strength. The ϕ12 samples show that failure of the clay-sand binder matrix occurs within the voids smaller than $1x10^6\mu m^3$ at approximately 1.55MPa and it is possible to assume that the clay-sand matrix within the larger samples would also fail in a similar way and has a similar compressive strength. The introduction of the gravel particles to the SBCM, and the resultant presence of inter-aggregate voids within the structure, however results in a reduced strength and it is suggested that this is because the larger voids introduce points of weakness from which cracks can propagate. The results from Chapter 4 show that cracks propagate away from the gravel particles within the SBCM and through the clay-sand matrix. Coupled with the knowledge that the gravel particles introduce larger voids within the sample, it suggests that gravel lowers the compressive strength of SBCM samples.

The triple-structure of voids suggested here has not been identified before in SBCMs. Unfortunately the trend towards XRCT investigations focussing on idealised, narrowly graded materials and the relative infancy of investigating the internal structure of SBCMs means there exists no data set to which these results can be compared. It is hoped therefore that these findings will provoke an interesting discussion into the internal structure of unsaturated soil mixtures.

5.7 Discussion on optimum sample size

The results obtained for the three different sample sizes have provided valuable insight into both compressive strength of SBCMs during unconfined compression tests and the internal structure of the material. It is also possible to also use the results obtained, and additional insights into the final resolution of the XRCT following analysis, to determine whether an optimum sample size exists which should be used more widely in the XRCT scanning of SBCMs. The ϕ12, ϕ38 and ϕ100 sample sizes are therefore now compared using three factors: image resolution, mechanical behaviour and material structure.

5.7.1 Image resolution

Table 5.4 shows the theoretical and measured smallest void dimensions obtained from the successful image processing of the XRCT data. This smallest void dimension can be taken as the true resolution of the XRCT results as it is a measure of the smallest identifiable feature following the scanning and image processing of the sample. The ϕ12 samples achieved the highest resolution for both the large field of view and small field of view scans, followed by the ϕ38 and ϕ100 samples. This is clearly the expected result since the initial scanned voxel size was smallest for the ϕ12 samples and largest for the ϕ100 samples. This result however does not necessarily mean that the ϕ12 samples are the best sample size to scan from either material behaviour or XRCT imaging perspectives.

The small field of view scans and image processing produced a resolution of 2.7μm for the ϕ12 and 4.6μm for the ϕ38 which in turn will have limited the smallest void volume identifiable to 19.7μm^3 and 97.4μm^3 respectively. This initially sounds like a dramatic difference in resolution, since the ϕ12 scans were able to identify voids one fifth of the size of the ϕ38 samples, however it is important to consider the void size distribution results obtained to fully understand these values. The voids in the ϕ12 samples smaller than 100μm^3 accounted for less than 0.09% of the total sample volume in each of the small field of view scans. This therefore means that if the ϕ12 samples had been scanned using the settings for the ϕ38 samples, at a 2.2μm pixel size, in the worst case of the ϕ12B bottom of layer pre-loading scan only 4% of the total volume of voids detected would not have been captured. Additionally it is clear that the largest changes in void volume following unconfined compression occurs within the largest voids in the sample and these would be equally successfully identified using the increased pixel size.

The XRM410 was unable to provide images of sufficient quality from the small field of view ϕ100 scans for the image processing to be performed. Without the small field of view scans it would have been impossible to discuss the void structure of the SBCM below 1x10$^6\mu m^3$ and the possible existence of the double void size macrostructure which was exhibited by the ϕ38 samples. Because of this it is suggested that the ϕ100 samples are too big for XRCT scanning to the highest resolution but still have a use when the features of interest are large enabling larger voxel size scans to be used.

Table 5.4: The theoretical and measured smallest void dimension achieved following post processing of all XRCT scans.

XRCT Scan	**Smallest Void Dimension (μm)**	
	Theoretical	**Measured**
ϕ12: Small field of view	1.0	2.7
ϕ12: Large field of view	12.3	35.7
ϕ38: Small field of view	2.2	4.6
ϕ38: Large field of view	20.3	43.5
ϕ100: Small field of view	7.9	No data
ϕ100: Large field of view	37.1	63.0

5.7.2 Mechanical behaviour

Figure 5.5 and the discussion in Section 5.4 clearly show that the change in sample size, and the required removal of the largest particles prior to manufacture, has had a significant impact on the mechanical response of the SBCM as it undergoes unconfined compressive strength tests. It can be assumed that the ϕ100 samples are the best representation of the mechanical response of SBCMs onsite, since no sieving was required prior to manufacture resulting in an internal structure most representative of on-site conditions. In comparison to this both the ϕ12 and ϕ38 samples overestimate the compressive strength, the ϕ38 to a lesser degree. However the number of layers in the sample is also likely to affect a sample's compressive strength and it could be possible to compact the ϕ38 samples with an additional layer, reducing the heterogeneity of the sample and potentially making the ϕ38 sample better match the ϕ100 sample compressive strength. Additionally the triaxial testing of 38mm diameter specimens is common practice within geotechnical laboratories, particularly when compared to 12mm diameter samples, and therefore any results obtained should be more comparable with other work and easier to perform using existing techniques and equipment.

5.7.3 Material structure

As discussed in Section 5.5 the ϕ38 samples small field of view scans show a double-structure within the void size distribution which is not visible within the ϕ12 samples due to removal of particles larger than 2mm. It is suggested that this double void structure also exists within the ϕ100 samples however the inability of the XRM410 to perform small field of view scans on the ϕ100 samples prevents this being further explored. This means that in order to fully examine the internal structure of SBCMs, capturing both the voids from within the sand-clay matrix and the larger voids present due to the gravel particles and larger aggregations, only the ϕ38 samples are suitable.

The void size distributions from the ϕ12 small field of view samples suggest that if it is only the void structure within the intra-aggregate sand-clay matrix that is of interest, and the links between this and the suction developed within the sample, then the ϕ12 can provide insights. However if the full void size distribution, including the inter-aggregate voids, needs examining, the ϕ12 samples do not capture this and the ϕ38 samples should be used instead.

Because the small field of view scans were located above and below the compaction layer, in order to examine the void size distribution at the top and bottom of layers, the compaction layer itself was not scanned and therefore any changes occurring at the layer interface was not captured. The large field of view scan however captures the entire sample including the compaction layer and therefore may be better suited for scanning samples during any mechanical testing as the chances of scanning the region in which failure occurs is greatly increased.

5.8 Summary and conclusions

Unconfined compression constant water content tests have been performed on three different SBCM sample sizes, ϕ12, ϕ38 and ϕ100, and void size distributions determined before and after testing using XRCT scanning and quantitative image processing. Two main conclusions have been drawn from the results: a new internal void structure for SBCM samples has been proposed and linked to the role of each void range within the compressive strength response of the samples; and it appears that standard small triaxial samples are well suited for investigating SBCMs using XRCT.

The small field of view scans performed on the ϕ38 samples, coupled with the double void structure of clay discussed in Chapter 2, has shown three distinct void volume ranges exist within the SBCM structure and is sketched in Figure 5.14. Firstly inter-elemental voids exist between individual clay particles which are smaller than $1x10^2\mu m^3$ and form the microstructure of the sample. The limits on the achievable XRCT resolution however meant these voids were too small to be identified in this investigation and not discussed in detail. Secondly intra-aggregate voids, with void volumes less than $1x10^6\mu m^3$, exist within the clay-sand binder matrix and were identified in both the ϕ12 and ϕ38 samples. Thirdly inter-aggregate voids exist, with void volumes between $1x10^7\mu m^3$ and $1x10^9\mu m^3$, formed due to the presence of the larger gravel particles within the SBCM and, coupled with the intra-aggregate voids, form the macrostructure of the SBCM investigated using XRCT. It is suggested that the inter-elemental and intra-aggregate voids affect the suction developed within the sample and are responsible for the strength of the clay-sand binder matrix and the elastic behaviour of the SBCM prior to compressive failure whilst the inter-aggregate voids affect the compressive strength of the samples since the addition of the gravel within the SBCM has been shown to reduce the compressive strength.

A discussion concludes that the improvement in image resolution obtained using ϕ12 samples is minimal when compared alongside the ϕ38 samples and that the larger ϕ100 samples are too big to enable small field of view scans to be performed. The use of the ϕ12 and ϕ38 samples does result in a reduction in compressive strength, when compared to the more representative ϕ100 samples, however the elastic response of all three sample sizes are similar and in order for the full inter-aggregate void structure of SBCMs to be observed the ϕ38 samples must be used.

Chapter 6

The effect of clay and sand during drying

6.1 Introduction

The properties and mechanical behaviour of the clay in an unstabilized soil based construction material (SBCM) mix has shown to be key to the material's compressive strength and, as discussed in previous chapters, it acts as a binder and is a source of suction within the dried material. The use of expansive clays in SBCM mixes is often avoided as it is known to crack during drying and adversely affect the final strength of the material (Walker et al., 2005). However clay found on a site using SBCMs may contain a small amount of expansive clay material resulting in the rejection of site dug clay and the importing of clay from other locations, and a large increase in construction costs and an adverse effect on environmental impact. Despite Walker et al. (2005) stating that expansive clay should be avoided in SBCM construction, and that being common practice within the construction industry, no scientific literature studying the effect of expansive clays on SBCMs can be found, either supporting the need to avoid its use or quantifying its effect in terms of performance. Therefore this chapter investigates the effect of using a small amount of expansive clay within SBCM samples on both the material's unconfined compressive strength and on the changes in the macrostructure during drying. The effect of changing the proportions of clay and sand within the mix is also investigated to better understand their role in a highly unsaturated SBCM.

6.2 Expansive clays

The early engineering study of unsaturated soils was influenced by the need to better understand expansive soils, i.e. soils that swell on the addition of water and shrink during during, (Fityus and Buzzi, 2009) with Parcher and Liu (1966) studying the differences in swelling for different planes of a unit of clay and Philip (1969) and Miller (1975) presenting early discussions of the generalized theory of swelling

for unsaturated soils. However the specific study of expansive soils has moved towards the use of swelling clays in specific applications (Fityus and Buzzi, 2009) including nuclear waste disposal (Gens et al., 2002) or its interaction with stabilized materials such as cement (Nehdi, 2014) and lime (Al-Mukhtar et al., 2012).

Research into mixtures of clay types, where small proportions of an expansive clay is added to a non-swelling clay, is scarce and Grabowska-Olszewska (2003) observes that the relationships between the percentage of individual clay types is not usually studied. The results by Grabowska-Olszewska (2003) show that the relationships between standard geotechnical descriptors, including liquid and plastics limits, and the percentage of bentonite and kaolinite clays are easily described, typically with a linear relationship proportional to the percentage of each clay type, and these results may therefore highlight the lack of interest in these relationships from a modelling perspective when only pure clay is investigated. In SBCMs however the complex nature of the material due to the broad grading of particle sizes means the simple trends observed for pure clay samples may not exist and quantifying the impact of the expansive clay on SBCMs is important.

The bi-modal void distribution of clay compacted dry of optimum, as discussed in detail in Chapter 2, is well established. During the wetting and drying of expansive clays, clay aggregations (in which the intra-aggregate voids, including the intra-elemental voids between individual clay particles, are located) remain saturated whilst the inter-aggregate voids undergo structural rearrangement and exist in a partially saturated state (Alonso et al., 1999; Fityus and Buzzi, 2009; Monroy et al., 2010; Mašín, 2013). The maintained saturated state of the clay aggregations is due to the sheet-like particle packing of the expansive clay particles with very small inter-particle voids, down to 3-4nm for montmorillonite clay, resulting in very high air entry values producing very high suctions (Holmes, 1955). As described by Fityus and Buzzi (2009) during the drying of an expansive clay an increase in suction causes the extraction of inter-layer water from between clay particles resulting in shrinkage. This shrinking of particles compresses the surrounding inter-particle voids which in turn increases the air-entry value of the clay aggregation and maintains the saturated state.

The soil shrinkage model proposed by McGarry and Malafant (1987) suggests there are three main phases of drying, and shrinkage, for a soil starting at field capacity. First water is drained under gravity from cracks and defects, resulting in little or no volume change. Second is the normal phase of shrinkage where, for a saturated soil, the soil reduces in volume by an amount equal to the volume of water lost. Finally, following the reaching of the air entry suction value, the soil enters the residual phase as air enters the voids and the soil desaturates. During this residual phase there is little or no shrinkage.

This shrinkage model is applicable to all soils but has to be carefully considered for SBCMs because the soil is compacted close to optimum water content and dries as an unsaturated soil. This means that

the SBCM will be within the residual phase of drying and little shrinkage should occur. For non-expansive clays, such as kaolinite, this residual phase should describe the entirety of the mix and therefore no major change in material structure should be observed. However for SBCMs containing expansive clays, such as montmorillonite clay, which result in clay aggregations remaining saturated to very high values of suction the clay binder matrix can still be said to be in the normal phase of shrinkage and should therefore reduce in volume as water is lost.

The shrinking of the montmorillonite clay particles during drying will occur at the nanometre scale and will therefore be too small to be observed using laboratory x-ray computed tomography (XRCT). However the shrinking of the individual montmorillonite clay particles will affect the size of any clay aggregations formed of both montmorillonite and kaolinite particles and it is expected that the shrinking of these clay aggregations will alter the larger void macrostructure, which is observable using XRCT scanning and image analysis.

6.3 Methodology

Throughout this investigation four different mixes are used which contain different proportions of montmorillonite clay, kaolinite clay and sharp sand. The experimental work can be divided into two clear strands, the first investigates the internal structure of the samples as they dry through the use of XRCT scanning whilst the second investigates the change in compressive strength of the samples as they dry through unconfined compression, constant water content tests. The compressive strength investigation examines the samples at five different stages of drying whilst the internal structure investigation only considers three stages due to the time required to scan and analyse each sample using XRCT.

The stages of drying are described using the dryness fraction (df) which gives an indication of how close the sample is to its equilibrated dry state in the current atmospheric conditions. The dryness fraction is used to describe the state of the soil since, under the same given environmental conditions, the samples of the four different mixes dried to different final water contents thus meaning that drawing comparisons relative to water content could be misleading. Additionally the use of degree of saturation, as commonly used in unsaturated soils investigations to compare different samples, was not possible since the presence of the expansive montmorillonite clay meant that clay aggregations could remain saturated to high values of suction and reduce in volume as the material dried. This change in void size therefore means determining the percentage of voids filled with water, when the total void volume is not constant, cannot be used as a consistent measure and any degree of saturation for a sample containing expansive clay during drying is probably meaningless (Fityus and Buzzi, 2009). The dryness fraction value of each sample is given as a value between zero and one: a sample of df=1.0 is in its driest state, where no further water loss will occur; and a sample of df=0.0 is at optimum water content following manufacture.

6.3.1 Materials

Four different mixes of sand and clay were used in this investigation and no gravel was present due to limitations on the sample size to ensure successful XRCT scanning and to enable the examination of the behaviour between the clay and sand without the addition of larger particles. Therefore the samples can be considered to be representative of the clay-sand binder matrix within SBCMs (Beckett, 2011). The first two mixes were speswhite clay and sharp sand combined by mass in a clay:sand ratio of 1:2 and 1:1. The speswhite clay (LL 64%, PL 33%), the same clay used in Chapter 5, was a pure kaolinite clay supplied by IMERYS Performance Minerals (Imerys, 2008) and required no pulverisation or processing prior to manufacturing the samples. The sharp sand was oven dried at 105^oC and passed through a 2mm sieve to prevent any gravel particles being present within the mix. In the second two mixes the speswhite clay was mixed with a Wyoming sodium bentonite clay (LL 575%, PL 69%) chosen because it is an example of a highly expansive montmorillonite clay commonly avoided by the SBCM industry. The Wyoming clay was supplied by RS Minerals as a natural sodium bentonite clay (Tolsa, 2008). This clay mixture combined by mass 1 part Wyoming sodium bentonite clay with 4 parts speswhite clay producing an 80% kaolinite 20% montmorillonite clay mixture. These second two mixes also combined the clay mixture with the sharp sand in a ratio of 1:2 and 1:1. The four mixes are referred to hereafter as Mix E, Mix F, Mix G and Mix H and Table 6.1 shows the target proportions of each constituent and the liquid limit, plastic limit and linear shrinkage values for all four manufactured mixes, determined using the procedures outlined in British Standard BS1377:1990 (British-Standards, 2002).

Figure 6.1 shows the particle grading curve for all four mixes after manufacture and have maximum weighted percentage error terms of 2.2, 2.0, 0.7 and 2.5 for Mix E, Mix F, Mix G and Mix H respectively. The mixes which contain the same ratio of sand and clay, i.e mixes E and G, have very similar particle grading curves with the only difference arising at 63μm from which it can be seen that the mixes containing the bentonite clay contain a smaller silt fraction by 3% of the total mass. The BS1377 Vibrating Hammer Test (British-Standards, 2002) was used to determine the optimum water content and target dry density values for all four mixes and the results are shown in Figure 6.2 and Figure 6.3.

Table 6.1: The constituents and key geotechnical parameters for all four mixes.

Mix Name	**Percentage of total mass**			**Liquid Limit (%)**	**Plastic Limit (%)**	**Linear Shrinkage (%)**
	Kaolinite (%)	**Montmor-illonite (%)**	**Sand (%)**			
Mix E	33.3	0	66.7	36	19	6.81
Mix F	50.0	0	50.0	43	24	7.14
Mix G	26.7	6.7	66.6	52	17	11.91
Mix H	40.0	10.0	50.0	70	21	13.75

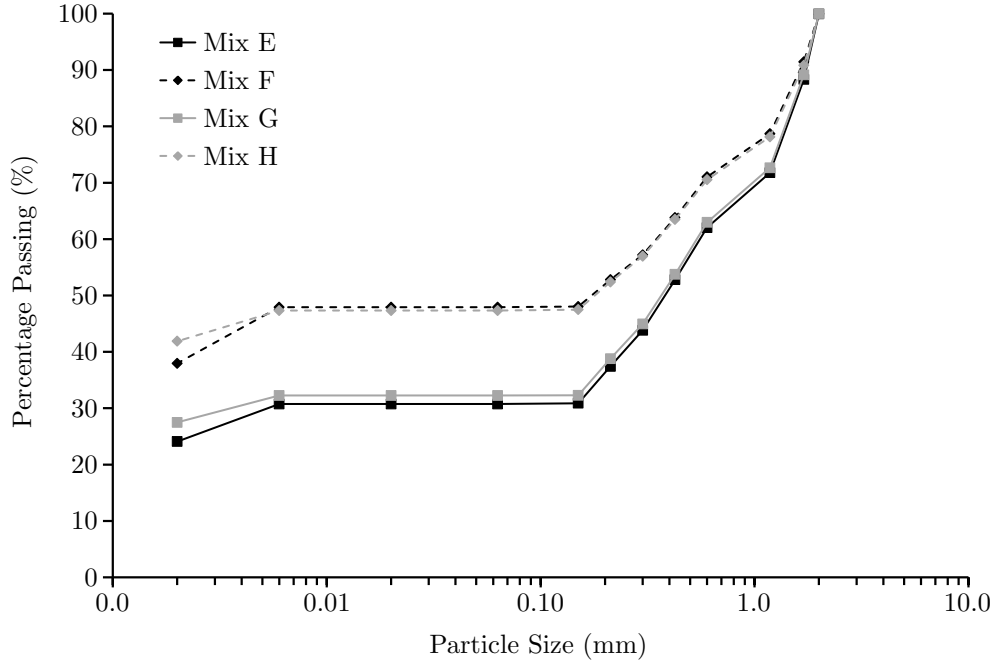

Figure 6.1: Particle size distribution plot for all four mixes.

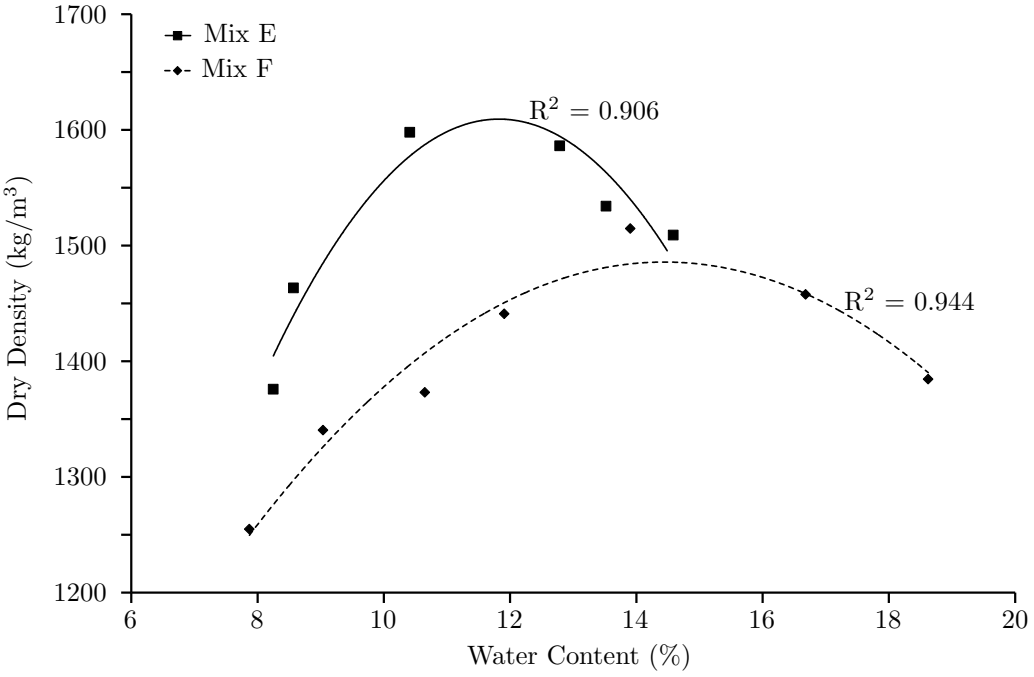

Figure 6.2: Dry density and water content values obtained for mixes E and F.

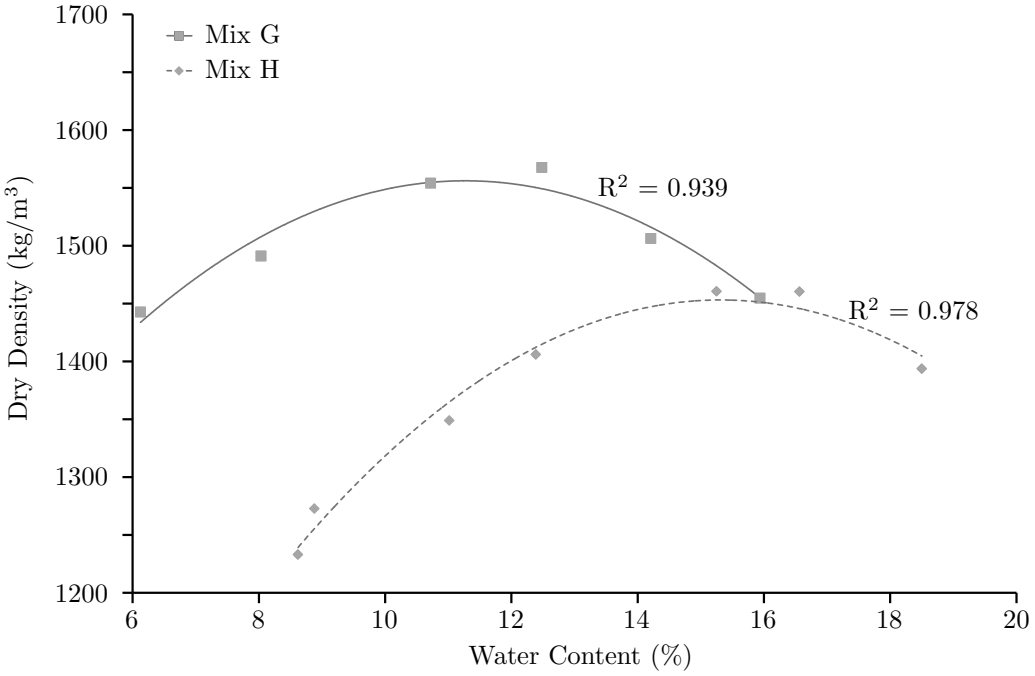

Figure 6.3: Dry density and water content values obtained for mixes G and H.

6.3.2 Sample manufacture

For each of the four mixes, 19 samples were manufactured. A single preliminary sample was manufactured for each mix to provide a drying curve for the samples and to enable estimated times of drying to be established for the detailed investigations. Three samples were used in the XRCT investigation determining the changes in void structure and 15 were used in the investigation into the development of compressive strength as the sample dries, of which three samples were used for each of the five stages of drying. The samples were standard small triaxial samples, 38.1mm in diameter and 76.2mm high, and compacted in two layers of equal depth.

For clarity, in the remainder of this chapter the samples are differentiated using the following system whereby the letter describes the soil mixture and the proceeding number differentiates between individual samples. The preliminary sample tested to determine the drying curve is numbered zero, the XRCT samples numbered one, two and three and the compressive strength samples are numbered between four and eighteen. The subscript value following the number and letter combination indicates the sample's target *df* value. For example, Sample $F2_{0.0}$ is manufactured from Mix F (containing 50% sharp sand and 50% kaolin clay) is the second of three samples scanned using XRCT and is at optimum water content.

Table 6.2 shows the target dry density values and optimum water content values for manufacturer of the four mixes obtained using the BS1377 Vibrating Hammer Test. The appropriate amount of water was added to the dry mix to achieve optimum water content and the mixture was sealed and left to equilibrate

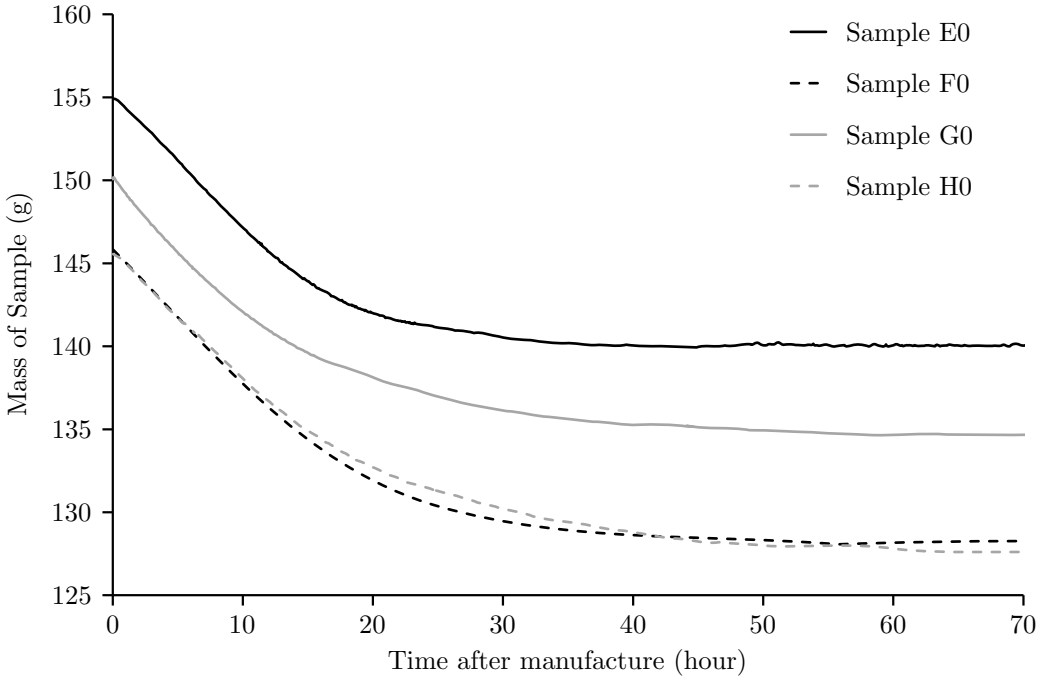

Figure 6.4: The drying curve for the four preliminary samples, one manufactured from each mix.

for 24 hours before manufacture. The correct mass of wet soil for each layer to achieve the target dry density was added to a small triaxial split mould and statically compacted to achieve the 38.1mm layer depth. Following the compaction of both layers the samples were removed from the mould and dried to their target mass within a temperature monitored room at 22±2^{o}C. Upon reaching the target mass plastic top and bottom caps were placed on the sample and a latex sheath fitted to prevent any further water loss. Three filter paper test samples for each stage of drying, each comprising of two 50mm diameter and 20mm high cylinders of soil, were also prepared alongside the small triaxial samples and provided total suction values for all five stages of drying. The samples were dried alongside the corresponding triaxial samples and then placed within a sealed jar for ten days. Following testing all samples were oven dried, at 105^{o}C for 24 hours, and water content values calculated.

The preliminary samples for each mix were manufactured and the sample mass was logged as the

Table 6.2: Target dry density and water content values for all four mixes at manufacture and target sample mass during drying.

Mix Name	**Target Dry Density (kg/m^3)**	**Optimum Water Content (%)**	**Sample Mass to achieve the target *df* (g)**				
			df=0.0	df=0.25	df=0.5	df=0.75	df=1.0
Mix E	1600	12.27	155.0	151.2	147.5	143.7	139.9
Mix F	1480	14.35	145.9	141.4	137.0	132.5	128.1
Mix G	1560	11.34	150.2	146.3	142.4	138.5	134.6
Mix H	1450	15.23	145.6	141.1	136.5	132.0	127.4

sample dried to obtain each mixes drying curve. Drying curves plot the change in mass of a sample against time from manufacture and show the water lost due to the sample drying and equilibrating with the environmental conditions. The drying curves, shown in Figure 6.4, enabled the sample mass associated with each of the five stages of drying to be determined and these target masses are given in Table 6.2.

6.3.3 Experimentation to investigate changes to internal structure

The three samples manufactured from each mix for XRCT scanning were immediately sealed following manufacture, at df=0.0, to capture the internal structure of the sample following compaction at optimum water content. The sealed samples were left for a minimum of 24 hours to allow the sample to equilibrate before being scanned using the XRadia/Zeiss XRM 410 (XRM410). Following scanning the latex sheath was removed and the sample left to dry to df=0.5 in a temperature monitored room at 22±2^{o}C. Upon reaching the target mass the samples were again sealed, left to equilibrate and scanned in the XRM410. The sheath was then removed a second time and the samples left to dry to df=1.0 before being sealed and scanned for a third time. Following the calculation of the true water content and dry density the XRCT samples were all within 2% of target values meaning variations in dryness fraction and dry density after manufacture were negligible.

A total of 36 XRCT scans were performed, three for each sample, and all were performed using the same parameters to ensure all the results could be easily compared. Only a single set of scan parameters were used for each sample scan which captured the entire diameter of the sample at a pixel size of 20µm. The scans were performed at the maximum power capabilities of the XRM410, 140kV and 10W, and 3201 images were taken per sample scan, with an exposure time of 4s, resulting in each scan taking approximately seven hours. These scan settings were the same as the ϕ38 large field of view scans used in Chapter 5. It is acknowledged that the small field of view scans would have enabled smaller voids to be detected within the sample however it was expected that cracks may appear within the samples as they dried and these were more likely to be captured by the large field of view scans due to the larger volume of sample being scanned. Additionally the small field of view scans in Chapter 5 took nearly three times as long as the large field of view scans and therefore the triplicate scan data could only be obtained for the seven hour scans due to the large number of samples being scanned and limited access to the XRM410.

In order to obtain quantitative results from the XRCT scans considerable post-processing of the data was required. The methods used are discussed in detail in Chapter 3 and the analysis procedure is outlined in Figure 6.5, a replication of the earlier Figure 3.13.

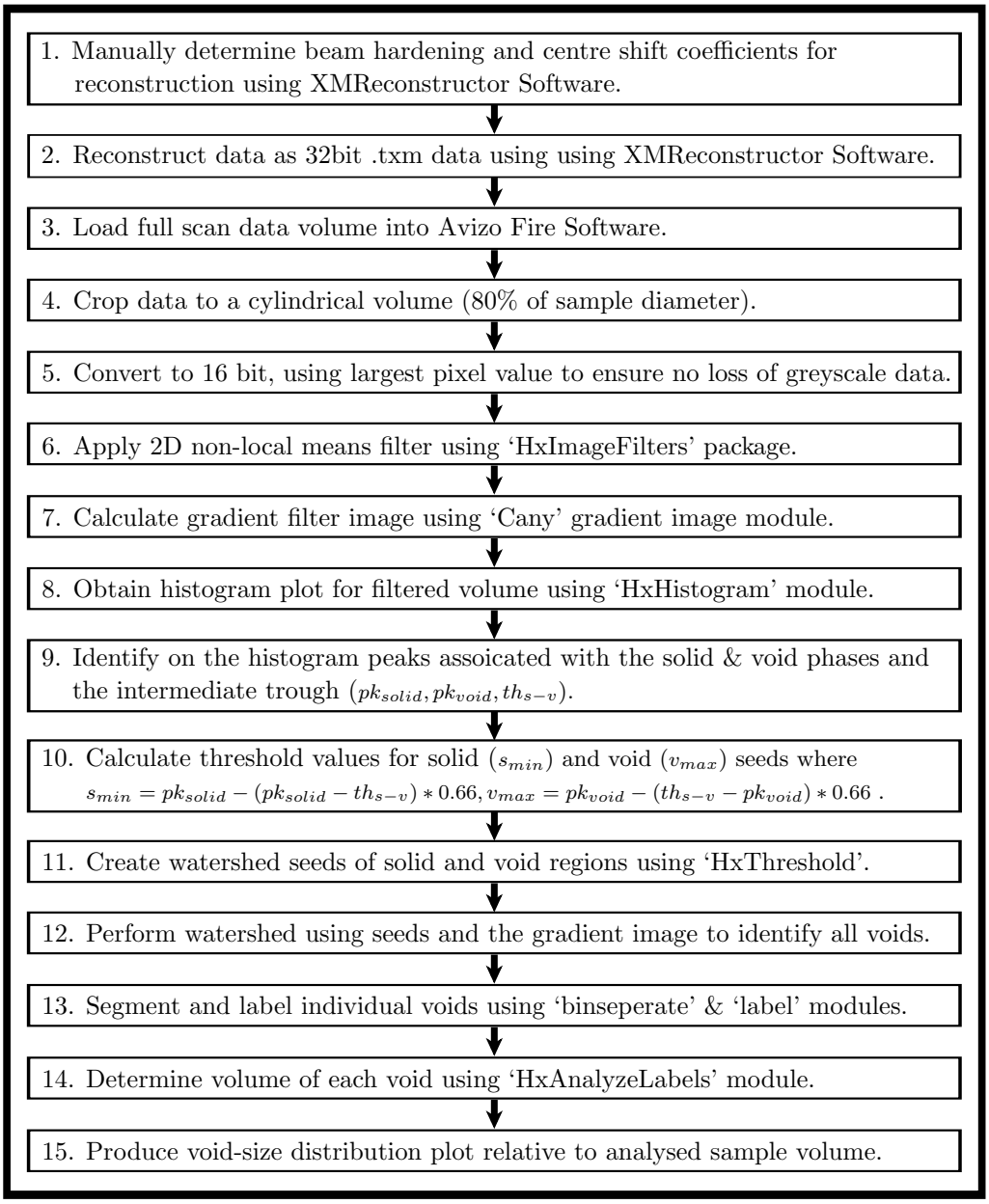

Figure 6.5: Flowchart of the Avizo Fire analysis used for XRCT data processing. Please note this is a replication of Figure 3.13 and included here for the readers convenience.

The key stages in the analysis process were:

- reconstruction of the data, using the XMReconstructor software provided with the scanner;
- reduction of file size, through the conversion of the data from 32bit to 16bit RAW data;
- enhancement of image quality, through a non-local means filter;
- identification of voids within the sample, through the analysis of the image histogram and use of the watershed algorithm;
- and the production of quantitative results, displayed as a void size distribution.

The final output of the analysis used here is very similar in form to that obtained in Chapter 5, a void size distribution plot for the scanned sample which shows the cumulative void volume as a percentage of sample volume plotted against the void volume. However the post-processing of the images used here was completely autonomous, as it required no user input to determine threshold values, and direct comparison of the void size distribution at three stages during drying enabled any change in macrostructure to be quantified.

6.3.4 Experimentation to investigate compressive strength

The fifteen samples manufactured from each mix for compressive strength testing were dried to the corresponding sample mass for five stages of drying, df=0.00, 0.25, 0.50, 0.75 and 1.00, using the drying curve data obtained from the preliminary samples. Following the calculation of the true water content of the triaxial and filter paper samples the wettest triaxial samples were found to be drier than optimum water content, and many of the intermediate stages of drying were also drier than initially intended, suggesting that the latex sheaths had not perfectly sealed the samples, and water loss had occurred before compression testing. Despite this variation in the dryness fraction in relation to the intended targets, the results are still valid as the compressive strength results and suction values obtained are all plotted against the individual samples' measured dryness fraction and trends in the results as the samples dry can still be observed. Additionally the dry density of all samples' were within 2% of the target manufactured dry densities ensuring the values obtained for compressive strength can be compared. The samples were tested using a Lloyd LR5K Plus testing machine, with a load cell rated at 5kN$\pm$0.5%, at a strain rate of 0.1mm/minute and tested to failure, observed by evidence of a load peak, after which compression was stopped and the load released.

6.4 Results and Discussion

6.4.1 Differences in macrostructure

Nineteen XRCT scans were successfully analysed using the automated analysis technique outlined in Figure 6.5 whilst the remaining 17 scans produced no useful quantitative data to describe the internal structure of the samples because the automated procedure was unable to correctly identify one or both of the void and solid peaks within the image histogram. The automated peak identification procedure resulted in two clearly different void size distributions depending on the location of the automatically identified void peak on the image histogram. Within each group of void size distributions the size of the threshold region varied by less than 0.5% which ensured any difference in void volumes measured was not due to differences in the grey scale threshold values applied. The first group of analysed XRCT scans, for which a low void peak greyscale value had been identified, had a calculated total void volume of less than 5% whilst the second group of analysed XRCT scans, for which a high void peak greyscale value had been identified, had calculated total void volumes above 15%. The large differences in total void volume prevents direct comparison of quantitative data from the two different groups of analysed XRCT scans and highlights the difficulties that can arise when selecting threshold values.

Samples from within each group of scans can however be directly compared and insights drawn using both groups' results as they capture different void sizes within the material structure. The second group of XRCT scans only captures voids larger than $1x10^8\mu m^3$ whilst the first group of XRCT scans identify voids larger than $5x10^6\mu m^3$. As discussed in detail in Chapter 2, voids far smaller than $1x10^8\mu m^3$ will exist within these materials and the results from Chapter 5 show that voids between $1x10^6\mu m^3$ and $1x10^8\mu m^3$ can be successfully captured when scanning ϕ38 samples using XRCT. This would suggest that the first group of scans, which identify voids between $1x10^6\mu m^3$ and $1x10^8\mu m^3$, are more appropriate however the total volume of voids should also be considered before firm conclusions are drawn. The ϕ38 samples in Chapter 5 were compacted to a much higher dry density than the samples used in this chapter and should therefore have a smaller total volume of voids. When the void size distribution plots from Chapter 5 are considered it is clear that the percentage of voids is only larger in the second group of XRCT scans which would suggest that the second group of XRCT scans has better captured the void structure of the SBCM. It is clear that for this investigation the void size distribution results from both groups of XRCT scans do not perfectly capture the void structure however the first group of scans captures the smaller voids within the sample whilst the second group captures the larger voids more accurately and therefore both sets of data can be used to gain insight into the sample structure as it dries.

The strengths and weaknesses of the analysis technique implemented in this investigation, with particular focus on the image processing techniques used, is discussed in detail in Chapter 3. For the remainder

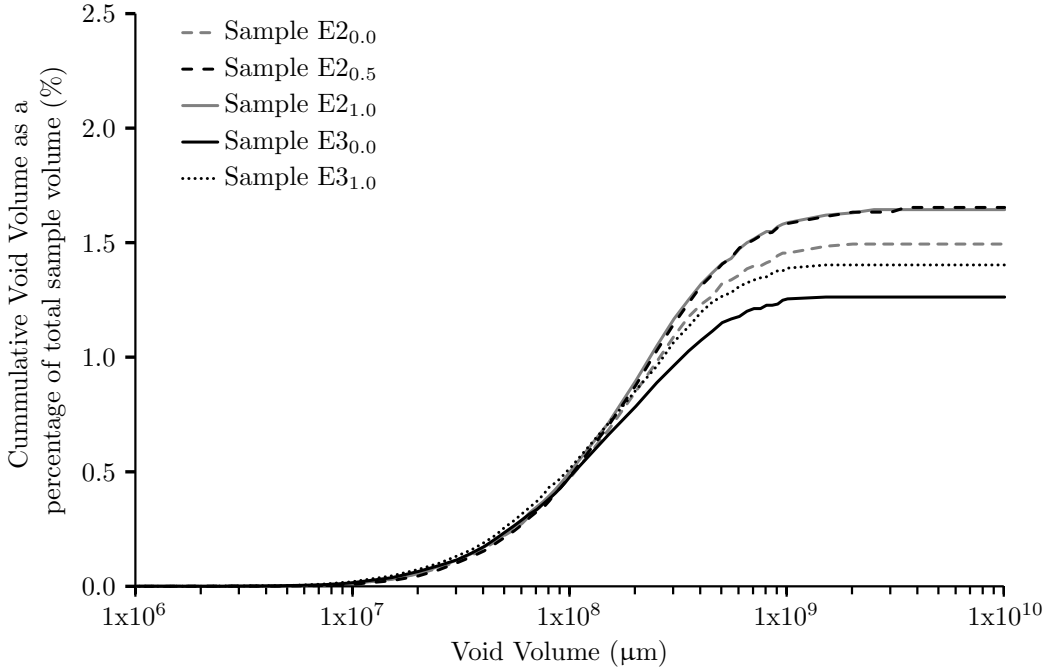

Figure 6.6: The void size distribution obtained for the Mix E samples which identified voids larger than 5x10^{6}μm^3.

of this chapter the available void size distribution data, shown in Figures 6.7, 6.6, 6.8 and 6.9, is used to inform the discussion regarding the change in macrostructure during drying and the effect of the presence of expansive clay within SBCM samples.

Firstly it is possible to observe differences between the macrostructure of samples compacted from the same material by comparing the different samples, within the same analysis group, at the same *df* value. Figure 6.7 plots the void size distributions of Sample G1 and Sample G3 and shows that the total volume of voids varies between the two samples at *df*=0.5 by 1.21% of the total sample volume and by 0.90% at *df*=1.0. Figure 6.6 similarly shows that the total volume of voids varies between Sample E2 and Sample E3 by 0.23% at *df*=0.0 and 0.24% of the total sample volume when at *df*=1.0. For the second group of samples, shown in Figures 6.8 and 6.9, similar differences in the total void volume can

Table 6.3: The largest difference in total void volume for comparable sets of samples.

Change in clay		**Change in sand:clay ratio**	
Comparable Samples	**Difference in total void volume**	**Comparable Samples**	**Difference in total void volume**
E2$_{0.0}$, E3$_{0.0}$, G3$_{0.0}$	0.68%		
E2$_{0.5}$, G1$_{0.5}$, G3$_{0.5}$	1.21%	E3$_{0.5}$, F1$_{0.5}$	0.30%
E2$_{1.0}$, E3$_{1.0}$, G1$_{1.0}$, G3$_{1.0}$	0.96%	G2$_{0.0}$, H2$_{0.0}$	0.07%
E3$_{0.5}$, G2$_{0.5}$	0.82%	G2$_{0.5}$, H1$_{0.5}$, H3$_{0.5}$	1.55%
F1$_{0.0}$, H2$_{0.0}$	0.43%		

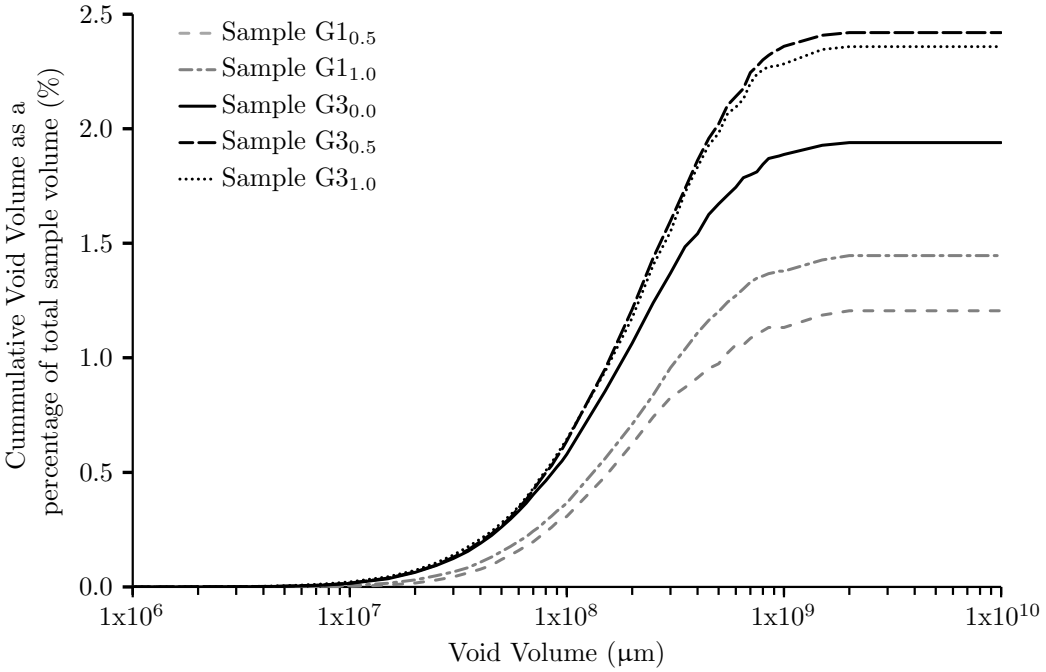

Figure 6.7: The void size distribution obtained for the Mix G samples which identified voids larger than 5x10^{6}μm^3.

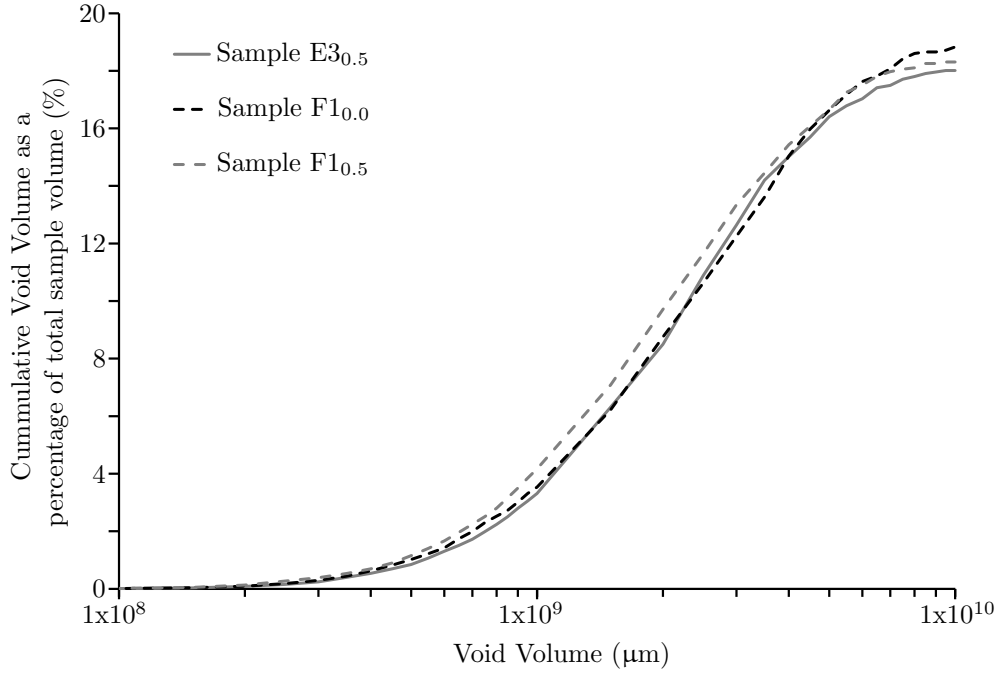

Figure 6.8: The void size distribution obtained for the Mix E and Mix F samples which identified voids larger than 1x10^{8}μm^3.

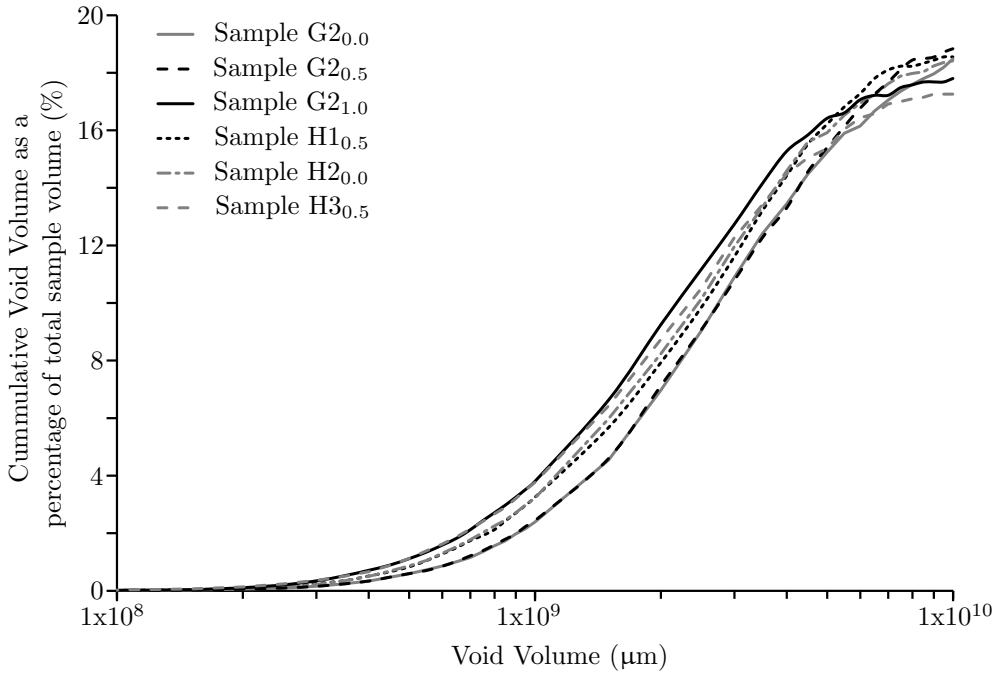

Figure 6.9: The void size distribution obtained for the Mix G and Mix H samples which identified voids larger than 1x10^{8}μm^3.

be observed with Sample H1 and Sample H3 at df=0.5 varying by 1.58% of the total sample volume. The differences between the samples shows that the void structure of the material, when compacted under the same conditions and from the same controlled particle mixture, can still vary between samples. These differences in void structure will result in differences in material behaviour and can also explain some of the variability often exhibited when performing unconfined compression tests on samples within a triplicate.

Secondly it is possible to draw comparisons between the macrostructure of samples manufactured from the different SBCM mixes, providing that samples are compared at the same dryness fraction and have void size distribution plots obtained from the same XRCT analysis group. The effect of expansive clay within the samples can be seen by considering comparable samples formed from mixes of the same clay:sand ratio (Mix E and Mix G or Mix F and Mix H) and the effect of changing the clay:sand ratio can be similarly seen by comparing samples from mixes containing the same clay (Mix E and Mix F or Mix G and Mix H). For each set of comparable samples, Table 6.3 lists the largest difference in total void volume. The differences in total void volume following the addition of expansive clay can be seen to be, at most, 1.21% of the total void volume and the difference in total void volume between the two clay:sand ratios is 1.55%. Both of these differences are smaller than the largest variation between samples from the same triplicate, 1.58%, and therefore suggests that the differences in the macrostructure caused by changes to the mix composition are less significant than the variation caused during the manufacture of

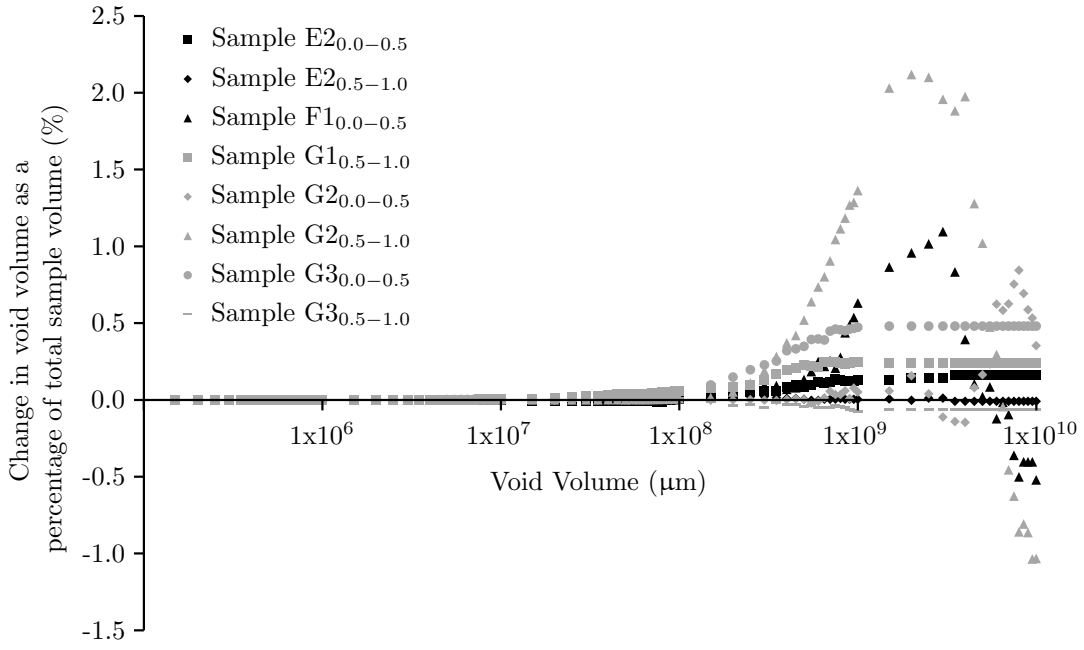

Figure 6.10: Change in void size distribution for individual samples between two values of dryness fraction.

the samples.

Finally it is possible to examine the change in macrostructure as individual samples dry. For the changes to be quantifiable individual samples must have void size distribution results for two consecutive drying stages (df=0.0 to df=0.5 or df=0.5 to df=1.0) and for the two results to fall within the same XRCT analysis group. Because void size distribution results are being compared for an individual sample scanned at two values of dryness fraction, the variation in macrostructure occurring from manufacture, as discussed above, should not impact the results and the changes observed will be due to the drying process. In total, eight drying transitions were directly comparable and Figure 6.10 shows the difference in the void size distribution for each sample transition. A positive change in void volume indicates a larger volume of voids following a increase in the dryness fraction value.

It is clear from Figure 6.10 that three different changes in macrostructure during drying have occurred in the samples successfully analysed. Sample E2$_{0.5-1.0}$ and Sample G3$_{0.5-1.0}$ show changes in void volume of less than 0.01% of the total sample volume. Samples E2$_{0.0-0.5}$, G1$_{0.5-1.0}$ and G3$_{0.0-0.5}$ show a maximum increase in void volume following drying of 0.16%, 0.25% and 0.48% respectively. It is also clear from Figure 6.10 that for these three samples the change in void volume predominately occurs in the void volumes between 1x10^{8}µm^3 and 1x10^{9}µm^3. Samples F1$_{0.0-0.5}$, G2$_{0.0-0.5}$ and G2$_{0.5-1.0}$, show much larger increase in void volumes, 1.10%, 0.84% and 2.12% respectively, for a specific void volume but also include a decrease in void volumes at other void volumes.

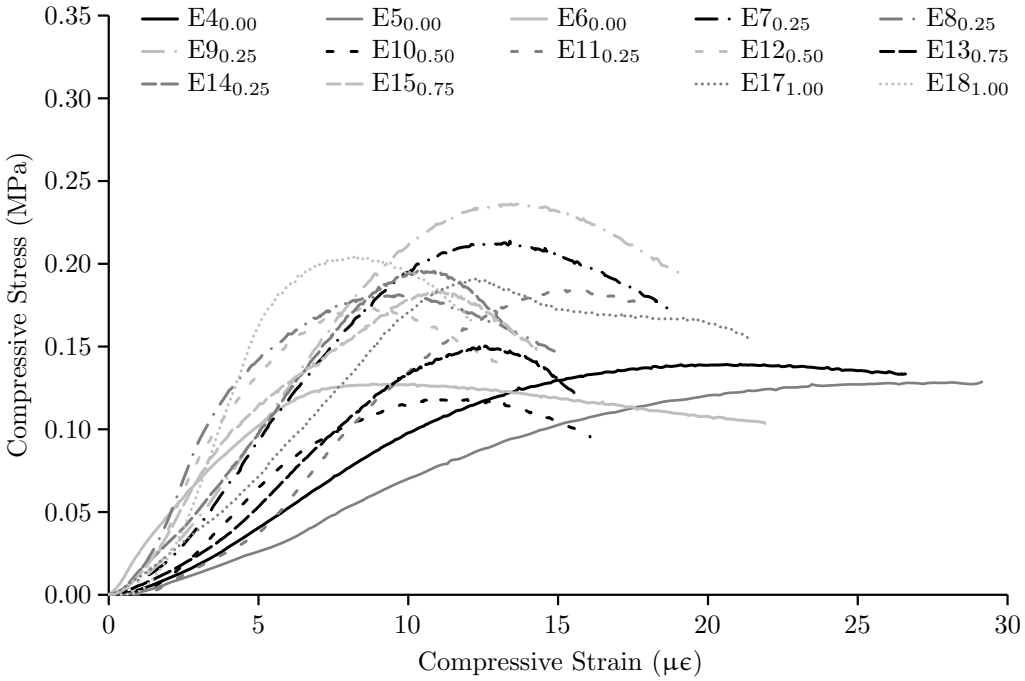

Figure 6.11: Stress strain plot for Mix E samples.

For both macrostructural evolutions for which void volume change was identified, the magnitude of the change in void volume is greater in the samples which contained expansive clay therefore suggesting that the expansive clay does affect the evolution in macrostructure as the SBCM sample dries by increasing the magnitude of any changes that occur. Unfortunately with so few samples in which the changes in void volume during drying can be directly compared any firm conclusions are difficult to draw and the reasons for the three different macrostructural evolutions are unclear. It is must also be noted that these evolutions in macrostructure occurring due to drying are of a similar magnitude to the changes in macrostructure identified between samples and therefore any changes occurring within a SBCM structure during the drying process are only likely to affect the material behaviour in a similar manner to the natural variations occurring in the macrostructure due to manufacture.

6.4.2 Compressive strength and stiffness

Fifty-eight unconfined compression, constant water content tests were completed with two samples, F11$_{0.50}$ and F14$_{0.75}$, broken prematurely during machine setup preventing any data being collected for either sample. Two of the 58 samples, H4$_{0.00}$ and E13$_{1.00}$, were found to have significantly lower water contents at testing than the other corresponding samples at their target df, by over 10%, and therefore were discounted from the analysis. The remaining 56 successful unconfined compression, constant water tests results are shown in Figures 6.11, 6.12, 6.13 and 6.14.

As has been observed and commented upon in previous chapters, the stress-strain results vary consid-

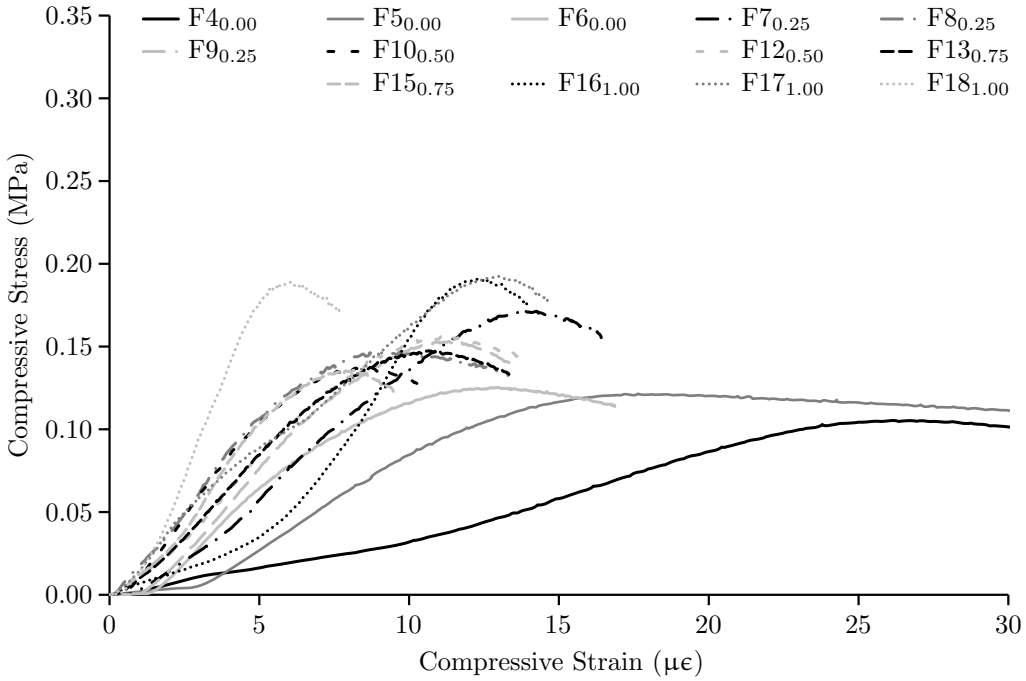

Figure 6.12: Stress strain plot for Mix F samples.

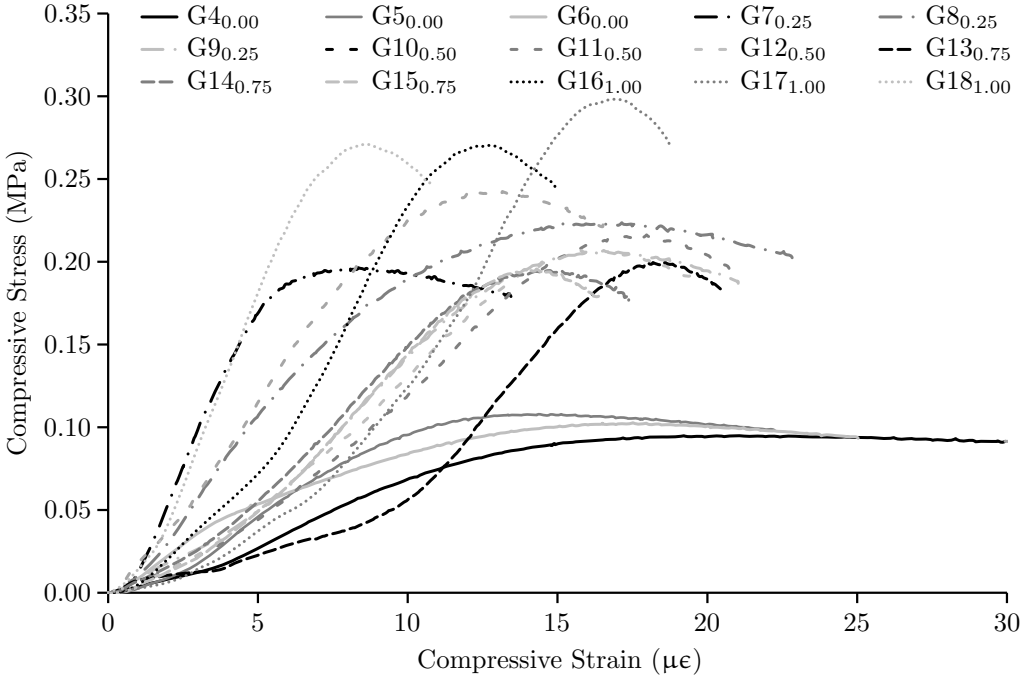

Figure 6.13: Stress strain plot for Mix G samples.

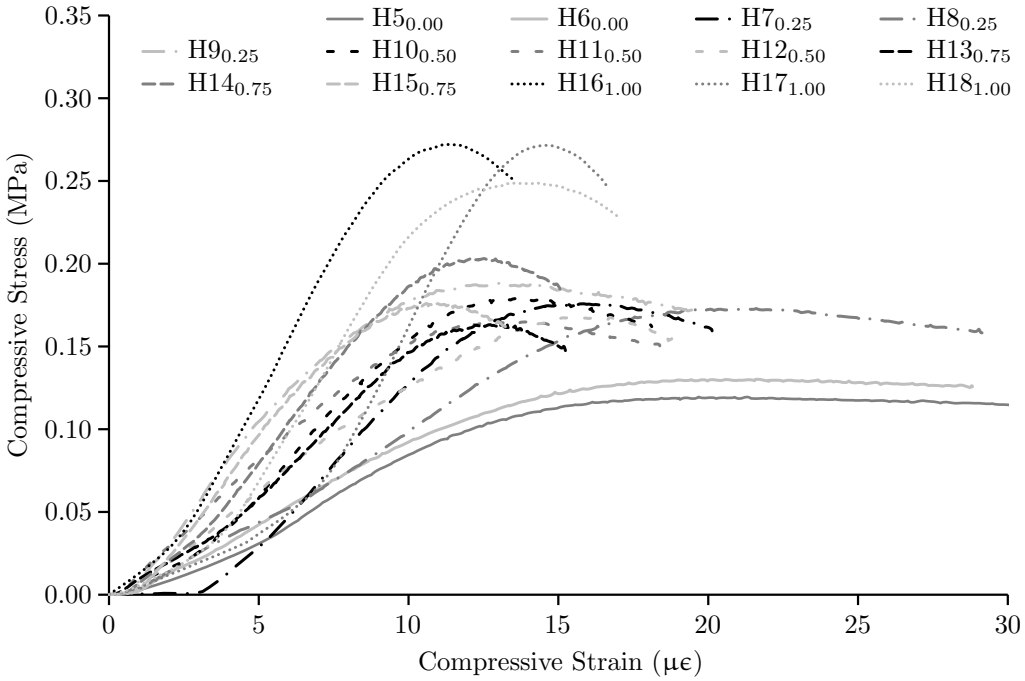

Figure 6.14: Stress strain plot for Mix H samples.

erably between samples within in a triplicate with the largest difference most commonly found at the start of the tests where a period of 'bedding in' is observed as larger strains are measured for a given increase in stress for one sample more than another. The reasons for this are not investigated in detail however it is likely the interfaces between the end caps and the sample are likely to cause this phenomenon. Despite this variability many insights can be drawn from the results of the unconfined compression tests, both with respect to the differences in behaviour with the presence of the expansive clay and the changes in pre-failure and post-failure response of the samples at different stages of drying.

It is immediately clear that the compressive strength of the samples manufactured from all four sand-clay mixes investigated in this chapter are considerably lower than the compressive strength values obtained by samples described in Chapter 5. This however can be explained by the considerably different densities to which the samples were compacted. As shown in Table 6.2 the target dry densities for the four mixes in this study ranged between 1450kg/m^3 and 1600kg/m^3 whilst the samples used in Chapter 5 had a target dry density of 2060kg/m^3. The difference in target dry densities arose because the investigation described in Chapter 5 used three different sample sizes, each using different particle fractions from a single SBCM mix, and all specimens were manufactured to the target dry density obtained from the vibrating hammer test results performed on the full SBCM mix, which contained particles up to 10mm in diameter. The investigation described in this chapter however only examines the clay-sand binder fraction within the SBCM and the vibrating hammer test was performed on the clay-sand mixture containing no

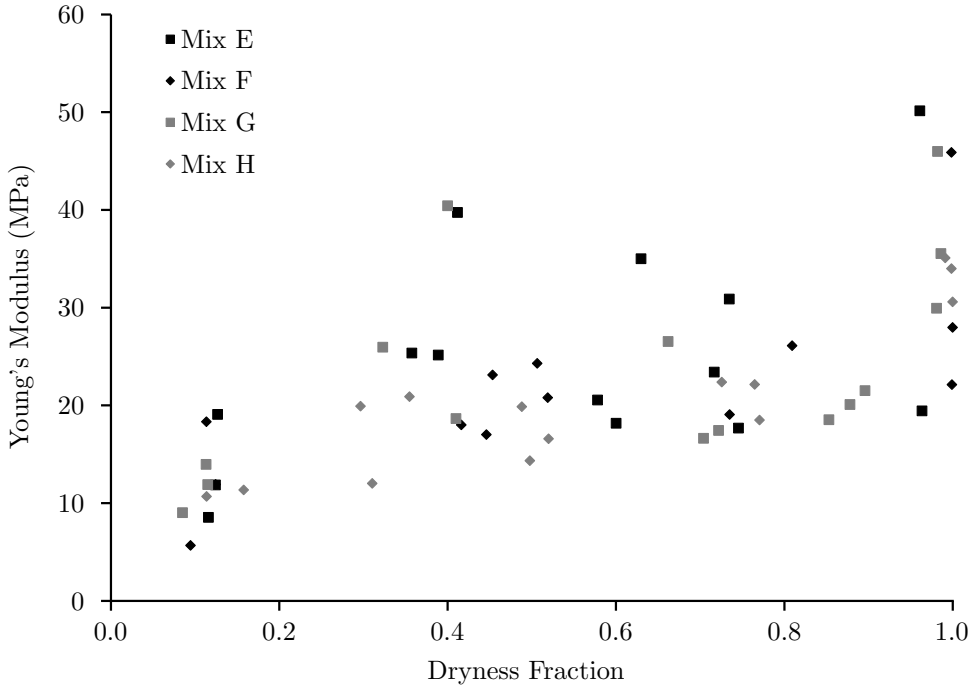

Figure 6.15: Young's modulus values plotted against dryness fraction for all samples.

gravel fraction. This difference in particle grading altered the dry density-water content curve obtained for the samples and the resulting difference in compaction density means comparisons cannot be directly drawn between the results obtained here and in Chapter 5. The compressive loading results for the four mixes used in this investigation can still be compared with one another as they were all manufactured under the same conditions and the target dry density was identified using the same procedure.

Following the period of 'bedding-in' during the unconfined compression tests all samples with a dryness fraction greater than 0.20 exhibit linear-elastic behaviour prior to brittle failure. The samples at df=0.00 however do not show brittle failure but a more ductile post peak failure response. This ductile behaviour has been observed by Miccoli et al. (2014) for dry cob SBCM samples in which straw fibres were added during manufacture but, to the author's knowledge, a ductile failure response has not been observed in any published literature on the compressive behaviour of SBCM samples not containing fibres. This is likely to be due to the focus on SBCMs at low water contents and this ductile response is only observable at water contents close to optimum water content which do not represent water contents in SBCM use.

Visual inspection of the shape of the stress-strain results plotted in Figures 6.11 to 6.14 suggests that the samples appear to get stiffer as they dry, with the gradient of the pre-failure elastic loading region steepening. The Young's modulus for each sample was calculated using the average gradient of the stress-strain curve, after the initial period of bedding-in was completed. Two samples, $E8_{0.25}$ and $G7_{0.25}$, showed unexpectedly high values of stiffness when compared with the other two samples within

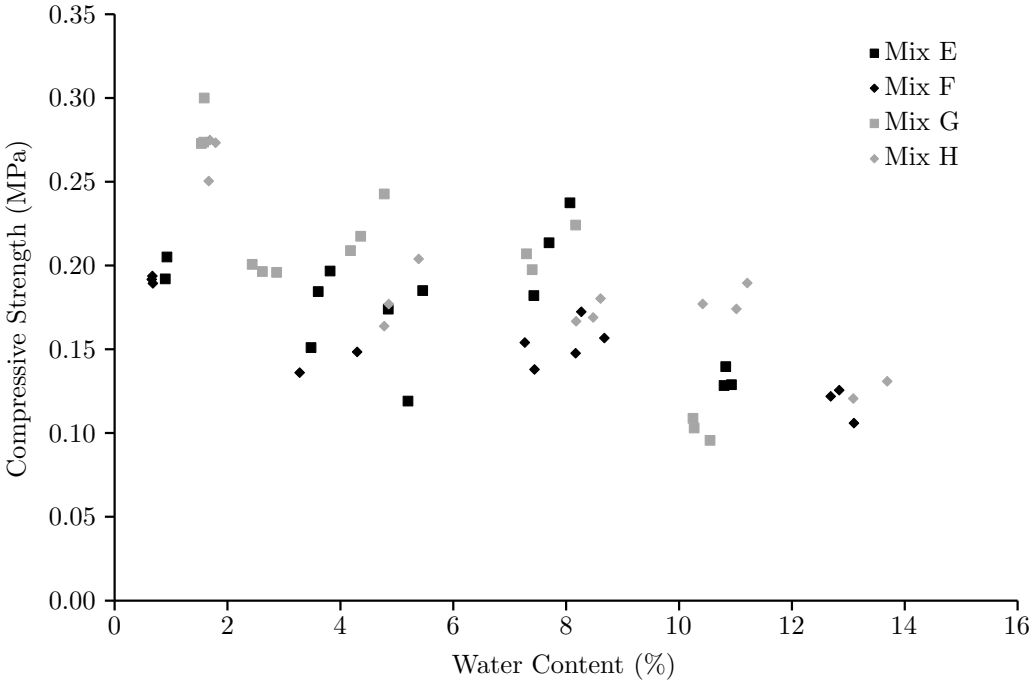

Figure 6.16: Compressive strength results for all four mixes plotted against water content at testing.

the triplicate set although reasons for this are unclear and the two values, with dryness fractions at approximately 0.4 and Young's moduli of 40MPa, are therefore included for completeness. Figure 6.15 shows the Young's modulus for all the samples against dryness factor from which a general trend can be observed that the Young's modulus increases as the sample dries. No clear difference can be identified between the four mixes, either with clay type or percentage, and this suggests that the stiffness of the SBCM samples are controlled more by the amount of water within the voids rather than the particles which form the internal structure.

Figure 6.16 shows the compressive strength for each sample against the sample's water content at testing and shows that, in general, the compressive strength increases as the water content decreases and that the samples containing montmorillonite clay tend to have higher compressive strengths at a given water content. However the comparison of samples' compressive strength at identical water contents is not an appropriate measure to enable insight to be drawn for the use of SBCM construction and therefore Figure 6.17 plots the average compressive strength against the average df for each sample set.

It is important to observe from the data presented in Figure 6.17 that the compressive strength results for the Mix E and Mix G samples around df=0.4 are unexpectedly high and the reasons for this are unclear. It is thought that these results may have arisen through differences in the samples at testing, since a high variability in both the compressive strengths and dryness fractions obtained for these samples can be seen when compared to the other results. These unexpectedly high results around df values of 0.4

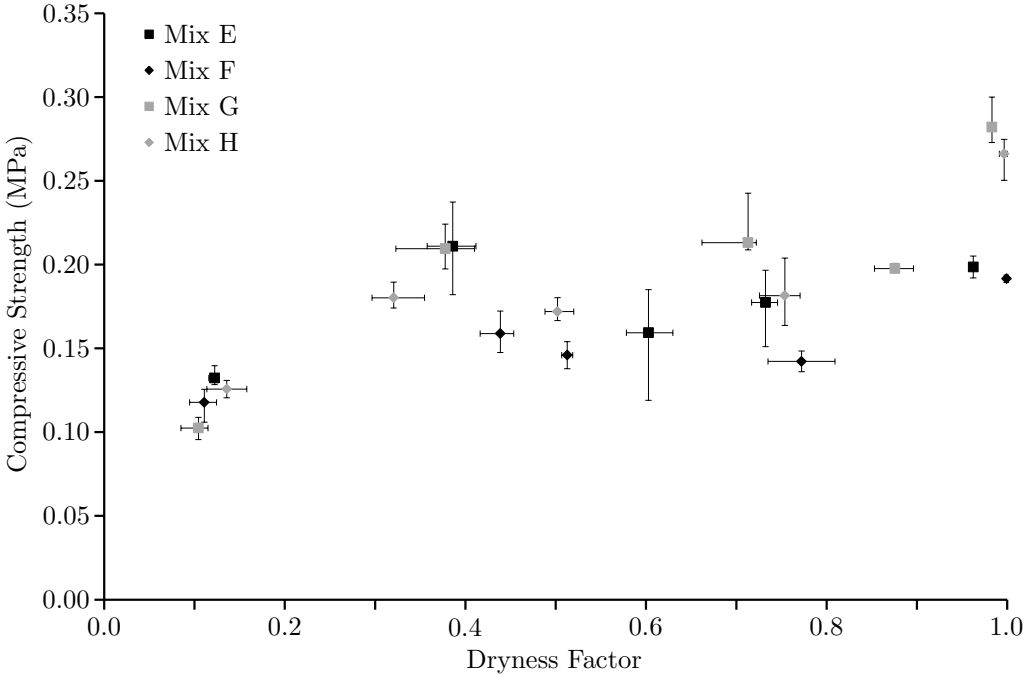

Figure 6.17: Average compressive strength results for all four mixes plotted against dryness fraction.

prevent any well defined relationship, either linear or otherwise, between dryness fraction and compressive strength being drawn for any of the four mixes although Figure 6.17 shows that compressive strength does increase with dryness factor and two key differences in the development of compressive strength between the four mixes used can be identified.

Firstly it is possible to examine the difference in compressive strength with different clay:sand ratios by comparing the results obtained for samples at the similar dryness fraction manufactured from Mix E and Mix F and also samples manufactured from Mix G and Mix H. At dryness fractions around 0.10 Figure 6.17 shows that all the samples containing 67% sand have lower compressive strengths than the comparable samples containing 50% sand and a reduction in the average compressive strength for each set of samples can be seen, 14kPa from Mix F to Mix E and 24kPa from Mix H to Mix G. However this result is reversed for the drier samples with the samples at dryness fractions around 0.75 showing an increase in average compressive strength of 35kPa from Mix F to Mix E and 32kPa from Mix H to Mix G and all comparable samples containing 67% sand achieved higher compressive strengths than those containing 50% sand. At dryness fractions close to 1.0 the difference in compressive strength is less pronounced, as only an increase in average compressive strength of 7kPa and 16kPa is measured for the Mix F to Mix E and Mix G to Mix H samples respectively, and Samples $E17_{1.0}$ and $G16_{1.0}$ had lower compressive strengths than Samples $F17_{1.0}$ and $H16_{1.0}$ respectively. For dry samples of rammed earth Beckett (2011) observed a similar increase in strength with samples containing more sand. Beckett

(2011) found samples of rammed earth containing 20% kaolinite clay, 70% sharp sand and 10% gravel achieved higher unconfined compressive strengths than samples containing 40% clay, 50% sand and 10% gravel. This trend, of increased compressive strength with reduced clay content, cannot be universally extrapolated since a removal of all clay is unlikely to produce a stronger material as the sample would at this point be an unsaturated sand. As discussed in Chapter 1 handbooks on SBCM construction, such as Houben and Guillaud (1989), propose limits for the percentage of the different fractions within SBCM mixes and it may be that the increased compressive strength with reduced clay content may apply within the limits proposed for SBCM construction. Further work on the relationship between the percentage of the different constituents and the compressive strength is clearly required to better understand the determination of the particle grading limits placed on SBCM construction by current guides and the expected differences between the mixes at different particle grading curves within these limits.

Secondly the difference in compressive strength between samples containing different clay types can be examined. For samples with dryness fractions greater than 0.4 an increase in the average compressive strength of samples containing montmorillonite clay is evident and for dryness fractions below this value no clear trend can be seen. For the samples at dryness fractions close to 1.0, Figure 6.17 shows that samples manufactured from Mix E and Mix F, which contain only kaolinite clay, achieve an average compressive strength of 199kPa and 192kPa. In contrast samples manufactured from Mix G and Mix H, which also contain montmorillonite clay, achieved an average compressive strength of 282kPa and 266kPa resulting in an increase of average compressive strength of 83kPa and 74kPa for the two comparable mixes respectively. Similarly Mix F and Mix H samples at dryness fractions around 0.5 and Mix E and Mix G samples at dryness fractions around 0.75 show an increase of average compressive strength for samples containing montmorillonite of 26kPa and 35kPa respectively. The limitations on time and XRCT machine availability prevented a wider range of samples containing different quantities of montmorillonite clay being tested and any relationship between the proportions of montmorillonite and kaolin clays and unconfined compressive strength being firmly established. However these results show that the presence of 20% expansive montmorillonite clay increases the compressive strength when the SBCM is in its dry state and may therefore have an advantageous effect in terms of increasing the compressive strength of SBCM structures operating at the expected dry conditions.

Figure 6.18 shows the total suction developed for a given water content within all four mixes measured obtained from the filter paper tests. Similar to the compressive strength results discussed above no clear differences between the mixes can be seen at water contents above two percent whilst at the lowest water contents it is clear that the mixes containing montmorillonite clay, Mix G and Mix H, develop higher suction than that of the samples containing only kaolinite clay, Mix E and Mix F. These results can be explained by considering the drying mechanisms occurring within the samples and the accessibility of

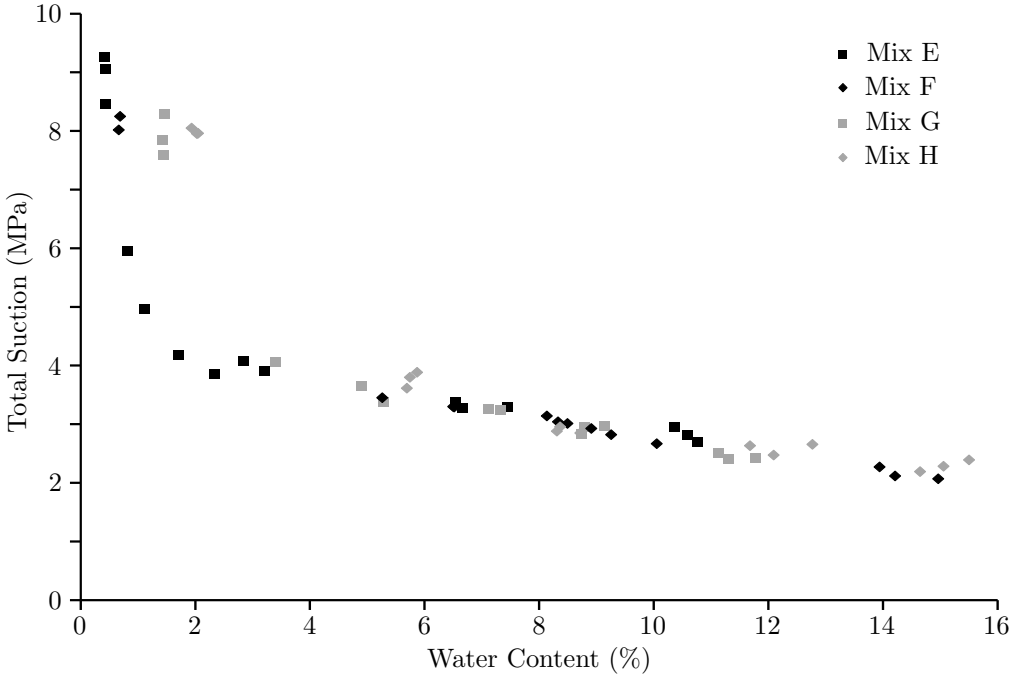

Figure 6.18: Total suction plot for all four mixes.

the water within the clay-sand matrix. At the higher water contents the water is lost from larger inter-aggregate voids, which the results in Section 6.4.1 show are similar for both clay types and sand-clay ratios, and therefore the samples can be expected to develop similar suction values for a given water content. At the lower water contents however, when the accessible water will have evaporated from the largest voids, the different clay mineralogy and structure is likely to contribute more significantly since the water will be removed from the intra-aggregate voids within the clay aggregations. As discussed in Section 6.2, expansive clay will shrink during drying, remaining saturated as water is lost from between the sheet-packed particles, and develop very high suction values (Fityus and Buzzi, 2009) and it is suggested that this is why higher suctions are measured within the samples of Mix G and Mix H for any given water content over Mix E and Mix F.

The development of higher suction values for any given water content could, simplistically, be used to explain the higher compressive strength results obtained for the samples containing montmorillonite clay. However when total suction is plotted against the dryness fraction, as shown in Figure 6.19, no difference between the total suction plots can be observed for the different mixtures. The dry unconfined compressive strength values for the four mixes were all performed at dryness fractions close to 1.0, rather than at a specific water content, and since Mix E and Mix F samples were tested at lower water contents, it is not possible to attribute the increase in compressive strength of the samples manufactured from Mix G and Mix H to the presence of higher suction forces within the samples at the commencement of testing

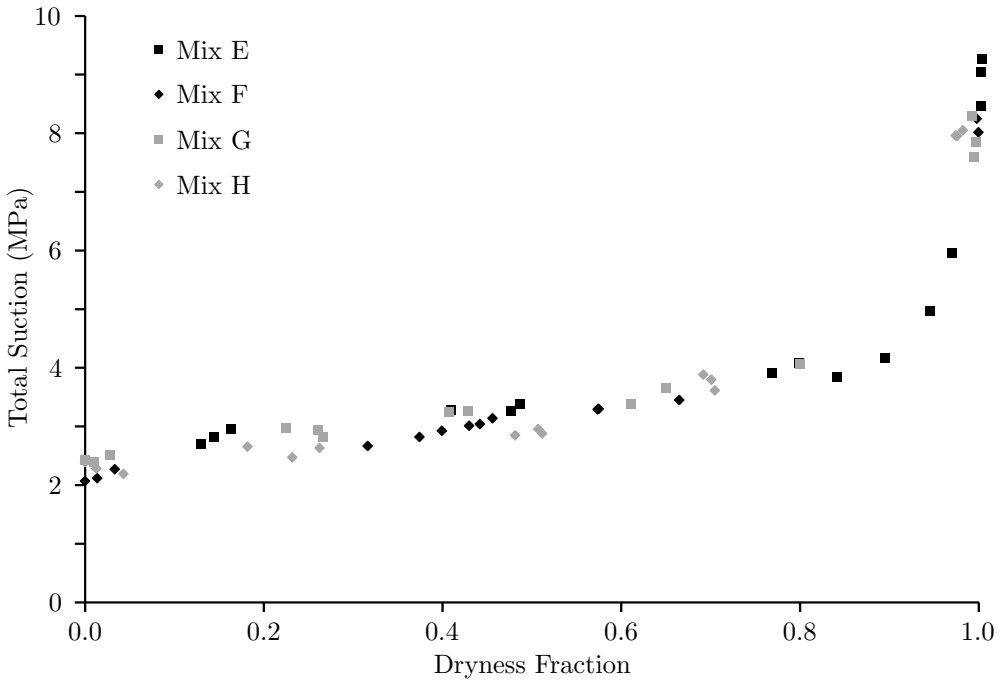

Figure 6.19: Total suction results for all four mixes plotted against dryness fraction.

using the filter paper total suction results obtained in this investigation. Without any measurements of total suction being recorded during the unconfined compression tests it is not possible to consider any changes in suction which may have occurred during compression of the samples and whether this evolution differed with the presence of the expansive plate-like montmorillonite clay particles in Mix G and Mix H. Jaquin et al. (2009) showed that a decrease in suction occurred during shearing of SBCM samples at low initial water contents and it is likely that, given the different structures of the clay particles present in the different mixes investigated in this chapter, that the evolution in suction during compression will have been different for the four sample mixes. It is therefore possible to speculate that this difference in suction evolution will have had a key part to play in the final compressive strength of the dry SBCM samples tested in this investigation although without any experimental data it is not possible to discuss this further. The link between the development of suction forces within any SBCM sample as it dries and the increase in compressive strength of the material has been established for individual SBCM mixes (Jaquin et al., 2009; Bui et al., 2014a) and has been supported by the results presented in this chapter, however it is clear that considerably more work is required, particulary focussing on the evolution of suction within the SBCM samples during loading, before any firm conclusions can be drawn about the effect of different clay types on SBCM compressive strength.

6.5 Summary and conclusions

Unconfined compression constant water content tests and XRCT scans have been performed on multiple clay-sand samples to investigate the development of compressive strength and change in macrostructure of the clay-sand matrix within SBCMs during drying. A highly expansive montmorillonite clay has been added to two of the mixes used to investigate the impact of expansive clay on SBCMs as soils containing expansive clays are currently avoided within the construction industry.

The differences in macrostructure for samples from within a triplicate, manufactured using the same mix of particles and scanned at the same dryness fraction, has been quantified with the total void volume, for voids above $1x10^8 \mu m^3$, varying up to 1.58% of the total volume. This variation between samples within a triplicate has been shown to be greater than any difference between samples containing different proportions of sand and clay, suggesting the differences in macrostructure caused by changes to mix compositions are less significant than the variations caused during sample manufacture. Additionally the evolution of void structure as the material dries has been investigated and Figure 6.10 shows that the magnitude of any change within the void structure is greater for samples containing the expansive montmorillonite clay.

The results from the 56 successful unconfined constant water content tests have provided valuable insights into the differences in compressive strength, both with changing clay:sand ratios and the addition of expansive clay, as well the changes in stiffness and the mode of failure as the SBCM samples dry. Figure 6.15 shows that the stiffness of the samples increases as samples dry and as discussed the wettest samples all exhibit a ductile post-peak failure response whilst brittle failure is observed for samples which have higher dryness fractions. The results shown in Figure 6.17 suggest that an increase in clay content reduces the compressive strength of the SBCM and that the presence of the expansive montmorillonite clay can increase the compressive strength for dried SBCM samples.

The link between total suction and strength has been established in previous SBCM literature (Jaquin et al., 2009; Bui et al., 2014a) and the results plotted in Figure 6.18 show a similar increase in total suction as the samples dry. However the results shown in Figure 6.19, in which very similar total suction - dryness fraction values are measured for the different mixes investigated, and in the associated discussion it is suggested that considerable investigation is still required into the differences in evolution of suction within samples undergoing compression testing, particularly when expansive clays are present.

In conclusion it has been shown that any evolution in macrostructure is amplified when an expansive montmorillonite clay is present, although these changes are of a similar magnitude to the differences occurring during sample manufacture. Additionally, the unconfined compressive strength of the material, for the dry samples, is increased when the expansive montmorillonite clay is present and the results presented in this chapter therefore suggest that the use of expansive clay within SBCMs should not be immediately dismissed by the SBCM industry.

Chapter 7

Concluding remarks

7.1 Thesis summary

Unstabilized soil based construction materials (SBCMs) is a term which captures a broad range of different construction techniques which use earth as their primary building material. As described in Chapter 1 five key stages exist in the construction of all SBCM structures from obtaining the raw soil, through sieving and drying to ensure the soil has the desired particle size distribution and is at the required water content, to the moulding or compaction of the material into shape before the compacted soil is left to dry and strengthen as it equilibrates with the environmental conditions. Despite a developing academic interest in SBCMs over the past decade only a very small number of rigorous, scientific journal articles have been published in which experimental results can be applied to SBCMs in a wider context. Rather than present site or soil specific results and conclusions these articles have improved experimental methods, considered the structural or mechanical response of SBCMs or explored the material's structure. Publications such as Gallipoli et al. (2014) and Augarde et al. (2015) have begun to introduce SBCMs to a wider geotechnical academic community and it is hoped that this will engage new researchers who can build upon key works including Jaquin et al. (2009) and Beckett (2011) which promote the investigation of SBCMs from an unsaturated soils geotechnical perspective, and discuss suction as major component of SBCM's strength. Throughout this thesis the mechanical behaviour and material structure of SBCMs has been investigated using a geotechnical approach, considering the material as a compacted and highly unsaturated soil, and the key elements of unsaturated soil behaviour (including suction, water retention behaviour, compaction and particle mineralogy) required to do this have been presented in Chapter 2.

In Chapters 4, 5 and 6 laboratory x-ray computed tomography (XRCT) has been used to investigate the internal structure of SBCMs and how compressive loading and the presence of expansive clay in the SBCM mix can affect the macrostructure of SBCMs. XRCT is a non-destructive 3D imaging process

capable of imaging internal structures within solid samples to a resolution of less than one micron and can therefore be used to produce quantitative results describing the voids within geotechnical samples. A detailed literature review of the use of XRCT in geotechnical research in Chapter 3, which surveyed three key journals (Géotechnique, Géotechnique Letters and Granular Matter) and the proceedings of two recent international conferences (UNSAT2014 and IS-Cambridge) for all work which used x-ray computed tomography, identified a number of shortcomings in the current use of XRCT within geotechnical literature. This review was followed by an investigation into the suitability of two different XRCT machines (the SkyScan1174 compact micro-CT scanner and the XRadia/Zeiss XRM 410) and three analysis procedures performed using two different software packages (ImageJ and Avizo Fire) which demonstrated that many of these shortcomings could be overcome.

The investigation described in Chapter 4 considered the compressive loading behaviour of four different SBCM mixes. Two different sized SBCM cylinders, 12mm diameter, 24mm high and 28mm diameter, 56mm high, were scanned using a SkyScan1174 compact micro-CT scanner before, during and after compressive loading and the percentage and position of cracks within the sample was analysed following post-processing of the XRCT data using ImageJ. The results obtained show that, through the use of the novel interaction index, existing cracks within a sample propagate through the clay-sand matrix material and away from the aggregations following unconfined compression. The unconfined compression, constant water content test results also showed that the removal of the gravel fraction prior to manufacture can considerably alter the compressive loading behaviour of SBCM samples, changing both the compressive strength and Young's Modulus of all four mixtures investigated.

The XRCT scan results and compression testing performed on three different cylindrical SBCM sample sizes is presented in Chapter 5. The samples (ϕ12, ϕ38 and ϕ100) were scanned using a XRadia/Zeiss XRM 410 before and after unconfined compression constant water content tests. Post-processing of the large field of view and small field of view scans in Avizo Fire produced void size distributions for the SBCMs. The discussion of the results suggests that standard small triaxial samples are well suited for investigating SBCMs using XRCT and, more importantly, enabled a new internal void structure for SBCM samples to be proposed with the role of each void range linked to the compressive strength response of the samples. The double-void macro structure, arising from inter-aggregate voids (between $1x10^7\mu m^3$ and $1x10^9\mu m^3$) caused by the presence of gravel particles and intra-aggregate voids ($>1x10^2\mu m^3$ and $<1x10^6\mu m^3$) within clay-sand aggregations, coupled with the existence of inter-elemental voids between clay particles ($<1x10^2\mu m^3$) results in three distinct void sizes within SBCMs as sketched in Figure 5.14.

The final investigation described in Chapter 6 performed unconfined compression, constant water content tests and XRCT scans on standard small triaxial samples (38mm diameter cylinders, 76mm high) to study the development of compressive strength and the change in macrostructure of the clay-

sand matrix within SBCMs during drying. The use of soil containing expansive clays is currently avoided within the SBCM industry and therefore a highly expansive montmorillonite clay was added to two of the four mixes used to investigate the impact of expansive clay on SBCMs. The results showed that any changes to the macrostructure are amplified when an expansive montmorillonite clay is present however these changes are of a similar magnitude to the differences occurring during sample manufacture. In addition the unconfined compressive strength of dry SBCMs was shown to increase when the expansive montmorillonite clay was present, when compared to the mixes containing a pure kaolinite clay.

For the remainder of this chapter the main conclusions of this thesis are identified, and linked back to the original aims of this research, the key implications of this thesis are then discussed in more detail for those in the SBCM industry and those using XRCT within geotechnical research, before suggestions are made for future research directions.

7.2 Thesis conclusions

In Chapter 1 the primary aim of this research was identified as studying the mechanical behaviour and void structure of SBCMs to provide knowledge to the SBCM industry. In relation to these aims the main conclusions of this thesis are:

- three distinct void volume ranges exist within the SBCM structure: inter-elemental voids between clays ($<1x10^2\mu m^3$), intra-aggregate voids within clay-sand aggregations ($>1x10^2\mu m^3$ and $<1x10^6\mu m^3$) and inter-aggregate voids caused by the gravel fraction (between $1x10^7\mu m^3$ and $1x10^9\mu m^3$);
- existing cracks, or macropores, propagate through the material and away from aggregations following compressive failure;
- the removal of large particles significantly increases the Young's modulus of samples and can also increase the compressive strength of samples when the gravel and clay-silt fractions are more similarly proportioned; and
- any evolution in macrostructure during drying is amplified when expansive clay is present, although these changes are similar in magnitude to the differences due to sample manufacture, and samples containing expansive montmorillonite clay achieve higher compressive strengths when dry.

It was also identified in Chapter 1 that the experience gained from the considerable use of XRCT to study highly unsaturated soil materials can also provide insights for the geotechnical research community. From this thesis five conclusions can be drawn;

- shortcomings exist in the current use of XRCT in geotechnical research, including a lack of information on scanning procedures and a tendency to scan small samples with a narrow particle size distribution;

- care should be taken when scanning soil samples at the limit of an XRCT machine's capabilities and when allowing external time constraints to determine scan settings;
- 38mm triaxial samples can be scanned using the more powerful XRCT scanners (for example the XRadia/Zeiss XRM 410) without requiring modification of existing geotechnical testing procedures or over stretching the current capabilities of XRCT technology;
- automated analysis of XRCT data to produce quantitative results is possible, however these techniques still produce results which require careful interpretation; and
- image resolution, rather than scan pixel size, should be presented when XRCT scan data is discussed.

7.3 Implications for the soil based construction materials industry

The numerous unconfined compression test results described in Chapters 4, 5 and 6 have shown that sieving of the SBCM mixture prior to manufacture, which removes the gravel fraction, significantly alters the mechanical behaviour of SBCMs. This has two major implications, the first on SBCM testing and the second for SBCM construction. In laboratory testing it is desirable to reduce the size of the samples to perform various tests, including shear box and triaxial compression tests, and to perform repeat experiments without needing to construct large SBCM structures however this often requires the removal of the largest particles from the SBCM mixture. The increase in the compressive strength of the samples from which the gravel fraction had been removed in Chapters 4 and 5 show that the sieving of SBCM soil mixtures for smaller samples used in laboratory testing should be avoided wherever possible or its effect acknowledged when compressive strength results on sieved samples are presented. Secondly the increase in compressive strength with the removal of the gravel fraction suggests that further investigation into the use of SBCM mixtures which contain no gravel fraction should be considered for SBCM construction projects. It is acknowledged that the sieving of all the gravel from within a soil dug from site will be a labour intensive and time consuming process, and that the removal of the gravel fraction may have a negative impact on the durability of the structure, however without detailed investigation it is difficult to assess whether these negative impacts outweigh the benefits from increased compressive strength.

The results from Chapter 6 suggest that the presence of expansive montmorillonite clay can increase the compressive strength for dried SBCM samples and any changes to the macro-structure of the SBCM occurring due to the shrinkage of expansive clay during drying is less significant than the variations caused during sample manufacture. The effect of the presence of expansive clays in a SBCM subjected to wetting and drying cycles is unknown however the results regarding the compressive strength when dry, and the lack of cracking during the initial drying of the material following construction, suggest that the use of expansive clay within SBCMs should not be immediately dismissed by the SBCM industry as is

currently the case.

Finally, the use of XRCT in Chapter 5 has shown three distinct void volume ranges exist within the SBCM structure and it is suggested that each of these void volumes are affected by the different particle fractions within a SBCM mix. The inter-aggregate voids, formed due to the presence of the larger gravel particles, adversely affect compressive strength and are the points from which the cracks propagate following material failure. The intra-aggregate voids, controlled by the sand, silt and clay fractions, coupled with the inter-elemental voids, controlled by the mineralogy of the clay, affect the suction developed within the sample and are responsible for the strength of the clay-sand binder matrix and the elastic behaviour of the SBCM prior to compressive failure. By understanding the internal structure of the SBCM and the role of the different soil fractions it is hoped that this should enable better design of SBCM mixes for use in construction projects.

7.4 Implications for geotechnical research using XRCT

The comprehensive review in Section 3.3 identified a number of shortcomings in the current use of XRCT within geotechnical literature including a tendency to scan materials containing no particles smaller than 0.1mm, i.e. the scanning of clay materials is commonly avoided, and the use of resin impregnated cores extracted from larger samples, which removes the non-destructive nature of XRCT scanning. Perhaps more importantly however, to help promote the use of XRCT in geotechnical research, more information regarding scanning and image post-processing procedures is required and more quantitative results should be presented to utilise the full potential of XRCT scanning.

The XRCT scans and quantitative analysis performed throughout this thesis has clearly shown that care should be taken when scanning soil samples within XRCT machines running at the limit of their capability and, as demonstrated by the lack of processable data from scans performed on the 12mm diameter samples in Chapter 4 and the small field of view 100mm diameter samples in Chapter 5, the determining of scan parameters with respect to experimental time constraints, rather than optimum scan settings, can lead to unusable data and should be avoided wherever possible. It is also suggested that for the more powerful XRCT scanners (for example the XRadia/Zeiss XRM 410) 38mm triaxial samples should be scanned, rather than the larger 100mm samples, which will ensure the samples scanned using XRCT do not require modification from existing geotechnical testing procedures without over stretching the current capabilities of XRCT scanning.

Finally, from a data processing and analysis perspective, two key points have been highlighted in this thesis. Firstly all stages within image processing have an impact upon the results obtained and it is important to present the results in a form understood by those reading the published results. Therefore the use of final image resolution to describe the processed XRCT scan data, which will include the effects

of filtering, scan artefacts and any segmentation or phase identification processes performed, rather than the pixel size of a scan, which only reports the XRCT machine scan parameters, should be presented for all quantitative XRCT results. Secondly the image-processing techniques performed using ImageJ and Avizo Fire show that it is possible to perform automated analysis of XRCT data to produce quantitative results with the impact of a human operator minimised, however these techniques are not infallible and can still produce results which require careful interpretation. With minimal discussion of analysis techniques in other geotechnical publications it is hard to develop or establish techniques that will be accepted across the geotechnical community and it is suggested that more discussion of any image-post processing should accompany XRCT results to aid the development of fully automated techniques to produce quantitative results, such as void size distributions, which can aid geotechnical investigations into a wide range of soil materials.

7.5 Future work

The implications of the research presented in this thesis show that there is still considerable work which could be undertaken to further the knowledge of both the SBCM industry and those using XRCT in other geotechnical investigations. Firstly, development of accepted automated XRCT post-processing techniques is essential for the development and acceptance of XRCT scanning within geotechnical research. Particular attention should be paid to the thresholding and segmentation of the distinct phases within soils without the need for human identification and it is suggested that the analysis performed in this thesis using watershed techniques and histogram analysis could be an initial starting point.

Secondly more detailed characterisation of the 'triple-void-structure' of SBCMs is required, using both XRCT and other techniques such as mercury intrusion porosimetry, to establish how the different particle fractions and compaction mechanisms affect the void structure of SBCM structures. It is suggested that particular attention should be paid to how the the gravel fraction, both in its proportion within the mix and its shape (i.e. smooth or angular), affects the largest inter-aggregation voids and whether adjustments to the clay, silt and sand fractions within the SBCM mix can control the intra-aggregate voids. By focussing research on the macro-structure of SBCMs considerable insight could be gained into the development of suction within the sample, which could potentially be used to increase the compressive strength of the clay-sand matrix through careful mix design, and the evolution of the cracks and largest macropores following compression loading, which may enable the negative impact of the gravel fraction on compressive strength to be reduced.

Finally further investigation into the use of expansive clays within SBCM mixes is required. Whilst the results from this thesis suggest that the addition of expansive montmorillonite clay can increase the compressive strength of the clay-sand matrix within SBCMs the effect of different proportions of expan-

sive clay and how its presence affects SBCM mixes containing the gravel fraction should be investigated. Additionally consideration should be given to the impact of wetting and drying cycles typically encountered by SBCM structures, as they adjust to the environmental conditions, on the strength, void structure and suction developed. It is also suggested that research into the durability of SBCMs containing expansive clays or no gravel fraction should be performed and whether the effort required to sieve a raw soil dug from a construction site is worth the benefit of the increased compressive strength also needs investigating.

References

Al-Mukhtar, M., S. Khattab, and J.-F. Alcover (2012). Microstructure and geotechnical properties of lime-treated expansive clayey soil. *Engineering Geology 139140*, 17–27.

Alley, P. (1955). Rammed earth construction. *New Zealand Engineering 10*.

Alonso, E., A. Gens, and A. Josa (1990). A constitutive model for partially saturated soils. *Géotechnique 40*, 405–430(25).

Alonso, E., A. Gens, and W. Yuk Gehling (1994). Elastoplastic model for unsaturated expansive soils. *Proceedings of the 3rd European Conference on Numerical Methods in Geotechnical Engineering*, 11–18.

Alonso, E., E. Romero, and C. Hoffmann (2011). Hydromechanical behaviour of compacted granular expansive mixtures: experimental and constitutive study. *Géotechnique 61*, 329–344(15).

Alonso, E., J. Vaunat, and A. Gens (1999). Modelling the mechanical behaviour of expansive clays. *Engineering Geology 54*(12), 173 – 183.

Atkinson, B. (1987). *Fracture mechanics of rock*. Academic Press, London (UK).

Augarde, C. (2015). Earthen construction: A geotechnical engineering perspective. *Proceedings from ICREC2015 Conference: Rammed Earth Construction*, 17–25.

Augarde, C., J. Smith, A. Corbin, D. Ciancio, C. Beckett, and P. Jaquin (in press 2015). Geotechnical aspects of earthen construction materials. *Proceedings of the XVI European Conference on Soil Mechanics and Geotechnical Engineering*.

Bailey, S. (1971). Summary of national and international recommendations on clay mineral nomenclature. *Clays and Clay Minerals 19*, 129–132.

Baker, R. and S. Frydman (2009). Unsaturated soil mechanics: Critical review of physical foundations. *Engineering Geology 106*(12), 26 – 39.

Baruchel, J., J.-Y. Buffiere, P. Cloetens, M. D. Michiel, E. Ferrie, W. Ludwig, E. Maire, and L. Salvo (2006). Advances in synchrotron radiation microtomography. *Scripta Materialia 55*(1), 41 – 46.

Baveye, P. C., M. Laba, W. Otten, L. Bouckaert, P. D. Sterpaio, R. R. Goswami, D. Grinev, A. Houston, Y. Hu, J. Liu, S. Mooney, R. Pajor, S. Sleutel, A. Tarquis, W. Wang, Q. Wei, and M. Sezgin (2010). Observer-dependent variability of the thresholding step in the quantitative analysis of soil images and x-ray microtomography data. *Geoderma 157*(12), 51 – 63.

Beckett, C. (2011). The role of material structure in compacted earthen building materials implications for design and construction. *PhD Thesis, Durham University*.

Beckett, C. and C. Augarde (2011). A novel image-capturing technique for the experimental study of soil deformations during compaction. *Geotechnical Testing Journal 34*(6), 571 – 578.

Beckett, C., M. Hall, and C. Augarde (2013). Macrostructural changes in compacted earthen construction materials under loading. *Acta Geotechnica 8*(4), 423–438.

Brewer, R. (1964). *Fabric and mineral analysis of soils*. Wiley, New York.

British-Standards (1990). *BS1377-4:1990 - part 7: Shear strength tests (total stress)*. BS1377-4:1990 - part 7: Shear strength tests (total stress).

British-Standards (2002). EN ISO 14688: 2002: Geotechnical investigation and testing–identification and classification of soil. *British Standards Institution, London*.

Bruchon, J., J. Pereira, M. Vandamme, N. Lenoir, P. Delage, and M. Bornert (2013). X-ray microtomography characterisation of the changes in statistical homogeneity of an unsaturated sand during imbibition. *Géotechnique Letters 3*, 84–88(4).

Buades, A., B. Coll, and J.-M. Morel (2005). A non-local algorithm for image denoising. In *IEEE Computer Society Conference on Computer Vision and Pattern Recognition*, Volume 2, pp. 60–65.

Bui, Q.-B., J.-C. Morel, S. Hans, and P. Walker (2014a). Effect of moisture content on the mechanical characteristics of rammed earth. *Construction and Building Materials 54*, 163 – 169.

Bui, T.-T., Q.-B. Bui, A. Limam, and S. Maximilien (2014b). Failure of rammed earth walls: From observations to quantifications. *Construction and Building Materials 51*, 295 – 302.

Ciancio, D. and C. Augarde (2013). Capacity of unreinforced rammed earth walls subject to lateral wind force: elastic analysis versus ultimate strength analysis. *Materials and Structures 46*(9), 1569–1585.

Ciancio, D., C. Beckett, and J. Carraro (2014). Optimum lime content identification for lime-stabilised rammed earth. *Construction and Building Materials 53*, 59 – 65.

Ciancio, D. and J. Gibbings (2012). Experimental investigation on the compressive strength of cored and molded cement-stabilized rammed earth samples. *Construction and Building Materials 28*, 294–304.

Ciancio, D., P. Jaquin, and P. Walker (2013). Advances on the assessment of soil suitability for rammed earth. *Construction and Building Materials 42*, 40 – 47.

Cnudde, V. and M. Boone (2013). High-resolution x-ray computed tomography in geosciences: A review of the current technology and applications. *Earth-Science Reviews 123*, 1–17.

Collins, K. and A. McGown (1974). The form and function of microfabric features in a variety of natural soils. *Géotechnique 24*, 223–254(31).

Dachverband, L. e., F. Volhard, and U. Rhlen (1999). *Lehmbau Regeln. Begriffe; Baustoffe; Bauteile.* Braunschweig/Wiesbaden, Germany.

Dehandschutter, B., S. Vandycke, M. Sintubin, N. Vandenberghe, and L. Wouters (2005). Brittle fractures and ductile shear bands in argillaceous sediments: inferences from oligocene boom clay (belgium). *Journal of Structural Geology 27*(6), 1095 – 1112.

Delgado, M. C. J. and I. C. Guerrero (2007). The selection of soils for unstabilised earth building: A normative review. *Construction and Building Materials 21*(2), 237 – 251.

Diamond, S. et al. (1970). Pore size distributions in clays. *Clays and clay minerals 18*(1), 7–23.

Eberl, D., V. Farmer, and R. Barrer (1984). Clay mineral formation and transformation in rocks and soils [and discussion]. *Philosophical Transactions of the Royal Society of London. Series A, Mathematical and Physical Sciences 311*(1517), 241–257.

FEI (2013). Avizo 8: Avizo's user guiide. URL: http://vsg3d.com/sites/default/files/AvizoUsersGuide.pdf (accessed 07/11/14).

FEI (2014). Avizo 3d software. URL: http://www.fei.com/software/avizo3d/ (accessed 31/10/2014).

Ferreira, T. and W. Rasband (2012). Imagej user guide. URL: http://rsbweb.nih.gov/ij/docs/guide/146.html (accessed 06/11/14).

Fityus, S. and O. Buzzi (2009). The place of expansive clays in the framework of unsaturated soil mechanics. *Applied Clay Science 43*(2), 150 – 155.

Fonseca, J., C. O'Sullivan, M. Coop, and P. Lee (2013). Quantifying the evolution of soil fabric during shearing using scalar parameters. *Géotechnique 63*, 818–829.

Fredlund, D. G., D. Sheng, and J. Zhao (2011, FEB). Estimation of soil suction from the soil-water characteristic curve. *Canadian Geotechnical Journal 48*(2), 186–198.

Gallipoli, D., A. Bruno, C. Perlot, and N. Salmon (2014). Raw earth construction: is there a role for unsaturated soil mechanics? *Proceedings from UNSAT2014 Conference: Unsaturated Soils: Research & Applications 1*, 55–62.

Gallipoli, D., A. Gens, R. Sharma, and J. Vaunat (2003). An elasto-plastic model for unsaturated soil incorporating the effects of suction and degree of saturation on mechanical behaviour. *Géotechnique 53*, 123–135(12).

Gens, A. (2010). Soil & environment interactions in geotechnical engineering. *Géotechnique 60*, 3–74(71).

Gens, A. and E. Alonso (1992). A framework for the behaviour of unsaturated expansive clays. *Canadian Geotechnical Journal 29*(6), 1013–1032.

Gens, A., L. N. Guimaraes, A. Garcia-Molina, and E. Alonso (2002). Factors controlling rockclay buffer interaction in a radioactive waste repository. *Engineering Geology 64*(23), 297 – 308.

Gens, A., B. Valleján, M. Sánchez, I. C., M. Villar, and M. Van-Geet (2011). Hydromechanical behaviour of a heterogeneous compacted soil: experimental observations and modelling. *Géotechnique 61*, 367–386(19).

Goldman, L. W. (2007). Principles of CT and CT Technology. *Journal of Nuclear Medicine Technology 35*(3), 115–128.

Grabowska-Olszewska, B. (2003). Modelling physical properties of mixtures of clays: example of a two-component mixture of kaolinite and montmorillonite. *Applied Clay Science 22*(5), 251 – 259.

Hall, M. and Y. Djerbib (2004). Rammed earth sample production: context, recommendations and consistency. *Construction & Building Materials 18*(4), 281–286.

Hall, M., S. Mooney, C. Sturrock, P. Matelloni, and S. Rigby (2013). An approach to characterisation of multi-scale pore geometry and correlation with moisture storage and transport coefficients in cement-stabilised soils. *Acta Geotechnica 8*(1), 67–79.

Helliwell, J., C. Sturrock, K. Grayling, S. Tracy, R. Flavel, I. Young, W. Whalley, and S. Mooney (2013). Applications of x-ray computed tomography for examining biophysical interactions and structural development in soil systems: a review. *European Journal of Soil Science 64*(3), 279–297.

Hendee, W. (1979). *Medical Radiation Physics 2nd edn.*, pp. 517. Year Book Medical Publishers, Chicago.

Holmes, J. W. (1955). Water sorption and swelling of clay blocks. *Journal of Soil Science 6*(2), 200–208.

Houben, H. and H. Guillaud (1989). *Earth Construction: A comprehensive guide*. Earth Construction Series. ITDG Publishing, London (UK).

Iassonov, P., T. Gebrenegus, and M. Tuller (2009). Segmentation of x-ray computed tomography images of porous materials: A crucial step for characterization and quantitative analysis of pore structures. *Water Resources Research 45*(9).

Imerys (2008). *DAT002K Speswhite data sheet*. IMERYS Performance Minerals.

Jacobs, P. and V. Cnudde (2009). Applications of x-ray computed tomography in engineering geology or looking inside rocks . *Engineering Geology 103*(34), 67–68.

Jaquin, P. and C. Augarde (2012). *Earth building: history, science and conservation*. IHS BRE Press, Watford, UK.

Jaquin, P., C. Augarde, D. Gallipoli, and D. Toll (2009). The strength of unstabilised rammed earth materials. *Géotechnique 59*(5), 487–490.

Jaquin, P., C. Augarde, and C. Gerrard (2008). Chronological description of the spatial development of rammed earth techniques. *International Journal of Architectural Heritage 4*, 377–400.

Jaquin, P., C. Augarde, and L. Legrand (2008). Unsaturated characteristics of rammed earth. *Unsaturated soils: advances in geo-engineering: proceedings of the 1st European Conference on Unsaturated Soils*, 417–422.

Karube, D. and K. Kawai (2001). The role of pore water in the mechanical behavior of unsaturated soils. *Geotechnical & Geological Engineering 19*(3-4), 211–241.

Keable, J. (1996). *Rammed earth structures : a code of practice*. Intermediate Technology Publications, London (UK).

Ketcham, R. and W. Carlson (2001). Acquisition, optimization and interpretation of x-ray computed tomographic imagery: applications to the geosciences. *Computers & Geosciences 27*(4), 381–400.

Kruth, J., M. Bartscher, S. Carmignato, R. Schmitt, L. De Chiffre, and A. Weckenmann (2011). Computed tomography for dimensional metrology. *CIRP Annals - Manufacturing Technology 60*(2), 821–842.

Lilley, D. and J. Robinson (1995). Ultimate strength of rammed earth walls with openings. *Proceedings of the ICE - Structures and Buildings 110*, 278–287(9).

Lu, N. and W. J. Likos (2004). *Unsaturated soil mechanics*. J. Wiley.

Maniatidis, V. and P. Walker (2003). A review of rammed earth construction. *DTI Project Report*.

Maniatidis, V. and P. Walker (2008). Structural capacity of rammed earth in compression. *Journal of Materials in Civil Engineering 20*(3), 230–238.

Marcelino, V., V. Cnudde, S. Vansteelandt, and F. Car (2007). An evaluation of 2d-image analysis techniques for measuring soil microporosity. *European Journal of Soil Science 58*(1), 133–140.

Marshall, C. (1964). *The physical chemistry and mineralogy of soils.* The Physical Chemistry and Mineralogy of Soils. Wiley, New York.

Mašín, D. (2013). Double structure hydromechanical coupling formalism and a model for unsaturated expansive clays. *Engineering Geology 165*, 73 – 88. Special Issue: Research and Applications in Unsaturated Soil Mechanics.

MATLAB (2011). *version 7.12.0 (R2011a).* Natick, Massachusetts: The MathWorks Inc.

McGarry, D. and K. Malafant (1987). The analysis of volume change in unconfined units of soil. *Soil Science Society of America Journal 51*, 290–297.

McHenry, P. (1984). *Adobe and Rammed Earth Buildings: Design and Construction.* University of Arizona Press.

Miccoli, L., U. Müller, and P. Fontana (2014). Mechanical behaviour of earthen materials: A comparison between earth block masonry, rammed earth and cob. *Construction and Building Materials 61*, 327 – 339.

Miller, E. E. (1975). Physics of swelling and cracking soils. *Journal of Colloid and Interface Science 52*(3), 434 – 443.

Mitchell, J. and K. Soga (2005). *Fundamentals of Soil Behavior, 3rd Edition.* John Wiley and Sons.

Monroy, R., L. Zdravkovic, and A. Ridley (2010). Evolution of microstructure in compacted london clay during wetting and loading. *Géotechnique 60*, 105–119(14).

Nehdi, M. (2014). Clay in cement-based materials: Critical overview of state-of-the-art. *Construction and Building Materials 51*, 372 – 382.

New-Mexico-Standards (1991). *New Mexico Adobe and Rammed Earth Building Code.* Regulation & Licencensing Department, New Mexico (USA).

Norton, J. (1997). *Building with Earth: A Handbook.* Intermediate Technology.

Nowamooz, H. and C. Chazallon (2011). Finite element modelling of a rammed earth wall. *Construction and Building Materials 25*(4), 2112 – 2121.

Nuth, M. and L. Laloui (2008). Advances in modelling hysteretic water retention curve in deformable soils. *Computers and Geotechnics 35*(6), 835 – 844.

Oda, M., T. Takemura, and M. Takahashi (2004). Microstructure in shear band observed by microfocus x-ray computed tomography. *Géotechnique 54*, 539–542(3).

Olsen, H. (1962). Hydraulic flow through saturated clay. *Proceedings of the ninth national conference on Clays and Clay minerals*, 131–161.

Orense, R., M. Pender, M. Hyodo, and Y. Nakata (2013). Micro-mechanical properties of crushable pumice sands. *Géotechnique Letters 3*, 67–71(4).

Parcher, J. and P. Liu (1966). Some swelling characteristics of compacted clays. *Journal of Soil Mechanics and Foundations Div, American Society of Civil Engineers 92*(SM4), 73–75.

Pedrotti, M. and A. Tarantino (2014). Physicochemical conceptual model on reversible and non-reversible volumetric variations in non-swelling clays. *Proceedings of the TC105 ISSMGE International symposium on Geomechanics from Micro to Macro*, 845–850.

Pender, M., R. Orense, and N. Kikkawa (2014). Japanese and new zealand pumice sands: Comparison of particle shapes and surface void structures. *Proceedings of the TC105 ISSMGE International symposium on Geomechanics from Micro to Macro*, 1111–1116.

Philip, J. R. (1969). Hydrostatics and hydrodynamics in swelling soils. *Water Resources Research 5*(5), 1070–1077.

Philip, J. R. (1977). Unitary approach to capillary condensation and adsorption. *The Journal of Chemical Physics 66*(11), 5069–5075.

Powrie, W. (2004). *Soil Mechanics: Concepts and Applications*. Spon Press.

Proctor, R. (1933). Fundamental principles of soil compaction. *Engineering News Record 111*(9), 245–248.

Reimers, P. and J. Goebbels (1983)). New possibilities of non-destructive evaluation by x-ray computed tomography. *Materials Evaluation 41*, 732737.

Romero, E., A. Gens, and A. Lloret (1999). Water permeability, water retention and microstructure of unsaturated compacted boom clay. *Engineering Geology 54*(1), 117–127.

Romero, E. and P. Simms (2008). Microstructure investigation in unsaturated soils: A review with special attention to contribution of mercury intrusion porosimetry and environmental scanning electron microscopy. *Geotechnical and Geological Engineering 26*(6), 705–727.

Rondeau, X., C. Affolter, L. Komunjer, D. Clausse, and P. Guigon (2003). Experimental determination of capillary forces by crushing strength measurements. *Powder Technology 130*(13), 124 – 131.

Sánchez, M., A. Gens, L. do Nascimento Guimarães, and S. Olivella (2005). A double structure generalized plasticity model for expansive materials. *International Journal for Numerical and Analytical Methods in Geomechanics 29*(8), 751–787.

Schindelin, J., I. Arganda-Carreras, E. Frise, V. Kaynig, M. Longair, T. Pietzsch, S. Preibisch, C. Rueden, B. Saalfeld, Stephan Schmid, J.-Y. Tinevez, D. J. White, V. Hartenstein, K. Eliceiri, P. Tomancak, and A. Cardona (2012). Fiji: an open-source platform for biological-image analysis. *Nature Methods 9*, 676–682.

Schneider, C., W. Rasband, and K. Eliceiri (2012). NIH Image to ImageJ: 25 years of image analysis. *Nature Methods 9*, 671–675.

Sheng, D. (2011). Constitutive modelling of unsaturated soils: Discussion of fundamental principles. *Unsaturated soils - Alonso EE, & Gens A, (eds) - CRC Press.*, 91 – 112.

Silva, R. A., D. V. Oliveira, T. Miranda, N. Cristelo, M. C. Escobar, and E. Soares (2013). Rammed earth construction with granitic residual soils: The case study of northern portugal. *Construction and Building Materials 47*, 181 – 191.

Sivakumar, V., W. Tan, E. Murray, and M. J.D. (2006). Wetting, drying and compression characteristics of compacted clay. *Géotechnique 56*, 57–62(5).

SkyScan-Brucker (2011). Nrecon user manual. URL: http://www.skyscan.be/next/NReconUserGuide.pdf (accessed 06/11/14).

SkyScan-Brucker (2012). Skyscan, x-ray microtomography. *SkyScan Product Brochure*.

Smith, J. and C. Augarde (2013a). A new classification for soil mixtures with application to earthen construction. *ECS Technical Report ECS-TR 2013/04, Published 20.09.2013.*

Smith, J. and C. Augarde (2013b). Optimum water content tests for earthen construction materials. *Proceedings of the ICE - Construction Materials 167*, 114–123.

Smith, J. and C. Augarde (2014). Xrct scanning of unsaturated soils: Microstructure at different scales? *Proceedings of the TC105 ISSMGE International symposium on Geomechanics from Micro to Macro*, 1137–1142.

Smith, J., C. Augarde, and C. Beckett (2014). The use of xrct to investigate highly unsaturated soil mixtures. *Proceedings from UNSAT2014 Conference: Unsaturated Soils: Research & Applications 1*, 719–726.

Standards-Australia (2002). *The Australian Earth Building Handbook*. SAI Global Ltd, Sydney (Australia).

Standards New Zealand (1998). NZS 4298: 1998 materials and workmanship for earth buildings incorporating amendment no. 1. *Standards New Zealand, Wellington, New Zealand*.

Strege, S., A. Weuster, H. Zetzener, L. Brendel, A. Kwade, and D. Wolf (2014). Approach to structural anisotropy in compacted cohesive powder. *Granular Matter 16*(3), 401–409.

Taina, I., R. Heck, and T. Elliot (2008). Application of x-ray computed tomography to soil science: A literature review. *Canadian Journal of Soil Science 88*(1), 1–19.

Tarantino, A. (2007). A possible critical state framework for unsaturated compacted soils. *Géotechnique 57*, 385–389(4).

Tarantino, A. (2009, NOV). A water retention model for deformable soils. *Géotechnique 59*(9), 751–762.

Tarantino, A. and S. Tombolato (2005, MAY). Coupling of hydraulic and mechanical behaviour in unsaturated compacted clay. *Géotechnique 55*(4), 307–317.

Taylor, H., C. O'Sullivan, and W. Sim (2014). Challenges in analyzing micro-ct images of dam filter materials. *Proceedings of the TC105 ISSMGE International symposium on Geomechanics from Micro to Macro*, 1147–1152.

Taylor, P., R. Fuller, and M. Luther (2008). Energy use and thermal comfort in a rammed earth office building. *Energy and Buildings 40*(5), 793 – 800.

Teasdale, D. and D. Hughes (1999). The glacial history of north east england. *Quaternary Research Association Field Guide to North East England*.

Thom, R., R. Sivakumar, V. Sivakumar, E. Murray, and P. Mackinnon (2007). Pore size distribution of unsaturated compacted kaolin: the initial states and final states following saturation. *Géotechnique 57*, 469–474(5).

Thompson, M. L., P. Singh, S. Corak, and W. E. Straszheim (1992). Cautionary notes for the automated analysis of soil pore-space images. *Geoderma 53*(34), 399 – 415.

Tolsa (2008). *Technical Information GWB Wyoming Bentonite data sheet, Issue 2*. Tolsa UK Limited.

Tuller, M., D. Or, and L. M. Dudley (1999). Adsorption and capillary condensation in porous media: Liquid retention and interfacial configurations in angular pores. *Water Resources Research 35*(7), 1949–1964.

Van Olphen, H. (1977). *An introduction to clay colloid chemistry: for clay technologists, geologists, and soil scientists*. Wiley Interscience publication. Wiley, New York.

Walker, P., R. Keable, J. Martin, and V. Maniatidis (2005). *Rammed earth : design and construction guidelines*. BRE Bookshop, Watford.

Wellington, S. and H. Vinegar (1987). X-Ray Computerized-Tomography. *Journal of Petroleum Technology 39*(8), 885–898.

XRadia-Inc. (2011). Imaging for science and innovation. *XRadia Product Brochure*.

Yan, Y., Y. Shi, T. Mukunoki, T. Sato, and J. Otani (2014). Visualisation of grain crushing using micro-focused X-ray CT scanning. *Proceedings of the TC105 ISSMGE International symposium on Geomechanics from Micro to Macro*, 1131–1136.

Yong, R. and D. Sheeran (1973). Fabric unit interaction and soil behaviour. *Proceedings of the International Symposium on Soil Structure*, 176–183.

Zacher, G., T. Paul, M. Halisch, and P. Westenberger (2014). Qualitative and quantitative investigation of soils and porous rocks by using very high resolution x-ray micro-ct imaging. *Proceedings from UNSAT2014 Conference: Unsaturated Soils: Research & Applications 1*, 699–702.

Zhao, B., J. Wang, and M. Coop (2014). Investigation of the fracture behaviour of individual lbs particle using nanofocus x-ray ct. *Proceedings of the TC105 ISSMGE International symposium on Geomechanics from Micro to Macro*, 1125–1130.